Universität Hamburg

DER FORSCHUNG | DER LEHRE | DER BILDUNG

Advancing the Perturbative Description of the Electroweak Phase Transition: Loops, Bubbles and Gravitational Waves

Dissertation

zur Erlangung des Doktorgrades

an der Fakultät für Mathematik, Informatik und Naturwissenschaften

Fachbereich Physik der Universität Hamburg

vorgelegt von

Andrii Dashko

Hamburg

2026

Gutachter/innen der Dissertation:	Prof. Dr. Georg Weiglein Prof. Dr. Geŕaldine Servant
Zusammensetzung der Prüfungskommission:	Prof. Dr. Georg Weiglein Prof. Dr. Geŕaldine Servant Dr. Thomas Konstandin Prof. Dr. Thomas Kupfer Prof. Dr. Michael Potthoff
Vorsitzende/r der Prüfungskommission:	Prof. Dr. Michael Potthoff
Datum der Disputation:	1. Juni 2026
Vorsitzender des Fach-Promotionsausschusses PHYSIK:	Prof. Dr. Johannes Haller
Leiter des Fachbereichs PHYSIK:	Prof. Dr. Markus Drescher
Dekan der Fakultät MIN:	Prof. Dr.-Ing. Norbert Ritter

Declaration on oath

I hereby declare and affirm that this doctoral dissertation is my own work and that I have not used any aids and sources other than those indicated.

If electronic resources based on generative artificial intelligence (gAI) were used in the course of writing this dissertation, I confirm that my own work was the main and value-adding contribution and that complete documentation of all resources used is available in accordance with good scientific practice. I am responsible for any erroneous or distorted content, incorrect references, violations of data protection and copyright law or plagiarism that may have been generated by the gAI.

Date: _____

Signature of doctoral candidate: _____

ABSTRACT

The nature of the electroweak phase transition (EWPT) in the early Universe plays a central role in connecting particle physics with cosmology. In the Standard Model (SM), the EWPT is a smooth crossover, forbidding electroweak baryogenesis and yielding no observable gravitational-wave (GW) signal. In contrast, many SM extensions allow for a strong first-order EWPT, opening the possibility of explaining the baryon asymmetry and generating stochastic GW backgrounds.

This thesis investigates the EWPT in Beyond the SM (BSM) scenarios, focusing on the challenge of reliably determining thermodynamic observables by reducing the remaining theoretical uncertainties. To address this, different perturbative approaches are contrasted, in particular conventional four-dimensional (4D) finite-temperature methods and a dimensionally reduced three-dimensional (3D) effective field theory (EFT) framework exploiting the separation of thermal scales.

In the complex singlet extension of the SM (cxSM) featuring a strong first-order EWPT, we employ residual gauge and scale dependence as a diagnostic tool to quantify theoretical uncertainties, showing that the 3D EFT framework yields more robust predictions within the regime of validity of the EFT expansion.

In the 3D EFT framework, we derive the renormalization group evolution of the effective couplings for the 3D EFT of the Standard Model Effective Field Theory (SMEFT), systematically incorporating higher-dimensional operators. This enables consistent resummation of logarithmic corrections and paves the way for more precise perturbative calculations and lattice simulations of the EWPT.

Furthermore, we develop a systematic framework to incorporate one-loop corrections into the nucleating bubble wall equation of motion, thereby enhancing the accuracy and reliability of bubble wall velocity calculations.

Overall, this thesis advances the precision program for EWPT studies by systematically addressing theoretical uncertainties, improving perturbative frameworks, and refining GW predictions. These developments are crucial for interpreting future observations, particularly from experiments such as LISA, and for using GWs as a probe of new physics in the early Universe.

ZUSAMMENFASSUNG

Die Natur des elektroschwachen Phasenübergangs (EWPT) im frühen Universum spielt eine zentrale Rolle bei der Verbindung von Teilchenphysik und Kosmologie. Im Standardmodell (SM) verläuft der EWPT als kontinuierlicher Crossover, was elektroschwache Baryogenese ausschließt und keine beobachtbaren Gravitationswellen (GW) zur Folge hat. Im Gegensatz dazu ermöglichen viele SM-Erweiterungen einen starken Phasenübergang erster Ordnung, wodurch sich die Möglichkeit ergibt, die Baryonenasymmetrie zu erklären und wodurch stochastische GW-Hintergründe erzeugt werden können.

Diese Arbeit untersucht den EWPT in Szenarien jenseits des SM (BSM) und konzentriert sich auf die Herausforderung, thermodynamische Observablen durch eine Verbesserung der theoretischen Unsicherheiten zuverlässig zu bestimmen. Dazu werden verschiedene perturbative Ansätze verglichen, insbesondere konventionelle vierdimensionale (4D) Methoden bei endlicher Temperatur und eine dimensionsreduzierte dreidimensionale (3D) effektive Feldtheorie (EFT), die die Trennung thermischer Skalen ausnutzt.

In der komplexen Singulett-Erweiterung des SM (cxSM) mit starkem Phasenübergang erster Ordnung verwenden wir die verbleibende Eich- und Skalenabhängigkeit als diagnostisches Werkzeug zur Quantifizierung theoretischer Unsicherheiten. Dabei zeigt sich, dass der 3D EFT-Rahmen innerhalb des Gültigkeitsbereichs der EFT-Anwendung robustere Vorhersagen liefert. Im Rahmen der 3D EFT leiten wir die Renormierungsgruppenevolution der effektiven Kopplungen für die 3D EFT der Standardmodell-Effektiven Feldtheorie (SMEFT) her und berücksichtigen dabei in systematischer Weise höherdimensionale Operatoren. Dies ermöglicht eine konsistente Resummation logarithmischer Korrekturen und ebnet den Weg für präzisere perturbative Rechnungen und Gitter-Simulationen des EWPT. Darüber hinaus entwickeln wir ein systematisches Rahmenwerk, um Ein-Schleifen-Korrekturen in die Bewegungsgleichung der Begrenzungsfläche der gebrochenen Phase einzubeziehen und so die Genauigkeit und Zuverlässigkeit der Berechnung der Geschwindigkeit der Begrenzungsfläche zu erhöhen.

Insgesamt trägt diese Arbeit zum Präzisionsprogramm für EWPT-Studien bei, indem sie theoretische Unsicherheiten systematisch untersucht, perturbative Methoden verbessert und GW-Vorhersagen verfeinert. Diese Entwicklungen sind entscheidend für die Interpretation zukünftiger experimenteller Ergebnisse, insbesondere von Experimenten wie LISA, und für die Nutzung von GWs für die Suche neuer Physik im frühen Universum.

ACKNOWLEDGMENTS

First and foremost, I would like to thank my PhD supervisor, Georg Weiglein, for the guidance, support, and freedom to explore that he provided throughout my PhD. His mentorship has been invaluable in shaping my research and helping me grow as a scientist.

I want to express my gratitude to Géraldine Servant for co-supervising and providing direction during my PhD, to Thomas Konstandin for offering expert advice on topics relating to this thesis and beyond, and for mentoring me as a young researcher. I also thank to Michael Potthoff and Thomas Kupfer for being part of my thesis committee and for their valuable feedback on this thesis.

I am deeply indebted to Maximilian Löschner for countless hours of physics discussions, for catching innumerable mistakes in my calculations, for his day-to-day guidance, and, most importantly, for helping me enjoy life in Hamburg and all the memorable bike trips with matjes.

Special mention goes to Andreas Ekstedt, who always had profound replies to my queries and insightful research ideas to pursue. I also thank Thomas Biekötter, who I worked with from my very first day as a PhD student and who brought structure to my research, and Guilherme Guedes, who I asked countless silly questions and always got unsilly answers. I truly appreciate the opportunity to have worked with each of them.

I want to thank all the wonderful people I met during my time at DESY, among others: my office mates Carlo and Jonas, and my across-the-corridor neighbours Mathias and Guilherme, for helping me settle into research life; and the whole 2HDM working group — Alain, Romal, Fran, Johannes, Felix, Mohamed, Marten, Monika, Panos, Julia, Kateryna, Max — for weekly working group meetings and 4:20 coffee breaks, both of which helped me solve many puzzles in my head.

Special thanks to Panos for keeping his door always open for me to annoy him with endless bugs I encounter, and for all the bananas he got me throughout these years. I thank Julia for endless unforgettable memories we collected and limitless stories to gossip about. I thank Kateryna, my academic sister, for making my stay in Hamburg joyful and for being a close friend always available.

I gratefully acknowledge the support of DESY, the Universität Hamburg, and the Cluster of Excellence “Quantum Universe” for funding my doctoral research and enabling my

participation in numerous scientific conferences and workshops.

I am deeply grateful to Mikael Chala for motivating me to pursue new projects, for inviting me to work in Granada, and for making my integration into the new workplace smooth. I also thank everyone in FTAE in Granada for their warm welcome. I specifically thank Andrea, Luis and Renato for insightful conversations on physics and beyond, and for helping me navigate daily life in Granada.

I also want to thank Panos, Max, Miki, Luis, Andrea and Renato for taking the time to review this thesis, for their valuable feedback, and for making me think of details I never thought of before.

I thank my dear friend Dmytro for making sure my knowledge of hadron physics is sharp enough to answer all of his spontaneous questions, and my close friend Nazar for making me feel supported and knowing that I can always count on him. I thank both of them for many adventures we got into through these years, and for always taking the time to discuss life matters and simply being there when I needed it the most. I also thank Dmytro and Priyanka for preserving my theory–experiment life balance and for always making feel so welcome.

Lastly, I would like to thank my family — my parents and grandparents — for their unconditional love and support before, during, and after my PhD; for giving me a moral compass, guiding me through difficult decisions, and keeping me focused during hard times.

In closing, and most importantly, I want to express my deepest gratitude to all those who have kept, and continue to keep, my home, my family, and myself safe. To those I know, and those I do not, who fight to defend Ukraine, I extend my heartfelt thanks — without them, this thesis would never have come to life.

Я хочу подякувати своїй родині — батькам і бабусям та дідусям — за їхню безумовну любов і підтримку до, під час та після моєї аспірантури; за те, що дали мені моральний компас, який допомагає у важких рішеннях; та за те, що допомагали мені залишатися зосередженим у ці складні часи. Я дякую усім друзям і колегам, які підтримували мене протягом цих років, за їхню дружбу, поради та допомогу у вирішенні як наукових, так і життєвих питань.

На завершення, і найважливіше, я хочу висловити найглибшу вдячність усім, хто береже і продовжує берегти мій дім, мою родину та мене. Тим, кого я знаю особисто, і тим, кого не знаю, хто бореться за захист України, я висловлюю щиру подяку — без них ця дисертація ніколи б не з'явилася на світ.

PUBLICATIONS

This thesis is based on the following publications [1–4]:

[1] Andrii Dashko and Andreas Ekstedt. "Bubble-wall speed with loop corrections". In: *JHEP* 03 (2025), p. 024. DOI: 10.1007/JHEP03(2025)024. arXiv: 2411.05075 [hep-ph].

[2] Mikael Chala, Andrii Dashko, and Guilherme Guedes. "Running couplings in high-temperature effective field theory". In: *Phys. Rev. D* 113.5 (2026), p. 055026. DOI: 10.1103/ptqg-5g38. arXiv: 2510.26878 [hep-ph].

[3] Thomas Biekötter, Andrii Dashko, Maximilian Löschner, and Georg Weiglein. "Perturbative aspects of the electroweak phase transition with a complex singlet and implications for gravitational wave predictions". In: (Nov. 2025). arXiv: 2511.14831 [hep-ph].

[4] Andrii Dashko and Maximilian Löschner. *Work in Progress.*

CONTENTS

CONVENTIONS

We work in natural units, $\hbar = c = k_B = 1$, unless specified otherwise, with all dimensionful quantities expressed in powers of energy (eV), where $1\,\text{eV} = 1.602 \times 10^{-19}\,\text{J}$.

The mostly-minus Minkowski metric is used,

$$\eta_{\mu\nu} = \text{diag}(+,-,-,-), \quad ds^2 = dt^2 - d\vec{x}^{\,2}.$$

Greek indices are spacetime, $a^\mu = (a^0, \vec{a})$, with Lorentz-invariant inner product $a \cdot b = a^\mu b_\mu = a^0 b^0 - \vec{a} \cdot \vec{b}$; Latin indices are spatial, $\vec{a} \cdot \vec{b} = \delta_{ij} a^i b^j$. Repeated indices are summed over their full range.

The d'Alembertian is $\Box \equiv \partial^2 \equiv \partial_\mu \partial^\mu = \partial_t^2 - \nabla^2$. A Wick rotation is performed as $t \to -it_E$, after which $\partial^2 \to -\partial_E^2$.

Dirac matrices satisfy $\{\gamma^\mu, \gamma^\nu\} = 2\eta^{\mu\nu}$, with $\gamma^5 = i\gamma^0\gamma^1\gamma^2\gamma^3$ and Feynman slash notation $\not{p} \equiv \gamma^\mu p_\mu$.

ACRONYMS

BBN	Big Bang Nucleosynthesis
BAU	Baryon Asymmetry of the Universe
BEH	Brout–Englert–Higgs
BSM	Beyond the Standard Model
CKM	Cabibbo–Kobayashi–Maskawa
CMB	Cosmic Microwave Background
CP	Charge-Parity
cxSM	Complex Singlet Extension of the Standard Model
DR	Dimensional Reduction
EFT	Effective Field Theory
EWPT	Electroweak Phase Transition
FLRW	Friedmann–Lemaître–Robertson–Walker

FV	False Vacuum
GR	General Relativity
GW	Gravitational Waves
IR	Infrared
ITF	Imaginary-Time Formalism
LHC	Large Hadron Collider
LISA	Laser Interferometer Space Antenna
ΛCDM	Lambda Cold Dark Matter
LO	Leading Order
NLO	Next-to-Leading Order
QCD	Quantum Chromodynamics
QFT	Quantum Field Theory
RG	Renormalization Group
RGE	Renormalization Group Equation
RP	Renormalization Prescription
SFOEWPT	Strong First-Order Electroweak Phase Transition
SM	Standard Model
SMEFT	Standard Model Effective Field Theory
SNR	Signal-to-Noise Ratio
TV	True Vacuum
UV	Ultraviolet
vev	Vacuum Expectation Value
WKB	Wentzel–Kramers–Brillouin

I – INTRODUCTION

We have to continually be jumping off cliffs
and developing our wings on the way down.

— Kurt Vonnegut

The Standard Model (SM) of particle physics is far from the final word on fundamental interactions: it neither explains the observed matter-antimatter asymmetry nor provides a candidate for dark matter, among other shortcomings. Many extensions of the SM predict a strong first-order electroweak phase transition (EWPT) in the early Universe — a dramatic event in which the Higgs field acquired its vacuum expectation value (vev) through the nucleation and expansion of broken-phase bubbles, and a cornerstone of electroweak baryogenesis scenarios [5–8]. At the same time, gravitational waves (GWs) have recently been observed across several frequency ranges [9, 10], opening an entirely new observational window into the cosmos. The electroweak epoch is otherwise largely inaccessible: while collider experiments can probe the particle physics of the electroweak scale directly, they cannot reconstruct the cosmological dynamics of the transition itself. The early Universe was opaque to electromagnetic radiation at those temperatures, and neutrinos remained in thermal equilibrium well below the electroweak scale, making GWs a unique cosmological messenger from that era. A strong first-order EWPT (SFOEWPT) would have generated a stochastic GW background accessible to upcoming detectors, providing a direct probe of physics beyond the Standard Model (BSM) complementing what can be learned at colliders [11–13]. The intersection of these two frontiers — BSM model building and GW cosmology — defines the central question of this thesis: *what does it take to turn the electroweak phase transition into a precision test of new physics?*

To appreciate the challenge, imagine the moment when the Laser Interferometer Space Antenna (LISA) or another future GW detector reports a stochastic signal potentially

originating from the early Universe. The immediate task would be to determine what such a signal reveals about particle physics and its implications for the evolution of the early Universe. Answering this question requires a precise theoretical framework capable of linking an observed GW spectrum back to its microscopic origin in a BSM model — a highly non-trivial challenge.

The EWPT has been studied for several decades, beginning with the formulation of the Standard Model (SM) and the Brout–Englert–Higgs (BEH) mechanism in the 1960s and 1970s [14–19]. Meanwhile, the framework for finite-temperature field theory [20–23] was established and it was realized that the EWPT could be first-order in some extensions of the SM, providing the conditions necessary for electroweak baryogenesis [5, 6]. However, it was not initially clear whether the phase transition within the SM itself was first-order or a smooth crossover. Non-perturbative lattice simulations played a crucial role in addressing this question, indicating that for Higgs masses above $m_h \gtrsim 70\,\text{GeV}$ the transition is not first-order but a smooth crossover [24, 25]. This picture was ultimately confirmed with the discovery of a Higgs boson at $m_h \simeq 125\,\text{GeV}$ in 2012, well within the crossover regime [26, 27]. At the same time, theorists began to explore the possibility that a first-order EWPT in BSM scenarios could generate a stochastic GW background [28, 29]. The interplay between particle physics, cosmology, and thermodynamics has remained at the core of these investigations.

Yet despite decades of progress, and with LISA expected to become operational within the next decade [30, 31], theoretical predictions for GW signals from the EWPT remain far from the level of precision required for meaningful interpretation [32–34]. The prediction of a GW signal involves a multi-step pipeline: from specifying the particle content of the theory, to determining the finite-temperature effective potential, to characterizing the phase transition, and finally to modeling bubble nucleation, expansion, and the resulting GW spectrum. Each step introduces its own uncertainties, which propagate and compound along the chain, making the overall prediction intrinsically challenging.

In recent years, there has been a surge of progress toward improving this situation, driven by advances in thermal field theory, resummation techniques, dimensional reduction, and increasingly refined treatments of phase transition dynamics and GW production mechanisms [35–44]. These developments have significantly improved the reliability of predictions. Nevertheless, theoretical uncertainties still remain substantial, and many questions are still unanswered, underscoring the need for further precision studies.

Bridging the gap between particle physics models and observable GW signals requires controlling a sequence of theoretical ingredients, each of which introduces its own sources of uncertainty. Even at the level of equilibrium thermodynamics, different perturbative approaches can lead to quantitatively different predictions. In particular, a central issue is the reliability of perturbation theory in a thermal environment, where the presence of multiple scales at play and infrared (IR) divergences can lead to poor perturbative convergence [23, 45, 46]. Closely tied to this is the question of theoretical consistency. Perturbative calculations of the phase transition observables are affected by residual scale dependence and gauge dependence, which are inverstigated in Section III.2, and which can obscure physical interpretations if not carefully addressed. In particular, in Section III.2.2, we present a general result for the $\hbar$-expansion of the effective potential and discuss differences among commonly employed gauge-fixing conditions, highlighting the importance of tracking gauge dependence in perturbative calculations. In Chapter V, we use these dependencies as diagnostic tools to assess the robustness of different perturbative methods across the parameter space of the phenomenologically motivated complex singlet extension of the SM (cxSM).

A particularly powerful framework for addressing the multi-scale nature of thermal field theory is dimensional reduction (DR), introduced in Section III.4. Originally developed in the context of high-temperature Quantum Chromodynamics (QCD) [47, 48], it provides a systematic effective field theory (EFT) description in which hard modes at the temperature scale are integrated out, yielding a three-dimensional (3D) theory that captures the relevant IR physics [49, 50]. This approach has since been successfully applied to the EWPT, where it allows for a controlled treatment of low-energy modes [24, 51]. Understanding the renormalization group (RG) running of the effective parameters in the 3D EFT, which is studied in Chapter IV, is crucial for achieving reliable predictions, as it controls the scale dependence and resums large logarithms that can arise from scale hierarchies. In addition to improving the convergence of perturbative expansions, 3D EFT paves the way for lattice simulations, a central tool for studies of the EWPT in the non-perturbative regime, since the RG running discussed in Chapter IV is essential for connecting lattice results to continuum predictions.

Beyond equilibrium properties, the dynamics of the phase transition introduces further challenges. The generation of GW depends sensitively on quantities such as the bubble nucleation rate and the expansion of the broken-phase bubbles through the plasma. In particular, the bubble wall velocity is governed by out-of-equilibrium interactions between the wall and the surrounding medium [52–56]. In Chapter VI, we develop a

framework to incorporate one-loop corrections to the wall equation of motion, providing a more accurate description of the bubble dynamics.

Taken together, these considerations highlight that predicting GW signals from the EWPT is not controlled by a single calculation, but by a chain of interconnected theoretical inputs — and that the central question is not merely whether a signal exists, but whether theoretical predictions are precise enough to interpret it. The work presented in this thesis is motivated by the same moment it prepares for: a potential detection of GWs by LISA, together with the challenge of separating a cosmological stochastic GW signal from astrophysical foregrounds — a task that demands precise theoretical predictions of the spectral shape and is essential for extracting meaningful BSM physics.

Following the introduction, in Chapter II, we review the foundations of the SM and modern cosmology, before discussing the open problems that motivate the search for BSM physics. In Chapter III, the theoretical tools used throughout the thesis are examined: thermal field theory, effective potentials, nucleation, DR, and their connection to GW observables are developed and discussed in detail. In Chapter IV, the renormalization-group running in the 3D EFT of the SM and the Standard Model Effective Field Theory (SMEFT) is studied, establishing the precision infrastructure required for reliable calculations. Perturbative methods for the EWPT in the cxSM are applied and compared in Chapter V, where their uncertainties are quantified through residual scale and gauge dependence. We further examine the bubble wall velocity, systematically incorporating one-loop corrections to the wall equation of motion in Chapter VI. Finally, in Chapter VII, the main results are summarized and future directions outlined. The appendices contain supporting technical material: Appendix A collects counterterms and beta functions for the 3D EFT including the contributions from the higher dimensional operators, Appendix B provides beta functions for the cxSM, and Appendix C outlines the derivation of the propagators in a homogeneous background.

II – CURRENT STATUS OF PARTICLE PHYSICS AND COSMOLOGY

The story so far:
In the beginning the Universe was created.
This has made a lot of people very angry
and been widely regarded as a bad move.

— Douglas Adams,
The Restaurant at the End of the Universe

This chapter provides a broad review of the theoretical and observational foundations of the modern understanding of particle physics and cosmology on which the rest of the thesis builds. We begin by introducing the SM of particle physics in Section II.1, covering its electroweak and strong gauge structure, field content, the BEH mechanism of electroweak symmetry breaking, as well as subtleties of physical predictions within the quantum field theory (QFT) framework and experimental evidence supporting the SM. Following that, we turn to the discussion of the standard cosmological model in Section II.2, including Friedmann–Lemaître–Robertson–Walker (FLRW) cosmology, the ΛCDM model (characterized by the cosmological constant Λ, cold dark matter, and ordinary matter), the energy budget of the Universe and its thermal history, GWs and main observational pillars backing the ΛCDM model. The chapter closes with a review of the unresolved questions in particle physics and cosmology that motivate the search for extensions beyond the current framework in Section II.3 and an overview of BSM extensions most relevant to this thesis in Section II.4.

The material presented here is largely based on the lecture notes by David Tong [57, 58], the books by Mark Thomson [59], Scott Dodelson [60] and Daniel Baumann [61] and on personal notes on the SM and cosmology compiled during the author's studies.

II.1 The Standard Model of particle physics

The SM of particle physics is a relativistic QFT built on the principle of local gauge invariance. It provides a unified description of the electromagnetic, weak and strong interactions of all known elementary particles, and has stood up to decades of experimental scrutiny with remarkable precision. The SM is arguably the most successful scientific theory ever constructed, with some predictions, such as the anomalous magnetic moment of the electron, confirmed at the level of parts per billion [62].

The structure of the SM is not derived from first principles but is instead fixed by experimental input. The choice of gauge symmetry group, the number of matter fields and their representations and the number of fermion generations are all empirical facts inferred from experimental observations: the $SU(3)_c$ color symmetry is established by deep inelastic scattering and jet physics [63, 64], the chiral $SU(2)_L$ structure reflects the observed maximal parity violation of the weak interaction [65, 66] and the $U(1)_Y$ hypercharges are fixed by the measured electric charges. The existence of exactly three fermion generations is supported by the measurement of the Z-boson invisible width, which constrains the number of active light neutrino species [67]. The scalar sector, containing a single $SU(2)_L$ doublet, is the minimal prescription consistent with the observed electroweak symmetry breaking pattern and the discovery of a Higgs boson at the Large Hadron Collider (LHC) [26, 27].

Therefore, the construction of the SM relies on three ingredients: the identification of a gauge symmetry group, the assignment of matter fields to representations of that group and the postulate of a scalar sector, whose vacuum structure spontaneously breaks the electroweak symmetry, generating the masses of gauge bosons and fermions. In the remainder of this section, we describe each of these ingredients in detail.

II.1.1 Gauge structure and field content

The guiding principle behind the formulation of the SM is *gauge invariance*: the requirement that the Lagrangian is invariant under local (i.e. spacetime-dependent) symmetry transformations of the fields. Once one specifies a gauge group and assigns how matter fields transform under it (which is equivalent to choosing the representations), the form of the interactions is essentially fixed by the constraint of gauge invariance.

The SM is built on the gauge group

$$\mathcal{G}_{\text{SM}} = SU(3)_c \times SU(2)_L \times U(1)_Y \,, \tag{2.1}$$

where the subscripts label color (c), left-handed weak isospin (L) and weak hypercharge (Y). Each symmetry factor is associated with a distinct force: $SU(3)_c$ governs the strong interaction, $SU(2)_L$ encodes the weak interaction and $U(1)_Y$ describes a hypercharge force that mixes with $SU(2)_L$ to produce electromagnetism after electroweak symmetry breaking.

The key idea of *local* gauge invariance is that the symmetry transformations are different at each spacetime point, unlike global transformations. For a field ψ charged under an Abelian group with the charge q, the transformation takes the form

$$\psi(x) \longrightarrow e^{iq\alpha(x)}\psi(x) \,, \tag{2.2}$$

where $\alpha(x)$ is an arbitrary real function of the spacetime coordinates. For the non-Abelian groups the transformation generalizes to

$$\psi(x) \longrightarrow U(x)\psi(x) \,, \quad U(x) = \exp\!\left(i\theta^a(x)T^a\right) \,, \tag{2.3}$$

where, T^a are the generators of the group, and $\theta^a(x)$ are independent spacetime-dependent parameters.

The ordinary derivative $\partial_\mu\psi$ is not covariant under these local transformations, since the spacetime dependence of the transformation parameters introduces extra terms. Restoring gauge invariance therefore requires the introduction of one gauge field for each generator of $\mathcal{G}_{\text{SM}}$ with the corresponding gauge transformation: eight gluon fields G^a_μ ($a = 1, \ldots, 8$) for $SU(3)_c$, three weak gauge fields W^a_μ ($a = 1, 2, 3$) for $SU(2)_L$, and a single hypercharge gauge field B_μ for $U(1)_Y$. For instance, under a $U(1)_Y$ transformation with local parameter $\alpha(x)$, the hypercharge gauge field transforms as

$$B_\mu(x) \;\longrightarrow\; B_\mu(x) + \frac{1}{g'}\,\partial_\mu\alpha(x) \,, \tag{2.4}$$

with g' being the $U(1)_Y$ gauge coupling. This exactly cancels the extra term generated in $\partial_\mu\psi$ and restores covariance.

Hence, the existence of the gauge fields that mediate the three fundamental forces within the SM is a direct consequence of imposing local gauge symmetry.

The full SM Lagrangian decomposes as

$$\mathcal{L}_{\text{SM}} \;=\; \mathcal{L}_{\text{YM}} + \mathcal{L}_{F} + \mathcal{L}_{\text{Higgs}} + \mathcal{L}_{\text{Yukawa}}\,, \tag{2.5}$$

where each term denotes the Yang–Mills gauge, fermion, Higgs, and Yukawa sectors, respectively. We describe each contribution in turn.

Yang–Mills sector

The dynamics of the gauge fields are governed by the Yang–Mills Lagrangian [68], whose form is uniquely fixed by local gauge invariance,

$$\mathcal{L}_{\text{YM}} \;=\; -\frac{1}{4}\,G^{a}_{\mu\nu}\,G^{a\,\mu\nu} - \frac{1}{4}\,W^{a}_{\mu\nu}\,W^{a\,\mu\nu} - \frac{1}{4}\,B_{\mu\nu}\,B^{\mu\nu}\,, \tag{2.6}$$

where the field-strength tensors are defined as

$$\begin{aligned} G^{a}_{\mu\nu} &= \partial_\mu G^{a}_{\nu} - \partial_\nu G^{a}_{\mu} + g_s f^{abc}\,G^{b}_{\mu} G^{c}_{\nu}, \\ W^{a}_{\mu\nu} &= \partial_\mu W^{a}_{\nu} - \partial_\nu W^{a}_{\mu} + g\varepsilon^{abc} W^{b}_{\mu} W^{c}_{\nu}\,, \\ B_{\mu\nu} &= \partial_\mu B_{\nu} - \partial_\nu B_{\mu}\,. \end{aligned} \tag{2.7}$$

The couplings g_s, g and g' correspond to $SU(3)_c$, $SU(2)_L$ and $U(1)_Y$, respectively, and f^{abc}, ε^{abc} are the structure constants of $SU(3)$ and $SU(2)$, respectively.

A crucial distinction arises between the Abelian and non-Abelian parts of the Yang–Mills Lagrangian. The $U(1)_Y$ field strength $B_{\mu\nu}$ is linear in the gauge field, just like in electrodynamics. By contrast, the non-Abelian field strengths contain terms quadratic in the gauge fields — the terms $\propto f^{abc}$ and $\propto \varepsilon^{abc}$ in Eq. (2.7). This results in cubic and quartic self-interactions among the gauge bosons. In other words, gluons scatter off other gluons, and the W bosons interact among themselves. This is fundamentally different from electrodynamics, where photons do not self-interact at tree level, and it is responsible for the distinctive properties of the strong and weak interactions, such as asymptotic freedom, confinement and the rich non-perturbative structure of non-Abelian gauge theories. Moreover, the self-interacting nature of non-Abelian gauge bosons, which themselves carry charge under the gauge group, enforces a universal coupling constant, in contrast to the Abelian case where the neutral gauge boson imposes no such constraint on the charge assignments of matter fields.

Fermionic sector

The matter content of the SM consists of three generations of chiral fermions — quarks and leptons — whose interactions are entirely determined by their gauge quantum numbers. Under $SU(3)_c \times SU(2)_L \times U(1)_Y$, the fermion fields of the i-th family ($i = 1, 2, 3$) transform as

$$\begin{aligned} Q_L^i &= \begin{pmatrix} u_L^i \\ d_L^i \end{pmatrix} \sim \left(\mathbf{3},\, \mathbf{2},\, \tfrac{1}{6}\right), \quad u_R^i \sim \left(\mathbf{3},\, \mathbf{1},\, \tfrac{2}{3}\right), \quad d_R^i \sim \left(\mathbf{3},\, \mathbf{1},\, -\tfrac{1}{3}\right), \\ L_L^i &= \begin{pmatrix} \nu_L^i \\ e_L^i \end{pmatrix} \sim \left(\mathbf{1},\, \mathbf{2},\, -\tfrac{1}{2}\right), \quad e_R^i \sim \left(\mathbf{1},\, \mathbf{1},\, -1\right), \end{aligned} \tag{2.8}$$

where the three entries in each bracket denote the representation under $SU(3)_c$, the representation under $SU(2)_L$ and the $U(1)_Y$ hypercharge, respectively. Here **3** is the fundamental triplet of $SU(3)_c$, **2** is the fundamental doublet of $SU(2)_L$, and **1** denotes a singlet (invariant under the corresponding group). The three families correspond to (u, d, ν_e, e), (c, s, ν_μ, μ) and (t, b, ν_τ, τ) (grouped into the left- and right-handed multiplets above), all with identical gauge quantum numbers but vastly different masses.

We emphasize that the SM is a *chiral* gauge theory: the left- and right-handed fermions carry different quantum numbers. Only the left-handed fields form $SU(2)_L$ doublets — and hence interact with the weak gauge bosons — while the right-handed fields are singlets and do not. This is a direct consequence of the experimentally observed maximal parity violation of the weak interaction [66].

The most striking feature of the SM fermion content is that it is free of gauge anomalies. The hypercharge assignments of the matter fields are not a free choice but are fixed by experiment; remarkably, they conspire to cancel all gauge anomalies exactly, generation by generation [69]. The cancellation of the Witten $SU(2)$ anomaly further requires an even number of $SU(2)_L$ doublets [70], thereby enforcing that quarks and leptons appear in complete generations.

The fermionic kinetic and gauge-interaction terms read

$$\mathcal{L}_F \;=\; \sum_f \bar{\psi}_f \, i \not{D} \, \psi_f \,, \tag{2.9}$$

where the sum runs over all chiral fermion fields $f \in \{Q_L^i, u_R^i, d_R^i, L_L^i, e_R^i\}$ for each

generation $i = 1, 2, 3$, and the full SM covariant derivative is

$$D_\mu \;=\; \partial_\mu - ig_s T^A G^A_\mu - ig\frac{\sigma^a}{2} W^a_\mu - ig' Y B_\mu \,, \tag{2.10}$$

where $T^A = \lambda^A/2$ and $\sigma^a/2$ are the generators of $SU(3)_c$ and $SU(2)_L$ in the fundamental representations, respectively, with λ^A the Gell-Mann matrices and σ^a the Pauli matrices; Y is the hypercharge of the field on which D_μ acts. For matter fields that are uncharged under certain gauge groups, the corresponding terms in the covariant derivative are simply absent.

Scalar sector

The final ingredient of the SM field content is a single complex scalar field Φ, Higgs field, transforming as a doublet under $SU(2)_L$ and carrying hypercharge $Y = 1/2$,

$$\Phi \;=\; \begin{pmatrix} \phi^+ \\ \phi^0 \end{pmatrix} \;\sim\; \left(\mathbf{1},\, \mathbf{2},\, \tfrac{1}{2}\right). \tag{2.11}$$

The Higgs sector of the SM Lagrangian can be written as

$$\mathcal{L}_{\text{Higgs}} = (D_\mu \Phi)^\dagger (D^\mu \Phi) - V_0(\Phi)\,, \tag{2.12}$$

with the covariant derivative as defined in Eq. (2.10). The most general renormalizable (with operators up to mass-dimension four) scalar potential $V_0(\Phi)$ consistent with $\mathcal{G}_{\text{SM}}$ depends only on the $SU(2)_L$- and $U(1)_Y$-invariant combination $\Phi^\dagger\Phi$, it takes the form

$$V_0(\Phi) = \mu_h^2 (\Phi^\dagger \Phi) + \lambda_h (\Phi^\dagger \Phi)^2\,, \tag{2.13}$$

with two real parameters: the mass parameter μ_h^2 and the quartic self-coupling λ_h. Vacuum stability of the potential requires $\lambda_h > 0$, whereas the sign of μ_h^2 is the decisive input: for $\mu_h^2 > 0$ the scalar potential has a unique minimum at the origin while for $\mu_h^2 < 0$, which is needed to describe nature, V_0 develops degenerate minima at $\Phi^\dagger\Phi = -\mu_h^2/(2\lambda_h)$, and the electroweak symmetry is spontaneously broken. It is the shape of the scalar potential and how it evolves as the Universe cools down that is the primary focus of this thesis.

II.1.2 Electroweak symmetry breaking

Within the SM, where $\mu_h^2 < 0$, the electroweak symmetry $SU(2)_L \times U(1)_Y$ is preserved by the SM Lagrangian, but is spontaneously broken by the Higgs condensate — the vev $\langle \Phi^\dagger \Phi \rangle = -\mu_h^2/(2\lambda_h)$. The Higgs potential of Eq. (2.13) is minimized on a continuous set of field values related by gauge transformations. Within our choice of notation, the vev of the Higgs field takes the form

$$\langle \Phi \rangle = \frac{1}{\sqrt{2}} \begin{pmatrix} 0 \\ v_{\rm EW} \end{pmatrix}, \qquad v_{\rm EW} \equiv \sqrt{-\frac{\mu_h^2}{\lambda_h}} \simeq 246\,{\rm GeV}\,, \tag{2.14}$$

which spontaneously breaks the electroweak gauge symmetry down to the unbroken electromagnetic subgroup $U(1)_{\rm em}$ with the generator given by $Q = T_3 + Y$ [71, 72], with $T_3 = \sigma^3/2$.

Expanding around the vacuum configuration,

$$\Phi = \begin{pmatrix} G^+(x) \\ \frac{1}{\sqrt{2}} \left(v_{\rm EW} + h(x) + i G^0(x) \right) \end{pmatrix}, \tag{2.15}$$

the field $h(x)$ describes the physical Higgs boson, while the three would-be Goldstone bosons $G^{\pm,0}(x)$ are the excitations of the Higgs doublet along the directions of the broken generators.

Gauge boson masses

The gauge boson masses arise from the kinetic term $D_\mu \Phi^\dagger D^\mu \Phi$ expanded around the vev of the Higgs field. Substituting Eq. (2.14), one finds non-zero mass terms for three linear combinations of the gauge fields.

In the mass eigenbasis, these correspond to the charged $W^\pm$ bosons and the neutral Z boson, given by

$$W_\mu^\pm = \frac{1}{\sqrt{2}} (W_\mu^1 \mp i W_\mu^2), \qquad \begin{pmatrix} Z_\mu \\ A_\mu \end{pmatrix} = \begin{pmatrix} \cos\theta_W & -\sin\theta_W \\ \sin\theta_W & \cos\theta_W \end{pmatrix} \begin{pmatrix} W_\mu^3 \\ B_\mu \end{pmatrix}, \tag{2.16}$$

where the weak mixing angle θ_W is defined by $\tan\theta_W = g'/g$. The resulting gauge

boson masses are

$$M_W = \frac{g v_{\text{EW}}}{2}\,, \qquad M_Z = \frac{v_{\text{EW}}}{2}\sqrt{g^2 + g'^2} = \frac{M_W}{\cos\theta_W}\,, \qquad M_A = 0\,. \tag{2.17}$$

The photon A_μ remains exactly massless: the $U(1)_{\text{em}}$ subgroup is left unbroken by the non-zero Higgs vev.

The three broken generators of $SU(2)_L \times U(1)_Y$, which would produce three massless Goldstone bosons $G^{\pm,0}$ for the case of a broken global symmetry, are absorbed as the longitudinal polarization degrees of freedom of the $W^\pm$ and Z bosons.

The ratio $\rho \equiv M_W^2/(M_Z^2 \cos^2\theta_W) = 1$ at tree level is a direct consequence of the doublet structure of the Higgs field and electroweak symmetry breaking pattern. While the resulting prediction receives higher-order corrections, it remains one of the most precisely tested predictions of the SM.

Higgs boson

The remaining degree of freedom within the Higgs doublet corresponds to the physical Higgs boson h which acquires its mass during the electroweak symmetry breaking,

$$M_h^2 = -2\mu_h^2 = 2\lambda_h v_{\text{EW}}^2\,. \tag{2.18}$$

In addition to interaction with the gauge bosons, generated by the kinetic term $D_\mu\Phi^\dagger D^\mu\Phi$, the scalar potential V_0, expanded around the vev, further generates self-interactions of the physical Higgs boson:

$$V_0 \supset \frac{M_h^2}{2}\,h^2 + \frac{M_h^2}{2v_{\text{EW}}}\,h^3 + \frac{M_h^2}{8v_{\text{EW}}^2}\,h^4\,. \tag{2.19}$$

The trilinear $\lambda_{hhh} = 3M_h^2/v$ and the quartic Higgs coupling at the tree level are both determined by M_h and v (or alternatively by μ_h^2 and λ_h) alone.

II.1.3 Yukawa sector

The Higgs doublet plays one further crucial role in the SM. A Dirac mass term for fermions, which is of the form $m\bar{\psi}_L^f\psi_R^f$, is explicitly forbidden by gauge invariance, since the left- and right-handed fermions are charged differently under $SU(2)_L$ and $U_Y(1)$.

The resolution to generate masses for elementary fermions is to couple them to the Higgs doublet through Yukawa interactions, which are gauge-invariant by construction,

$$\mathcal{L}_{\text{Yukawa}} = -Y^u_{ij}\bar{Q}^i_L\tilde{\Phi}u^j_R - Y^d_{ij}\bar{Q}^i_L\Phi d^j_R - Y^e_{ij}\bar{L}^i_L\Phi e^j_R + \text{h.c.}\,, \tag{2.20}$$

where $\tilde{\Phi} = i\sigma^2\Phi^*$ is the conjugate Higgs doublet (with hypercharge $Y = -1/2$, required to give mass to up-type quarks), and $Y^{u,d,e}$ are 3×3 complex matrices in fermion generation space. Once the Higgs acquires its vev, Yukawa interactions generate mass terms for the fermions,

$$M^f_{ij} = \frac{v_{\text{EW}}}{\sqrt{2}}\,Y^f_{ij}\,. \tag{2.21}$$

The physical fermion masses are obtained by biunitary diagonalization of the mass matrix M^f, using independent unitary rotations U^f_L and U^f_R of the left- and right-handed fields.

This rotation, however, leads to non-diagonal couplings of the fermions in the mass eigenbasis to the charged gauge bosons. For quarks, this mismatch results in the Cabibbo–Kobayashi–Maskawa (CKM) mixing matrix $V_{\text{CKM}} = (U^u_L)^\dagger U^d_L$, which is responsible for flavor-changing charged-current interactions and is parametrized by three mixing angles and a charge-parity (CP)-violating phase.

It is worth noting that since the SM contains only left-handed neutrinos, the Yukawa sector does not provide a recipe to generate masses for them and neutrinos remain exactly massless within the SM.

II.1.4 Quantum Chromodynamics

Quantum chromodynamics (QCD) is described by the $SU(3)_c$ gauge sector of the SM and determines the strong interaction between quarks and gluons.

As in any interacting QFT, couplings are scale dependent: quantum loop corrections modify the interactions, so that the effective interaction strength depends on the characteristic energy scale μ of a process.

Within the SM, QCD, like the weak $SU(2)_L$ interaction, is an asymptotically free theory: the strong coupling g_s decreases at high energies and becomes weakly coupled in the ultravioltet (UV) regime [19, 73]. This is a direct consequence of the non-Abelian nature of the $SU(3)_c$ gauge group and matter content coupled to it.

The crucial phenomenological difference between QCD and the electroweak interaction is that the color gauge symmetry is not spontaneously broken: gluons remain massless, and the $SU(3)_c$ remains unbroken at all energy scales.

Confinement and hadronization

The IR counterpart of asymptotic freedom is *confinement*. At energy scales around $\Lambda_{\text{QCD}} \sim 200\,\text{MeV}$ [74] the strong gauge coupling becomes non-perturbative. Since $SU(3)_c$ remains unbroken, physical asymptotic states must be gauge-invariant color singlets. As a result, isolated quarks and gluons, which carry color charge, never appear in the low-energy spectrum. For instance, quarks are always confined within bound states called hadrons. The most familiar examples are *mesons*, which are quark-antiquark pairs $q\bar{q}$ (e.g. pions, kaons), and *baryons*, which are three-quark states qqq (e.g. protons, neutrons).

Although QCD does not directly drive the EWPT, it enters crucially in precision EWPT calculations. In particular, g_s and the top quark Yukawa coupling y_t enter essential loop corrections to the Higgs scalar potential.

II.1.5 From the Lagrangian to physical predictions

The SM Lagrangian constructed in the preceding sections is a classical object. In order to take into account the quantum nature of fundamental physics and extract physical predictions, such as cross sections and decay rates, we need to quantize the theory. The modern approach is the path integral formalism: rather than quantizing fields as operators, one sums over all field configurations weighted by the phase $e^{iS[\varphi]}$, encoding the quantum interference between different configurations of the fields. The action is defined as

$$S[\varphi] = \int d^4x \mathcal{L}[\varphi]\,, \tag{2.22}$$

where φ collectively denotes all fields. The correlation functions of the fields, which enter physical observables, are determined using the generating functional

$$Z[J] = \int \mathcal{D}\varphi \exp\left\{iS[\varphi] + i\int d^4x J(x)\varphi(x)\right\}, \tag{2.23}$$

where J are external sources coupled to the fields.

In practice, the path integral is often evaluated perturbatively as an expansion in the coupling constants, where the resulting terms are represented diagrammatically by Feynman diagrams. This formulation of vacuum ($T = 0$) QFT is used extensively throughout this thesis; the QFT framework at finite temperature, which underlies the treatment of the scalar potential at $T \neq 0$, is developed in Chapter III.

Gauge fixing and quantization of vector fields

Quantizing gauge theories requires additional care: in the Lagrange formalism, a Lorentz vector field A_μ has four components, but a massless spin-1 particle has only two physical transverse polarizations.

One of the unphysical degrees of freedom is removed by the equations of motion — for an on-shell massless vector the transversality condition eliminates one polarization — while the remaining one is pure gauge redundancy. It is this last unphysical degree of freedom that must be removed by gauge fixing to avoid overcounting in the path integral.

The standard resolution is to impose a gauge-fixing condition, which removes the redundant degree of freedom, by adding terms explicitly breaking gauge invariance to the Lagrangian. For instance, in the case of an Abelian gauge field, one may add the covariant gauge-fixing term

$$\mathcal{L}_{\text{gf}} \;=\; -\frac{1}{2\xi}\,(\partial_\mu A^\mu)^2\,, \tag{2.24}$$

to the Lagrangian, where the gauge parameter ξ labels a family of gauges. In non-Abelian theories, gauge fixing also introduces Faddeev–Popov ghost fields: unphysical fields which are required to preserve the consistency of the perturbative expansion. Explicit gauge-fixing terms for the SM gauge groups are introduced in Chapter III.

Physical observables are independent of the gauge-fixing condition and the value of ξ, a fact that provides an important consistency check on perturbative calculations. Unphysical gauge dependencies of intermediate quantities play an important role throughout this thesis, as we shall see when discussing gauge dependence in the context of phase transitions in Chapter V.

Divergences, regularization and renormalization

Loop corrections in QFT involve integrals over the momenta of virtual particles that generically diverge in the UV, a manifestation of the sensitivity of local QFTs to arbitrarily short distances.

To make sense of these infinities, one first *regularizes* the theory, rendering the divergent integrals mathematically well-defined. Next, the divergences are absorbed into a redefinition of the Lagrangian parameters of the theory — *renormalizing* the theory.

The common choice for perturbative regularization, used throughout this thesis, is the *dimensional regularization*, where the theory is continued to

$$d = 4 \longrightarrow 4 - 2\epsilon \tag{2.25}$$

spacetime dimensions, so that divergences appear as poles in $1/\epsilon$.

The bare Lagrangian is then split into renormalized quantities and counterterms,

$$\mathcal{L}_{\text{bare}} \;=\; \mathcal{L}_{\text{ren}}(m, \lambda, g, \ldots) + \mathcal{L}_{\text{ct}}(\delta Z, \delta m^2, \delta\lambda, \delta g, \ldots)\,, \tag{2.26}$$

where the counterterms ensure that physical observables are finite order by order in perturbation theory. Renormalization is far more than a prescription for removing infinities: it defines the precise relationship between the parameters of the Lagrangian and measurable quantities — physical masses, scattering cross sections, decay widths — and introduces a residual dependence on the renormalization scale μ, governed by the renormalization group equations (RGEs). The scale dependence of physical predictions provides a measure of the truncation error of the perturbative expansion within a calculation. This becomes particularly relevant for the discussion of the perturbative description of the EWPT.

It is useful to note two complementary viewpoints on renormalizability. In the traditional sense, the SM is a renormalizable theory: all operators have mass dimension ≤ 4, so a finite set of counterterms suffices to absorb all divergences. From an EFT perspective, however, one may view the SM as the leading part of an EFT valid below some cutoff Λ (at the latest $\bar{M}_{\text{Pl}} = (8\pi G)^{-1/2} \simeq 2.43 \times 10^{18}$ GeV, beyond which gravitational effects become non-negligible). Higher-dimensional operators suppressed by powers of $1/\Lambda$ then encode possible new physics at higher scale. They are not pathological for calculations but simply parametrize our ignorance of shorter-distance dynamics.

This EFT viewpoint is central to the SMEFT framework discussed in Section II.4 and to the DR procedure employed in Chapters III and IV.

II.1.6 The SM as a complete theory: parameter count

With the gauge, fermionic, scalar and Yukawa sectors all in place, the SM is fully specified as a renormalizable QFT by *19 free parameters*. Three of these are the gauge couplings g', g and g_s associated with $U(1)_Y$, $SU(2)_L$ and $SU(3)_c$ respectively. Two parameters lie within the Higgs potential: the mass parameter μ_h^2 and the quartic self-coupling λ_h (or equivalently the Higgs boson mass m_h and the vev $v_{\rm EW}$). Nine encode the fermion masses through the Yukawa sector: six quark masses $(m_u, m_d, m_c, m_s, m_b, m_t)$ and three charged-lepton masses (m_e, m_μ, m_τ). Four describe quark mixing: the three CKM angles $\theta_{12}, \theta_{13}, \theta_{23}$ and the CP-violating phase δ.

The nineteenth one is the QCD vacuum angle $\bar{\theta}$, which multiplies the topological term $\bar{\theta} G\tilde{G}$ allowed in the QCD Lagrangian. The extremely small experimental bound $|\bar{\theta}| \lesssim 10^{-10}$ [75] constitutes the strong CP problem [76].

None of these 19 numbers is predicted by the theory. They are empirical inputs, fixed by experiment and otherwise unconstrained by the symmetry structure. The fact that 19 parameters suffice to describe particle physics to extraordinary precision across a vast range of energies and processes stands as the SM's central achievement, and is what makes the open questions of Section II.3 so pervasive.

II.1.7 Experimental successes

The SM's 19 parameters, once fixed by measurements, turn the Lagrangian from a definition into a predictive tool. The history of experimental particle physics is largely a history of those predictions being confirmed. The successes are far too numerous to catalogue; they span five decades of experiments and range from proving the existence of particles predicted before their discovery to agreement with precision measurements at the level of parts per billion. We highlight three that are most directly connected to the topic of this thesis.

- **Higgs boson discovery**

  The discovery of a Higgs boson by ATLAS and CMS at the LHC in July 2012 [26, 27], with mass $m_h = 125.11 \pm 0.11\,\text{GeV}$ [77], was the capstone of the SM. It

confirmed that the BEH mechanism of Section II.1.2 is the correct description of electroweak symmetry breaking, and that the vev $v_{\rm EW} \simeq 246\,\text{GeV}$ is a physical, observable quantity. Subsequent measurements of Higgs coupling strengths in the $\gamma\gamma$, ZZ^*, WW^*, $b\bar{b}$, $\tau^+\tau^-$ and $\mu^+\mu^-$ channels are all consistent with SM predictions at the $\mathcal{O}(10\%)$ level [78, 79], confirming that the discovered boson couples to other particles in proportion to their masses, exactly as the Yukawa sector of Section II.1.1 requires. The one aspect of the Higgs potential that is not yet directly measured is its self-couplings. Current LHC constraints on the trilinear coupling λ_{hhh} from hh production permit $\mathcal{O}(1)$ deviations from the SM value [78, 80], with even larger deviations allowed for the quartic Higgs self-coupling. Thus, the precise shape of the scalar potential — and hence the character of the EWPT — remains an open experimental question. This is particularly relevant in extended Higgs sectors, where additional scalar fields can significantly modify the shape of the potential.

- **Electroweak precision tests**

  The electroweak sector has been probed with extraordinary precision at LEP, SLD and the Tevatron, even before the discovery of the Higgs boson. The Z-boson lineshape, its partial decay widths, the W mass, and the weak mixing angle θ_W all agree with SM predictions at the per-mille level [67, 74]. Perhaps most strikingly, the quantum corrections test the *loop structure* of the electroweak theory: they probe virtual effects of particles too heavy to be produced directly, and their agreement with data confirms that the perturbative expansion is under control. The consistency of these precision tests places stringent constraints on any extensions of the SM.

- **Prediction and discovery of the top quark**

  Long before it was observed directly, the existence and approximate mass of the top quark could already be inferred from electroweak radiative corrections. Precision measurements of the Z-boson properties at LEP and SLD are sensitive to virtual top-quark contributions. Global fits to these observables in the early 1990s predicted a heavy top quark with $m_t \sim 170\,\text{GeV}$ [81, 82].

  This prediction was confirmed with the discovery of the top quark by the CDF and DØ collaborations at the Tevatron in 1995 [81, 82]. The agreement between the indirectly predicted mass and the directly measured value remains one of the clearest demonstrations that the loop structure of the SM has correctly described

physics well above the energy scales directly probed by experiments at that time.

The large top Yukawa coupling makes the top quark the dominant fermionic contributor to radiative corrections of the Higgs scalar potential, playing a central role in determining the shape of the scalar potential and hence the nature of the EWPT.

II.2 The standard cosmological model

The SM of particle physics describes the fundamental constituents of matter and their interactions, but its most dramatic consequences are not found in laboratory experiments — they played out in the first fractions of a second after the Big Bang. At those early times, the Universe was a hot, dense thermal plasma at temperatures far exceeding those achievable at any collider, with all SM degrees of freedom thermally populated and in equilibrium. The evolution of this plasma — how symmetries broke, how particles fell out of equilibrium, how the baryon asymmetry was generated — is governed by the same Lagrangian reviewed in the preceding section, now determining the physics at finite temperature. Connecting particle physics to observable predictions in this way requires a cosmological framework: a description of how the Universe expands, cools, and evolves. Yet the standard cosmological model, to which we now turn, does not merely provide this backdrop — it also poses its own profound open questions, including the nature of dark matter and dark energy, the origin of the baryon asymmetry of the Universe (BAU) and the mechanism behind the initial conditions of the hot Big Bang.

The standard cosmological model, also known as the ΛCDM, provides a remarkably successful description of the evolution and large-scale structure of the Universe. It rests on two empirical pillars: the cosmological principle, which states that the Universe is homogeneous and isotropic on sufficiently large scales, and general relativity (GR) as the theory of spacetime dynamics. Within this framework, the Universe is found to be spatially flat, dominated at late times by a cosmological constant Λ and cold dark matter, and to have originated in a hot, dense initial state — the Big Bang. In this section, we review the key elements of the standard cosmological model that are relevant to the physics of phase transitions and GW production studied in subsequent chapters.

II.2.1 FLRW universe and Friedmann equations

In the general theory of relativity, the geometry of spacetime is encoded in the metric tensor $g_{\mu\nu}$, which enters the invariant line element $ds^2 = g_{\mu\nu}\, dx^\mu dx^\nu$ and determines how distances and time intervals are measured. The metric generalizes the flat Minkowski line element $ds^2 = dt^2 - d\vec{x}^2$ of special relativity to curved spacetimes, and its dynamics are governed by the Einstein field equations,

$$G_{\mu\nu} = \frac{T_{\mu\nu}}{\bar{M}_{\rm Pl}^2} \tag{2.27}$$

where $G_{\mu\nu} \equiv R_{\mu\nu} - \frac{1}{2} g_{\mu\nu} R$ is the Einstein tensor, with $R_{\mu\nu}$ the Ricci tensor and $R = g^{\mu\nu} R_{\mu\nu}$ the Ricci scalar, $\bar{M}_{\rm Pl} = (8\pi G)^{-1/2} \simeq 2.43 \times 10^{18}$ GeV is the reduced Planck mass, and $T_{\mu\nu}$ is the energy-momentum tensor of the matter and radiation fields in the Universe.

Specifying the metric is therefore equivalent to specifying the gravitational background in which all other physics takes place.

The cosmological principle — homogeneity and isotropy of the Universe on large scales — uniquely constrains the metric to the FLRW form, parametrized by a single time-dependent scale factor $a(t)$ and a spatial curvature parameter $k \in \{-1, 0, +1\}$. Observations of the cosmic microwave background (CMB) by the Planck satellite constrain the spatial curvature to be consistent with zero at the sub-percent level [83], hence, setting $k = 0$ henceforth, the flat FLRW line element reads

$$ds^2 = dt^2 - a^2(t) \left[dr^2 + r^2 \left(d\theta^2 + \sin^2\theta \, d\phi^2 \right) \right], \tag{2.28}$$

where t and (r, θ, ϕ) are the time and spatial comoving spherical coordinates. All physical distances scale with $a(t)$: a comoving separation Δr corresponds to a proper distance $d_p = a(t)\Delta r$; the evolution of the scale factor $a(t)$ is governed by the Einstein field equations Eq. (2.27).

Assuming the cosmic energy-momentum tensor takes the perfect-fluid form, $T^{\mu\nu} = \mathrm{diag}(\rho, p, p, p)$, where ρ is the energy density and p is the pressure, the

$(0,0)$ and trace components of the field equations yield the two Friedmann equations,

$$\begin{aligned} H^2 \equiv \frac{\dot{a}}{a} &= \frac{\rho}{3\bar{M}_{\rm Pl}^2}\,, \\ \dot{H} + H^2 \equiv \frac{\ddot{a}}{a} &= -\frac{1}{6\bar{M}_{\rm Pl}^2}(\rho + 3p)\,, \end{aligned} \tag{2.29}$$

where the Hubble rate $H \equiv \dot{a}/a$ measures the rate of cosmic expansion, and dots denote derivatives with respect to t. The stress-energy tensor conservation law, $\nabla_\mu T^{\mu\nu} = 0$, leads to the continuity equation

$$\dot{\rho} + 3H(\rho + p) = 0\,. \tag{2.30}$$

Together these equations completely determine the expansion once the content of the Universe together with the equation of state $w \equiv p/\rho$ is specified for each component. The equation of state w takes characteristic values depending on the dominant form of energy: $w = 0$ for pressureless (cold, $m_\varphi \gg T$) matter, $w = 1/3$ for radiation (including all relativistic species $m_\varphi \ll T$) and $w = -1$ for a cosmological constant Λ. Integrating Eq. (2.30) gives

$$\rho \propto a^{-3(1+w)}, \tag{2.31}$$

so that radiation energy density drops as $\rho_r \propto a^{-4}$, matter as $\rho_m \propto a^{-3}$, and $\rho_\Lambda = \text{const}$. The spatially flat Universe must have a total energy density equal to the critical density,

$$\rho_c \equiv 3\bar{M}_{\rm Pl}^2 H_0^2\,, \tag{2.32}$$

with H_0 being the present time value of the Hubble rate.

The Friedmann equations Eq. (2.29) can be conveniently expressed in terms of the density parameters for each species i, which parametrize the energy budget of the Universe, defined as the ratio of its present-day energy density $\rho_{i,0}$ to the critical density,

$$\Omega_i \equiv \frac{\rho_{i,0}}{\rho_c}\,, \tag{2.33}$$

with the flatness condition reading $\sum_i \Omega_i = 1$. Eq. (2.29) then becomes

$$H^2(z) = H_0^2\left[\Omega_r(1+z)^4 + \Omega_m(1+z)^3 + \Omega_\Lambda\right], \tag{2.34}$$

where $z \equiv a_0/a - 1$ is the cosmological redshift. This expression encapsulates the full expansion history of the Universe: first, at large z (early times) radiation dominated,

then, at intermediate values of z matter dominated, and finally starting from $z \sim 0.4$ the cosmological constant started to drive accelerated expansion.

Current observations give $\Omega_\Lambda \simeq 0.69$, $\Omega_m \simeq 0.31$ (of which $\Omega_b \simeq 0.05$ is baryonic) and $\Omega_r \simeq 9 \times 10^{-5}$, consistent with $\Omega_{\text{tot}} = 1$ [83]. The Hubble constant is measured to be

$$H_0 = 100h\,\text{km}\,\text{s}^{-1}\text{Mpc}^{-1}, \quad h \simeq 0.674\,, \tag{2.35}$$

although a statistically significant tension between early-Universe (CMB-based, $h \simeq 0.674$) and late-Universe (distance-ladder-based, $h \simeq 0.730$) measurements of H_0 currently remains unresolved [84, 85].

The EWPT occurs at temperatures around the electroweak scale, $T \sim 100\,\text{GeV}$, corresponding to $z \sim 10^{15}$, deep in the radiation-dominated epoch when $H^2 \approx \rho_r/(3\bar{M}_{\text{Pl}}^2)$.

II.2.2 Energy content of the Universe

The energy budget of the Universe is shared among four qualitatively distinct components: radiation, baryonic matter, dark matter and dark energy (cosmological constant). Their relative abundances change with time due to the different scalings of Eq. (2.31), as established in Section II.2.1. We briefly review each component with emphasis on the properties relevant to the early, radiation-dominated Universe where the EWPT takes place.

Radiation

In the early Universe, when temperatures exceeded the rest masses of the elementary particles, all SM degrees of freedom were relativistic and in thermal equilibrium. The energy density of a gas of non-interacting relativistic species in thermal equilibrium at temperature T is

$$\rho_r = \frac{\pi^2}{30} g_*(T) T^4\,, \tag{2.36}$$

where $g_*(T)$ is the effective number of relativistic degrees of freedom,

$$g_*(T) = \sum_{\text{bosons}} g_i \left(\frac{T_i}{T}\right)^4 + \frac{7}{8} \sum_{\text{fermions}} g_i \left(\frac{T_i}{T}\right)^4 . \tag{2.37}$$

Here g_i counts internal degrees of freedom (spin, color, charge conjugate states), T_i is the temperature of species i, and the factor $7/8$ arises from Fermi–Dirac versus Bose–Einstein statistics for fermions and bosons, respectively. At $T \gg m_t \simeq 172.5\,\text{GeV}$ [86], all SM particles are relativistic and $g_*(T) = 106.75$. As the Universe cools and successive species become non-relativistic, they transfer their entropy to the thermal bath and g_* decreases stepwise; by the time of neutrino decoupling ($T \sim 3\,\text{MeV}$) only photons and neutrinos remain relativistic, giving $g_* \simeq 3.36$ and today $g_* \simeq 2$ (photons only). The present-day radiation density is negligible, $\Omega_r \simeq 9 \times 10^{-5}$, but radiation dominated the expansion history for all $T \gtrsim 1\,\text{eV}$ and is the sole relevant component at the temperatures of interest for electroweak baryogenesis and phase transitions.

Similarly, the entropy density and pressure of the radiation bath are

$$s = \frac{2\pi^2}{45}\, g_{*s}(T)\, T^3\,, \qquad p_r = \frac{\rho_r}{3}\,, \tag{2.38}$$

where $g_{*s}(T)$ is the effective number of entropy degrees of freedom, defined analogously to Eq. (2.37) but with T_i^3 rather than T_i^4. Away from decoupling transitions $g_{*s} \approx g_*$. The total comoving entropy $S = sa^3$ is conserved in the absence of entropy production, which allows one to track the temperature as a function of scale factor: $T \propto g_{*s}^{-1/3} a^{-1}$.

Baryonic matter

Baryonic matter (quarks, gluons and their bound states) accounts for only $\Omega_b \simeq 0.05$ of the total energy density today [83]. At temperatures above the QCD confinement scale ($T \gtrsim 200\,\text{MeV}$) the baryonic component exists as a quark–gluon plasma embedded within a large radiation bath. Below confinement, quarks and gluons are bound into hadrons, whose subsequent annihilations and decays leave only the lightest baryons (protons and neutrons), with a small relic abundance set by the BAU. The baryon-to-photon ratio,

$$\eta_B \equiv \frac{n_B - n_{\bar{B}}}{n_\gamma} \simeq 6 \times 10^{-10}\,, \tag{2.39}$$

is one of the key observational inputs for Big Bang nucleosynthesis (BBN) [83] and a quantity that any successful mechanism of baryogenesis must reproduce. The origin of $\eta_B \neq 0$ — the BAU — remains an open question, and the EWPT is a promising setting for its generation, see Section II.3.

Dark matter

A wide range of independent observations — galactic rotation curves, gravitational lensing, cluster mass reconstructions, CMB power spectra and large-scale structure surveys — point to the existence of a non-luminous, non-baryonic matter component [87, 88]. This dark matter contributes $\Omega_{\rm DM} \simeq 0.26$ and clusters gravitationally in the same way as ordinary matter, with equation of state $w = 0$ and energy density diluting as $\rho_{\rm DM} \propto a^{-3}$. The SM contains no viable dark matter candidate; its identity remains one of the outstanding open problems of fundamental physics, discussed further in Section II.3.

Dark energy and the cosmological constant

The accelerated expansion of the Universe, first established by Type Ia supernova observations in 1998 [89, 90], is attributed to dark energy. In the simplest realization, dark energy is a cosmological constant Λ in Einstein's equations, corresponding to vacuum energy density

$$\rho_\Lambda = \bar{M}_{\rm Pl}^2 \Lambda \,, \tag{2.40}$$

with equation of state $w = -1$. The observed value, $\rho_\Lambda^{1/4} \simeq 2.3 \times 10^{-3}$ eV, is some 120 orders of magnitude smaller than the naive QFT estimate from summing up zero-point energies of all SM fields, which constitutes the cosmological constant problem. The ΛCDM model simply takes Λ as a free parameter fit to data, and $\Omega_\Lambda \simeq 0.69$ accounts for the largest share of the present-day energy budget and drives the accelerated expansion at present day. For the physics of the early Universe and the electroweak epoch, dark energy is entirely negligible.

II.2.3 Thermal history

Starting from an extremely hot, dense initial state, the Universe cooled as it expanded, and a sequence of phase transitions and decoupling events shaped the matter and radiation content observed today. The key epochs in chronological (decreasing-temperature) order are:

- **Inflation** ($T_{\rm rh} \sim ?$): Prior to the hot Big Bang, the Universe is believed to have undergone a period of accelerated, quasi-exponential expansion driven by one or more inflaton fields [91–93]. Inclusion of the inflation stage resolves the horizon

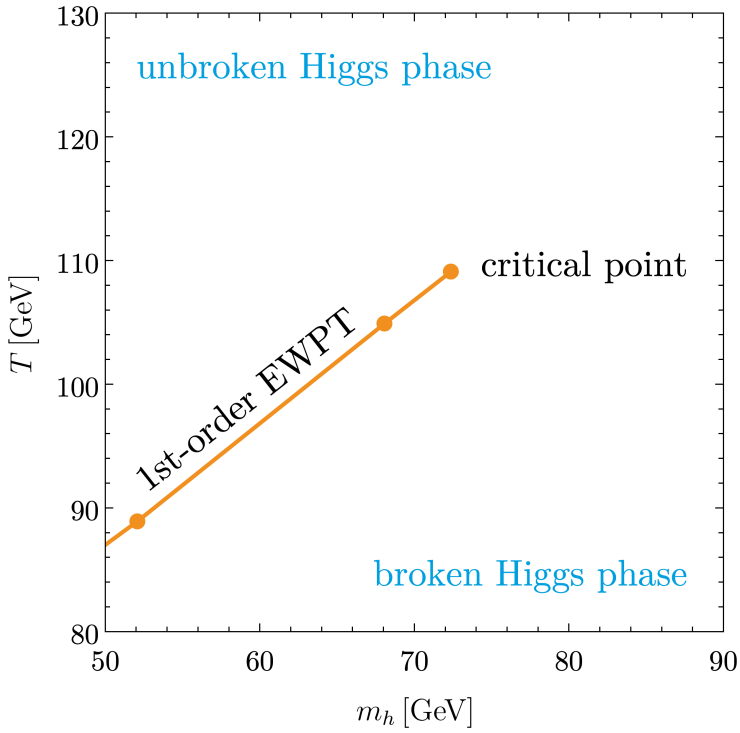

Figure 2.1: The phase diagram of the SM with the varied mass of the Higgs boson. A first-order phase transition occurs for $m_h \lesssim 72\,\text{GeV}$, while for the observed value $m_h \simeq 125\,\text{GeV}$ lies in the crossover region. The blobs represent the lattice simulation points, while the solid line is a fit between them. Figure adapted from [94].

and flatness problems and seeds the nearly scale-invariant adiabatic perturbations observed in the CMB. At the end of inflation, reheating converts inflaton energy into SM radiation, with reheating temperatures ranging from $\sim 10^{15}\,\text{GeV}$ down to $\mathcal{O}(\text{MeV})$ depending on the inflation model.

- **Electroweak epoch** ($T \sim 100\,\text{GeV}$): Above this scale, the symmetry $SU(2)_L \times U(1)_Y$ is restored with $\langle\Phi\rangle = 0$. As the Universe cools, the symmetry breaks down to $U(1)_{\text{em}}$, the Higgs condensate forms and the W/Z bosons and fermions acquire mass. In the SM with $m_h \simeq 125\,\text{GeV}$, this is a smooth crossover rather than a first-order transition, as shown in Fig. 2.1.

- **QCD confinement** ($T \sim 150\,\text{MeV}$): Near $T_{\text{QCD}} \simeq 150\,\text{MeV}$, quarks and gluons hadronize into color-neutral states. The effective relativistic degrees of freedom drop sharply ($g_* \approx 52 \to 17$), and subsequent hadron–antihadron annihilation leaves a small baryon excess set by η_B.

- **Neutrino decoupling and e^+e^- annihilation** ($T \sim 3\,\text{MeV}$): Neutrinos remain in equilibrium until $\Gamma_\nu \sim G_F^2 T^5$ falls below the Universe expansion rate H, at

$T_{\nu,\mathrm{dec}} \simeq 3\,\mathrm{MeV}$. Later, around $T \simeq 0.5\,\mathrm{MeV}$, e^+e^- annihilation heats photons relative to decoupled neutrinos, giving $T_\nu/T_\gamma = (4/11)^{1/3}$, where T_γ denotes the CMB photon temperature.

- **Big Bang nucleosynthesis** ($0.05\,\mathrm{MeV} \lesssim T \lesssim 2\,\mathrm{MeV}$): Neutrons freeze out at $T \simeq 0.8$ MeV, setting the neutron-to-proton ratio $n/p \simeq 1/6$. As the temperature drops further to $T \simeq 0.07$ MeV, light nuclei such as D, ^{3}He, ^{4}He and ^{7}Li are synthesized. The predicted primordial abundances agree well with observations, providing an early test of a radiation-dominated expansion [95, 96]. In this context, the effective number of relativistic neutrino species, $N_{\mathrm{eff}} \simeq 3$, is also experimentally tested, since changes in N_{eff} would alter the expansion rate and hence the light-element abundances.

- **Matter–radiation equality** ($T \simeq 0.75\,\mathrm{eV}$): Equality between matter ρ_m and radiation ρ_r energy densities occurs around $1 + z_{\mathrm{eq}} \simeq \Omega_m/\Omega_r \simeq 3400$. Expansion changes from radiation domination ($a \propto t^{1/2}$) to matter domination ($a \propto t^{2/3}$), enabling efficient structure formation in the Universe.

- **Recombination and last scattering** ($T \simeq 0.26\,\mathrm{eV} \simeq 3000\,\mathrm{K}$): At $T \simeq 3000\,\mathrm{K} \approx 0.26\,\mathrm{eV}$, electrons and protons combine into neutral hydrogen. The photon mean free path rises sharply, photons decouple, and the CMB free-streams to us from the last-scattering surface. Precision CMB anisotropy measurements constrain primordial perturbations and ΛCDM parameters [83].

- **Matter–Λ equality** ($T_\gamma \simeq 3.8\,\mathrm{K}$): At late times, the matter and dark-energy densities become comparable, $\rho_m \simeq \rho_\Lambda$, with $1 + z_{m\Lambda} \simeq (\Omega_\Lambda/\Omega_m)^{1/3} \simeq 1.3$. Beyond this point, the cosmological constant dominates the expansion and drives accelerated growth of the scale factor.

- **Today** ($T_\gamma \simeq 2.7\,\mathrm{K}$): The present-day Universe is in the dark energy dominated era, with approximate energy fractions $\Omega_\Lambda \simeq 0.69$, $\Omega_m \simeq 0.31$ and $\Omega_r \simeq 9 \times 10^{-5}$. Structures formed during the matter domination epoch continue evolving, while accelerated expansion suppresses further growth on the largest scales. Today, we can measure imprints of the early Universe through electromagnetic waves (up to the CMB last-scattering surface), GWs and primordial magnetic fields.

II.2.4 Gravitational waves

GWs are the propagating perturbations of the metric tensor $g_{\mu\nu}$ — predicted by Einstein's GR and first directly detected by the LIGO collaboration in 2015 [9]. They carry information about their sources that is entirely inaccessible to electromagnetic observations, making them a qualitatively new window on the Universe. In this section we review how GWs emerge from GR, characterize their properties and survey the cosmological sources of them.

Gravitational waves in linearized general relativity

The starting point is the linearization of GR around flat Minkowski spacetime. Writing $g_{\mu\nu} = \eta_{\mu\nu} + h_{\mu\nu}$ with $|h_{\mu\nu}| \ll 1$, the Einstein field equations to first order in $h_{\mu\nu}$ give the wave equation for the trace-reversed perturbation $\bar{h}_{\mu\nu} \equiv h_{\mu\nu} - \frac{1}{2}\eta_{\mu\nu}h$,

$$\Box \bar{h}_{\mu\nu} = -\frac{2\,T_{\mu\nu}}{\bar{M}_{\rm Pl}^2}\,, \tag{2.41}$$

in the Lorenz gauge $\partial^\mu \bar{h}_{\mu\nu} = 0$, where $\Box \equiv \partial_\mu \partial^\mu$ and $T_{\mu\nu}$ is the energy-momentum of the GW source. In vacuum, Eq. (2.41) reduces to $\Box \bar{h}_{\mu\nu} = 0$, a massless wave equation admitting solutions $\bar{h}_{\mu\nu} \propto \epsilon_{\mu\nu} e^{ik_\alpha x^\alpha}$ with $k^\alpha k_\alpha = 0$ (waves propagating at the speed of light) and $\epsilon_{\mu\nu}$ being the polarization tensor.

The counting of physical degrees of freedom follows the same logic as in electromagnetism, and it is instructive to run both arguments in parallel. The vector potential A_μ carries 4 components. Imposing the gauge-fixing condition, in particular, the Lorenz gauge $\partial^\mu A_\mu = 0$ removes one degree of freedom, while fixing the residual gauge freedom $A_\mu \to A_\mu + \partial_\mu \alpha$, with $\Box \alpha = 0$ in vacuum, eliminates one more. The result is $4 - 1 - 1 = 2$ physical, transverse polarizations. The gravitational perturbation $\bar{h}_{\mu\nu}$ is a symmetric tensor with 10 independent components. Imposing the Lorenz gauge $\partial^\nu \bar{h}_{\mu\nu} = 0$ imposes 4 conditions, reducing the count to 6, and fixing the residual gauge freedom $\bar{h}_{\mu\nu} \to \bar{h}_{\mu\nu} + \partial_\mu \xi_\nu + \partial_\nu \xi_\mu$ with $\Box \xi^\mu = 0$ in vacuum removes 4 further components, leaving $10 - 4 - 4 = 2$ physical degrees of freedom.

It is convenient to work in the transverse-traceless (TT) gauge, where $\bar{h}^{0\mu} = 0$, $\bar{h}^{ii} = 0$, $\partial^j \bar{h}_{ij} = 0$ such that $\bar{h}_{\mu\nu} = h_{\mu\nu}$. For a wave travelling in the $\hat{z}$ direction, in TT-gauge, a perturbation takes the form

$$h_{\mu\nu}^{\mathrm{TT}} = \begin{pmatrix} 0 & 0 & 0 & 0 \\ 0 & h_+ & h_\times & 0 \\ 0 & h_\times & -h_+ & 0 \\ 0 & 0 & 0 & 0 \end{pmatrix} \cos(\omega(t-z)) \,, \tag{2.42}$$

with two independent polarization amplitudes h_+ (plus) and $h_\times$ (cross). Both polarizations act by stretching space in one transverse direction while simultaneously squeezing it in the other, producing a time-varying quadrupolar distortion. It is this oscillating deformation of proper distances between freely falling test masses that interferometric detectors measure as the dimensionless strain.

As in electromagnetism, gravitational radiation is sourced by time-varying multipoles, however, due to mass-energy conservation and universality of gravity, dipole radiation is absent in GR. Hence, the leading GW emission is quadrupolar: spherically symmetric configurations do not radiate, while non-spherical accelerated motion does.

Astrophysical and cosmological sources of gravitational waves

GW sources span a wide range of frequencies, physical mechanisms and cosmological epochs. Compact-binary systems (inspiralling and merging pairs of black holes and neutron stars) radiate in the LIGO/Virgo/KAGRA band around 10–10^3 Hz and account for all confirmed individual detections to date [9]. At nanohertz frequencies, pulsar-timing arrays have reported evidence for a stochastic GW background [10, 97, 98], although its physical source is not yet understood.

At much lower frequencies, inflationary tensor perturbations would imprint a nearly scale-invariant stochastic GW background, potentially observable as B-mode polarization of the CMB [83]. Cosmic-string and domain-wall networks, formed in symmetry-breaking transitions in the early Universe, can produce both individual burst events and a broad-band stochastic background [99]. First-order phase transitions in the early Universe generate a stochastic GW background whose peak frequency is set by the Hubble rate at the time of the transition. For electroweak-scale transitions at $T \sim 100\,\mathrm{GeV}$, this peak falls squarely in the mHz band targeted by the LISA space-based observatory [30, 100, 101]. The prediction of this signal and its sensitivity to the microphysics of the transition is a central topic of this thesis. Together, these sources make the stochastic GW background a unique multi-messenger probe of the Universe, spanning energies and epochs inaccessible to any electromagnetic observatory.

II.2.5 Observational pillars

The success of the standard cosmological model rests on the consistency of multiple independent observational probes spanning very different stages of the Universe and physical processes. Together, these measurements support a spatially flat, expanding Universe whose dynamics is well described by the ΛCDM parameter set. Non-exhaustively, the main observational pillars validating this framework include:

- **Cosmic microwave background**

  The CMB provides a high-precision snapshot of the Universe at recombination. Its blackbody spectrum, acoustic peak structure and polarization anisotropies constrain the baryon density, matter density, scalar perturbation amplitude, optical depth and spatial curvature. In particular, CMB data from Planck show that the Universe is very close to spatially flat and are fully consistent with the six-parameter ΛCDM framework [83].

- **Big Bang nucleosynthesis**

  BBN predicts primordial abundances of light elements (D, ^{3}He, ^{4}He, ^{7}Li) from weak-interaction freeze-out and nuclear reaction networks in the early Universe. The observed abundances, especially deuterium and helium, broadly agree with the BBN predictions for the baryon density inferred from the CMB, providing a powerful cross-check between MeV- and eV-era cosmology and constraining the effective number of relativistic species to be close to $N_{\rm eff} \simeq 3$, consistent with three light neutrino degrees of freedom within the SM [95, 96].

- **Type Ia supernovae**

  Type Ia supernovae serve as standardisable candles: their peak luminosity can be calibrated from the shape and decline rate of their light curves, providing distance measurements across vast cosmological scales. Observations of high-redshift supernovae by the Supernova Cosmology Project revealed that the expansion of the Universe is accelerating [89, 90], providing the first direct evidence for a non-zero cosmological constant Λ. Combined with CMB and baryon acoustic oscillations data, Type Ia supernovae measurements tightly constrain the dark energy equation of state and provide an independent determination of Ω_m and Ω_Λ, consistent with the flat ΛCDM framework.

II.3 Open questions and motivations for new physics

Despite the extraordinary success of the SM and ΛCDM, both frameworks are evidently incomplete. A number of open questions remain, ranging from purely theoretical conundrums to problems with direct observational consequences. These limitations suggest that the current frameworks are barely an effective descriptions of a more fundamental theory and motivate the exploration of physics beyond the SM.

Many such issues have been discussed extensively in the literature [74], including the origin of neutrino masses, the nature of dark matter, the BAU, the hierarchy problem associated with the Higgs sector, inflation in the early Universe, the flavor puzzle, the strong CP problem of QCD and the absence of a quantum description of gravity. We briefly review those that are most directly relevant to the subject of this thesis.

- **Gravity as a quantum theory**

  GR is a classical field theory, while the SM is a quantum theory. No experimentally established, UV-complete quantum theory of gravity is currently known. Perturbative quantization of Einstein gravity is non-renormalizable, indicating that GR could only be interpreted as an EFT valid below the Planck scale $M_{\rm Pl}$. Understanding how gravity is consistently unified with quantum mechanics remains one of the deepest open problems in fundamental physics.

- **Dark matter**

  The SM contains no viable dark matter candidate, and the cosmological evidence reviewed in Section II.2 requires one. This strongly motivates new physics beyond the SM.

  Among the most extensively studied candidates are weakly interacting massive particles (WIMPs) [102], whose relic abundance can naturally arise from thermal freeze-out in the early Universe via interactions at the electroweak scale, motivating decades of direct detection, indirect detection and collider searches. Other well-motivated candidates include axions and axion-like particles (ALPs) [103], originally proposed to resolve the strong CP problem, sterile neutrinos arising in extensions of the neutrino sector [104], and primordial black holes formed in the early Universe [105]. Alternative production mechanisms, such as freeze-in or non-thermal scenarios, further broaden the landscape of possibilities. Despite an extensive experimental program spanning underground detectors, gamma-ray

telescopes and collider searches, no dark matter particle has yet been conclusively identified, making the nature of dark matter one of the outstanding open problems of fundamental physics (see e.g. [87, 106] for reviews).

- **The Higgs mass hierarchy problem**

  The Higgs mass parameter μ_h^2 in the SM receives quantum corrections that are quadratically sensitive to high-energy scales. In other words, any heavy state coupled to the Higgs contributes a correction proportional to the square of its mass, potentially driving the electroweak scale far above the measured value $v_{\rm EW} \simeq 246\,\text{GeV}$. Explaining why the Higgs mass remains so light in the presence of potentially huge UV scales, such as the Planck scale $M_{\rm Pl}$, without invoking extreme cancellations between bare parameters and radiative corrections is the core of the hierarchy problem. This apparent fine-tuning motivates new mechanisms that stabilize the Higgs mass, such as symmetry-based protection (e.g. supersymmetry), compositeness, or the existence of new weak-scale states that cancel or soften the large quantum contributions.

  In addition, the measured Higgs mass, $m_h \simeq 125\,\text{GeV}$, is striking from a theoretical perspective. It lies in a range where the SM vacuum is neither obviously stable nor catastrophically unstable [107], a near-critical situation that can be viewed as an additional fine-tuning within the Higgs sector [108, 109]. This coincidence highlights another puzzling feature of the scalar sector within the SM.

  At the same time, precision measurements of Higgs couplings at the LHC are increasingly constraining simple extensions of the SM. Reconciling the observed Higgs properties with the need for a SFOEWPT, necessary for mechanisms such as electroweak baryogenesis, is a key motivation for the extended scalar sectors explored in this thesis. These extensions can provide additional contributions to the scalar potential, enhancing the strength of the transition while remaining consistent with current experimental data.

- **Baryon asymmetry of the Universe**

  The Universe exhibits a pronounced matter–antimatter asymmetry quantified by the baryon-to-photon ratio (defined in Eq. (2.39)) as determined from measurements of the CMB and the BBN.

  Any successful dynamical mechanism for generating the BAU must satisfy the three Sakharov conditions [5]:

- **Baryon-number violation**: processes that can change the net baryon number;
- **C and CP violation**: interactions that distinguish between particles and antiparticles, allowing an imbalance to develop;
- **Out of thermal equilibrium**: conditions under which forward and reverse reactions do not cancel, so that asymmetries generated are not washed out.

The SM, with the measured Higgs mass, cannot generate the observed matter–antimatter asymmetry. Electroweak symmetry breaking proceeds through a smooth crossover rather than a first-order phase transition, and the amount of CP violation in the CKM sector is far too small to produce a significant BAU.

In extensions of the SM, a first-order EWPT can naturally provide the required departure from thermal equilibrium. During such a transition, bubbles of the broken phase nucleate and expand within the surrounding symmetric plasma (see comprehensive discussion in Chapter III). CP-violating interactions with the advancing bubble walls generate chiral charge asymmetries, which are partially converted into baryon number by sphaleron processes in front of the wall. If sphalerons are sufficiently suppressed inside the broken phase the generated asymmetry can survive to late times.

Baryon-number violation in this context is provided by nonperturbative sphaleron transitions [6, 110, 111], while additional sources of CP violation arise from Beyond the SM interactions. Because the EWPT in the SM is a smooth crossover, this mechanism cannot operate efficiently, motivating extensions of the scalar sector capable of producing a SFOEWPT, which is the focus of this thesis.

II.4 Beyond the Standard Model

The open problems surveyed in Section II.3 call for new physics beyond the SM. The landscape of BSM constructions is vast: it includes supersymmetry, composite Higgs models, extra dimensions, grand-unified theories, neutrino-mass frameworks, axion and dark-sector models and extensions of the scalar sector. Instead of attempting to comprehensively survey all of them, we focus here on the class of extensions most directly relevant to this thesis — those that modify the structure of the Higgs potential and thereby affect the character of the EWPT.

The reason for this focus is straightforward. In the SM with $m_h \simeq 125$ GeV, the EWPT is a smooth crossover (see Fig. 2.1): there is no potential barrier between the symmetric and broken-phase minima, hence no nucleation of bubbles and no departure from thermal equilibrium occurs that is strong enough to generate the BAU. Both electroweak baryogenesis and a detectable stochastic GW signal require instead a first-order transition, driven by a barrier in the finite-temperature scalar potential. The most straightforward way to generate such a barrier is to extend the scalar sector. Additional scalar degrees of freedom could contribute new cubic or quartic terms to the effective potential, reshape the thermal mass corrections, open new field directions for nucleation or induce a two-step transition — all of which can trigger a first-order EWPT in regions of parameter space compatible with current collider search bounds.

Extended Higgs sector

The simplest BSM extensions of the scalar sector are obtained by augmenting the SM with additional scalar fields that carry no new gauge charges but modify the shape of the finite-temperature scalar Higgs potential.

Adding a real or complex gauge singlet is the most minimal option: the singlet couples to the SM only through a portal interaction $\Phi^\dagger\Phi S^n$, which can generate a tree-level barrier between the symmetric and broken phases and strengthen the electroweak transition while remaining compatible with collider bounds across sizable regions of parameter space [112–114]. Two Higgs doublet models (2HDMs) provide a richer vacuum structure: the enlarged scalar spectrum introduces additional sources of CP violation, a more intricate pattern of phase transitions and additional charged and neutral Higgs states that are directly testable at colliders [115–119]. Scalar triplet extensions, such as those arising in the Georgi-Machacek model or in left-right symmetric frameworks, can also yield strong first-order transitions but are constrained by precision electroweak measurements through their effect on the ρ parameter [120, 121].

A qualitatively distinct class of models are those with classical conformal symmetry, in which the scalar potential contains no dimensionful (e.g. mass) parameters at tree level, and electroweak symmetry breaking is instead triggered directly by radiative corrections. The absence of a tree-level mass term naturally suppresses the Higgs mass relative to a UV cutoff, and the loop-induced barrier generically produces a strong first-order transition, making these models particularly motivated targets for GW observatories [122–124].

Across all these extensions, the common thread is that the scalar sector controls both the strength of the EWPT and the spectrum of new states accessible at colliders, making extended Higgs sectors a natural link between terrestrial experimental searches for new particles and GW probes such as LISA.

The SMEFT as a model-independent framework

Complementary to explicit BSM models, new heavy physics can be encoded in a model-independent way through the Standard Model Effective Field Theory (SMEFT). If new degrees of freedom are present at some high scale $\Lambda \gg v_{\rm EW}$, they can be integrated out, leaving their imprint as a tower of higher-dimensional operators built from SM fields and consistent with the SM gauge symmetries,

$$\mathcal{L}_{\rm SMEFT} = \mathcal{L}_{\rm SM} + \sum_i \frac{c_i^{(5)}}{\Lambda}\,\mathcal{O}_i^{(5)} + \sum_i \frac{c_i^{(6)}}{\Lambda^2}\,\mathcal{O}_i^{(6)} + \cdots . \tag{2.43}$$

The Wilson coefficients $c_i^{(d)}$ encode the details of the BSM physics, while the operator basis is fixed entirely by the SM field content and symmetries. This description assumes the new physics couples to the SM through a linear representation of the Higgs doublet; more general non-linear realizations are captured by the Higgs Effective Field Theory (HEFT) [125, 126].

The only dimension-five operator is the Weinberg operator $(\tilde{\Phi}^\dagger L)^2/\Lambda$, which violates lepton number and generates Majorana neutrino masses upon electroweak symmetry breaking.

Among the bosonic dimension-six operators, the scalar sector plays a central role in electroweak symmetry breaking and its thermal history. The ϕ^6 class contains the single operator

$$\mathcal{O}_\phi = (\Phi^\dagger\Phi)^3, \tag{2.44}$$

which modifies the Higgs potential directly, shifting the trilinear and quartic self-couplings away from their SM values and may introduce a tree-level barrier between the symmetric and broken phases that can turn the electroweak crossover into a genuine first-order transition [11, 127]. The $\phi^4 D^2$ class contributes two further operators, which in the Warsaw basis [128] read

$$\mathcal{O}_{\phi\Box} = (\Phi^\dagger\Phi)\Box(\Phi^\dagger\Phi), \qquad \mathcal{O}_{\phi D} = (\Phi^\dagger D^\mu\Phi)^\dagger(\Phi^\dagger D_\mu\Phi), \tag{2.45}$$

which modify the Higgs kinetic term and the W–Z mass relation respectively, feeding into the electroweak precision parameters while simultaneously affecting the scalar potential via loop corrections.

Going beyond the scalar sector alone, two-fermion operators of the $\psi^2\phi^3$ class also leave their mark on the phase transition. The top-quark Yukawa modifier,

$$\mathcal{O}_{t\phi} = (\Phi^\dagger\Phi)(\bar{Q}_L^3\tilde{\Phi}u_R^3) + \text{h.c.}, \tag{2.46}$$

alters the top–Higgs interaction, and, crucially, enters the loop corrections to the finite-temperature scalar potential, which governs the EWPT.

Remarkably, moderately positive values of $c_{t\phi}$, consistent with current experimental bounds, are sufficient to drive a strong first-order transition even in the complete absence of $\mathcal{O}_\phi$ [37]. This broadens the class of operators in the SMEFT relevant to the EWPT well beyond the scalar sector.

The SMEFT therefore provides a systematic bridge between precision measurements and the cosmological EWPT discussed in this thesis, making it possible to translate collider bounds directly into constraints on the thermal evolution of the Universe, see e.g. [129–131].

III – THEORETICAL FRAMEWORK

The mathematician plays a game in which he himself invents the rules while the physicist plays a game in which the rules are provided by Nature, but as time goes on it becomes increasingly evident that the rules which the mathematician finds interesting are the same as those which Nature has chosen.

— Paul Dirac

This chapter presents the theoretical framework underlying the study of the EWPT. We begin in Section III.1 with a brief review of QFT at finite temperature, introducing the imaginary-time formalism and the basic structure of thermal correlation functions. We then turn to the effective action and effective potential in Section III.2, which provide the central tools for describing symmetry breaking and phase transitions, including a discussion of their renormalization-scale and gauge dependence.

In Section III.3, we discuss false-vacuum decay and bubble nucleation, followed by the dynamics of bubble expansion and friction effects in the plasma. We then introduce the DR approach in Section III.4, emphasizing the relevant thermal scales and the breakdown of perturbation theory at high temperature, and motivating the construction of effective three-dimensional descriptions. In Section III.5, we connect these microscopic considerations to macroscopic thermodynamic observables, before turning in Section III.6 to their implications for GW signals from cosmological phase transitions.

III.1 Quantum field theory at finite temperature

The EWPT takes place at finite temperature $T \sim \mathcal{O}(100\,\mathrm{GeV})$, where the hot plasma of the early Universe acts as a thermal bath — a regime not captured by the vacuum formulation of Section II.1. The appropriate framework is *thermal field theory*, which generalizes the path-integral formulation of vacuum QFT to systems at finite temperature $T = 1/\beta$, where thermal equilibrium is assumed.

In vacuum QFT the generating functional in Minkowski space is given by

$$Z[J] = \int \mathcal{D}\phi \exp\left\{ iS[\phi] + i\int d^4x J(x)\phi(x) \right\}, \tag{3.1}$$

where $S[\phi] = \int d^4x \mathcal{L}(\phi, \partial_\mu \phi)$ is the Minkowski action extending over all of $\mathbb{R}^{3,1}$. The connected functional $W[J] = -i \log Z[J]$ generates all connected n-point correlation functions, which enter the determination of physical observables.

At finite temperature, the central object is instead the *thermal partition function*

$$\mathcal{Z} = \mathrm{Tr}\left[e^{-\beta \hat{H}} \right], \tag{3.2}$$

which is the *canonical* partition function, describing a system in thermal equilibrium at fixed temperature $T = 1/\beta$. From it the Helmholtz free energy $F = -T \log \mathcal{Z}$ and all thermodynamic observables follow, as discussed in Section III.5.

III.1.1 The imaginary-time formalism

The connection between Eqs. (3.1) and (3.2) becomes transparent after the Wick rotation $t \to -it_E$: the Boltzmann weight $e^{-\beta \hat{H}}$ is then formally the Euclidean time-evolution operator $e^{-t_E \hat{H}}$ evaluated at $t_E = \beta$. The trace in Eq. (3.2) identifies the field configuration at $t_E = 0$ with that at $t_E = \beta$, rendering the imaginary-time direction periodic. This compactification is the core idea of the imaginary-time formalism (ITF):

$$\mathbb{R}^4 \longrightarrow S^1_\beta \times \mathbb{R}^3, \qquad t_E \in [0,\, \beta]\,, \tag{3.3}$$

where S^1_β is a circle of circumference $\beta = 1/T$; in the limit $T \to 0$ the circle decompactifies, recovering the vacuum theory.

The thermal partition function thereby admits the path-integral representation

$$\mathcal{Z} = \int_{\phi(0,\vec{x})=\phi(\beta,\vec{x})} \mathcal{D}\phi \exp\{-S_E[\phi]\}\,, \tag{3.4}$$

with the Euclidean action

$$S_E[\phi] = \int_0^\beta dt_E \int d^3x\ \mathcal{L}_E(\phi, \partial_\mu \phi)\,, \tag{3.5}$$

where $\mathcal{L}_E$ is obtained from the Minkowski Lagrangian under $t \to -it_E$. Bosonic fields satisfy *periodic* boundary conditions $\phi(0,\vec{x}) = \phi(\beta,\vec{x})$, while fermionic fields satisfy *antiperiodic* conditions $\psi(0,\vec{x}) = -\psi(\beta,\vec{x})$, the sign arising from the trace over the fermionic Fock space.

Matsubara frequencies

The periodic (or antiperiodic) boundary conditions in t_E discretize the Fourier decomposition of fields in the imaginary-time direction:

$$\phi(t_E,\vec{x}) = T\sum_{n=-\infty}^{\infty} \int \frac{d^3k}{(2\pi)^3} \tilde{\phi}(\omega_n,\vec{k}) e^{i\omega_n t_E + i\vec{k}\vec{x}}\,, \tag{3.6}$$

with the boundary conditions constraining the allowed frequencies to the discrete set:

$$\omega_n = \begin{cases} 2\pi n T & \text{(bosons)}\,, \\ (2n+1)\pi T & \text{(fermions)}\,, \end{cases} \qquad n \in \mathbb{Z}\,, \tag{3.7}$$

which are called *Matsubara frequencies*. Hence, integration over the energy component is replaced by a discrete sum over the allowed Matsubara frequencies, while the momentum integrals over the three spatial directions remain continuous:

$$\int \frac{d^4k}{(2\pi)^4} \longrightarrow T\sum_n \int \frac{d^3k}{(2\pi)^3}\,. \tag{3.8}$$

This replacement is the single most important computational rule in the imaginary-time formalism, appearing in calculations of loop diagrams, i.e. in the perturbative expansion of the generating functional.

In vacuum, the scalar propagator (two-point function) for a free real scalar of mass m,

after the Wick rotation, takes the form:

$$\Delta_E^0(k_{E,0}, \vec{k}) = \frac{1}{k_{E,0}^2 + \vec{k}^2 + m^2}. \tag{3.9}$$

At finite temperature, the compactification Eq. (3.3) discretizes the continuous Euclidean energy $k_{E,0}$ to the Matsubara frequencies ω_n of Eq. (3.7), giving the thermal propagator

$$\Delta^0(\omega_n, \vec{k}) = \frac{1}{\omega_n^2 + \vec{k}^2 + m^2}\,. \tag{3.10}$$

The thermal propagator Eq. (3.10) can be rewritten as

$$\Delta^0(\omega_n, \vec{k}) = \frac{1}{\vec{k}^2 + m_n^2}\,, \qquad m_n^2 \equiv \omega_n^2 + m^2\,, \tag{3.11}$$

which makes manifest that finite-temperature field theory in imaginary time can be viewed as a theory of an infinite tower of *three-dimensional* (3D) modes, each with an effective Matsubara mass m_n. The bosonic zero mode ($n = 0$, $\omega_0 = 0$, $m_0 = m$) is the lightest, while all higher modes acquire thermal masses $m_{n\neq 0} \sim 2\pi n T$ and decouple at high temperature. This hierarchy underlies the DR discussed in Section III.4.

Real-time formalism

An alternative formulation of finite-temperature field theory is the *real-time* (Schwinger–Keldysh or closed-time-path) formalism, in which the time variable remains real and the integration contour is deformed accordingly. In thermal equilibrium, the Kubo–Martin–Schwinger (KMS) condition is imposed on the contour, recovering the equilibrium real-time formalism discussed in [132, 133]. More generally, the same framework accommodates non-equilibrium initial states where KMS relation need not hold, giving access to time-dependent quantities such as spectral functions, transport coefficients, and out-of-equilibrium dynamics. However, throughout this thesis we work in the *static limit*, where all relevant quantities — the effective potential, thermal masses, and phase-transition parameters — are independent of external frequencies. In this limit the ITF is the most natural and efficient choice, and we do not employ the real-time formalism further.

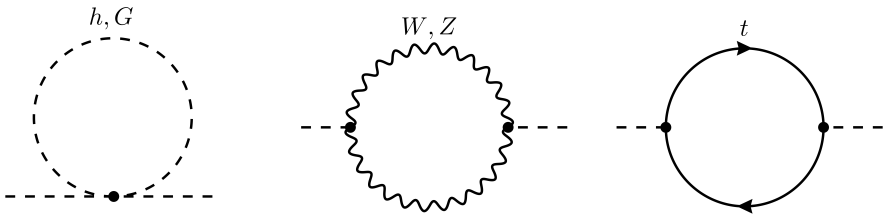

Figure 3.1: One-loop diagrams contributing to the Higgs thermal self-energy.

III.1.2 Thermal correlation functions

Similarly to the vacuum case, the correlation functions at finite temperature receive loop corrections, computed perturbatively from the generating functional. In momentum space, the two-point function $\Delta(\omega_n, \vec{k})$, which takes the form of Eq. (3.10) in case of a free theory, receives loop corrections

$$\Delta^{-1}(\omega_n, \vec{k}) = \omega_n^2 + \vec{k}^2 + m^2 + \Pi(\omega_n, \vec{k}) \,, \tag{3.12}$$

where $\Pi(\omega_n, \vec{k})$ is the thermal self-energy, in direct analogy with the Dyson equation at zero temperature [134]. The self-energy Π encodes both quantum corrections containing the UV divergences (absorbed into counterterms as in Eq. (2.26)) and genuine thermal corrections that modify the dispersion relation of the quasi-particle excitations.

In general, finite temperature does not alter the UV structure of the theory: the short-distance divergences $L \ll 1/T$ are unaffected by thermal effects and remain identical to those at $T = 0$. As a result, renormalization can be carried out using the same $T = 0$, temperature-independent counterterms.

The Higgs thermal self-energy

As a concrete illustration of the imaginary-time formalism, we compute the one-loop self-energy of the Higgs field h in the ITF in the high-temperature limit. This calculation is relevant for the thermal mass that enters the high-temperature expansion of the effective potential, as will be discussed in Section III.2, and connects with the DR procedure described in Section III.4.

The relevant one-loop diagrams are shown in Fig. 3.1; neglecting contributions from the light fermions, these are: the scalar, the top quark and the gauge-boson loops.

In the ITF, the contribution from the quartic scalar coupling λ_h, arising from loops of the Higgs and Goldstone bosons, is given by

$$\Pi_h^{(\lambda)} = 6\lambda_h T \sum_n \int \frac{d^3p}{(2\pi)^3} \frac{1}{\omega_n^2 + \vec{p}^2 + M_h^2}\,, \tag{3.13}$$

where $\omega_n = 2\pi n T$ are the bosonic Matsubara frequencies for the loop momentum. Performing the Matsubara sum via contour integration [132] and focusing on the thermal part, we obtain

$$\Pi_h^{(\lambda)} = 6\lambda_h \int \frac{d^3p}{(2\pi)^3} \frac{n_B(E_p)}{E_p}\,, \tag{3.14}$$

where $E_p = \sqrt{\vec{p}^2 + M_h^2}$ and $n_B(E_p) = 1/(e^{E_p/T} - 1)$ is the Bose–Einstein distribution. In the high-temperature limit $T \gg M_h$, the dominant contribution arises from hard momenta $p \sim T$, for which the mass can be neglected, $E_p \simeq p$. The integral then reduces to

$$\Pi_h^{(\lambda)} \simeq 6\lambda_h \int \frac{d^3p}{(2\pi)^3} \frac{n_B(p)}{p}\,, \tag{3.15}$$

which can be evaluated exactly using

$$\int \frac{d^3p}{(2\pi)^3} \frac{n_B(p)}{p} = \frac{T^2}{12}\,, \tag{3.16}$$

yielding

$$\Pi_h^{(\lambda)} \overset{T \gg M_h}{=} 6\lambda_h \frac{T^2}{12} = \frac{\lambda_h T^2}{2}\,. \tag{3.17}$$

Including the top quark and gauge boson contributions analogously, the full leading-order thermal correction to the Higgs self-energy in the high-temperature limit is

$$\Pi_h(T) = \frac{1}{48}\left(24\lambda_h + 9g^2 + 3g'^2 + 12y_t^2\right) T^2\,, \tag{3.18}$$

where we neglected the subleading contributions from other fermions.

This result shows that the Higgs boson acquires an effective thermal mass from its interactions with the plasma, $M_{h,T}^2(T) = M_h^2 + \Pi_h(T)$, which modifies its propagation and plays a crucial role in the dynamics of the EWPT, discussed in Section III.2.

III.2 Effective action and effective potential

The central objects for studying the thermodynamics of the EWPT are the *effective action* $\Gamma[\phi]$ and the *effective potential* $V(\phi, T)$. These generalize the classical action and the scalar potential, respectively, to include quantum and thermal loop corrections. The shape of $V(\phi, T)$ as a function of the background field ϕ and temperature T encodes the vacuum structure of the theory at finite temperature, thereby determining the nature of the phase transition.

The 1PI effective action

Starting at zero temperature, the generating functional coupled to an external source $J(x)$ is given by Eq. (3.1); the *connected generating functional* $W[J] = -i \log Z[J]$ generates all connected correlation functions in the theory. The *classical field*

$$\phi_c(x) \equiv \frac{\delta W[J]}{\delta J(x)} = \langle \phi(x) \rangle_J \tag{3.19}$$

is the vev of ϕ in the presence of the source. Inverting $\phi_c = \delta W / \delta J$ to express J as a functional of ϕ_c defines the one-particle irreducible (1PI) *effective action* as the Legendre transform of $W[J]$ [135, 136],

$$\Gamma[\phi_c] = W[J] - \int d^4x J(x)\, \phi_c(x). \tag{3.20}$$

By construction, $\Gamma[\phi_c]$ is the generating functional of 1PI diagrams and satisfies

$$\frac{\delta \Gamma[\phi_c(x)]}{\delta \phi_c(x)} = J(x). \tag{3.21}$$

Setting $J = 0$ selects the physical vacuum as the field configuration that extremises the effective action.

The effective action encodes the full quantum dynamics of the theory through its functional derivatives, which generate 1PI correlation functions. As a result, evaluating the effective action at tree level, i.e. treating it as a classical action without further loop corrections, already incorporates all quantum effects and yields a systematic description of the underlying theory.

In the following, we drop the subscript c and simply write ϕ for the classical field where

it appears as the argument of Γ or V.

The effective action $\Gamma[\phi]$ is a non-local functional of the background field $\phi(x)$, but it admits a derivative expansion,

$$\Gamma[\phi] = \int d^4x \left[-V(\phi) + \frac{1}{2} Z(\phi)(\partial_\mu \phi \, \partial^\mu \phi) + \cdots \right], \tag{3.22}$$

where $V(\phi)$ is the effective potential and $Z(\phi)$ is a field-strength renormalization. Under the assumption of homogeneity of the background field ϕ, the effective potential becomes a density of the effective action; it is the quantum-corrected generalization of the classical potential $V_0(\phi)$ and encodes the vacuum structure of the theory. The physical vacua of the theory are then simply determined by

$$\left. \frac{dV(\phi)}{d\phi} \right|_{\phi = \phi_{\min}} = 0, \tag{3.23}$$

which provides a convenient route to determining the vacuum structure and the character of phase transitions.

The loop expansion of the effective potential

A convenient method to evaluate $\Gamma[\phi]$ and $V(\phi)$ is to employ the *background field method* [136, 137], in which one splits the scalar field into a classical background ϕ and a quantum fluctuation η, and performs the path integral over η to obtain the effective action as a functional of ϕ,

$$S[\phi + \eta] = S[\phi] + \frac{1}{2} \int d^4x \, \eta(x) \left[-\partial^2 - m^2(\phi) \right] \eta(x) + \mathcal{O}(\eta^3), \tag{3.24}$$

where $m^2(\phi) = d^2V_0(\phi)/d\phi^2$ is the background-field-dependent mass. For brevity, only the scalar contribution is shown; the full calculation includes all fields of the theory, each contributing an analogous term with its corresponding background-field-dependent mass. Performing the Gaussian path integral over η-fields yields the one-loop contribution to the effective action,

$$\Gamma_1[\phi] = \frac{i}{2} \operatorname{Tr} \log \left[-\partial^2 - m^2(\phi) \right]. \tag{3.25}$$

For a constant background field, Eq. (3.25) reduces to a trace over momentum eigenstates.

Writing out the momentum integral after a Wick rotation to Euclidean momenta yields:

$$V_1(\phi) = \frac{1}{2}\int \frac{d^4k_E}{(2\pi)^4}\,\log\left[k_E^2 + m^2(\phi)\right], \tag{3.26}$$

which is UV divergent. By employing the dimensional regularisation scheme, the divergence is isolated as a pole in $\epsilon = (4-d)/2$,

$$V_1(\phi) \underset{\text{dimReg}}{=} \frac{m^4(\phi)}{64\pi^2}\left[-\frac{1}{\epsilon} + \log\frac{m^2(\phi)}{\mu^2} - \frac{3}{2} + \mathcal{O}(\epsilon)\right], \tag{3.27}$$

where the $1/\epsilon$ pole is absorbed into an appropriate counterterm of the tree-level potential in the $\overline{\text{MS}}$ renormalization scheme and μ is the renormalization scale. The finite part is the one-loop correction to the effective potential, commonly referred to as the Coleman–Weinberg potential [135, 136].

Throughout this thesis, we denote the tree-level scalar potential as V_0, the one-loop contribution as V_1, and the two-loop contribution as V_2, so that the loop expansion of the effective potential reads

$$V(\phi) = V_0(\phi) + V_1(\phi) + V_2(\phi) + \cdots . \tag{3.28}$$

We can relate the calculation performed via the Gaussian path integral to a Feynman diagrammatic expansion by noting that the one-loop effective potential is given by the sum of all 1PI vacuum diagrams with background-field-dependent masses. Specifically, for the simple theory which only includes a scalar field with $V_0(\phi) = \mu_\phi^2\phi^2/2 + \lambda_\phi\phi^4/4$, we can rewrite Eq. (3.26) as:

$$V_1(\phi) = \frac{1}{2}\int \frac{d^4k_E}{(2\pi)^4}\,\log\left[k_E^2 + \mu_\phi^2 + 3\lambda_\phi\phi^2\right] = \sum_{n=1}^{\infty}\frac{1}{2n}\int\frac{d^4k_E}{(2\pi)^4}\left(\frac{3\lambda_\phi\phi^2}{k_E^2+\mu_\phi^2}\right)^n, \tag{3.29}$$

which corresponds to the sum of all one-loop vacuum diagrams with n insertions of the quartic interaction with the background field, see Fig. 3.2, matching the diagrammatic expansion.

There exists a complementary method to evaluate the effective potential, which relates its first field derivative to tadpole diagrams — 1PI diagrams with a single external background-field leg [138, 139]. Since the tadpole involves fewer propagators and vertices than the full set of 1PI vacuum diagrams that enter direct computations of the effective potential, this approach significantly simplifies higher-loop calculations.

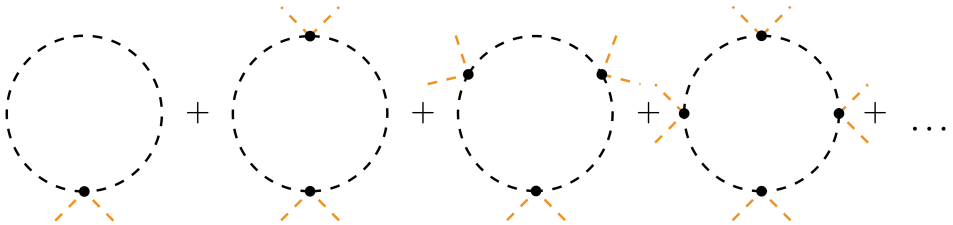

Figure 3.2: One-loop vacuum diagrams contributing to the effective potential, representing the expansion of Eq. (3.29). Each diagram corresponds to a term in the expansion, with n insertions of the quartic interaction between the background (orange) and fluctuation fields.

In the full theory, the one-loop effective potential is obtained by summing over contributions from all fields (see Eq. (3.27)), each with its own background-field-dependent mass $m_i^2(\phi)$. In the $\overline{\text{MS}}$ renormalization scheme, this results in the general expression:

$$V_1(\phi, \mu) = \sum_i \frac{n_i}{64\pi^2} m_i^4(\phi) \left[\log \frac{m_i^2(\phi)}{\mu^2} - c_i \right], \tag{3.30}$$

where the sum runs over all field-dependent mass eigenstates. The factors n_i are $n_i = d - 1$ for gauge fields, $n_i = -4N_c$ for Dirac fermions, $n_i = -2$ for ghosts, and $n_i = 1$ for scalar fields; $c_i = 3/2$ for scalars and fermions and $c_i = 5/6$ for gauge bosons [45, 140]. The residual μ-dependence is governed by the renormalization group equations, as discussed in Section III.2.1.

Higher-loop contributions to the effective potential may be computed analogously by retaining higher-order terms in the η-expansion and evaluating the path integral perturbatively. This corresponds to summing all 1PI vacuum diagrams with background-field-dependent masses, which can be done using standard Feynman diagram techniques.

Finite-temperature effective potential

At non-zero temperature T, the Euclidean time direction is compactified on a circle of circumference $\beta = 1/T$ and the fields acquire (anti)periodic boundary conditions, as established in Section III.1. As a consequence, the zero-temperature momentum integral in Eq. (3.26) is replaced by the thermal sum-integral of Eq. (3.8), leading to the finite-temperature one-loop effective potential

$$V_1(\phi, T) = \frac{T}{2} \sum_{n=-\infty}^{\infty} \int \frac{d^3k}{(2\pi)^3} \log\left[\omega_n^2 + \vec{k}^2 + m^2(\phi)\right], \tag{3.31}$$

where $\omega_n = 2\pi nT$ for bosons and $\omega_n = (2n+1)\pi T$ for fermions. The infinite sum over Matsubara frequencies ω_n can be performed using the standard techniques of contour integration; this yields a decomposition of the effective potential into a zero-temperature part (see Eq. (3.30)) and a thermal contribution,

$$V_1(\phi, T, \mu) = V_1(\phi, \mu)^{T=0} + V_1(\phi, T)^{T\neq 0}, \tag{3.32}$$

with

$$V_1(\phi, T)^{T\neq 0} = \frac{T^4}{2\pi^2} \sum_i n_i \, J_{B/F}\left(\frac{m_i^2(\phi)}{T^2}\right). \tag{3.33}$$

We have conveniently written $V_1^{T\neq 0}$ in terms of the dimensionless bosonic and fermionic thermal functions [45, 140],

$$J_B(y^2) = \int_0^\infty dx\, x^2 \log\left(1 - e^{-\sqrt{x^2+y^2}}\right), \tag{3.34}$$

$$J_F(y^2) = -\int_0^\infty dx\, x^2 \log\left(1 + e^{-\sqrt{x^2+y^2}}\right), \tag{3.35}$$

for bosons and fermions, respectively. The sign differences between the two thermal J-functions trace back to the (anti)periodic boundary conditions on the Euclidean circle. Ghost fields, which are Grassmann-valued but satisfy bosonic boundary conditions, contribute with the same J_B function as gauge bosons, but with a negative sign due to their Grassmann nature.

In the high-temperature limit, where $y^2 = m_i^2/T^2 \ll 1$, the thermal J-functions can be expanded as

$$\begin{aligned} J_B(y^2) &\approx -\frac{\pi^4}{45} + \frac{\pi^2}{12} y^2 - \frac{\pi}{6} y^3 + \mathcal{O}(y^4), \\ J_F(y^2) &\approx -\frac{7\pi^4}{360} + \frac{\pi^2}{24} y^2 + \mathcal{O}(y^4). \end{aligned} \tag{3.36}$$

Notably, only the bosonic function J_B contains a cubic term $\propto y^3 = (m_i(\phi)/T)^3$ in the high-temperature expansion, reflecting the fact that only bosonic fields possess zero Matsubara modes, which do not acquire thermal masses and can therefore give rise to non-analytic contributions to the effective potential [21, 136]. It is this cubic term that can generate a potential barrier in the Higgs potential capable of driving a first-order EWPT [45, 140, 141].

The complete one-loop effective potential at finite temperature is

$$V(\phi, T, \mu) = V_0(\phi) + V_1(\phi, \mu)^{T=0} + V_1(\phi, T)^{T\neq 0}. \tag{3.37}$$

III.2.1 Renormalization scale dependence

At finite loop order, the effective potential inherits a spurious dependence on the regularization scheme and associated renormalization parameters. For instance, in dimensional regularization with the $\overline{\text{MS}}$ scheme, this appears as a dependence on the scale μ, which is a consequence of truncating the perturbative expansion. There is both an explicit dependence on μ and an implicit scale dependence through the running of the couplings and the fields. The full μ-dependence of the perturbatively evaluated effective potential is governed by the RGE,

$$\left(\mu\frac{\partial}{\partial\mu} - \gamma\phi\frac{\partial}{\partial\phi} + \beta_i\frac{\partial}{\partial g_i}\right) V = 0\,, \tag{3.38}$$

which simply expresses the fact that $dV/d\mu = 0$ if all loop orders are taken into account. This equation shows that the explicit scale dependence of the effective potential cancels against the respective contributions from the scale dependence of the couplings g_i and the field ϕ, expressed in terms of the beta functions β_i and the anomalous dimension γ.

Equation (3.38) holds order by order in perturbation theory. For instance, the explicit scale dependence of the one-loop potential is canceled by the running of parameters and fields (which enters at one loop, i.e. at $\mathcal{O}(\hbar)$) in the tree-level potential:

$$\mu\frac{\partial}{\partial\mu}V_1 = \left(\gamma_1\phi\frac{\partial}{\partial\phi} - \beta_{i,1}\frac{\partial}{\partial g_i}\right) V_0, \tag{3.39}$$

where γ_1 and $\beta_{i,1}$ are the one-loop anomalous dimension and beta functions, respectively. The inclusion of the running of couplings and fields can therefore serve as a consistency check for the loop-improved potential. If one includes the running of parameters also in the *one-loop* effective potential, the residual, uncanceled scale dependence will be of two-loop order, i.e.

$$\left(\mu\frac{\partial}{\partial\mu} - \hbar\gamma_1\phi\frac{\partial}{\partial\phi} + \hbar\beta_{i,1}\frac{\partial}{\partial g_i}\right)(V_0 + \hbar V_1) = \mathcal{O}(\hbar^2), \tag{3.40}$$

where we explicitly write out the powers of $\hbar$ to indicate the respective loop orders for each term. This residual scale dependence propagates to predictions for physical ob-

servables derived from the loop-improved potential, providing an estimate of the size of missing higher-loop terms. Comparing the μ-dependence of the prediction of an observable at successive loop orders therefore serves as an important indicator of the validity of the perturbative expansion when truncated at a given loop order.

As an aside, we note that the potential may contain scale-dependent, but field-independent terms (*cosmological constant* or *vacuum energy* terms) whose running is not canceled by using loop-improved couplings. Such scale dependencies can be dealt with by including the running of a vacuum energy term in Eq. (3.38) (see Ref. [142]). Since field-independent terms do not affect the vacuum structure of the theory, we do not include the running of the vacuum energy in the analyses of this thesis.

There is an additional scale dependence of the effective potential: it depends on the initial scale μ_{in} at which it is first determined before evolving it to another scale μ. This additional scale dependence is governed by the RGE-like equation [143]

$$\mu_{\text{in}} \frac{\partial}{\partial \mu_{\text{in}}} V(\phi, \mu_{\text{in}}, \mu) = \gamma \phi \frac{\partial}{\partial \phi} V(\phi, \mu_{\text{in}}, \mu), \tag{3.41}$$

where γ is the anomalous dimension of the scalar field. This equation states that the dependence of V as a function of ϕ on the initial scale μ_{in} can be compensated by a rescaling of the field ϕ according to its anomalous dimension. Importantly, at an extremum of the potential where $\partial V/\partial \phi = 0$, the right-hand side vanishes identically, so the value of the potential at its extrema is independent of μ_{in}. Away from extrema, however, V does carry μ_{in}-dependence, which is analogous to the gauge-parameter dependence discussed below — both are unphysical artifacts that cancel in physical observables.

III.2.2 Gauge dependence

The effective action Eq. (3.20) is defined in the presence of a non-zero external source J, which breaks the Ward-Takahashi identity [144], the quantum analog of Noether's conservation theorem. As a consequence, in gauge theories such as the SM, the effective action and the effective potential derived from it are intrinsically gauge-dependent quantities.

The gauge dependence is governed by the Nielsen identity [145], which, for the effective potential, takes the form

$$\xi \frac{\partial}{\partial \xi} V(\phi, \xi) = C(\phi, \xi) \frac{\partial}{\partial \phi} V(\phi, \xi), \tag{3.42}$$

where ξ represents a set of gauge-fixing parameters. Equation (3.42) follows from the BRST invariance [144, 145] of the effective action and holds to all orders in perturbation theory. The functions $C(\phi, \xi)$ are correlation functions involving the ghost fields and the gauge-fixing function, and can be determined order-by-order in perturbation theory independently of V [146, 147]. Eq. (3.42) can be viewed as the leading term in the derivative expansion of the more general Nielsen identity for $\Gamma[\phi]$ [146].

The Nielsen identity shows that the effective potential is gauge-independent at its extremal points ϕ_{min},[1]

$$\xi \frac{\partial}{\partial \xi} V(\phi_{\text{min}}, \xi) = 0 \,. \tag{3.43}$$

The field value at the extremum, however, is gauge-dependent:

$$\frac{\partial \phi_{\text{min}}}{\partial \xi} = C(\phi_{\text{min}}, \xi) \,, \tag{3.44}$$

which is not problematic, since ϕ_{min} is not a physical, gauge-invariant observable.

Away from the extrema, Eq. (3.42) shows that the gauge dependence can be expressed in terms of field redefinitions governed by the functions $C(\phi, \xi)$.

This can also be understood from the fact that gauge transformations correspond to a special case of field redefinitions; as a consequence of the general invariance under such redefinitions, the values of the potential at the extrema are gauge-independent (see Fig. 3.3).

Since the values of the effective potential at its stationary points are gauge-independent, any physical observable that depends solely on these values inherits this property. For instance, the critical temperature T_c, defined as the temperature at which two local minima become degenerate (see Section III.5 for a precise definition), is gauge-independent.

Because Eq. (3.42) holds to all orders in perturbation theory, it requires careful treatment if a calculation is truncated at finite loop order. The interplay between gauge fixing and the loop expansion is therefore not merely a formal concern but has concrete consequences for the reliability of perturbative phase-transition calculations. Schematically, at one-loop order, we have

$$\xi \frac{\partial}{\partial \xi} V_1 = C_1(\phi, \xi) \frac{\partial}{\partial \phi} V_0, \tag{3.45}$$

[1] We denote the extremal points of the effective potential by ϕ_{min}, as minimum points are of the most interest for the phase transition phenomenology. However, Eq. (3.43) applies to any stationary point, including the local maxima.

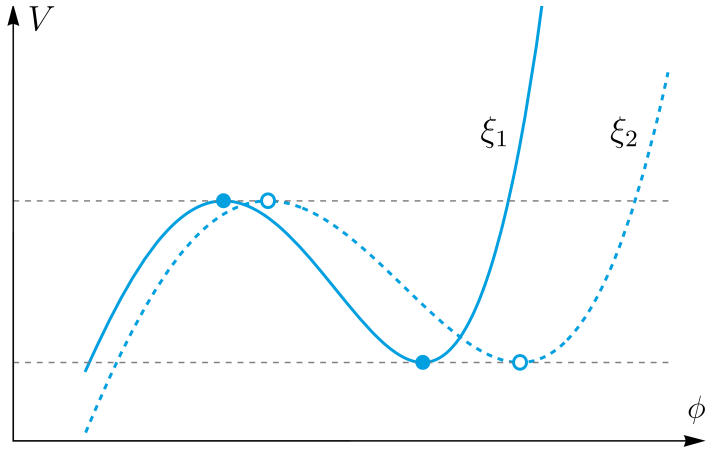

Figure 3.3: Illustration of the gauge dependence of the effective potential, adapted from [148]. The effective potential values at the extrema are gauge-independent, but the field values at which the extrema occur are gauge-dependent.

where we indicate the respective loop orders by the subscripts. Notice that the r.h.s. of Eq. (3.45) vanishes at the extremal points of the tree-level potential, ϕ_0, which does not coincide with the extremal points of the one-loop potential. This lies at the heart of the so-called *$\hbar$-expansion* [144, 148], which we explore in this section.

In order to systematically implement the $\hbar$-expansion, we need to determine the effective potential and its minima order-by-order in a loop expansion, where we use $\hbar$ as an expansion parameter:

$$\begin{aligned} V(\phi) &= V_0(\phi) + \hbar\, V_1(\phi) + \hbar^2\, V_2(\phi) + \mathcal{O}(\hbar^3), \\ \phi_{\text{min}} &= \phi_0 + \hbar\, \phi_1 + \hbar^2\, \phi_2 + \mathcal{O}(\hbar^3). \end{aligned} \tag{3.46}$$

Inserting the minimum field expansion in the effective potential yields

$$\begin{aligned} V_{\text{min}} &\equiv V(\phi_{\text{min}}) \\ &= V_0(\phi_0) + \hbar \left(V_1 + \phi_1 \frac{\partial V_0}{\partial \phi} \right)(\phi_0) \\ &\quad + \hbar^2 \left(V_2 + \phi_2 \frac{\partial V_0}{\partial \phi} + \phi_1 \frac{\partial V_1}{\partial \phi} + \frac{\phi_1^2}{2} \frac{\partial^2 V_0}{\partial \phi^2} \right)(\phi_0) \\ &\quad + \mathcal{O}(\hbar^3). \end{aligned} \tag{3.47}$$

Note that we can write the expressions within brackets in closed form for any loop order L. For this we write

$$V(\phi_{\text{min}}) = V_0(\phi_0) + \hbar V^{(1)} + \cdots + \hbar^L V^{(L)} + \mathcal{O}(\hbar^{L+1}) \tag{3.48}$$

and find

$$V^{(L)}(\phi_0) = \sum_{\{p_L\}} \frac{1}{P_L!} \binom{L}{p_1 \dots p_L} \prod_{k=1}^{L} \phi_k^{p_k} \times \sum_{n=0}^{L} \left(\partial_\phi^{P_L} V_n\right)(\phi_0)\, \delta\Big(\sum_{m=1}^{L} m \cdot p_m, L - n\Big) \tag{3.49}$$

where $\sum_{\{p_L\}} = \sum_{p_1=0}^{L} \sum_{p_2=0}^{L-1} \cdots \sum_{p_L=0}^{1}$, $P_L = \sum_{j=1}^{L} p_j$ and $\delta(a,b) = \delta_{a,b}$ is a Kronecker-delta which extracts the terms of correct loop order from the summations over products of different field and potential derivative powers.

The minimum ϕ_{min} is simply determined via the vanishing of the first field derivative of the effective potential,

$$\left.\frac{dV(\phi)}{d\phi}\right|_{\phi=\phi_{\text{min}}} = 0. \tag{3.50}$$

We can use this to determine the loop corrected field minima ϕ_L from each term $V^{(L)}$. It turns out that ϕ_L can be recursively defined via lower loop-order field solutions exclusively, namely via an inhomogeneous nonlinear recurrence relation of the form

$$\phi_L = \varphi(L; \phi_{L-1}, \dots, \phi_1), \tag{3.51}$$

where fixing ϕ_0 by minimizing $V_0(\phi)$ serves as a boundary condition. For this we note that Eq. (3.49) is linear in ϕ_L (it only appears as a term $\phi_L V_0'$), so we can easily solve for it. The result is

$$\phi_L = -\frac{1}{V_0''}\Bigg[\sum_{\{p_{L-1}\}} \frac{1}{P_{L-1}!} \binom{L}{p_1 \dots p_{L-1}} \prod_{k=1}^{L-1} \phi_k^{p_k} \times \sum_{n=0}^{L} \left(\partial^{1+P_{L-1}} V_n\right) \delta\Big(\sum_{m=1}^{L-1} m \cdot p_m, L - n\Big)\Bigg], \tag{3.52}$$

and we note again that the product only depends on the fields up to order $L-1$. For instance, the first few terms read

$$\begin{aligned} \phi_1 &= \left(-\frac{V_1'}{V_0''}\right)(\phi_0), \\ \phi_2 &= \left(-\frac{V_2'}{V_0''} + \frac{V_1'' V_1'}{(V_0'')^2} - \frac{V_0''' (V_1')^2}{2(V_0'')^3}\right)(\phi_0), \end{aligned} \tag{3.53}$$

where we denote field derivatives by a prime for brevity. The complexity of the recurrence relation Eq. (3.51) suggests that it is virtually impossible to find a closed-form solution for ϕ_L solely in terms of derivatives of the potential. Nevertheless, Eq. (3.52) can be used to determine ϕ_L in a straightforward, algorithmic manner.

Inserting these field solutions into Eq. (3.47) and applying the tree-level minimum condition $V_0'(\phi_0) = 0$ yields

$$\begin{aligned} V_{\text{min}} = V_0(\phi_0) + \hbar V_1(\phi_0) + \hbar^2 \left(V_2 - \frac{(V_1')^2}{2V_0''} \right)(\phi_0) \\ + \hbar^3 \left(V_3 - \frac{V_1' V_2'}{V_0''} + \frac{(V_1')^2 V_1''}{2(V_0'')^2} - \frac{V_0'''(V_1')^3}{6(V_0'')^3} \right)(\phi_0) + \mathcal{O}(\hbar^4). \end{aligned} \tag{3.54}$$

Curiously, the number of terms appearing at each loop order in Eq. (3.54), which is the result of the $\hbar$-expansion around the tree-level minimum, $\{1, 1, 2, 4, 11, 27, 68, 158 \dots\}$, does not appear to be a known sequence in the literature [149].

The Nielsen identity of Eq. (3.42) guarantees that V_{min} is gauge-independent, so each term in Eq. (3.54) must individually be gauge-independent as well. This means that the gauge dependence of the two-loop effective potential at the minimum is fully governed by field derivatives of the one-loop and tree-level expressions, i.e.

$$\frac{\partial V_2}{\partial \xi}(\phi_0, \xi) = \left(\frac{V_1'}{V_0''} \frac{\partial V_1'}{\partial \xi} - \frac{1}{2} \left(\frac{V_1'}{V_0''} \right)^2 \frac{\partial V_0''}{\partial \xi} \right)(\phi_0, \xi). \tag{3.55}$$

This pattern persists at any loop order: the gauge dependence of the L-loop effective potential V_L at the minimum is fully determined by field derivatives of contributions at $(L-1)$-loop order and below. This can be seen by extracting two crucial terms in Eq. (3.49), namely the ones where $n = 0, k = L$ (the Kronecker-delta then only allows $(p_L = 1, p_1 = \dots p_{L-1} = 0)$ or $p_L = 0$) and $n = L$ (only $p_1 = \dots = p_L = 0$ is non-vanishing). The former term is $\phi_L V_0'(\phi_0)$ and vanishes due to the definition of ϕ_0 as the tree-level minimum. Therefore, we can write Eq. (3.49) as

$$\begin{aligned} V^{(L)}(\phi_0) = & V_L(\phi_0) \\ & + \sum_{\{p_{L-1}\}} \frac{1}{P_{L-1}!} \binom{L}{p_1 \dots p_{L-1}} \prod_{k=1}^{L-1} \phi_k^{p_k} \\ & \times \sum_{n=0}^{L-1} \left(\partial_\phi^{P_{L-1}} V_n \right)(\phi_0)\, \delta\Big(\sum_{m=1}^{L-1} m \cdot p_m, L - n \Big), \end{aligned} \tag{3.56}$$

where, crucially, we see that only the first term is of loop-order L. Applying the Nielsen identity (and shifting $L \to L+1$), we find

$$\frac{\partial V_{L+1}(\phi_0)}{\partial \xi} = -\frac{\partial}{\partial \xi}\Bigg[\sum_{\{p_L\}} \frac{1}{P_L!}\binom{L+1}{p_1 \dots p_L} \prod_{k=1}^{L} \phi_k^{p_k} \times \sum_{n=0}^{L} \big(\partial_\phi^{P_L} V_n\big)(\phi_0)\, \delta\Big(\sum_{m=1}^{L} m \cdot p_m, L-n\Big)\Bigg]. \tag{3.57}$$

This equation expresses the gauge dependence of V_{L+1} entirely in terms of lower-order quantities — the fields $\phi_{n\leq L}$ and loop potentials $V_{n\leq L}$ — evaluated at the tree-level minimum.

A second consequence is the cancellation of IR divergences related to the presence of the massless Goldstone bosons (i.e. in Landau gauge) at each power in $\hbar$, allowing one to extract said divergences at $(L+1)$-loop order from L-loop results [150].

Gauge-independent results are obtained by determining the minimum of the effective potential order by order in perturbation theory: at each loop order, the dependence on the gauge-fixing parameters cancels in accordance with Eq. (3.42). By contrast, naively minimizing the n-loop improved potential numerically leaves an uncanceled gauge dependence in $V(\phi_{\text{min}})$.

The $\hbar$-expansion is, however, inherently perturbative, and its reliability deteriorates whenever loop contributions are parametrically enhanced — for instance, in the high-temperature regime (see Section III.4.2) or if the potential barrier is radiatively generated [146]. In both cases, higher-order corrections become parametrically of a similar order to the lower-order ones, and hence the $\hbar$-expansion can deviate significantly from a direct minimization [148]. The perturbative expansion must therefore be reorganized accordingly, for instance as an expansion in the gauge coupling (see Section III.4.2).

Gauge-fixing conditions

We now turn to the choice of gauge-fixing condition, which plays an important role both in the practical implementation of the $\hbar$-expansion and in the reliability of perturbative phase-transition calculations more generally.

The general gauge-fixing Lagrangian [151], summed over all gauge group generators a,

reads

$$\mathcal{L}_{\text{gf}} = -\sum_a \frac{1}{2\xi_1^a}\left(\partial^\mu A_\mu^a + i\xi_2^a g_a t_{ik}^a \tilde{\phi}_i \phi_k\right)^2, \tag{3.58}$$

where g_a is the gauge coupling, t_{ik}^a are the representation matrices, ξ_1^a, ξ_2^a and $\tilde{\phi}_i$ are the gauge-fixing parameters and ϕ_k are the scalar field components. The common gauge-fixing choices are:

- **Fermi gauge**: $\xi_2^a = 0$. In this gauge, ghost fields are background-field independent, but the calculations are complicated by the fact that the cross-terms between gauge and scalar fields in the kinetic Lagrangian are not canceled, leading to scalar–vector propagator mixing for $\xi_1^a \neq 0$. Massless Goldstone bosons also lead to IR divergences in this gauge, which must be dealt with appropriately, see e.g. [152, 153].

- **Standard R_ξ^{std}-gauge**: $\tilde{\phi} = \phi_{\text{min}}$, where ϕ_{min} is the tree-level vev, and $\xi_1^a = \xi_2^a$. This choice cancels scalar–vector mixing at the tree-level minimum $\phi = \phi_{\text{min}}$, but not away from it.

- **Background R_ξ^{bkgd}-gauge**: $\tilde{\phi} = \phi$, where ϕ is the dynamical background field, and $\xi_1^a = \xi_2^a$. It has the advantage of cancelling the scalar–vector propagator mixing for all field values ϕ, which significantly simplifies the effective potential beyond tree level. However, employing a different gauge-fixing condition for each value of ϕ should be approached with caution [144], also see the further discussion below.

- **Landau gauge**: special case of both the Fermi and R_ξ-gauge families, with $\xi_1^a = \xi_2^a = 0$. The gauge propagators become purely transverse, ghost masses vanish, and there is no scalar–vector kinetic mixing. This choice of gauge-fixing parameters is RG invariant and is often regarded as the preferred choice for high-loop calculations, e.g. [154]. Similar to the Fermi gauge, massless Goldstone bosons lead to IR divergences in Landau gauge.

- **Unitary gauge**: $\xi_1^a = \xi_2^a \to \infty$. In this gauge, Goldstone bosons and ghosts decouple from the other degrees of freedom; however, the perturbative expansion must be reorganized [21, 155, 156].

The two gauge-fixing parameters ξ_1^a and ξ_2^a run independently under the RG at one-loop order in four space-time dimensions; consequently, any relation between them is not pre-

served under RG evolution, with the sole exception of the fixed point $\xi_1^a = \xi_2^a = 0$. However, since the tree-level potential V_0 is independent of ξ, the running of the gauge-fixing parameters first affects the effective potential at two-loop order, through $\beta_\xi \, \partial V_1/\partial\xi$. We therefore treat ξ_1^a and ξ_2^a as fixed, scale-independent parameters throughout.

Within the SM, after electroweak symmetry breaking, it is natural to express the gauge-fixing in the mass eigenstate basis. The massive $W^\pm$ and Z bosons each develop a mixing term with their respective Goldstone bosons $G^\pm$ and G^0. Denoting the gauge-fixing functions as

$$\begin{aligned} \mathcal{G}_{W^\pm} &= \partial^\mu W_\mu^\pm \mp i\xi_2^W \frac{g}{2}\tilde{\phi} G^\pm, \\ \mathcal{G}_Z &= \partial^\mu Z_\mu - \xi_2^Z \frac{g_Z}{2}\tilde{\phi} G^0, \\ \mathcal{G}_A &= \partial^\mu A_\mu, \end{aligned} \tag{3.59}$$

where $g_Z = \sqrt{g^2 + g'^2}$, the gauge-fixing Lagrangian takes the form

$$\mathcal{L}_{\text{gf}} = -\frac{1}{\xi_1^W}\mathcal{G}_{W^+}\mathcal{G}_{W^-} - \frac{1}{2\xi_1^Z}\mathcal{G}_Z^2 - \frac{1}{2\xi_1^A}\mathcal{G}_A^2. \tag{3.60}$$

Since the gauge group $SU(2)_L \times U(1)_Y$ has rank two, the gauge-fixing Lagrangian Eq. (3.58) is not invariant under transformations of the gauge-group index a; therefore, the gauge-fixing condition depends on the choice of basis for the generators [151]. In the SM, the natural choice is the mass eigenstate basis $\{W^\pm, Z, A\}$, which is related to the $SU(2)_L \times U(1)_Y$ eigenstate basis $\{W^{1,2,3}, B\}$ by the rotation with mixing angle θ_W. Writing the gauge fixing in the mass eigenstate basis, as in Eq. (3.60), ensures that the Goldstone masses and propagator poles are aligned with the physical spectrum, which simplifies the calculations.

Using Eq. (3.60) as the gauge-fixing condition, we obtain the gauge-dependent mass eigenvalues of vectors, Goldstone bosons, and ghosts. The physical vector degrees of freedom have background-field-dependent mass eigenvalues:

$$\begin{aligned} M_W^2 &= \frac{g^2\phi^2}{4}, \\ M_Z^2 &= \frac{(g^2 + g'^2)\phi^2}{4}, \end{aligned} \tag{3.61}$$

with ϕ being the background field along the physical Higgs direction in the SM. On the other hand, the unphysical degrees of freedom of the vector bosons mix with Goldstone

modes and their mass eigenvalues read (for compactness, we introduce the subscript $V = \{W, Z\}$):

$$\begin{aligned} M^2_{V_\pm} &= \frac{1}{2}\left(M^2_G + 2M^2_V \frac{\tilde{\phi}}{\phi}\sqrt{\xi^V_1 \xi^V_2} \pm M_G \sqrt{M^2_G - 4M^2_V \left(\xi^V_1 - \frac{\tilde{\phi}}{\phi}\sqrt{\xi^V_1 \xi^V_2}\right)} \right), \\ M^2_{c_V} &= M^2_V \frac{\tilde{\phi}}{\phi}\sqrt{\xi^V_1 \xi^V_2}, \end{aligned} \tag{3.62}$$

where $M^2_G = \mu^2_h + \lambda_h \phi^2$, $M^2_{c_V}$ is the ghost mass eigenvalue and $M^2_{V_\pm}$ are the two mass eigenvalues of the mixed vector–Goldstone degrees of freedom. Then, for the gauge-fixing choices discussed above and used in the perturbative calculations in Chapter V, we have

- **Fermi gauge** ($\xi^V_1 = \xi^V, \xi^V_2 = 0$):

$$M^2_{V_\pm} = \frac{1}{2}\left(M^2_G \pm M_G \sqrt{M^2_G - 4M^2_V \xi^V_1} \right), \quad M^2_{c_V} = 0; \tag{3.63}$$

- **Background R^{bkgd}_ξ-gauge** ($\xi^V_1 = \xi^V_2 = \xi^V, \tilde{\phi} = \phi$):

$$M^2_{V_+} = M^2_G + \xi^V M^2_V, \quad M^2_{V_-} = \xi^V M^2_V, \quad M^2_{c_V} = \xi^V M^2_V; \tag{3.64}$$

- **Standard R^{std}_ξ-gauge** ($\xi^V_1 = \xi^V_2 = \xi^V, \tilde{\phi} = \phi_{\text{min}}$):

$$\begin{aligned} M^2_{V_\pm} &= \frac{1}{2}\left(M^2_G + 2M^2_V \xi^V \frac{\phi_{\text{min}}}{\phi} \pm M_G \sqrt{M^2_G - 4M^2_V \xi^V \frac{\phi - \phi_{\text{min}}}{\phi}} \right), \\ M^2_{c_V} &= \xi^V M^2_V \frac{\phi_{\text{min}}}{\phi}; \end{aligned} \tag{3.65}$$

- **Landau gauge** ($\xi^V_1 = \xi^V_2 = 0$):

$$M^2_{V_+} = M^2_G, \quad M^2_{V_-} = 0, \quad M^2_{c_V} = 0. \tag{3.66}$$

Background vs standard R_ξ-gauges

We now compare the two R_ξ variants introduced above — the background R^{bkgd}_ξ-gauge and the standard R^{std}_ξ-gauge.

The background-field gauge R_ξ^{bkgd} is widely used in the phase-transition literature, e.g. [44, 157, 158], because it eliminates the scalar–vector propagator mixing for any value of the background field ϕ, which simplifies the loop calculations of the effective potential considerably. However, it has a conceptual peculiarity: the gauge-fixing condition itself depends on the value of the background field through $\tilde{\phi} = \phi$. This means that as ϕ is varied across field space to trace out the effective potential, the theory is being gauge-fixed differently for each field value. In other words, $V(\phi_1)$ and $V(\phi_2)$ are computed for two distinct gauge conditions, making a direct comparison between different field-space points formally inconsistent. In the standard gauge R_ξ^{std}, by contrast, the gauge-fixing is anchored to the fixed tree-level vev $\tilde{\phi} = \phi_{\text{min}}$.

We examine whether the effective potential in both variants correctly reproduces the 1PI n-point functions at zero external momentum. As introduced in Eq. (3.20), the effective action $\Gamma[\phi]$ is a generating functional for 1PI diagrams, and hence the field derivatives of the effective potential at the minimum $\phi = \phi_{\text{min}}$ correspond to the zero-momentum 1PI n-point functions,

$$\left.\frac{d^n V(\phi)}{d\phi^n}\right|_{\phi=\phi_{\text{min}}} = \Gamma^{(n)}(p_1 = \cdots = p_n = 0), \tag{3.67}$$

where $\Gamma^{(n)}$ denotes the 1PI scalar n-point function evaluated at vanishing external momenta. We compare field derivatives of V at the minimum with direct perturbative 1PI calculations in the $\overline{\text{MS}}$ scheme, noting that the standard diagrammatic calculation of the n-point functions is performed at $\phi = \phi_{\text{min}}$, where the gauge-fixing condition coincides in both R_ξ variants.

First, we check that the first field derivative of the effective potential at the minimum, which corresponds to the tadpole diagram, is correctly generated by the effective potential evaluated in both R_ξ^{std} and R_ξ^{bkgd}. At one-loop order, the effective potential is given by Eq. (3.30), summing over all background-field-dependent mass eigenvalues of the theory, including the gauge-dependent vector, scalar and ghost modes given in Eq. (3.62).

We find that both R_ξ^{std} and R_ξ^{bkgd} agree with the direct perturbative computation of the tadpole (1-point function) at one-loop order [144],

$$\left.\frac{dV_1^{R_\xi^{\text{std}}}}{d\phi}\right|_{\phi=\phi_{\text{min}}} = \quad = \left.\frac{dV_1^{R_\xi^{\text{bkgd}}}}{d\phi}\right|_{\phi=\phi_{\text{min}}}, \tag{3.68}$$

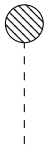

where the blob represents all one-loop contributions to the Higgs tadpole diagram. At two-loop order, the first derivative — corresponding to the tadpole — of the effective potential in the R_ξ^{bkgd}-gauge disagrees with the perturbative calculation, while the R_ξ^{std}-gauge continues to yield agreement with it.

Moving to the second field derivative, which corresponds to the self-energy diagram, the situation changes. The two gauge choices yield different results starting from the one-loop order, and the equivalence with the direct diagrammatic computation is recovered only in the standard R_ξ^{std}-gauge,

$$\left.\frac{d^2V_1^{R_\xi^{\text{std}}}}{d\phi^2}\right|_{\phi=\phi_{\text{min}}} = \quad \left.\right|_{p^2=0} \neq \left.\frac{d^2V_1^{R_\xi^{\text{bkgd}}}}{d\phi^2}\right|_{\phi=\phi_{\text{min}}}, \tag{3.69}$$

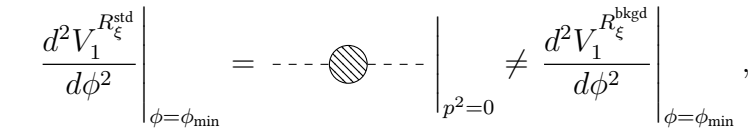

where the diagram evaluated is the proper (1PI) one-loop self-energy at zero momentum in R_ξ-gauge, without tadpole insertions.

In R_ξ^{std}, the mixing between Goldstone and vector bosons is properly accounted for through the propagator mixing included in the effective potential, even though no such mixing appears in the perturbative propagators at $\phi = \phi_{\text{min}}$. The Goldstone and vector boson sector contribution to $V_1^{R_\xi^{\text{std}}}$ is related to the perturbative Higgs self-energy at zero momentum by

$$\left.\frac{d^2V_{1,\{Z_+,W_+,Z_-,W_-,Z,W\}}^{R_\xi^{\text{std}}}}{d\phi^2}\right|_{\phi=\phi_{\text{min}}} \tag{3.70}$$

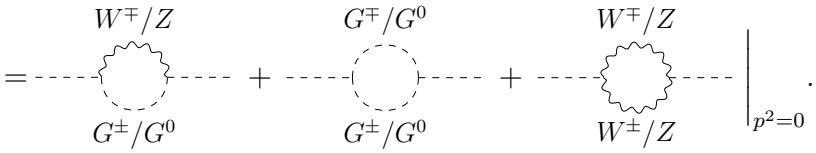

The contribution from the first diagram on the right-hand side of (3.70) is absent in V_1 computed in R_ξ^{bkgd}, since in that gauge the Goldstone–vector mixing vanishes for all field values.

This can also be understood diagrammatically: taking field derivatives and then inserting the vev corresponds to attaching zero-momentum external scalar lines to the vacuum diagrams contained in V. Only V_1 in R_ξ^{std}-gauge contains diagrams with mixed vector–Goldstone propagators, which can be attached to the external scalar lines to generate the first diagram on the right-hand side of (3.70).

It is then clear that at one-loop order, both gauge choices give the same tadpole — no mixing diagram of this type exists on the perturbative side — while they differ for the self-energy and higher n-point functions, owing to mixing diagrams such as the first one in (3.70). It may seem counterintuitive that no propagator mixing appears in the perturbative calculation, yet such mixing must be present in the effective potential to reproduce the correct 1PI functions.

In order to further isolate contributions in (3.70), we note that a subtlety arises: $\partial_\phi^2 V^{R_\xi^{\text{std}}}_{1,\{V_+\}}$ and $\partial_\phi^2 V^{R_\xi^{\text{std}}}_{1,\{V_-\}}$ diverge in the limit $\phi \to \phi_{\text{min}}$, since $M_G^2 \to 0$ and the expression contains terms proportional to $1/M_G^2$. However, these divergences cancel between the Goldstone and the unphysical scalar gauge boson modes (V_+ and V_-), which contribute with opposite signs, so that the total sum in (3.70) of them is finite. One can introduce a counterterm that cancels the divergence in each contribution individually:

$$\delta_{V_+} = -\delta_{V_-} = \frac{1}{4\pi^2\phi^2}\frac{(\xi_V M_V^2)^3}{M_G^2}\left[1 - \log\left(\frac{\xi_V M_V^2}{\mu^2}\right)\right]. \tag{3.71}$$

This allows the Goldstone and vector boson contributions to be kept separate and unambiguously matched to individual perturbative diagrams. In full detail, this becomes

$$\left(\frac{d^2 V^{R_\xi^{\text{std}}}_{1,\{Z_+,W_+\}}}{d\phi^2} + \delta_{W_+/Z_+}\right)\Bigg|_{\phi=\phi_{\text{min}}}$$

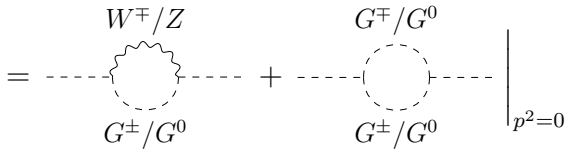

(3.72)

and

$$\left(\frac{d^2 V^{R_\xi^{\text{std}}}_{1,\{Z_-,W_-,Z,W\}}}{d\phi^2} + \delta_{W_-/Z_-}\right)\Bigg|_{\phi=\phi_{\text{min}}}$$

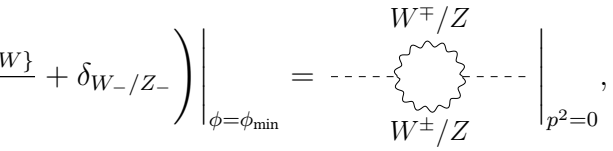

(3.73)

where $V^{R_\xi^{\text{std}}}_{1,\{Z_-,W_-,Z,W\}}$ contains the contributions from both physical and unphysical vector boson modes.

The mismatch persists for higher n-point functions at one loop (e.g. 3-point functions, known in the literature as the trilinear Higgs coupling [159, 160]). In the R_ξ^{bkgd}-gauge, Goldstone contributions to the effective potential fail to reproduce the corresponding perturbative diagrams, whereas the R_ξ^{std}-gauge correctly accounts for all mixing effects

and yields agreement with the perturbative calculation in R_ξ-gauge. Similarly, the contribution from the ghost modes in the effective potential matches the corresponding ghost diagram in the perturbative calculation of the self-energy at zero momentum only in the R_ξ^{std}-gauge.

III.3 False vacuum decay and nucleation rate

During the EWPT governed by the effective action and potential introduced in the previous section, the Higgs field evolves from the symmetric phase ($\phi = 0$) to the broken phase ($\phi = v_{\text{EW}}$), as reviewed in Section III.2.

If the transition is first order, the symmetric phase can persist as a metastable false vacuum below the critical temperature. In this case, the conversion to the true, broken-phase vacuum does not occur homogeneously throughout space. Instead, it proceeds via the stochastic nucleation of bubbles of the broken phase within the surrounding thermal plasma of the symmetric phase.

The central quantity governing this process is the false-vacuum decay rate per unit volume, γ, which controls how rapidly bubbles are nucleated, when the transition completes, and ultimately determines the resulting GW signal discussed in Section III.6. In this section, we develop the theoretical framework for computing γ, beginning with vacuum decay at zero temperature and subsequently extending the analysis to the finite-temperature transitions relevant for the EWPT in the early Universe.

We also discuss the subsequent evolution of nucleated bubbles, focusing in particular on the dynamics of the bubble walls as they expand through the surrounding plasma. The bubble wall velocity is determined by a competition between the driving force from the vacuum energy difference and the friction exerted by interactions with the thermal plasma. This interplay is crucial for determining the efficiency of energy transfer to the plasma and, consequently, the characteristics of the resulting GW signal.

III.3.1 Bubble nucleation

The formalism for false-vacuum decay in QFT is inspired by the well-known quantum-mechanical problem of barrier penetration (see e.g. [161] for a pedagogical review). In quantum mechanics, consider a potential $V(q)$ with a local minimum at q_1 — the false

vacuum — separated from a deeper minimum by a barrier, and let q_2 be the point on the far side of the barrier where $V(q_2) = V(q_1)$. The tunneling amplitude for a particle of unit mass starting at rest at q_1 is given in the semi-classical Wentzel–Kramers–Brillouin (WKB) approximation by

$$\gamma \sim \exp\left(-2\int_{q_1}^{q_2} dq\,\sqrt{2(V(q)-V(q_1))}\right). \tag{3.74}$$

This expression can be recast in a path-integral interpretation: the tunneling amplitude is dominated by the classical trajectory $q_b(t_E)$ in imaginary time $t_E = it$, along which the Euclidean action,

$$S_E[q] = \int_{-\infty}^{+\infty} dt_E \left[\frac{1}{2}\left(\frac{dq}{dt_E}\right)^2 + V(q)\right], \tag{3.75}$$

is extremised ($\delta S_E[q] = 0$) subject to the boundary conditions

$$q(t_E \to \pm\infty) = q_1\,, \qquad \dot{q}(t_E = 0) = 0\,, \tag{3.76}$$

i.e. the trajectory starts and ends at the false-vacuum minimum q_1, making a round trip through the barrier. The Euclidean equations of motion are time-reversal invariant, so the solution is symmetric, $q_b(t_E) = q_b(-t_E)$, reaching the turning point q_2 at $t_E = 0$. Then the tunneling rate is controlled by $\gamma \sim e^{-S_E[q_b]}$, exactly reproducing the semi-classical Eq. (3.74) above. The Wick rotation $t \to -it_E$ effectively corresponds to inverting the potential, $V \to -V$: a barrier in Minkowski space becomes a valley in Euclidean space, and the classically forbidden tunneling trajectory becomes an allowed classical path in Euclidean time.

In QFT, this picture generalizes directly. The false-vacuum decay rate is dominated by classical solutions of the Euclidean equations of motion, i.e. field configurations that extremise S_E, subject to boundary conditions. These are the *instantons* [162, 163]: solutions localised in Euclidean spacetime, existing only over a finite extent in both space and Euclidean time. The localization is a direct consequence of the finite-action requirement: non-localized solutions are suppressed in the path integral.

The relevant instanton for vacuum decay is the *bounce solution* ϕ_b: the field configuration that starts from the false vacuum, crosses the barrier and reaches the true-vacuum side, then returns — making a round trip in field space in $t_E \in [-\infty, \infty]$, hence the name. In the inverted-potential picture discussed above, this corresponds to a particle rolling

off the local maximum at $\phi_{\rm FV}$, sliding through the valley toward $\phi_{\rm TV}$, and climbing back up to $\phi_{\rm FV}$ by time-reversal symmetry. The instanton is the dominant saddle-point contribution to the path integral, and its *bounce action* $B \equiv S_E[\phi_b]$ controls the exponential suppression of the tunneling rate. Evaluating the path integral semiclassically around the bounce gives

$$\gamma = Ae^{-B}\,, \tag{3.77}$$

where the prefactor A arises from integrating over fluctuations around the bounce and represents higher-order corrections to the false-vacuum decay rate [162–164].

Vacuum decay at $T = 0$

At zero temperature the Euclidean time t_E is uncompactified, running from $-\infty$ to $+\infty$. It can be shown [165] that among all field configurations satisfying the boundary conditions, the one that minimizes the Euclidean action — and hence dominates the path integral — is $O(4)$-symmetric, depending only on the radial coordinate $\rho = \sqrt{t_E^2 + \vec{x}^2}$; any angular variation costs kinetic energy without aiding tunneling, so the optimal bounce is spherically symmetric in four-dimensional Euclidean space.

Then, the decay rate per unit volume is given by Eq. (3.77), with B being the Euclidean action evaluated on the $O(4)$-symmetric bounce solution ϕ_b. Exploiting the $O(4)$ symmetry, the angular integration over the unit three-sphere can be performed analytically, reducing the $O(4)$-symmetric Euclidean action S_4 to a one-dimensional radial integral,

$$B \equiv S_4[\phi_b] = 2\pi^2 \int_0^\infty d\rho\, \rho^3 \left[\frac{1}{2}\left(\frac{d\phi_b}{d\rho}\right)^2 + V_0(\phi_b) - V_0(\phi_{\rm FV})\right], \tag{3.78}$$

where the subtraction of $V_0(\phi_{\rm FV})$ ensures convergence of the integral as $\phi_b \to \phi_{\rm FV}$ at $\rho \to \infty$. The bounce profile then satisfies

$$\frac{d^2\phi_b}{d\rho^2} + \frac{3}{\rho}\frac{d\phi_b}{d\rho} = \frac{\partial V_0}{\partial \phi}\,, \qquad \left.\frac{d\phi_b}{d\rho}\right|_{\rho=0} = 0\,, \quad \phi_b(\rho \to \infty) = \phi_{\rm FV}\,, \tag{3.79}$$

which follows from extremising the Euclidean action $\delta S_4[\phi_b] = 0$. Note that the boundary condition at $\rho = 0$ only fixes the first derivative to vanish (regularity at the origin) — the central field value $\phi_0 \equiv \phi_b(0)$ is itself a free parameter, determined by requiring that the solution reaches $\phi_{\rm FV}$ at infinity. In general, ϕ_0 lies on the true-vacuum side of the barrier, but need not coincide with $\phi_{\rm TV}$.

At one-loop order, the prefactor A is obtained by evaluating the Gaussian path integral over fluctuations $\eta = \phi - \phi_b$ around the bounce. Expanding $S_4[\phi_b+\eta]$ to second order and integrating over η yields a ratio of functional determinants of the fluctuation operator $\mathcal{M} \equiv -\partial_E^2 + V_0''(\phi)$, evaluated on the bounce and on the false-vacuum background respectively,

$$A = \left(\frac{S_4}{2\pi}\right)^2 \left|\frac{\det' \mathcal{M}[\phi_b]}{\det \mathcal{M}[\phi_{\rm FV}]}\right|^{-1/2}, \tag{3.80}$$

where $\det'$ denotes the functional determinant with zero modes excluded.

The spectrum of $\mathcal{M}[\phi_b]$ contains three distinct types of eigenvalues. First, there is one *negative mode*: a radially symmetric deformation that shrinks or expands the bubble, corresponding to the unstable direction in field space. It produces an imaginary contribution to the vacuum energy, which is the field-theory signature of metastability [163]. Second, the bulk of the spectrum consists of strictly *positive modes*, encoding stable fluctuations around the bubble wall; these contribute a well-defined real factor to the functional determinant. Third, there are four *zero modes*, one per Euclidean spacetime direction, arising from the translational invariance of the bounce. They require special treatment via collective coordinates: each zero mode is replaced by an integration over the corresponding component of the bounce center z_μ, contributing a Jacobian factor of $\sqrt{S_4/2\pi}$. The four zero modes together yield the $(S_4/2\pi)^2$ factor in Eq. (3.80), while integrating over all bounce positions in Euclidean spacetime produces a factor of the spacetime volume, making γ the natural volume-independent quantity [162].

The physical interpretation of the bounce becomes clear upon Wick-rotating back to Minkowski time $t = -it_E$. The slice $t_E = 0$ of the bounce profile, $\phi_b(\rho)\big|_{t_E=0} = \phi_b(|\vec{x}|)$, describes the field configuration of the *critical bubble* at the moment of nucleation: a spherical region of the broken phase embedded in the false vacuum, with a smooth interpolating wall profile. For $t > 0$, the field inside the bubble is no longer constrained by the Euclidean equations of motion but instead evolves classically, rolling down toward $\phi_{\rm TV}$ and driving the bubble to expand.

Nucleation at $T \neq 0$

At finite temperature, the Euclidean time direction is compactified on a circle of circumference $\beta = 1/T$, and the false-vacuum decay rate is dominated by the periodic instanton that minimizes the action subject to this compactification [166, 167]. The character of

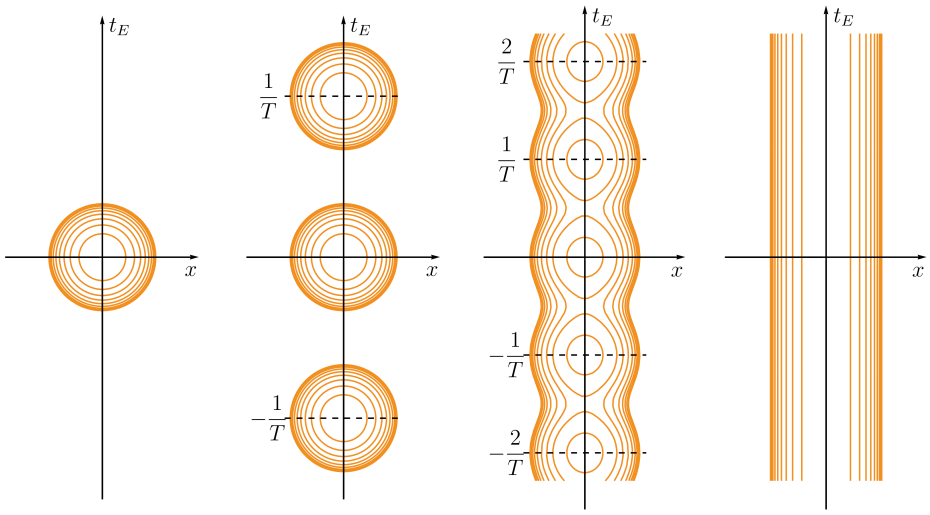

Figure 3.4: Contour plots of the bounce solution in the $(\vec{x}, t_E)$ plane at increasing temperatures, from left to right, adopted from [167]. *Far left*: $T = 0$. A single $O(4)$-symmetric instanton with circular contours; the Euclidean time direction is uncompactified. *Center left*: low T. Euclidean time is compactified on a circle of circumference β; the bounce radius $R \ll \beta$ so the instanton fits comfortably within one period and retains its $O(4)$ shape. The dominant configuration is a periodic array of identical $O(4)$ instantons. *Center right*: intermediate T. As T increases, β shrinks toward the instanton size R; periodic images overlap and the contours deform — the bounce no longer has exact $O(4)$ symmetry and the action interpolates between S_4 and S_3/T. *Far right*: high T. At $\beta \ll R$, the bounce becomes independent of t_E and reduces to an $O(3)$-symmetric three-dimensional instanton; the contours are vertical lines. The tunneling rate is controlled by $e^{-S_3/T}$.

the dominant saddle depends on the ratio of the bounce radius R to the thermal length β, as illustrated in Fig. 3.4.

- At *low temperatures*, $\beta \gg R$: the bounce fits within a single thermal period and retains its $O(4)$ shape. The rate is still controlled by S_4, with corrections suppressed by $e^{-1/(TR)}$.

- At *intermediate temperatures*, $\beta \sim R$: periodic images of the bounce begin to overlap, the $O(4)$ symmetry is broken, and the bounce action interpolates between S_4 and S_3/T (defined below in Eq. (3.82)).

- At *high temperature*, $\beta \ll R$: the bounce can no longer vary in the t_E direction and becomes independent of Euclidean time, acquiring $O(3)$ symmetry in the three spatial directions [167, 168]. The decay rate per unit volume is given by Eq. (3.77)

with the bounce action

$$B_T = \frac{S_3[\phi_b]}{T}, \tag{3.81}$$

where the factor of $1/T$ arises from integrating over the compactified Euclidean time.

The 3D Euclidean action,

$$S_3[\phi_b] = 4\pi \int_0^\infty dr\, r^2 \left[\frac{1}{2}\left(\frac{d\phi_b}{dr}\right)^2 + V(\phi_b, T) - V(\phi_{\rm FV}, T)\right], \tag{3.82}$$

is the direct analog of Eq. (3.78) with $V_0(\phi) \to V(\phi, T)$, the temperature-dependent scalar potential. The bounce profile $\phi_b(r)$ satisfies Eq. (3.79) with the replacements $3/\rho \to 2/r$ and $V_0(\phi) \to V(\phi, T)$, reflecting the three-dimensional geometry.

Physically, the high-T bounce describes *thermal activation*: thermal fluctuations drive the field over the barrier rather than through it [167, 168]. This is in contrast to the $T = 0$ regime, which is governed by quantum tunneling. The crossover between the two regimes occurs at $T \sim 1/R$. For electroweak-scale transitions the relevant temperatures satisfy $T \gg 1/R$, placing the system firmly in the $O(3)$ regime, which we adopt throughout.

The thermal prefactor naturally splits into a statistical and a dynamical part [169–171],

$$A_T = A_{\rm dyn} \cdot A_{\rm stat}\,. \tag{3.83}$$

The statistical part is obtained analogously to Eq. (3.80), by evaluating the Gaussian path integral over fluctuations around the $O(3)$-symmetric bounce. The relevant fluctuation operator is now three-dimensional,

$$\mathcal{M}_T \equiv -\nabla^2 + V''(\phi_b, T)\,, \tag{3.84}$$

and the statistical prefactor takes the form

$$A_{\rm stat} = \left(\frac{S_3}{2\pi T}\right)^{3/2} \left|\frac{\det' \mathcal{M}_T[\phi_b]}{\det \mathcal{M}_T[\phi_{\rm FV}]}\right|^{-1/2}. \tag{3.85}$$

Compared to Eq. (3.80), two differences arise. First, since the bounce is uniform in t_E, there are only *three* translational zero modes — one per spatial direction — each contributing $\sqrt{S_3/2\pi T}$, yielding the factor $(S_3/2\pi T)^{3/2}$. Second, the Eu-

clidean time direction no longer produces a zero mode; instead, integration over the thermal circle of circumference $\beta = 1/T$ contributes the overall factor of T.

The dynamical prefactor A_{dyn} encodes the response of the thermal plasma to the nucleating bubble and requires a real-time computation in the presence of a thermal bath [168, 170, 172]. At leading order (LO) it is set by the growth rate ω_- of the unstable mode of $\mathcal{M}_T$, which controls how rapidly the critical bubble expands after nucleation.

Solving for the bounce

The bounce equation Eq. (3.79) is a nonlinear boundary-value problem that generally has no closed-form solution and must be solved numerically. The standard approach is the *shooting method*: one guesses an initial field value $\phi_0 = \phi_b(0)$ at the bubble center (with $\dot{\phi}_b(0) = 0$) and integrates the equation of motion outward in ρ, then iterates ϕ_0 until the boundary condition $\phi_b(\rho \to \infty) \to \phi_{\text{FV}}$ is satisfied.

The iteration has a simple physical interpretation in the mechanical analogy: mapping $\rho \to t$ and $V_0 \to -V_0$, Eq. (3.79) describes a particle rolling down the inverted potential $-V_0(\phi)$ subject to a d-dimensional friction term $-(d-1)\dot{\phi}/\rho$. A starting value too close to the true-vacuum side causes the particle to *overshoot* — it gains enough energy to roll past the false vacuum and to infinity; starting too close to the barrier maximum results in an *undershoot* — the particle stalls before reaching ϕ_{FV}. The unique bounce solution lies between these two regimes and is found by bisection. This procedure is implemented in several public codes, including `FindBounce` [173] and `CosmoTransitions` [174].

A practical complication of the shooting method arises near the origin $\rho \to 0$, where the friction term $\sim (d-1)\dot{\phi}/\rho$ becomes singular. Numerical integration in this region therefore requires special care to ensure stability and accuracy. The method also becomes challenging in the *thin-wall limit*, where the two minima are nearly degenerate ($V_0(\phi_{\text{FV}}) \approx V_0(\phi_{\text{TV}})$). In this regime, the bubble wall becomes parametrically thin compared to the bubble radius, and the bounce profile develops a steep, localised transition region that demands very fine step sizes to resolve reliably. In theories with multiple scalar fields, the problem is further complicated by the need to determine a trajectory in a multi-dimensional field space. The shooting direction is then promoted to a vector, and naive generalizations of the single-field method typically suffer from poor convergence. In practice, this necessitates more sophisticated approaches, such as path-deformation

methods, in which an initial field-space path is iteratively deformed toward the true bounce solution. These techniques are numerically non-trivial and can be computationally expensive.

A conceptually distinct reformulation is provided by the *tunneling-potential* method [175, 176]. Instead of solving for the bounce profile $\phi_b(\rho)$ as a function of the radial coordinate, one introduces a function $V_t(\phi) \equiv V(\phi) - \dot{\phi}_b^2/2$, referred to as the tunneling potential. This quantity satisfies the differential equation

$$d(V_t')^2 = (d-1)\left(V'V_t' - 2(V - V_t)V_t''\right) , \tag{3.86}$$

where primes denote derivatives with respect to ϕ and d is the number of Euclidean dimensions. The tunneling potential is subject to the boundary conditions $V_t(\phi_{\rm FV}) = V(\phi_{\rm FV})$ and $V_t(\phi_0) = V(\phi_0)$, where ϕ_0 denotes the release point of the bounce.

Once V_t is known, the bounce action can be expressed directly as an integral over field space,

$$S_d[\phi_b] = \frac{(d-1)^{d-1}(2\pi)^{d/2}}{\Gamma(d/2+1)} \int_{\phi_{\rm FV}}^{\phi_0} d\phi \, \frac{(V - V_t)^{d/2}}{|V_t'|^{d-1}} , \tag{3.87}$$

thereby completely eliminating the need to solve for the radial profile.

Crucially, the tunneling-potential method reformulates the problem as a minimization, rather than searching for the saddle-point of the Euclidean action. This provides a more stable numerical problem, avoids the singular friction term of the radial differential equation, and makes the geometry of the tunneling path explicit. The tunneling-potential equation Eq. (3.86) is effectively a first-order equation for V_t', and can be solved numerically with appropriate boundary conditions. In multi-field theories, the method can be combined with a parametrization of the path in field space, reducing the problem to a one-dimensional evolution along the path. While this avoids the direct difficulties of multi-dimensional shooting, it still requires determining the optimal tunneling trajectory, which remains numerically non-trivial. This method has been implemented in the publicly available software `ELENA` [177].

III.3.2 Wall propagation and friction

Once a bubble has nucleated, it expands outward into the surrounding symmetric-phase plasma. The equation of motion for the bubble profile configuration of the scalar field $\overline{\phi}$

in the plasma frame takes the general form

$$\Box\overline{\phi} + V'(\overline{\phi}, T) \;=\; \mathcal{F}[\overline{\phi}]\,, \tag{3.88}$$

a prime denotes differentiation with respect to the field, $V' \equiv \partial_\phi V$, and $\mathcal{F}[\overline{\phi}]$ is the friction force exerted by the thermal plasma on the moving wall, whose form is determined by the microphysics of particle–wall interactions. Well after nucleation, when the bubble radius greatly exceeds the wall thickness $L_w \sim m_h^{-1}$, the wall can be treated as planar and the profile $\overline{\phi}$ as depending only on the coordinate z normal to the wall.

The friction has several physical origins [178, 179]. First, particles acquire a position-dependent mass $m_i^2(\overline{\phi}(z))$ as they traverse the wall. This pushes them away from their equilibrium states and generates a back-reaction on the wall. Second, particles whose kinetic energy is insufficient to surpass the mass barrier are reflected, transferring momentum directly to the wall. Third, at large wall Lorentz factors $\gamma_w \gg 1$, particles changing mass rapidly inside the wall can radiate (*transition radiation*), providing an additional drag.

To describe this out-of-equilibrium dynamics, the distribution function of each species i is split into an equilibrium part and a small deviation δf_i sourced by the moving bubble wall. The equilibrium piece resulting in the driving pressure is accounted for by V; the deviation δf_i, which generates the friction, is governed by a linearised Boltzmann equation with elastic collision terms [178, 180, 181]. The collision terms, characterized by a thermal interaction rate Γ_i, oppose the displacement from equilibrium and drive the system back toward local equilibrium. The out-of-equilibrium deviations back-react on the wall, resulting in the friction term in Eq. (3.88), explicitly written as

$$\mathcal{F}[\overline{\phi}] = -\sum_i \frac{dm_i^2(\overline{\phi})}{d\overline{\phi}} \int \frac{d^3p}{(2\pi)^3} \frac{1}{2E_p} \delta f_i(\vec{p}, \vec{x})\,, \tag{3.89}$$

where the sum runs over all particle species i in the plasma, $E_p = \sqrt{\vec{p}^2 + m_i^2(\overline{\phi})}$ is the local quasi-particle energy, and δf_i is the out-of-equilibrium deviation of the distribution function. The total friction pressure exerted on the wall is $p_{\text{fric}} = -\int dz \mathcal{F}[\phi(z)]\partial_z\overline{\phi}(z)$.

A widely used simplification is to approximate the full Boltzmann result by a *constant friction coefficient* η, in which case

$$\mathcal{F}[\overline{\phi}] = -\eta u \cdot \partial\overline{\phi}, \tag{3.90}$$

where u^μ is the plasma four-velocity. Two parameterisations of η are commonly used. The first treats it as a genuine constant,

$$\eta = \zeta T_c = \text{const.}, \tag{3.91}$$

where T_c is the critical temperature, setting the natural mass scale, and ζ absorbs the model-dependent microphysics. This choice is used in the majority of large-scale hydrodynamical simulations [182–184]. The second is field- and temperature-dependent,

$$\eta(\overline{\phi}, T) = \chi \frac{\overline{\phi}^2}{T}, \tag{3.92}$$

which arises naturally in models where the plasma particle masses scale with the scalar vev as $m_i \propto \overline{\phi}$ [185, 186], so that friction vanishes in the symmetric phase and grows with the condensate. In both cases ζ and χ are dimensionless constants of order unity that are in principle computable from the microphysics but are often treated as free parameters. The two parameterisations have been found to differ quantitatively rather than qualitatively in their effect on the wall velocity [184, 187].

Terminal velocity

The wall reaches terminal velocity v_w when the driving pressure equals the friction:

$$\Delta p \;=\; p_{\text{fric}}\,, \tag{3.93}$$

where $\Delta p \equiv V(\phi_{\text{FV}}, T) - V(\phi_{\text{TV}}, T) > 0$ is the thermodynamic driving force. In principle, the full thermodynamic pressure of the system also receives a field-independent contribution from the plasma radiation, $p \sim T^4$. In the uniform-temperature, planar-wall approximation used here this piece is identical on both sides of the interface and therefore cancels in Δp; in a more complete treatment that accounts for the temperature variation across the wall and the hydrodynamic backreaction from the fluid, this cancellation no longer holds and such contributions must be included explicitly.

Equation Eq. (3.93) together with the bubble-profile equation in the wall rest frame,

$$-\partial_z^2 \overline{\phi} + V'(\overline{\phi}, T) \;=\; \mathcal{F}[\overline{\phi}]\,, \qquad \lim_{z\to-\infty} \overline{\phi} = \phi_{\text{FV}}\,, \qquad \lim_{z\to+\infty} \overline{\phi} = \phi_{\text{TV}}\,, \tag{3.94}$$

must be solved self-consistently for v_w (which appears in the friction term) and $\overline{\phi}(z)$.

Deflagrations, detonations, and hybrids

The wall velocity also determines how the latent heat is distributed between the bubble interior and the surrounding plasma. The hydrodynamic solutions admit qualitatively distinct modes depending on v_w relative to the speed of sound c_s and the Chapman–Jouguet velocity v_J [182, 188]. The speed of sound $c_s = 1/\sqrt{3}$ is the equation-of-state result for a relativistic ideal gas, a good approximation for the electroweak plasma where most of the SM degrees of freedom are light relative to the temperature.

- *Deflagrations* ($v_w < c_s$): the wall moves subsonically. The latent heat released at the wall drives a compression (shock) wave ahead of the bubble, which reheats the plasma in front and reduces the local pressure difference driving the wall. The shock front and the wall are spatially separated.
- *Detonations* ($v_w \geq v_J$): the wall is supersonic and outruns any perturbation it generates. The plasma ahead remains undisturbed until the wall arrives; behind it, a rarefaction wave develops. The minimum detonation speed is the Chapman–Jouguet velocity v_J, at which the trailing rarefaction wave exactly keeps pace with the wall.
- *Hybrids* ($c_s < v_w < v_J$): an intermediate regime that combines a leading compression shock ahead of the wall with a trailing rarefaction behind, continuously interpolating between the two limiting cases.

The efficiency with which latent heat is converted into bulk plasma motion, and hence into GWs, depends sensitively on v_w [188]. The efficiency factors entering the GW spectrum are discussed in Section III.6.

Loop corrections to the bubble wall profile

The framework developed above treats the driving force at the level of the effective potential V, including thermal corrections. At high temperature, however, the correct starting point is to first integrate out the leading thermal fluctuations driving the phase transition — the DR approach described in the next Section III.4. Working within this EFT, one can then systematically compute loop corrections to the scalar equation of motion in the inhomogeneous bubble-wall background, capturing how thermal fluctuations modify both the wall profile $\overline{\phi}(z)$ and the terminal wall velocity v_w. This is the approach pursued in Chapter VI.

III.4 Effective theory at high temperature

The thermal field theory introduced in Section III.1 provides a framework for studying the EWPT, but applying it directly in perturbation theory runs into immediate difficulties. For simplicity, in this chapter we illustrate the main points through the example of a scalar-gauge theory with gauge coupling g, and for brevity we assume $\lambda \sim g^2$; the arguments generalize straightforwardly to the full SM and its extensions.

For a phase transition to occur, the thermal mass correction of the nucleating scalar field, $\Pi_T \sim g^2T^2$ (see Section III.1), must bring the effective thermal mass close to zero near the transition temperature: $m_T^2 = m^2 + \Pi_T \approx 0$, implying $m^2 \sim \Pi_T \sim g^2T^2$. In other words, the leading thermal corrections are not small compared to the tree-level potential — they are of the same order and drive the transition. The loop expansion diverges near the phase transition, and perturbation theory must be reorganized. This section describes the hierarchy of scales at play at high temperature, the resulting breakdown and the systematic solution based on EFT techniques, provided by the DR [49, 50, 189] — the framework underpinning the calculations in Chapters IV to VI.

III.4.1 Thermal scales at high temperature

The discussion here assumes the high-temperature regime, $T \gg m_i$, for all particle masses m_i in the theory, so that no zero-temperature mass scales intervene the scales described and the thermal effects dominate. The generalization beyond this limit follows along the same lines, with heavy particles whose masses are comparable to or exceed the relevant thermal scales integrated out at the appropriate scale.

In the high-temperature limit, a weakly coupled gauge theory with $g \ll 1$ develops a hierarchy of well-separated momentum scales, each playing a distinct dynamical role:

- **Hard scale**, $k \sim \pi T$: The typical momentum of thermal particles. The non-zero bosonic Matsubara frequencies $\omega_n = 2\pi nT$ ($n \neq 0$) and all fermionic frequencies $\omega_n = (2n+1)\pi T$ occur at this scale. In the high-temperature regime, hard modes are weakly coupled (see below) and can be treated perturbatively; they are the main source of leading thermal corrections to masses and couplings.
- **Soft scale**, $k \sim gT$: The thermal state breaks Lorentz invariance, distinguishing the temporal direction from the spatial ones. As a result, the temporal components of gauge fields A_0 acquire a Debye screening mass $m_D \sim gT$ from

hard-mode loop corrections to their self-energy. Soft modes are parametrically lighter than the hard scale and are *classical* in the sense that occupation numbers $\sim T/k \sim 1/g \gg 1$.

- **Ultrasoft scale**, $k \sim g^2T$: The scale of magnetostatic screening is set by the spatial gauge-field coupling, g^2T. In contrast to the Debye mass, the magnetic mass is intrinsically non-perturbative: there exists no IR-safe perturbative expansion for purely magnetic correlators beyond $\mathcal{O}(g^6)$. The reason the ultrasoft scale is non-perturbative is *Linde's Infrared Problem* [23]: at finite temperature, Bose–Einstein statistics enhances loop integrals: for a bosonic mode of energy E in a thermal bath at temperature T, the effective loop-expansion parameter is not g^2 but rather

$$g^2 \longrightarrow g^2\, n_B(E,T) = \frac{g^2}{e^{E/T}-1} \overset{E\ll T}{\approx} \frac{g^2T}{E}\,. \tag{3.95}$$

  For hard modes with $E \sim \pi T$ this is simply g^2/π, and perturbation theory is valid. For soft modes with $E \sim gT$, the effective coupling grows to $g^2T/(gT) = g$, which is still small, so perturbation theory remains tractable at this scale — though only after the resummation of the zero modes discussed in Section III.4.2. At the ultrasoft scale, $E \sim g^2T$, the effective coupling saturates to $g^2T/(g^2T) = \mathcal{O}(1)$: the spatial gauge-boson zero-modes become genuinely strongly coupled regardless of how small g is. IR divergences from these modes appear in the free energy at four-loop order and are not removed by any finite-order resummation [23, 190]; the ultrasoft scale therefore sets a fundamental non-perturbative limit for the perturbative approach.

The scalar thermal mass $m_T^2 = m^2 + \Pi_T$ is a sum of the zero-temperature mass squared and the thermal self-energy; depending on the model and the pattern of symmetry breaking, these two contributions can cancel to any degree, placing m_T^2 anywhere from the soft scale down to the ultrasoft scale, see Sections IV.2 and V.1 for explicit examples.

A distinct case of this cancellation occurs for radiatively generated potential barriers, where $m_T^2 \sim g^3T^2$, placing the scalar at an intermediate *supersoft* scale $k \sim g^{3/2}T$ between the soft and ultrasoft scales [171]; this example is discussed in Chapter IV. The full scale hierarchy $g^2T \ll g^{3/2}T \ll gT \ll \pi T$ is illustrated in Fig. 3.5, together with the relevant dynamical degrees of freedom at each scale.

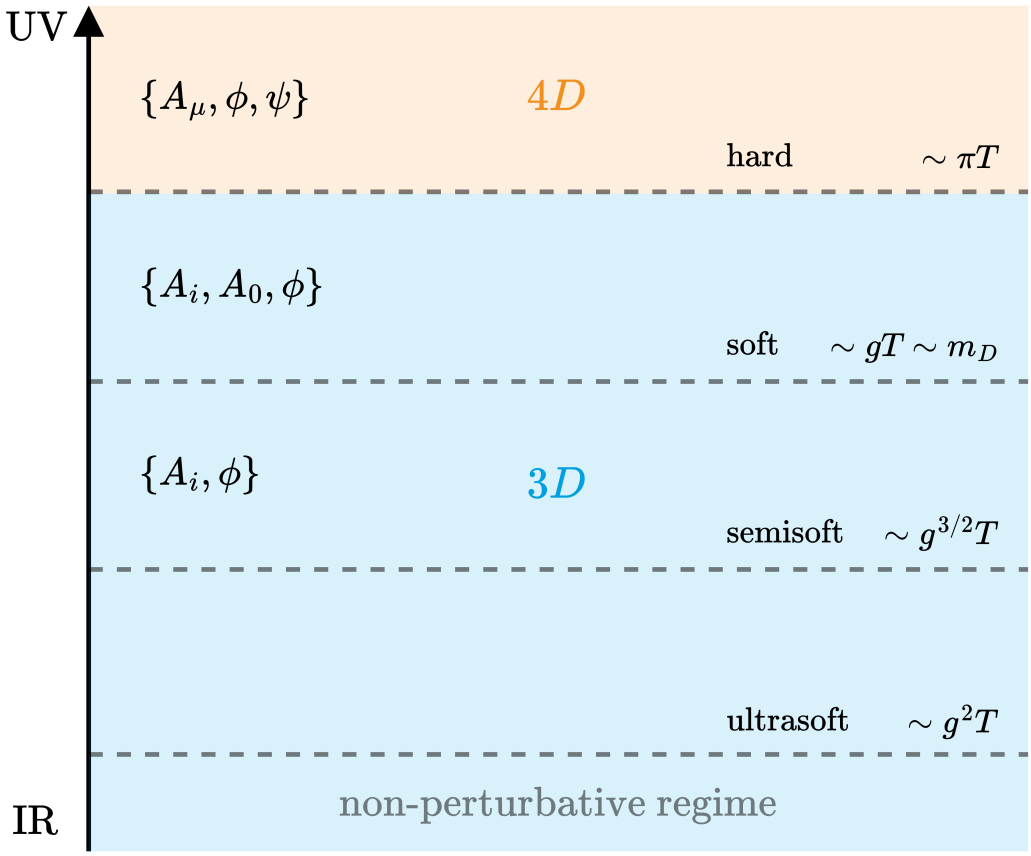

Figure 3.5: The EFT describing the phase transition is constructed by sequentially integrating out modes at each scale, starting from the hard modes at $k \sim \pi T$ (via the DR) down to the scale where nucleation occurs. Between scales, the effective couplings are evolved using the appropriate RGE.

III.4.2 Breakdown of perturbation theory

The scale hierarchy of Section III.4.1 reveals that the condition $m^2 \sim g^2 T^2$ places the scalar zero mode below the hard scale, where the loop expansion is marginal and where the Linde problem signals a complete failure at the ultrasoft scale. In the effective potential construction, discussed in Section III.2, this hierarchy is not respected, and three distinct problems arise if perturbation theory is applied naively near the phase transition.

Infrared problem and daisy resummation

The breakdown of the perturbative expansion at high temperature is most evident for the bosonic zero Matsubara mode ($\omega_0 = 0$). Near the phase transition, where $m^2 \sim g^2 T^2$,

thermal corrections to the propagator of the soft modes lead to IR divergences, signaling a breakdown of the perturbative expansion and the need for its reorganization.

In the calculation of the effective potential, this manifests itself through *daisy diagrams* [21]: ring insertions of the one-loop self-energy into the zero-mode propagator, as shown in Fig. 3.6. An N-petal daisy consists of the zero-mode ($\omega_0 = 0$) propagator running around the inner loop, with N non-zero Matsubara $\omega_{n\neq 0} \propto T$ mode loops (petals) attached at vertices of coupling $\lambda \sim g^2$:

$$V_N \propto g^{2N} \left[T \int \frac{d^3p}{(2\pi)^3} \frac{1}{\left(\vec{p}^{\,2} + m^2\right)^N} \right] \left[T \sum_{n\neq 0} \int \frac{d^3k}{(2\pi)^3} \frac{1}{\omega_n^2 + \vec{k}^{\,2}} \right]^N , \tag{3.96}$$

where the right bracket is the hard-mode (non-zero Matsubara) contribution to the self-energy. In the high-temperature limit (retaining only the leading T^2 piece) the hard-mode sum-integral evaluates to

$$T \sum_{n\neq 0} \int \frac{d^3k}{(2\pi)^3} \frac{1}{\omega_n^2 + \vec{k}^{\,2}} \approx \frac{T^2}{12} , \tag{3.97}$$

consistent with the self-energy computation of Eq. (3.17). The zero-mode integral scales as $T \int d^3p/(2\pi)^3 \, (\vec{p}^{\,2} + m^2)^{-N} \sim m^{3-2N} T$, so the full N-petal contribution is

$$V_N \propto m^3 T \left(\frac{g^2 T^2}{m^2} \right)^N \left(= m^3 T \left(\frac{\Pi_T(T)}{m^2} \right)^N \right) . \tag{3.98}$$

In the proximity of the phase transition, where $g^2T^2/m^2 \sim 1$, diagrams with any number of petals are contributing at the same order. Furthermore, for $N \geq 2$, it is IR divergent (in the limit $m^2 \to 0$). Both issues can be cured by resumming all daisy insertions, effectively replacing the bare mass by the thermally corrected mass:

$$m^2 \longrightarrow \bar{m}^2(T) \equiv m^2 + \Pi_T(T) , \tag{3.99}$$

where $\Pi_T(T) \sim g^2T^2$ is the one-loop thermal self-energy, which leads to the IR safe result $\bar{m}^3 T$.

Physically, resumming the soft modes corresponds to the screening effects in a thermal plasma — Debye screening. Computationally, this means that in order to go beyond the leading $\mathcal{O}(g^2)$ order contributions to the thermal effective potential (originating from loops of hard modes), the daisy diagrams that contribute at $\mathcal{O}(g^3)$ order must be re-

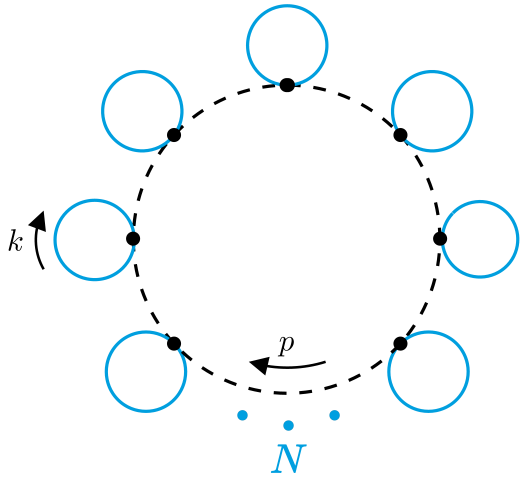

Figure 3.6: Daisy diagrams entering the effective potential at high temperature. The inner loop is the bosonic zero Matsubara mode, while the blue petals are non-zero Matsubara modes that generate the thermal self-energy Π_T. Resumming all daisy insertions effectively replaces the bare mass by the thermally corrected mass $\bar{m}^2 = m^2 + \Pi_T$.

summed. Two standard prescriptions implement this resummation in the effective potential Eq. (3.37):

- **Arnold–Espinosa (AE)** [45]: only the zero Matsubara modes are resummed in Eq. (3.31), adding to V the contribution

$$V_{\text{daisy}}^{\text{AE}}(\phi, T) = -\frac{T}{12\pi} \sum_i n_i \left[\bar{m}_i^3(\phi, T) - m_i^3(\phi)\right], \tag{3.100}$$

  where the sum runs over bosonic species, including temporal components of the gauge field, with n_i degrees of freedom and field-dependent mass $m_i^2(\phi)$, and $\bar{m}_i^2 = m_i^2 + \Pi_{i,T}(T)$. This prescription cleanly isolates the IR-sensitive zero modes responsible for the breakdown of perturbation theory and avoids double counting; however, it does not resum thermal effects in non-zero Matsubara modes, which can limit its accuracy away from the strict high-temperature regime.

- **Parwani** [191]: the thermal self-energy is substituted into all Matsubara modes, replacing $m_i^2 \to m_i^2 + \Pi_{i,T}(T)$ everywhere in the one-loop potential Eq. (3.31). It preserves the correct low-temperature limit, e.g. [192]. On the other hand, it mixes perturbative orders and can lead to double counting of higher-order contributions and generate spurious linear terms in the effective potential [40, 193].

Daisy resummation captures non-analytic effects, $\sim T(m^2(\phi) + \Pi_T(T))^{3/2}$, which generate the ϕ^3-type terms potentially inducing a radiative barrier. Without resummation, such IR-sensitive effects are missed, and the effective potential may not capture the correct phase structure evolution.

Despite restoring a perturbative description, both prescriptions are heuristic fixes: they improve the IR behavior but introduce inconsistencies at higher loop orders and do not systematically resum the full tower of sub-leading corrections; daisy resummation becomes even more cumbersome at higher loop orders, see e.g. [40, 194].

Scale and gauge dependence at high temperature

The scale dependence of the effective potential, discussed in Section III.2.1, is well under control at zero temperature: the explicit μ-dependence of the one-loop $T = 0$ potential exactly cancels the running of the tree-level parameters, leaving only a two-loop (i.e. $\mathcal{O}(g^4)$) residual dependence. At high temperature, however, this cancellation breaks down in a fundamental way [46].

Near a phase transition $m^2 \sim g^2T^2$, the one-loop thermal effective potential contains a leading thermal correction

$$\Pi_T\phi^2 \sim g^2T^2\phi^2\,, \tag{3.101}$$

whose renormalization-scale dependence is

$$\mu\frac{d}{d\mu}\Pi_T\phi^2 \sim g^4T^2\phi^2\,, \tag{3.102}$$

where we dropped a factor of $1/(4\pi)^2$ for brevity. This contribution is parametrically of the same order as the scale dependence of the tree-level mass term $m^2\phi^2$ (cf. Eq. (3.39)). However, unlike the zero-temperature case, it is not canceled by an explicit scale dependence in the one-loop potential; the latter is insensitive to the temperature and therefore cannot compensate for the running of Π_T [46].

The one-loop daisy-resummed effective potential, Eqs. (3.37) and (3.100), is therefore scale-dependent at $\mathcal{O}(g^4)$, which results in a significant uncertainty for physical predictions, see Chapter V. Only a complete $\mathcal{O}(g^4)$ calculation — requiring two-loop contributions — can render the effective potential scale-independent at this order. This breakdown is a direct consequence of the misalignment between the loop expansion and the coupling expansion at high temperature. With the power counting $m^2 \sim \Pi_T \sim g^2T^2$

that is appropriate near the transition, the thermal effective potential organizes as a series in g, rather than as a fixed loop expansion.

A related breakdown concerns gauge invariance. As established in Section III.2.2, the Nielsen identity guarantees that V is gauge-independent at its extrema provided the loop expansion is carried out consistently order by order. The $\hbar$-expansion implements this by expanding all field-dependent quantities around the *tree-level* minimum ϕ_0: at each order in $\hbar$ the right-hand side of Eq. (3.45) vanishes at ϕ_0, and gauge independence is maintained.

At high temperature, however, this scheme fails already at LO. The thermal self-energy $\Pi_T \sim g^2T^2$ is formally a one-loop correction, but near the phase transition it is of the same size as the tree-level mass term. The one-loop correction therefore shifts the field minimum by an amount comparable to ϕ_0 itself. The $\hbar$-expansion, which treats the one-loop shift as a small perturbation around the tree-level minimum, is no longer valid — the expansion parameter is not small, and successive orders do not improve the convergence.

The situation is worsened once daisy resummation is applied: resumming the zero-mode self-energy inserts Π_T directly into the propagator, so the resummed propagator mixes contributions from formally different loop orders. This explicit mixing of loop orders breaks the $\hbar$-counting on which the Nielsen identity relies [148].

Bubble nucleation and double-counting

A less-appreciated but equally fundamental inconsistency of the direct perturbative approach concerns the bubble nucleation rate and the bounce action B_T, see Section III.3.

The standard prescription promotes the tree-level potential in the bounce equation, Eqs. (3.79) and (3.82), by the replacement $V_0 \to V(\phi, T)$, so that the vacuum structure and the barrier are thermally corrected [167, 168]. While this prescription may seem justified, it suffers from several independent problems [32]. First, V generically develops a non-zero imaginary part in the region between the two phases, which must be discarded by hand when computing the bounce. Second, the bounce, evaluated using the effective potential, which is gauge-dependent, as discussed in the previous subsubsection, ends up being gauge-dependent as well, which is unphysical since the nucleation rate is a physical observable.

Third, the prescription double-counts fluctuations. Computing $V(\phi, T)$ amounts to integrating over all field fluctuations: every momentum mode of every field, including

the scalar ϕ itself. The bounce solution Eq. (3.79), however, is an inhomogeneous background with spatial dependence on scales set by the bubble wall width $\sim 1/m_\phi$. Using V in place of V_0 promotes ϕ to a spatially dependent degree of freedom that was already formally integrated out. The same fluctuations are therefore counted twice: once inside V, and again in the functional determinant of the prefactor A_T, Eq. (3.85), which is computed by integrating over fluctuations of the scalar field around the bounce background.

This also causes a breakdown of the derivative expansion, Eq. (6.34): since V includes the scalar mode at mass m_ϕ, which is the same scale as the bounce profile gradient, higher-derivative terms in the expansion of the effective action are not suppressed and the expansion does not converge [32].

The resolution is to exploit the UV/IR separation that underlies any well-defined nucleation rate [169, 195]: UV physics shapes the barrier, while IR modes perform the actual tunnelling. In case of thermally driven phase transitions, this separation is physically transparent — hard modes at $k \sim \pi T$, which generate LO thermal masses, cubic terms, and other corrections to the free energy, shape the barrier. The nucleation itself is an IR process, driven by low-energy fluctuations $\sim m_\phi$.

III.4.3 Dimensional reduction

The presence of well-separated thermal scales allows one to utilize the powerful machinery of EFT to systematically reorganize the perturbative expansion and resolve the issues described above. In this way, UV physics is encoded in Wilson coefficients, and the IR dynamics relevant for the phase transition is described by a low-energy theory [47, 49, 50, 189].

DR gets its name from the fact that, after integrating out the non-zero Matsubara modes, the thermal theory is effectively reduced to a three-dimensional (3D) Euclidean EFT for the bosonic zero modes. Concretely, the resulting theory contains the spatial components of gauge fields A_i, the temporal components A_0 which behave as adjoint scalars with Debye masses $m_D \sim gT$, and the scalar zero modes, with all masses and couplings promoted to temperature-dependent Wilson coefficients. For the SM and the SMEFT, the explicit form of the 3D Lagrangian is given in Eq. (4.1).

In practice, the EFT construction may involve several threshold matchings. If a model contains particles whose zero-temperature masses are parametrically larger than the relevant thermal scales, these degrees of freedom are integrated out at the appropriate

matching scale. One then performs the DR at the hard scale $\mu \sim \pi T$, integrating out the non-zero Matsubara modes. In gauge theories, this is followed by a further soft matching at $\mu \sim m_D \sim gT$ to integrate out Debye-screened temporal gauge fields. Which EFT one ultimately uses depends on the characteristic nucleation scale: the matching is carried out down to the scale relevant for the dynamics of interest.

After matching, the EFT couplings are evolved with the appropriate RGEs to resum large logarithms (e.g. $\log(\pi T/m_\phi)$, $\log(\pi T/m_D)$); this running is essential for reducing residual matching-scale dependence. In particular, evolving the couplings from the matching scale down to the characteristic dynamical scale of the process is crucial for obtaining reliable predictions, as it ensures that the EFT parameters are evaluated at the scale where the relevant physics takes place. In Chapter IV, we derive these RGEs for the 3D EFT of the SM and the SMEFT including higher-dimensional operators.

Conceptually, this construction resolves several issues of the direct thermal expansion at once [32, 46, 114]. First, the perturbative series is reorganized as an expansion in powers of g, which systematically controls scale dependence order by order. Second, the leading thermal corrections to V are captured in EFT Wilson coefficients, so the loop expansion in the EFT is no longer destabilized by parametrically large contributions, and the $\hbar$-expansion becomes effective again. Third, for bubble nucleation, UV and IR physics are cleanly separated: UV (hard) modes shape EFT parameters, while IR modes are kept dynamical in the bounce problem, avoiding double-counting. Systematic improvements are then straightforward: one includes higher-order matching corrections for EFT couplings and computes additional loop corrections in the prefactor around the EFT bounce.

Another major advantage of the DR is that the resulting 3D EFT is ideally suited for lattice simulations. After integrating out non-static modes, one is left with a purely bosonic 3D Euclidean theory. This setup cleanly isolates the long-distance non-perturbative dynamics of the phase transition and enables precise first-principles determinations of thermodynamic observables that can be directly compared with perturbative EFT predictions [51, 190, 196].

The 3D EFT is, in general, non-renormalizable: it contains higher-dimensional operators suppressed by powers of the heavy scales that have been integrated out, parametrically $(m/\pi T)^n$ for the DR. Their numerical impact provides a direct validity check of the EFT truncation: if these operators induce sizable shifts in physical observables, the truncation of the EFT operator series is not reliable. This is particularly relevant for SFOEWPTs,

which often lie close to the edge of EFT applicability; in such cases, retaining higher-dimensional operators can be essential for quantitatively accurate predictions [36, 38]. The role of higher-dimensional operators in the 3D EFT for EWPT predictions in the cxSM is studied in Section V.5.

Explicit matching

In the dimensional-reduction step, matching is performed by equating soft ($\omega_n = 0$) 1PI Green's functions of the full four-dimensional (4D) theory and the 3D EFT for bosonic zero modes at the hard scale [50]. Since the 3D EFT is intended to describe long-distance physics, the matching is performed in an expansion in external momenta, $p_i \ll \pi T$. Schematically, for an n-point function this reads

$$G_n^{4D}\big(\{p_i\};\omega_n = 0\big)\Big|_{\mu\sim\pi T} = G_n^{3D}\big(\{p_i\}\big)\,. \tag{3.103}$$

The 3D EFT describes the long-distance, time-independent sector of bosonic zero modes; non-static Matsubara modes are integrated out, and their effects are encoded in Wilson coefficients. Order by order in g, this yields schematic relations,

$$\begin{aligned}
m_{3D}^2 &= \overbrace{\underbrace{m^2}_{\text{tree}} + \underbrace{\#g^2T^2}_{\text{1-loop}}}^{\mathcal{O}(g^2)} + \overbrace{\underbrace{\#g^2m^2}_{\text{1-loop}} + \underbrace{\#g^4T^2}_{\text{2-loop}}}^{\mathcal{O}(g^4)} + \mathcal{O}(g^6)\,,\\
\lambda_{3D} &= \overbrace{\underbrace{\lambda T}_{\text{tree}}}^{\mathcal{O}(g^2)} + \overbrace{\underbrace{\#g^4T}_{\text{1-loop}}}^{\mathcal{O}(g^4)} + \mathcal{O}(g^6)\,,\\
g_{3D}^2 &= \overbrace{\underbrace{g^2T}_{\text{tree}}}^{\mathcal{O}(g^2)} + \overbrace{\underbrace{\#g^4T}_{\text{1-loop}}}^{\mathcal{O}(g^4)} + \mathcal{O}(g^6)\,.
\end{aligned} \tag{3.104}$$

Here, with underbraces we indicate which loop order contributes to the matching while overbraces show the respective coupling order, assuming the $m^2 \sim g^2T^2$, $\lambda \sim g^2$ scaling. Expressions of the form $\#g^n$ denote dimensionless factors at $\mathcal{O}(g^n)$, which generally depend on the scalar self-couplings and gauge charges.

In particular, the thermal mass contribution $\Pi_T \sim g^2T^2$ (which for the SM Higgs field reads as given in Eq. (3.18)) appears directly in m_{3D}^2, so the ad-hoc daisy resummation required in the direct 4D approach is automatically encoded in the EFT parameters through matching [32, 49, 50]. Note that in three dimensions, scalar quartic couplings and gauge

couplings carry mass dimension one, while scalar and gauge fields have mass dimension one-half, which explains the overall factors of T in the matching relations.

Other scales are integrated out analogously: at each threshold, one computes the relevant Green's functions in both the theory above and the EFT below the matching scale, and equates them in the appropriate kinematic regime. In practice, this involves expanding the Green's functions in the momentum region relevant for the EFT (e.g. $p \ll \mu_{\text{match}}$), and absorbing any differences into Wilson coefficients of the EFT.

The matching procedure outlined above has been implemented algorithmically in the public package `DRalgo` [197], which automates the DR for generic BSM models. `DRalgo` computes two-loop thermal masses and super-renormalizable effective couplings in the 3D EFT, together with the associated RGEs; it also supports the matching of sextic scalar renormalizable operators.

Effective potential in the 3D EFT

After separating UV physics through matching, one can compute thermodynamic observables perturbatively within the EFT itself: constructing the effective potential and solving for bounce solutions, as outlined in Sections III.2 and III.3, now using the 3D effective theory.

For the effective potential, calculated within the 3D EFT, we can schematically write [32]:

$$V(\phi, T) \simeq T V^{3D}(\phi_{3D})\big|_{\phi_{3D} \simeq \phi/\sqrt{T}}, \tag{3.105}$$

where V is the 4D effective potential computed in the full theory, Eqs. (3.31) and (3.100), while V^{3D} is the effective potential computed within the 3D EFT employing similar techniques as described in Section III.2. At LO, the 3D field is simply related to the 4D field by $\phi_{3D} = \phi/\sqrt{T}$; however, at higher orders, momentum-dependent thermal corrections modify the relation, and these effects are systematically incorporated through the 3D EFT matching.

Because the loop expansions in both the 4D and 3D theories are truncated in practice, Eq. (3.105) holds only up to the order at which both expansions are consistently matched. The tree-level potential of the dimensionally reduced theory already contains the effects of hard modes through matching. Loop corrections computed within the 3D EFT then encode the soft (zero-mode) fluctuations. In this way, the separation between hard and

soft physics is explicit, and the cubic term associated with daisy resummation is reproduced by soft loops in the EFT.

As discussed above, beyond $\mathcal{O}(g^3)$, the 4D one-loop approach is incomplete: for full $\mathcal{O}(g^4)$ accuracy, one must include both two-loop matching for the EFT Wilson coefficients and a two-loop computation of V^{3D} within the 3D EFT. Truncating the matching relations and/or the 3D potential at lower loop orders can lead to significant residual scale dependence in the computed observables, as explored in Chapter V.

III.5 Macroscopic thermodynamic observables

The nucleation and percolation of bubbles are described by a small number of macroscopic thermodynamic parameters that encode the dynamics of the phase transition and ultimately determine the strength and spectral shape of the GW signal. This section bridges the field-theoretic description — centered on the effective potential and the nucleation rate introduced in Sections III.2 and III.3 — and the macroscopic thermodynamic observables that characterize the transition.

Free energy, pressure, and the effective potential

The partition function of the thermal system encodes all thermodynamic information; its logarithm yields the free-energy density, which in the background-field method is identified with the effective potential $V(\phi, T)$. The thermodynamic pressure in each phase, labeled by the field value at the local minimum $\phi^{(i)}_{\text{min}}$, is therefore

$$p^{(i)}(T) = -V\left(\phi^{(i)}_{\text{min}}, T\right). \tag{3.106}$$

In the dimensionally reduced 3D EFT (see Section III.4), temperature enters only through the effective couplings and V^{3D} has mass dimension three. The corresponding pressure acquires an additional factor of T,

$$p^{(i)}(T) = -TV^{3D}\left(\phi^{(i)}_{\text{min}}\right), \tag{3.107}$$

reflecting the DR from four to three dimensions.

In both cases the energy density follows from $\rho = -p + T\partial p/\partial T$. For the 4D potential,

$$\rho^{(i)}(T) = V\left(\phi^{(i)}_{\rm min}, T\right) - T\frac{\partial V}{\partial T}\left(\phi^{(i)}_{\rm min}, T\right), \tag{3.108}$$

while for the 3D EFT approach with $V = TV^{3D}$,

$$\rho^{(i)}(T) = -T^2\frac{dV^{3D}}{dT}\left(\phi^{(i)}_{\rm min}\right). \tag{3.109}$$

All observables below are derived from the pressure difference between the false-vacuum and true-vacuum phases,

$$\Delta p(T) \equiv p^{(\rm FV)}(T) - p^{(\rm TV)}(T) = V(\phi_{\rm TV}, T) - V(\phi_{\rm FV}, T)\ . \tag{3.110}$$

Throughout, $\Delta X \equiv X^{(\rm FV)} - X^{(\rm TV)}$ denotes the difference of any quantity X evaluated in the false and true vacuum phases, respectively.

Thermodynamic observables

- **Critical temperature T_c.** The *critical temperature* is the temperature at which the two phases are degenerate in pressure,

$$p^{(\rm FV)}(T_c) = p^{(\rm TV)}(T_c) \quad \Longleftrightarrow \quad \Delta p(T_c) = 0\,. \tag{3.111}$$

  Above T_c the symmetric phase is the global minimum; below it the broken phase is energetically preferred. For a first-order transition a barrier separates the two minima at T_c, and the system remains trapped in the metastable false vacuum until thermal fluctuations drive nucleation at $T_n < T_c$.

- **Latent heat L_c.** The *latent heat* is the discontinuity in energy density between the two phases at the critical temperature,

$$L_c = \Delta\rho\big|_{T_c} = T_c\frac{d\Delta p}{dT}\bigg|_{T_c} = -T_c\frac{d\Delta V}{dT}\bigg|_{T_c}, \tag{3.112}$$

  where $\Delta V \equiv -\Delta p$. L_c quantifies the energy released when the Universe transitions from the false to the true vacuum: a large latent heat signals a strong first-order transition and is a prerequisite for both efficient baryogenesis and an observable GW amplitude.

- **Nucleation temperature T_n.** The false-vacuum phase persists below T_c as long as the probability to nucleate a bubble within a Hubble volume during a Hubble time remains small, i.e. $\gamma(T) \ll H^4(T)$. The *nucleation temperature* is defined as the temperature at which, on average, one bubble nucleates per Hubble volume per Hubble time [166, 198],

$$\int_{T_n}^{T_c} \frac{dT}{T} \frac{\gamma(T)}{H(T)^4} \approx 1 \,, \tag{3.113}$$

where, during the radiation-dominated era, the Hubble rate is given by $H^2 = \rho_{\rm rad}/(3\bar{M}_{\rm Pl}^2)$, with $\rho_{\rm rad} = (\pi^2/30)\, g_* T^4$ (see Section II.2.1). Since $S_3(T)/T$ varies slowly near T_n, Eq. (3.113) reduces approximately to a parametric condition [30, 199],

$$\frac{S_3(T_n)}{T_n} \approx 141 + \ln\!\left(\frac{A_T}{T^4}\right) - 4\ln\!\left(\frac{T_n}{100\,\text{GeV}}\right) - \ln\!\left(\frac{\beta/H}{100}\right) , \tag{3.114}$$

where A_T is the nucleation prefactor, defined in Section III.3. A large separation $T_c \gg T_n$ signals strong supercooling: the Universe remains trapped in the false vacuum well below T_c, allowing substantial vacuum energy to accumulate.

- **Percolation temperature T_p.** Even after T_n, the transition of the Universe is not instantaneous: bubbles must grow and merge before the whole Hubble volume converts into the true vacuum. The *percolation temperature* $T_p \leq T_n$ is defined as the temperature at which the fraction of space in the new phase reaches $\approx 34\%$ [34, 198],

$$\frac{4\pi}{3} H(T_p)^3 \int_{T_p}^{T_c} \frac{dT}{T} \frac{\gamma(T)}{H(T)^4} R(T_p, T)^3 \approx 0.34 \,, \tag{3.115}$$

where $R(T_p, T) = v_w(1 - T/T_p)/H(T)$ is the radius of a bubble at T_p nucleated at temperature T. This corresponds to the probability $P_f(T_p) = e^{-0.34} \approx 71\%$ that a random point of space is still in the false vacuum. The extended volume double counts the overlapping regions of the bubbles, which is removed by exponentiating it [34].

Similarly to the nucleation case, this condition can be approximated [30],

$$\frac{S_3(T_p)}{T_p} \approx 131 + \ln\!\left(\frac{A_T}{T^4}\right) - 4\ln\!\left(\frac{T_p}{100\,\text{GeV}}\right) - 4\ln\!\left(\frac{\beta/H}{100}\right) + 3\ln v_w \,. \tag{3.116}$$

For strong first-order transitions with moderate supercooling — the typical regime

for electroweak baryogenesis — T_p and T_n differ by only a few percent. The bulk of the GW signal is generated around T_p, so GW observables are conventionally evaluated at the percolation temperature [200, 201].

- **Transition strength α.** The *transition strength* α is the ratio of the released vacuum energy density — quantified by the trace anomaly difference — to the radiation density, evaluated at T_p [34, 188]. In the 4D description,

$$\alpha = \left.\frac{\Delta\theta}{\rho_{\rm rad}}\right|_{T_p}, \qquad \Delta\theta = \Delta V - \frac{T}{4}\frac{d\Delta V}{dT}, \tag{3.117}$$

where $\Delta\theta \equiv (\Delta\rho - 3\Delta p)/4$ is the trace of the energy-momentum tensor difference. In the 3D EFT, using Eqs. (3.107) and (3.109), the same quantity reads [36]

$$\alpha = \left.\frac{1}{\rho_{\rm rad}}\left(\frac{3T}{4}\Delta V^{3D} - \frac{T^2}{4}\frac{d\Delta V^{3D}}{dT}\right)\right|_{T_p}, \tag{3.118}$$

where $\Delta V^{3D} \equiv V^{3D}(\phi_{\rm FV}) - V^{3D}(\phi_{\rm TV})$. A large α signals a strong first-order transition and typically drives an enhanced GW signal.

- **Inverse duration β/H.** The *inverse duration* characterizes how rapidly the nucleation rate changes with time, which sets the typical bubble size. One defines

$$\frac{\beta}{H} = T\frac{d}{dT}\left(\frac{S_3}{T}\right)\Bigg|_{T_p}. \tag{3.119}$$

A large β/H corresponds to a rapid transition producing many small bubbles; a small β/H implies a prolonged transition with a few large bubbles. The mean bubble separation is given by [30]

$$R_* \approx \frac{(8\pi)^{1/3}}{\beta}\tilde{v}, \qquad \tilde{v} \equiv \max(v_w, c_s), \tag{3.120}$$

where $\tilde{v}$ is the velocity of the outermost fluid disturbance: the bubble wall for detonations ($v_w > c_s$) and the leading shock front for deflagrations ($v_w < c_s$, where the shock propagates at c_s). R_* sets the characteristic length scale entering both the peak frequency and amplitude of the GW spectrum [30, 202].

- **Sphaleron suppression parameter ξ.** The ratio of the Higgs vev to temperature,

$$\xi(T) \equiv \frac{\phi_{\rm TV}(T)}{T}, \tag{3.121}$$

where $\phi_{\mathrm{TV}}(T)$ is the vev in the broken phase, is directly relevant to electroweak baryogenesis. For the baryon asymmetry produced during the transition to survive, sphaleron processes (transitions over the electroweak energy barrier that violate baryon number conservation) must be sufficiently suppressed in the broken phase immediately after the wall passes. The *baryon number preservation condition* requires the sphaleron rate to be exponentially suppressed, which translates into [6, 111]

$$\xi_n \equiv \frac{\phi_{\mathrm{TV}}(T_n)}{T_n} \gtrsim 1\,. \tag{3.122}$$

Note that ξ is *not* a gauge-invariant quantity beyond tree level: the position of the broken minimum of the loop-corrected V depends on the gauge parameter away from the stationary points, see the discussion in Section III.2. The condition Eq. (3.122) should therefore be understood as an order-of-magnitude criterion, with a gauge-independent formulation requiring a more careful treatment, for example via the 3D EFT framework where the vev is computed from the gauge-independent 3D potential [148].

The parameter set $(\alpha,\ \beta/H,\ T_p,\ v_w)$ constitutes the complete macroscopic input to the GW signal templates described in Section III.6. The sensitivity of the GW predictions to the perturbative calculation of the thermodynamic observables is a central subject of this thesis.

III.6 Gravitational wave predictions from phase transitions

A cosmological first-order phase transition is a violent, spatially inhomogeneous event: bubbles nucleate, expand, collide, and stir the surrounding plasma. Each stage of this process sources a stochastic GW background that is imprinted on the GW radiation content of the Universe and can, in principle, be detected by space-based interferometers such as LISA [30, 34, 100]. The GW signal from the EWPT is characterized by its spectral shape $\Omega_{\mathrm{GW}}(f)h^2$, peak frequency f_{peak}, and peak amplitude $\Omega_{\mathrm{GW,peak}}h^2$, all of which are functions of the macroscopic transition parameters $(\alpha, \beta/H, T_p, v_w)$ defined in Section III.5.

Sources of gravitational radiation

Three physically distinct mechanisms contribute to the GW background from a first-order phase transition [30, 100]:

- **Bubble wall collisions.** As expanding bubble walls collide, the gradient energy stored in the scalar field is converted into GWs. This mechanism dominates only in the runaway regime ($v_w \to 1$, $\gamma_w \to \infty$), where plasma friction is insufficient to establish a terminal velocity. For EWPT scenarios with moderate α, friction prevents runaway, strongly suppressing this contribution.
- **Sound waves.** After bubble walls reach their terminal velocity and begin to overlap, the energy deposited in the plasma drives long-lived acoustic oscillations that propagate through the fluid. These sound waves persist after the transition and act as a *long-duration* source of GWs, making them the dominant contribution for non-runaway transitions with $\alpha \lesssim \mathcal{O}(1)$ [182, 202].
- **MHD turbulence.** A fraction of the kinetic energy deposited in the plasma eventually cascades into magnetohydrodynamic (MHD) turbulence, driven by the vortical motion generated at bubble collisions and by the fluid shear behind sound fronts [203]. For transitions of weak to intermediate strength ($\alpha \lesssim 0.1$), the turbulent contribution is subdominant relative to sound waves [204]. Its spectral shape and the fraction of kinetic energy converted to turbulent motion remain incompletely characterized by current simulations [31], introducing an additional free parameter if included.

Sound wave spectrum

In this thesis we focus on the sound-wave contribution as the dominant GW source for non-runaway EWPTs, using it as a probe of the theoretical uncertainties arising from the perturbative calculation of the thermodynamic parameters.

The spectral energy density of GWs from sound waves, expressed as a fraction of the critical energy density, is well approximated by the broken power law [30, 202, 205]

$$\Omega_{\mathrm{GW}}^{\mathrm{sw}}(f)\,h^2 \;\approx\; \Omega_{\mathrm{GW,peak}}\,h^2 \left(\frac{f}{f_{\mathrm{peak}}}\right)^3 \left(\frac{7}{4+3\left(f/f_{\mathrm{peak}}\right)^2}\right)^{7/2}, \tag{3.123}$$

where the spectral shape $\propto f^3$ at $f \ll f_{\rm peak}$ and $\propto f^{-4}$ at $f \gg f_{\rm peak}$, as found in numerical simulations of acoustic motions in the plasma. The peak frequency today is

$$f_{\rm peak} \;\approx\; 26\,\mu{\rm Hz} \times \frac{1}{H_* R_*} \left(\frac{T_*}{100\,{\rm GeV}}\right) \left(\frac{g_*}{100}\right)^{1/6}, \tag{3.124}$$

where R_* is the mean bubble separation at percolation, g_* is the effective number of relativistic degrees of freedom, and T_* is the plasma temperature immediately after the transition. The latter accounts for reheating by the released latent heat: $T_* = T_p(1+\alpha)^{1/4} \approx T_p$ for moderate α.

The peak amplitude is given by

$$\Omega_{\rm GW,peak}\, h^2 \;\approx\; 4.1 \times 10^{-7}\, R_* H_* \left(1 - \frac{1}{\sqrt{1 + 2\tau_{\rm sw} H_*}}\right) \left(\frac{\kappa_{\rm sw}\,\alpha}{1+\alpha}\right)^2 \left(\frac{100}{g_*}\right)^{1/3}, \tag{3.125}$$

where the factor in parentheses encodes the *finite duration* of the sound-wave source: the acoustic phase shuts off when shocks form, at a time $\tau_{\rm sw} \approx R_*/\bar{U}_f$ after the transition, where $\bar{U}_f \approx \sqrt{3\alpha\kappa_{\rm sw}/4(1+\alpha)}$ is the root-mean-square four-velocity of the plasma [206].

The efficiency factor $\kappa_{\rm sw}$ quantifies the fraction of the released vacuum energy that is converted into bulk kinetic energy of the plasma. It is determined from numerical hydrodynamic fits as a function of α and v_w [188]; in the detonation regime it reads approximately

$$\kappa_{\rm sw}(\alpha) \;\approx\; \frac{\alpha}{0.73 + 0.083\sqrt{\alpha} + \alpha}, \tag{3.126}$$

valid at $v_w \simeq 1$. The sound-wave spectrum, Eqs. (3.123) and (3.125), is the formula used in Chapter V to compute the GW signal from the EWPT in the singlet extension of the SM.

More recent analyses have proposed improved spectral templates for the sound-wave contribution that go beyond the single broken power law of Eq. (3.123). In particular, accounting for the finite thickness of the sound shells and their eventual collision leads to a *double broken power law*, with a second spectral break appearing at frequencies above the peak [31].

Uncertainties in gravitational wave predictions

The GW spectrum predicted from a first-order EWPT carries uncertainties from two broad classes of sources.

On the *particle-physics side*, the transition parameters $(\alpha, \beta/H, T_*)$ are derived from the effective potential and nucleation rate, both computed perturbatively. The dominant uncertainties are renormalization-scale and gauge dependence of the effective potential, which in the 4D daisy-resummed approach propagate to orders-of-magnitude uncertainty in the GW peak amplitude. The dimensionally reduced 3D approach reduced the uncertainties by pushing the predictions to higher perturbative orders [32]; the RG equations governing the 3D EFT are studied in Chapter IV. An additional, irreducible uncertainty arises from the non-perturbativity of the magnetic gauge-boson sector at the ultrasoft scale g^2T [23, 190], which no finite perturbative order can remove and which sets a fundamental floor on the precision of any perturbative GW prediction. The impact of renormalization-scale dependence, gauge dependence, and the high-temperature expansion on GW observables in the cxSM is the central subject of Chapter V.

On the *cosmological and hydrodynamic side*, the spectral profile, Eq. (3.123), and its normalization are calibrated against numerical simulations in a simplified setup [182, 202], and the sound-wave lifetime $\tau_{\rm sw}$ and efficiency factor $\kappa_{\rm sw}$ carry their own uncertainties [31, 188, 206]. Most directly, the bubble wall velocity, v_w, determination requires solving the full Boltzmann problem in the bubble background, with current estimates carrying $\mathcal{O}(1)$ uncertainties [207]. The loop-corrected wall velocity and its uncertainty are studied in Chapter VI.

IV – RUNNING IN THE 3D EFT OF THE SM(EFT)

Everything flows.

— Heraclitus

The 3D EFT, even when restricted to SM fields alone, is highly predictive: not only does it meticulously capture the IR dynamics of the SM at high temperature (see Section III.4), but it also serves as a universal description of a broad class of UV extensions. In the LO truncation of the m_h/T expansion (considering only super-renormalizable scalar interactions), the electroweak sector of this EFT has been simulated on the lattice [24, 208, 209], with the conclusion that the SM cannot realize a EWPT strong enough to source observable GWs. The situation changes once higher-order terms in the m_h/T expansion are retained. These manifest as higher-dimensional operators in the 3D EFT, and recent studies [3, 35, 36, 38, 210] have demonstrated that their impact is essential to capture strong phase transitions.

Precise knowledge of the RG evolution of the 3D EFT coefficients is fundamental both in perturbative calculations (addressing the renormalization scale dependence from which other 4D methods suffer [3, 32] (also see Chapter V)) and in the study of the 3D theory in the lattice simulations [49, 208]. The computation of such RGE constitutes the main objective of the present chapter. Namely, these results pave the way for the future inclusion of effective parameters (in particular, Higgs sextic interactions) in lattice studies of EWPTs. Results presented in this chapter are also of a direct use in the DR computations, as IR divergences arising from the matching procedure must be consistently reproduced by the UV divergences we compute within the EFT. Furthermore, these results are also relevant for the study of critical phenomena through ϵ expansion [211–213].

IV.1 Dimensionally reduced EFT of the SM and the SMEFT

We are interested in the dynamics of the nucleating field that takes place below the hard scale, characterized by the temperature T, and where only SM fields matter. It is described by a dimensionally reduced theory (see Section III.4 for the detailed discussion), where temperature enters the theory only through Wilson coefficients. Considering, for simplicity, only the $SU(2)_L$ part of the SM for now (the contributions from the $U(1)_Y$ coupling g_3' can be found in Appendix A), the 3D EFT Lagrangian can be written as:

$$
\begin{aligned}
\mathcal{L}_{3D} = & \frac{1}{4}W^I_{rs}W^I_{rs} + (D_r\Phi)^\dagger(D_r\Phi) + m_3^2|\Phi|^2 + \lambda_3|\Phi|^4 + c_{\phi^6}|\Phi|^6 \\
& + c_{\phi^8}|\Phi|^8 + c_{\phi^2W^2}|\Phi|^2W^I_{rs}W^I_{rs} \\
& + c^{(1)}_{\phi^4D^2}|\Phi|^2\Box|\Phi|^2 + c^{(2)}_{\phi^4D^2}(\Phi^\dagger D_r\Phi)^\dagger\Phi^\dagger D_r\Phi + r^{(3)}_{\phi^4D^2}|\Phi|^2(D_r\Phi)^\dagger D_r\Phi \\
& + \frac{1}{2}(D_rW^I_0)(D_rW^I_0) + \frac{1}{2}m_D^2W^I_0W^I_0 + \lambda_{W_0^4}(W^I_0W^I_0)^2 + \lambda_{\phi^2W_0^2}|\Phi|^2W^I_0W^I_0 \\
& + c_{W_0^6}(W^I_0W^I_0)^3 + c_{\phi^2W_0^4}|\Phi|^2(W^I_0W^I_0)^2 \\
& + c^{(1)}_{\phi^4W_0^2}|\Phi|^4(W^I_0W^I_0) + c^{(2)}_{\phi^4W_0^2}(\Phi^\dagger\sigma^I\Phi)(\Phi^\dagger\sigma^J\Phi)(W^I_0W^J_0) \\
& + c^{(1)}_{\phi^6W_0^2}|\Phi|^6(W^I_0W^I_0) + c^{(2)}_{\phi^6W_0^2}|\Phi|^2(\Phi^\dagger\sigma^I\Phi)(\Phi^\dagger\sigma^J\Phi)(W^I_0W^J_0) \\
& + c^{(1)}_{\phi^2W_0^2D^2}|\Phi|^2(D_rW^I_0)(D_rW^I_0) + c^{(2)}_{\phi^2W_0^2D^2}\epsilon^{IJK}(\Phi^\dagger\sigma^I i\overleftrightarrow{D}_r\Phi)(W^J_0D_rW^K_0) \\
& + r^{(3)}_{\phi^2W_0^2D^2}\Phi^\dagger(-i\overleftrightarrow{D}_r)\Phi(D^rW^I_0)W^I_0 + r^{(4)}_{\phi^2W_0^2D^2}\left[D^2(\Phi^\dagger)\Phi + \Phi^\dagger D^2\Phi\right]W^I_0W^I_0 \\
& + r^{(5)}_{\phi^2W_0^2D^2}D^2(W^I_0)W^I_0|\Phi|^2 + r^{(6)}_{\phi^2W_0^2D^2}\epsilon^{IJK}D^2(W^I_0)W^J_0\Phi^\dagger\sigma^K\Phi + \cdots ,
\end{aligned}
\tag{4.1}
$$

in which we explicitly show operators up to mass dimension four and where the ellipses stand for terms with higher-dimensional operators. As before, Φ represents the Higgs doublet, W denotes the $SU(2)_L$ gauge boson with coupling g_3 and W_0 is its temporal component. Note that among dimension-four operators, we only consider those containing fewer than four gauge fields, since operators involving more gauge fields are suppressed in the DR procedure by extra powers of the gauge coupling. In addition, we omit formally present operators of fractional dimensions, e.g. $|\Phi|^2(\Phi^\dagger\sigma^I\Phi)W^I_0$; they are not generated in DR, as diagrams with an odd number of external momentumless W_0 fields result in vanishing contribution.

Finally, it is also worth commenting that we ignored gluon operators in the 3D EFT because they cannot arise from tree-level matching in DR, though they could add small corrections to the RG results presented below. Operators in gray in Eq. (4.1) are redundant, which can be removed with a proper field redefinition [36], discussed below.

IV.2 Possible realizations of the first-order EWPT within the SMEFT

For a first-order phase transition to occur within the SMEFT, the effective scalar potential must develop a structure with two local minima separated by a barrier. The form and origin of the broken minimum and the barrier depend on the size and hierarchy of the 3D Wilson coefficients of Eq. (4.1). The barrier can arise in qualitatively different ways, each with its own power-counting scheme, scale hierarchy, and domain of perturbative validity. Three qualitatively distinct realizations of a first-order EWPT are possible within the SMEFT: a *tree-level barrier*, a *radiatively generated barrier* and *radiative symmetry breaking* via the Coleman-Weinberg mechanism [135]. All three mechanisms can in principle be realized within the Higgs sector of the SMEFT for appropriate choices of Wilson coefficients (see Section II.4 for an overview of the SMEFT framework and the role of the Higgs-sector operators in the EWPT), and the corresponding regions of the SMEFT parameter space remain compatible with current experimental constraints [214].

For the power-counting analysis, it is convenient to assign scalings with respect to the gauge coupling g (treated as a small parameter, $g \ll 1$) to all components of the 3D EFT potential, and demand that the terms contributing to the shape of the potential resulting in the first-order EWPT are of the same order.

We further assume that the theory in Eq. (4.1) is a result of the DR of the SMEFT and the latter is itself an effective description of generic BSM physics, characterized by an UV gauge coupling $\tilde{g}$ and valid up to scales $\Lambda \gtrsim T$.

The SMEFT couplings (see Section II.4), denoted with a bar in this chapter, are matched to the effective couplings of Eq. (4.1) via [36]. Parametrically, the leading matching relations for the Higgs-only operators are:

$$\begin{aligned} m_3^2 &\sim \mu_h^2 + g^2 T^2, \\ \lambda_3 &\sim \lambda_h T + \bar{c}_{\phi^6} T^3, \\ g_3^2 &\sim g^2 T, \\ c_{\phi^6} &\sim T^2 \bar{c}_{\phi^6} \sim \tilde{g}^4 \frac{T^2}{\Lambda^2}, \\ c_{\phi^8} &\sim T^3 \bar{c}_{\phi^8} \sim \tilde{g}^6 \frac{T^3}{\Lambda^4}, \\ c_{\phi^4 D^2} &\sim T \bar{c}_{\phi^4 D^2} \sim \tilde{g}^2 \frac{T}{\Lambda^2}, \end{aligned} \tag{4.2}$$

where we assumed the following power counting for non-renormalizable 4D terms [215]:

$\bar{c}_{\phi^6} \sim \tilde{g}^4/\Lambda^2, \bar{c}_{\phi^4 D^2} \sim \tilde{g}^2/\Lambda^2, \bar{c}_{\phi^2 W^2} \sim \tilde{g}^2 g^2/\Lambda^2, \bar{c}_{\phi^8} \sim \tilde{g}^6/\Lambda^4$. In addition, one can consider an additional $(1/16\pi^2)$ suppression factor for $\bar{c}_{\phi^2 W^2}$ under the assumption of a weakly-coupled completion of the SMEFT, as this coefficient is only generated at one loop [216].

The question of which barrier type is realized is thus determined, via these matching relations, by the underlying parameter values in the SMEFT. In the following subsections we describe each of the possible realizations in turn.

We parametrize the Higgs doublet as $\Phi = \left(G^+, \frac{1}{\sqrt{2}}(\phi + h + iG^0)\right)^T$ (see Section II.1.2 for details), where ϕ is the background field value, with symmetry breaking studied along this direction.

IV.2.1 Tree-level barrier

The simplest way to generate a potential barrier is to have one already present at the tree level in the 3D scalar potential. This requires simultaneously $m_3^2 > 0$, $\lambda_3 < 0$, and $c_{\phi^6} > 0$, so that the scalar potential

$$V(\phi) = \frac{m_3^2}{2}\phi^2 + \frac{\lambda_3}{4}\phi^4 + \frac{c_{\phi^6}}{8}\phi^6 \tag{4.3}$$

develops a local maximum between the symmetric minimum at $\phi = 0$ and a broken minimum at $\phi \neq 0$.

For all three terms in Eq. (4.3) to contribute at the same order, one demands $m_3^2\phi^2 \sim |\lambda_3|\phi^4 \sim c_{\phi^6}\phi^6$. Combining this with the perturbativity requirement $V \gg g^6 T^3$ [23] and the validity of the high-T expansion $m_3^2 \ll T^2$, one obtains the power-counting scheme for the tree-level barrier [36, 214]:

$$m_3^2 \sim g^2 T^2, \qquad \lambda_3 \sim g^2 T, \qquad c_{\phi^6} \sim g^2, \tag{4.4}$$

which is the standard power-counting regime underlying many studies of the EWPT with a dimension-six Higgs operator in the the SMEFT [35, 38].

Hence, the Higgs-field nucleation occurs at the soft scale, $m_3 \sim gT$, and the full set of operators in Eq. (4.1) is dynamically relevant.

Translating back to the 4D theory through Eq. (4.2) gives $\lambda_3 \sim g^2$ and $\bar{c}_{\phi^6} \sim g^2/T^2$, where $\bar{c}_{\phi^6}$ is the Wilson coefficient of the dimension-six operator $\mathcal{O}_\phi = (\Phi^\dagger\Phi)^3$ of the

SMEFT Lagrangian (see Eq. (2.43) and Section II.4). Combined with $c_{\phi^6} \sim \tilde{g}^4 T^2/\Lambda^2$ from Eq. (4.2), this yields the following parametric relation between the BSM and SM couplings:

$$\tilde{g}^2 \sim g\frac{\Lambda}{T}. \tag{4.5}$$

Given this, we can establish the scalings of the effective couplings in Eq. (4.1); for instance, the octic Higgs effective coupling parametrically is $c_{\phi^8} \sim g^3/\Lambda$.[1] This establishes that the dimension-four operators in Eq. (4.1) feature an additional numerical suppression beyond the $1/T$ scaling from EFT counting alone. It is therefore consistent to restrict our calculations to a single insertion of operators with mass dimension four.

IV.2.2 Radiatively generated barrier

If m_3^2 is parametrically smaller than the gauge-boson mass, given by $\sim g_3\phi$, a hierarchy of scales develops within the 3D EFT, which can lead to the formation of the loop-induced barrier. The cubic term, originating from loops of gauge field, acts as the barrier, giving rise to the LO scalar potential [214, 217, 218]:

$$V(\phi) = \frac{m_3^2}{2}\phi^2 - \frac{g_3^3}{16\pi}\phi^3 + \frac{\lambda_3}{4}\phi^4\,, \tag{4.6}$$

in which, in contrast to the tree-level barrier, the quartic coupling must be positive for stability.

The scale hierarchy,

$$m_3^2 \sim g^3T^2 \ll g_3^2\phi^2 \sim g^2T^2 \ll (\pi T)^2\,, \tag{4.7}$$

is essential: it guarantees that the gauge-boson contribution can be computed perturbatively and that the expansion of the nucleation EFT is well-behaved. The power-counting scheme consistent with Eq. (4.7) is:

$$m_3^2 \sim g^3T^2, \qquad \lambda_3 \sim g^3T. \tag{4.8}$$

When the Wilson coefficient c_{ϕ^6} is large enough to contribute at the same order as the gauge-boson cubic term, an additional ϕ^6 term enters the LO scalar potential that gov-

[1] The c_{ϕ^8} term could also be generated by $\bar{c}_{\phi^6}^2$, which parametrically is $\sim g^4/T$.

erns the nucleation,

$$V(\phi) = \frac{m_3^2}{2}\phi^2 - \frac{g_3^3}{16\pi}\phi^3 + \frac{\lambda_3}{4}\phi^4 + \frac{c_{\phi^6}}{8}\phi^6\,, \tag{4.9}$$

in which case λ_3 is allowed to be negative, for positive c_{ϕ^6}. This leads to the following relation between the BSM and the SM couplings:

$$\tilde{g}^2 \sim g^{1.5}\frac{\Lambda}{T}. \tag{4.10}$$

Crucially, the Higgs-field dynamics is at the supersoft scale $m_3 \sim g^{3/2}T$ [217, 218], hence the relevant dynamical degrees of freedom consist of the scalar field Φ and spatial vector W_i modes, as temporal vector modes W_0 are heavy ($\sim gT$) and are integrated out; the dimensionally reduced theory describing the nucleation is of the form of Eq. (4.1), but without operators containing temporal components of the gauge fields.

IV.2.3 Radiative symmetry breaking

A third qualitatively distinct possibility is radiative symmetry breaking via the Coleman-Weinberg mechanism [135]: the tree-level $T = 0$ potential contains no spontaneous symmetry breaking, but a broken minimum is generated entirely by loop corrections.

At zero temperature this requires the quartic coupling to be very small, $\lambda \sim g^4$ [146, 219], so that gauge-boson loop corrections dominate and drive symmetry breaking; this happens, for instance, within classically conformal models where such a suppressed quartic arises naturally [122, 220].

At finite temperature the radiative symmetry breaking scenario is more involved [217, 221]. Since the gauge bosons have masses of order the hard scale πT, they cannot be integrated out within the standard high-T expansion, and they have to be systematically integrated out together with the thermal fluctuations; in this hierarchy, the Higgs field nucleation occurs at the soft scale [214].

We note that the RG equations derived in this chapter are relevant to all barrier types discussed above, as they govern the scale dependence of the Wilson coefficients of Eq. (4.1) at and below the soft scale and are a necessary input for any precise perturbative or lattice calculation of phase-transition observables.

IV.3 Counterterms and beta functions

The main goal of this chapter is to renormalize the dimensionally reduced theory of Eq. (4.1) at the leading, two-loop order.

We work in dimensional regularization (dimReg) with spacetime dimension $d = 3 - 2\epsilon$. Working in 3D simplifies the calculations, compared to the 4D case. In particular:

- There are no logarithmic divergences at one loop, and therefore neither sub-divergences nor double poles in two-loop diagrams. Therefore, integrals can be IR regulated with a simple mass term, even in the presence of gauge fields.
- In 3D, the only divergent integral is

$$\int \frac{d^3q}{(2\pi)^3}\frac{d^3r}{(2\pi)^3}\frac{1}{(q^2+m_1^2)(r^2+m_2^2)((q+r)^2+m_3^2)} \underset{\text{dimReg}}{=} \frac{1}{64\pi^2\epsilon}+\frac{1}{16\pi^2}\left(\log\frac{\mu_{3D}}{m_1+m_2+m_3}+\frac{1}{2}\right)+\mathcal{O}(\epsilon)\,, \tag{4.11}$$

  with μ_{3D} being the renormalization scale. The general form of this integral in d dimensions can be found in Ref. [222].
- Contrary to the 4D case, the number of relevant redundant operators is significantly reduced (see Eq. (4.1)): all others that exist in 4D, e.g. $D^2\Phi^\dagger D^2\Phi$ and $D_r W^I_{rs}(\Phi^\dagger \overleftrightarrow{D_s}\sigma^I\Phi)$, are of higher energy dimension in 3D.
- In contrast to the 4D case, gauge and quartic couplings are dimensionful. This, together with the topological restriction $E = -2 + \sum_i (i-2)n_i$ — where n_i stands for the valence of a given vertex i and E is the number of external legs — significantly constrains the relevant diagrams contributing to the renormalization.

The last point is particularly useful to renormalize c_{ϕ^8} and $c_{\phi^6 W_0^2}$, since the number of two-loop diagrams with eight external legs is prohibitively large. For instance, ignoring W_0 interactions, the topological constraint restricts the possible combinations of couplings entering the RG equations of c_{ϕ^8} (with exactly one insertion of $c_{\phi^4D^2}, c_{\phi^8}, c_{\phi^2W^2}$) to: $c_{\phi^6}c_{\phi^8}$, $c_{\phi^4D^2}c_{\phi^6}^2$, $c_{\phi^4D^2}c_{\phi^6}g_3^4$, $c_{\phi^8}\lambda_3^2$, $c_{\phi^4D^2}\lambda_3^2 c_{\phi^6}$, $c_{\phi^4D^2}g_3^6\lambda_3$, $c_{\phi^4D^2}c_{\phi^6}g_3^2\lambda_3$, $c_{\phi^4D^2}g_3^2\lambda_3^3$, $c_{\phi^8}g_3^4$, $c_{\phi^4D^2}g_3^4c_{\phi^6}$, $c_{\phi^4D^2}c_{\phi^6}g_3^2\lambda_3$, $c_{\phi^4D^2}g_3^4\lambda_3^2$, $c_{\phi^4D^2}g_3^2\lambda_3^3$, $c_{\phi^2W^2}c_{\phi^6}\lambda_3 g_3^2$, $c_{\phi^2W^2}\lambda_3^3 g_3^2$, $c_{\phi^2W^2}\lambda_3^2 g_3^4$, $c_{\phi^2W^2}\lambda_3 g_3^6$, $c_{\phi^2W^2}\lambda_3 g_3^6$ and $c_{\phi^2W^2}g_3^8$; representative diagrams are shown

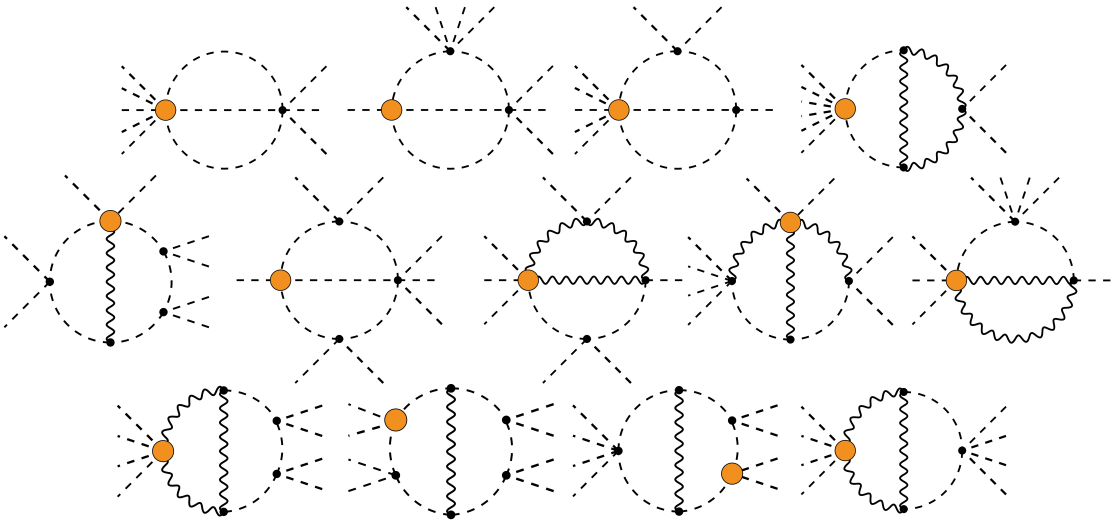

Figure 4.1: Example diagrams for the renormalization of c_{ϕ^8}. Orange blobs represent effective operators of dimension four of Eq. (4.1), while black dots stand for renormalizable gauge, quartic and sextic scalar couplings.

in Fig. 4.1. However, only the first two combinations result in the correct energy dimension, hence contributing to the c_{ϕ^8} running.[2]

Taking into account these considerations, we proceed by generating Feynman rules with `FeynRules` [223] and performing a suitable rotation to Euclidean space. Subsequently, we evaluate two-loop n-point off-shell functions employing the background-field method [137], using `FeynArts` [224] and `FeynCalc` [225], and expand the relevant two-loop integrals in the UV region, yielding the integrals of the form of Eq. (4.11).

Tree-level barrier

As discussed in Section IV.2, in case of the tree-level barrier presence, the nucleation of the scalar Higgs field occurs at the soft scale, where dynamical degrees of freedom are $\{\Phi, W_i, W_0\}$, hence all of the operators in Eq. (4.1) are relevant for the renormalization. The calculation of the counterterms, as outlined above, results in the following two-loop counterterms in Feynman gauge in the $\overline{\text{MS}}$ subtraction scheme:

[2] This argument can be further refined in fewer words. The coefficient c_{ϕ^8} can be only renormalized by loops involving effective operators, so either including c_{ϕ^8} itself, $c_{\phi^4 D^2}$ or $c_{\phi^2 W^2}$. The last one comes necessarily with powers of g_3, as it includes a gauge boson in the loop, which increases the total energy dimension. We therefore end up with only $c_{\phi^8} c_{\phi^6}$ and $c_{\phi^4 D^2} c_{\phi^6}^2$.

$$
\begin{aligned}
I_2^{-1}\delta Z_\phi &= 2c_{\phi^2W^2}g_3^2 + c^{(1)}_{\phi^4D^2}\left(5g_3^2 - 8\lambda_3\right) - c^{(2)}_{\phi^4D^2}\left(\frac{3}{2}g_3^2 - 2\lambda_3\right) \\
&\quad - 2c^{(1)}_{\phi^2W_0^2D^2}\lambda_{\phi^2W_0^2} + 4c^{(2)}_{\phi^2W_0^2D^2}g_3^2 \\
I_2^{-1}\delta m_3^2 &= -\frac{39}{16}g_3^4 - 9g_3^2\lambda_3 + 12\lambda_3^2 - 12g_3^2\lambda_{\phi^2W_0^2} + 6\lambda^2_{\phi^2W_0^2} \\
&\quad - m_3^2\Bigg[18c_{\phi^2W^2}g_3^2 + c^{(1)}_{\phi^4D^2}\left(9g_3^2 - 24\lambda_3\right) \\
&\quad - c^{(2)}_{\phi^4D^2}\left(\frac{3}{2}g_3^2 - 6\lambda_3\right) - 6c^{(1)}_{\phi^2W_0^2D^2}\lambda_{\phi^2W_0^2}\Bigg] \\
&\quad + m_D^2\left[-24c_{\phi^2W^2}g_3^2 + 12c^{(1)}_{\phi^2W_0^2D^2}\left(g_3^2 - \lambda_{\phi^2W_0^2}\right) - 12c^{(2)}_{\phi^2W_0^2D^2}g_3^2\right],
\end{aligned}
\tag{4.12}
$$

where we have factored out $I_2^{-1} = 64\pi^2\epsilon$ – the two-loop $\overline{\text{MS}}$ ϵ-pole of Eq. (4.11). For brevity, we only explicitly show counterterms associated with the Higgs mass operator and the Higgs field-strength renormalization; the rest of the counterterms are given in Appendix A.

We proceed by canonically normalizing the kinetic terms of the scalar and gauge fields and removing the redundant operators $\mathcal{O}^{(3)}_{\phi^4D^2}$, $\mathcal{O}^{(4)}_{\phi^2W_0^2D^2}$ and $\mathcal{O}^{(5)}_{\phi^2W_0^2D^2}$ (see Eq. (4.1)), by redefining $\Phi \to \Phi - \frac{1}{2}r^{(3)}_{\phi^4D^2}\Phi(\Phi^\dagger\Phi) + r^{(4)}_{\phi^2W_0^2D^2}\Phi W_0^I W_0^I$, $W_0^I \to W_0^I + r^{(5)}_{\phi^2W_0^2D^2}|\Phi|^2 W_0^I$. This results in the following shifts for the counterterms:

$$
\begin{aligned}
\delta m_3'^2 &= \delta m_3^2 - \delta Z_\phi m_3^2\,, \\
\delta m_D'^2 &= \delta m_D^2 - \delta Z_{W_0} m_D^2\,, \\
\delta\lambda_3' &= \delta\lambda_3 - 2\delta Z_\phi\lambda_3 - m_3^2\delta r^{(3)}_{\phi^4D^2}\,, \\
\delta\lambda'_{\phi^2W_0^2} &= \delta\lambda_{\phi^2W_0^2} - (\delta Z_\phi + \delta Z_{W_0})\lambda_{\phi^2W_0^2} + m_3^2\delta r^{(4)}_{\phi^2W_0^2D^2} + m_D^2\delta r^{(5)}_{\phi^2W_0^2D^2}\,, \\
\delta\lambda'_{W_0^4} &= \delta\lambda_{W_0^4} - 2\delta Z_{W_0}\lambda_{W_0^4}, \\
\delta c'_{\phi^6} &= \delta c_{\phi^6} - 3\delta Z_\phi c_{\phi^6} - 2\lambda_3\delta r^{(3)}_{\phi^4D^2}\,, \\
\delta c'_{\phi^2W_0^4} &= \delta c_{\phi^2W_0^4} - (\delta Z_\phi + 2\delta Z_{W_0})c_{\phi^2W_0^4} + 2\lambda_{\phi^2W_0^2}\delta r^{(4)}_{\phi^2W_0^2D^2} + 4\lambda_{W_0^4}\delta r^{(5)}_{\phi^2W_0^2D^2}\,, \\
\delta c^{(1)\prime}_{\phi^4W_0^2} &= \delta c^{(1)}_{\phi^4W_0^2} - (2\delta Z_\phi + \delta Z_{W_0})c^{(1)}_{\phi^4W_0^2} + 4\lambda_3\delta r^{(4)}_{\phi^2W_0^2D^2} + 2\lambda_{\phi^2W_0^2}\delta r^{(5)}_{\phi^2W_0^2D^2}\,, \\
\delta c^{(2)\prime}_{\phi^4W_0^2} &= \delta c^{(2)}_{\phi^4W_0^2} - (2\delta Z_\phi + \delta Z_{W_0})c^{(2)}_{\phi^4W_0^2}\,, \\
\delta c'_{W_0^6} &= \delta c_{W_0^6} - 3\delta Z_{W_0}c_{W_0^6}\,, \\
\delta c^{(1)\prime}_{\phi^4D^2} &= \delta c^{(1)}_{\phi^4D^2} + \frac{1}{2}\delta r^{(3)}_{\phi^4D^2}\,, \\
\delta c^{(2)\prime}_{\phi^4D^2} &= \delta c^{(2)}_{\phi^4D^2}\,,
\end{aligned}
\tag{4.13}
$$

$$
\begin{aligned}
\delta c'_{\phi^8} &= \delta c_{\phi^8} - 3 c_{\phi^6} \delta r^{(3)}_{\phi^4 D^2} \,, \\
\delta c'_{\phi^2 W^2} &= \delta c_{\phi^2 W^2} \,, \\
\delta c^{(1)\prime}_{\phi^6 W_0^2} &= \delta c^{(1)}_{\phi^6 W_0^2} + 2 c^{(1)}_{\phi^4 W_0^2} \delta r^{(5)}_{\phi^2 W_0^2 D^2} + 6 c_{\phi^6} \delta r^{(4)}_{\phi^2 W_0^2 D^2} \,, \\
\delta c^{(2)\prime}_{\phi^6 W_0^2} &= \delta c^{(2)}_{\phi^6 W_0^2} + 2 c^{(2)}_{\phi^4 W_0^2} \delta r^{(5)}_{\phi^2 W_0^2 D^2} \,, \\
\delta c^{(1),(2),\prime}_{\phi^2 W_0^2 D^2} &= \delta c^{(1),(2)}_{\phi^2 W_0^2 D^2} \,,
\end{aligned}
$$

in which we only kept counterterms with up to one insertion of dimension-four operators.

Following these shifts, the running of the $\overline{\text{MS}}$ parameters is determined simply by [226]:

$$
\beta_c \equiv 16\pi^2 \mu \frac{dc}{d\mu} = 64\pi^2 \epsilon \delta c \,, \tag{4.14}
$$

and for the effective couplings under scope, reads:

$$
\begin{aligned}
\beta_{m_3^2} = & \overbrace{-\frac{39}{16} g_3^4 - 9 g_3^2 \lambda_3 + 12 \lambda_3^2 - 12 g_3^2 \lambda_{\phi^2 W_0^2} + 6 \lambda^2_{\phi^2 W_0^2}}^{\beta^{\text{LO}}_{m_3^2}} \\
& - m_3^2 \Big[20 c_{\phi^2 W^2} g_3^2 + c^{(1)}_{\phi^4 D^2} \left(14 g_3^2 - 32 \lambda_3 \right) - c^{(2)}_{\phi^4 D^2} \left(3 g_3^2 - 8 \lambda_3 \right) \\
& - 8 c^{(1)}_{\phi^2 W_0^2 D^2} \lambda_{\phi^2 W_0^2} + 4 c^{(2)}_{\phi^2 W_0^2 D^2} g_3^2 \Big] \\
& + m_D^2 \Big[-24 c_{\phi^2 W^2} g_3^2 + 12 c^{(1)}_{\phi^2 W_0^2 D^2} \left(g_3^2 - \lambda_{\phi^2 W_0^2} \right) - 12 c^{(2)}_{\phi^2 W_0^2 D^2} g_3^2 \Big] \,,
\end{aligned} \tag{4.15}
$$

The first line of $\beta_{m_3^2}$ in Eq. (4.15) is the exact running of the mass parameter, m_3^2, if we were to truncate the 3D Lagrangian in Eq. (4.1) to only include super-renormalizable operators [49], while the rest of the running is triggered by the presence of other effective couplings, corresponding to the higher-dimensional operators. The quartic, λ_3, and the sextic, c_{ϕ^6}, scalar operators get renormalized starting with the inclusion of the dimension-three operators.

The remaining beta functions for the effective couplings are provided in Appendix A, for conciseness.

We remark that, in the physical basis, none of the effective couplings in the class $c_{\phi^4 D^2}$, nor $c_{\phi^2 W_0^2 D^2}$ run at the two-loop level with up to one insertion of the dimension-four

operators. This can be understood as a consequence of the topology of the relevant diagrams (which are themselves a consequence of the energy dimensions of the effective coefficients) that result in divergent contributions, relevant for renormalization, proportional to p^2 (p — external momentum for the relevant process), which, in our choice of basis, will always be captured by redundant operators that are reduced to higher-dimensional operators.

As a cross-check, we have verified that the running of m_3^2, λ_3, c_{ϕ^6}, and c_{ϕ^8} in Eq. (4.15), neglecting operators with derivatives, precisely reproduces the logarithmic dependence, $\log(\mu_{3D})$, of the two-loop effective potential, V_2^{3D} (see Section III.2), explicitly showing the better control of the renormalization-scale dependence allowed by the derived RGEs.

The significance of the running of the effective parameters can be estimated based on the power counting introduced in Section IV.2; in case of the tree-level barrier presence, the running of the effective couplings is parametrically given by:

$$\begin{aligned}
\frac{\partial \log m_3^2}{\partial \log \mu_{3D}} &\sim \overbrace{g^2}^{\text{LO}} + g^3 \frac{T}{\Lambda}\,, \\
\frac{\partial \log \lambda_3}{\partial \log \mu_{3D}} &\sim \frac{\partial \log c_{\phi^6}}{\partial \log \mu_{3D}} \sim \frac{\partial \log c_{\phi^8}}{\partial \log \mu_{3D}} \sim g^2\,, \\
\frac{\partial \log g_3^2}{\partial \log \mu_{3D}} &\sim g^5 \frac{T}{\Lambda}\,.
\end{aligned} \tag{4.16}$$

It indicates that the LO m_3^2 running — triggered by the super-renormalizable operators — is parametrically of the same order as the quartic, sextic and octic running.

To illustrate how these couplings run, we estimate the values of the Wilson coefficients according to Eq. (4.2) and assume $g = 0.1$, $\Lambda = 1\,\text{TeV}$ and $T = 100\,\text{GeV}$. Moreover, for simplicity, through this section, we assume that $\lambda_{\phi^2 W_0^2} = g_3^2/4$, which holds up to higher-order corrections [49]. We numerically solve the coupled RG equations and present the benchmark running from the hard scale ($2\pi T$) down to μ_{3D} in Fig. 4.2.

As evident from Fig. 4.2, the effective operators trigger the running of λ_3, c_{ϕ^6}, resulting in changes of their values at the level of ten percent, while the correction due to next-to-leading order (NLO) m_3^2 running is on a percent level. Notably, for the chosen benchmark points, c_{ϕ^8} changes significantly, flipping its sign as it evolves towards small scales; the running of c_{ϕ^8} is additionally enhanced by large numerical values in its beta function compared to the estimate in Eq. (4.16). Although we present only two reference benchmark points, we find that this behavior is universal within the parameter space cor-

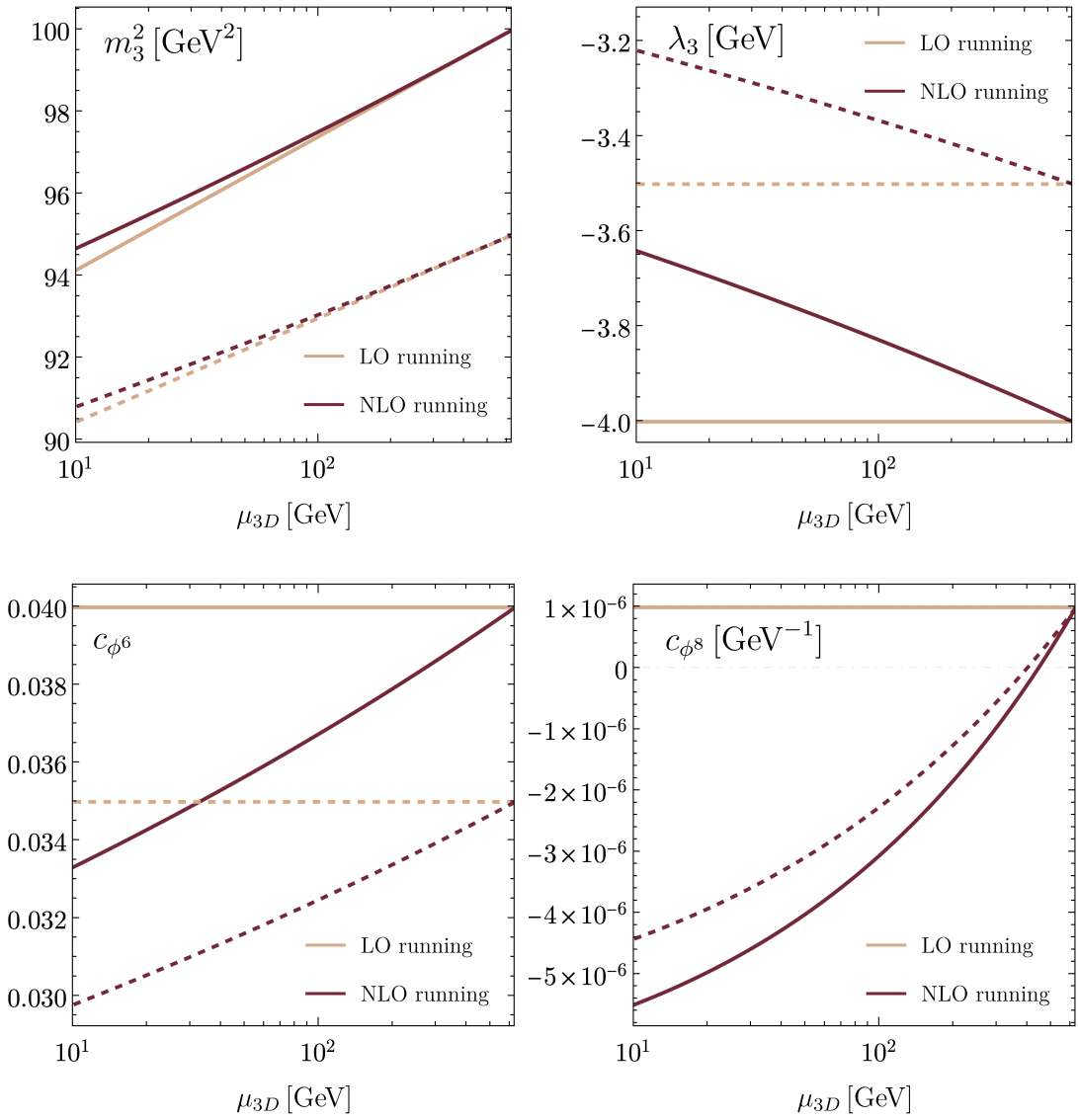

Figure 4.2: Running of the effective couplings m_3^2, λ_3, c_{ϕ^6} and c_{ϕ^8} from the hard scale $2\pi T$ down to μ_{3D}. We assume $T = 100\,\text{GeV}$, and take the effective couplings $\{m_3^2, m_D^2, \lambda_3, \lambda_{W_0^4}, c_{\phi^6}, c_{\phi^4 D^2}^{(1)}, c_{\phi^4 D^2}^{(2)}, c_{\phi^8}, g_3^2\}$ to be $\{100, 100, -4, 0.01, 0.04, 10^{-4}, 10^{-4}, 10^{-6}, 2\}$ (solid) and $\{95, 100, -3.5, 0.01, 0.035, 10^{-4}, 10^{-4}, -10^{-6}, 2\}$ (dashed) with all values given in GeV at the hard scale, with the rest of effective coupling taken to be zero.

responding to tree-level barrier nucleation, except for cases where tree-level-enhanced dimension-four operators are present.

Next, we assess the numerical relevance of the NLO correction to the running of the mass parameter, m_3^2. In Fig. 4.3, we plot the relative correction to the m_3^2 beta function from the effective couplings, by defining $\beta_{m_3^2}^{\text{LO}}$ — super-renormalizable part of m_3^2 running — and

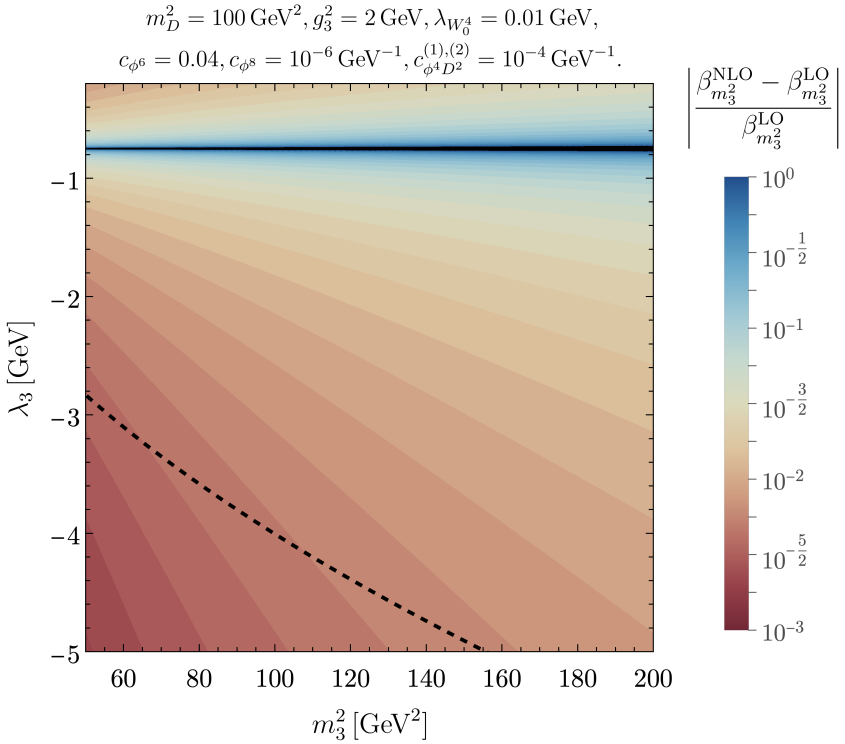

Figure 4.3: Relative correction to the m_3^2 beta function from the effective operators. The black dashed line denotes the parameter values for which two minima of the scalar potential are degenerate.

$\beta_{m_3^2}^{\mathrm{NLO}}$ — full two-loop running of m_3^2 — per Eq. (4.15). The black dashed line represents the values of the parameters for which two local minima of the potential become degenerate in energy (this corresponds to T being the critical temperature); therefore, below this line, the broken minimum is the global minimum of the scalar potential. The relative correction to the m_3^2 running is small (typically on a percent level) for the wide range of parameter space; however, in the vicinity of the region given by $\lambda_3 = -3g_3^2/8$ (taking $\lambda_{\phi^2 W_0^2} = g_3^2/4$ as discussed above), where the LO running vanishes, i.e. where $\beta_{m_3^2}^{\mathrm{LO}} = 0$), corrections from the effective operators to the beta function become dominant.

Radiatively generated barrier

For sufficiently large gauge coupling within the dimensionally reduced theory, a barrier can be radiatively generated, which enables a SFOEWPT.

In this scenario, the nucleation of the scalar Higgs field occurs below the soft scale [214, 218]; consequently, the relevant dynamical degrees of freedom are $\{\Phi, W_i\}$ and the dimensionally reduced theory describing the nucleation is of the form of Eq. (4.1), but

without dynamical temporal components of the gauge fields (namely, only operators of the first three lines of Eq. (4.1) are relevant). Following the same steps as in the case of a tree-level barrier, we determine the counterterms for the theory under scope, which read:

$$\begin{aligned} I_2^{-1}\delta Z_\phi &= 2c_{\phi^2W^2}g_3^2 + c^{(1)}_{\phi^4D^2}\left(5g_3^2 - 8\lambda_3\right) - c^{(2)}_{\phi^4D^2}\left(\frac{3}{2}g_3^2 - 2\lambda_3\right) , \\ I_2^{-1}\delta m_3^2 &= -\frac{51}{16}g_3^4 - 9g_3^2\lambda_3 + 12\lambda_3^2 \\ &\quad - m_3^2\left[18c_{\phi^2W^2}g_3^2 + c^{(1)}_{\phi^4D^2}\left(9g_3^2 - 24\lambda_3\right) - c^{(2)}_{\phi^4D^2}\left(\frac{3}{2}g_3^2 - 6\lambda_3\right)\right] . \end{aligned} \tag{4.17}$$

In order to canonically normalize the fields and remove the redundant operator, we perform the shifts between the counterterms

$$\begin{aligned} \delta m_3'^2 &= \delta m_3^2 - \delta Z_\phi m_3^2 , \\ \delta\lambda_3' &= \delta\lambda_3 - 2\delta Z_\phi\lambda_3 - m_3^2\delta r^{(3)}_{\phi^4D^2} , \\ \delta c'_{\phi^6} &= \delta c_{\phi^6} - 3\delta Z_\phi c_{\phi^6} - 2\lambda_3\delta r^{(3)}_{\phi^4D^2} , \\ \delta c'^{(1)}_{\phi^4D^2} &= \delta c^{(1)}_{\phi^4D^2} - 2\delta Z_\phi c^{(1)}_{\phi^4D^2} + \frac{1}{2}\delta r^{(3)}_{\phi^4D^2} , \\ \delta c'^{(2)}_{\phi^4D^2} &= \delta c^{(2)}_{\phi^4D^2} - 2\delta Z_\phi c^{(2)}_{\phi^4D^2} , \\ \delta c'_{\phi^8} &= \delta c_{\phi^8} - 4\delta Z_\phi c_{\phi^8} - 3c_{\phi^6}\delta r^{(3)}_{\phi^4D^2} , \\ \delta c'_{\phi^2W^2} &= \delta c_{\phi^2W^2} - \delta Z_\phi c_{\phi^2W^2} - \delta Z_W c_{\phi^2W^2} . \end{aligned} \tag{4.18}$$

and compute the corresponding beta functions for the effective couplings, by employing Eq. (4.14), which results in:

$$\begin{aligned} \beta_{m_3^2} &= \overbrace{-\frac{51}{16}g_3^4 - 9g_3^2\lambda_3 + 12\lambda_3^2}^{\beta^{\rm LO}_{m_3^2}} \\ &\quad + m_3^2\left[c^{(1)}_{\phi^4D^2}\left(-14g_3^2 + 32\lambda_3\right) + c^{(2)}_{\phi^4D^2}\left(3g_3^2 - 8\lambda_3\right) - 20c_{\phi^2W^2}g_3^2\right] . \end{aligned} \tag{4.19}$$

The full set of counterterms and beta functions for the dimensionally reduced theory below the soft scale is presented in Appendix A.

We estimate the size of the running of effective couplings, employing the power counting

relevant for the radiatively generated barrier scenario (see Section IV.2), which reads:

$$\begin{aligned}
\frac{\partial \log m_3^2}{\partial \log \mu_{3D}} &\sim \overbrace{g^1}^{\text{LO}} + g^{3.5}\frac{T}{\Lambda}\,, \\
\frac{\partial \log \lambda_3}{\partial \log \mu_{3D}} &\sim g^2, \\
\frac{\partial \log c_{\phi^6}}{\partial \log \mu_{3D}} &\sim \frac{\partial \log c_{\phi^8}}{\partial \log \mu_{3D}} \sim g^3\,, \\
\frac{\partial \log g_3^2}{\partial \log \mu_{3D}} &\sim g^{5.5}\frac{T}{\Lambda}\,,
\end{aligned} \tag{4.20}$$

and notice that in the case of the radiatively generated barrier, the running of λ_3 and c_{ϕ^6}, triggered by operators beyond the super-renormalizable ones, is parametrically suppressed with respect to the LO running of m_3^2, in contrast to the case of the tree-level barrier (see Eq. (4.16)). The NLO running becomes less significant, once c_{ϕ^6} is not assumed to be enhanced.

IV.4 Impact on the scalar potential

Next, we investigate the impact of the running of the effective parameters on the shape of the scalar potential and the predictions for the phase-transition phenomenology. Focusing on the case of the tree-level barrier, we compare the scalar potential with and without the inclusion of the running of the effective parameters, as well as the shift in the position of the broken minimum and the potential difference between two local minima.

In Fig. 4.4, the shape of the scalar potential is shown with and without the inclusion of the running of the effective parameters. As evident from the figure, contributions from the effective couplings can substantially alter the shape of the scalar potential and shift the position of the broken minimum. The main difference between including only the LO mass running and the NLO running with effective operators arises from the running of the quartic and sextic scalar couplings, λ_3 and c_{ϕ^6}, respectively; additional terms in the mass parameter running have only a minor effect on the scalar potential. It is worth recalling that the inclusion of the running to the scalar potential can be seen as resumming higher effective potential loops.

We further investigate the impact of the running by studying the shift in the broken minimum field value $v = \phi_{\text{min}}$. This is a key parameter, since the ratio $\xi = v/T$ charac-

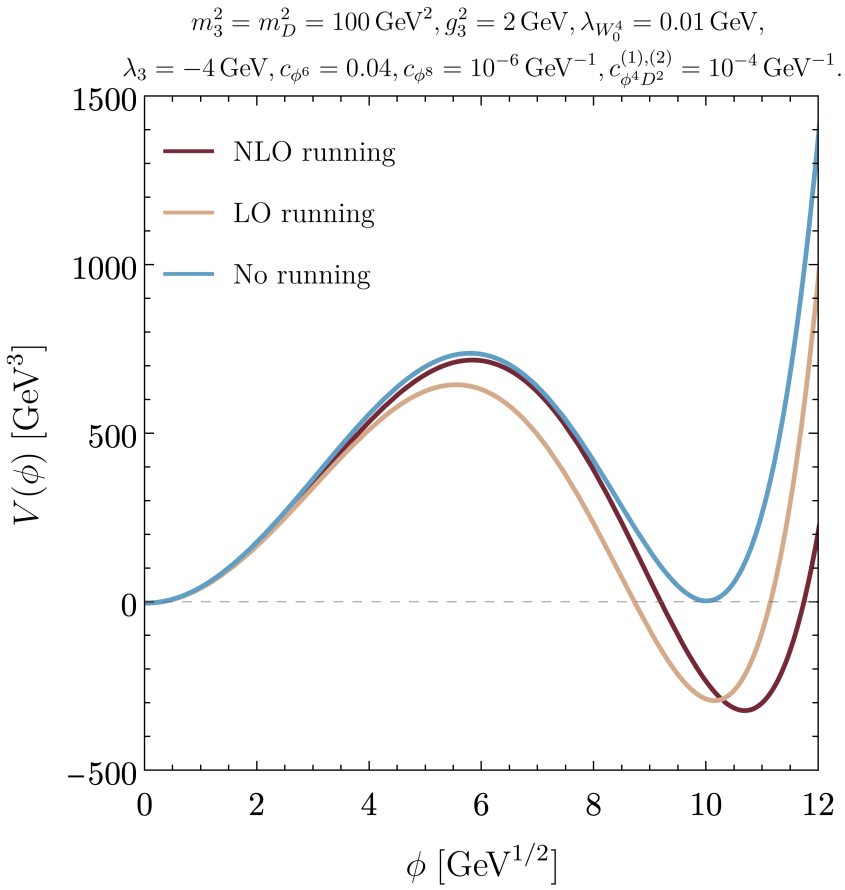

Figure 4.4: Scalar potential $V(\phi)$ without running, with LO running, and with NLO running of the effective couplings. Parameters run from $2\pi T$ down to gT, with $g = 0.1$ and $T = 100$ GeV.

terizes the baryon washout during the baryogenesis at the first-order EWPT [148], also see discussion in Section III.5.

In Fig. 4.5, the shift in this quantity caused by including the running of the effective parameters is illustrated. The *left* (*right*) panel shows the shift when only the LO running of the mass parameter (NLO running of all operators) is taken into account. Including the NLO running of the effective parameters can alter the broken field value by tens of percent, while the LO running (where only m_3^2 runs) produces a much smaller shift, at the few-percent level. The difference between LO and NLO running becomes even more prominent with the increase of the effective couplings, e.g. $c_{\phi^4 D^2}$.

As before, the black-dashed line in Fig. 4.5 represents the parameter values for which the broken and unbroken minima are degenerate. Below this line, the broken minimum becomes the global minimum, and it is within this region that the nucleation occurs; hence, it is of the main interest to the EWPT phenomenology. In this region, the LO

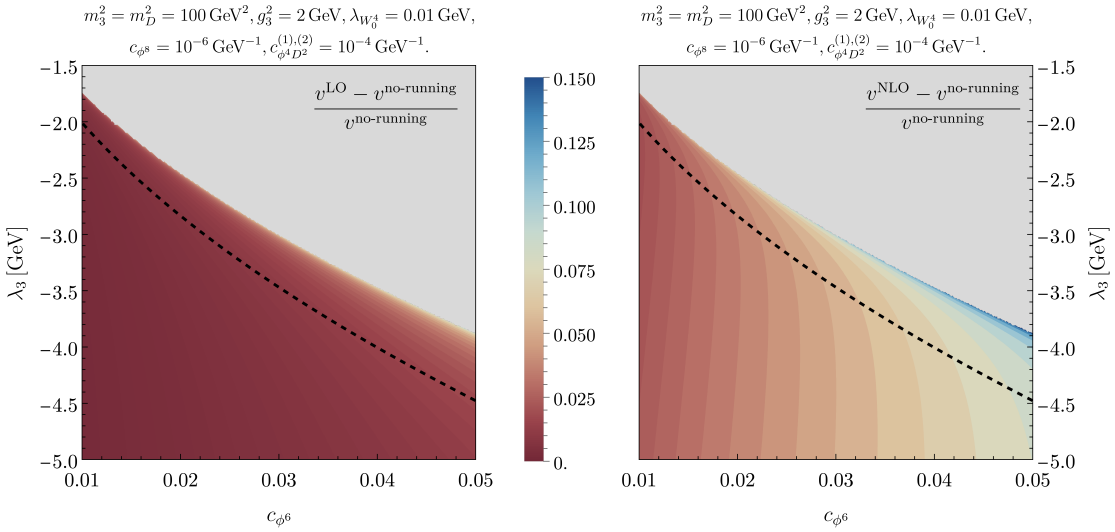

Figure 4.5: Relative change of the position of the broken minimum of the scalar potential (v) with the inclusion of the LO mass parameter running only *(left)* and NLO running of the effective parameters *(right)*. Parameters run from $2\pi T$ down to gT, with $g = 0.1$ and $T = 100$ GeV. Gray regions represent the parameter space where the broken minimum is absent in case no running is included. The black-dashed line denotes the parameter values for which two minima of the potential are degenerate in the absence of RG running.

running can only lead to a few percent shift to the broken minimum value, while the NLO running of the effective couplings could result in changes on the order of tens of percent, specifically for large values of the sextic coupling c_{ϕ^6}.

Similarly, the NLO correction to the running of the effective parameters affects the difference in the potential values between two local minima, which in turn determines the strength of the EWPT. In Fig. 4.6, we present the relative change in the potential difference ΔV between the unbroken and broken minima when comparing the inclusion of LO and NLO running of the effective parameters. As can be seen from the figure, the potential difference can change by up to tens of percent, depending on the specific parameter point, therefore modifying the strength of the EWPT. The blue diagonal region simply points to the values of the couplings where ΔV^{LO} crosses zero value, while $\Delta V^{\mathrm{LO}} = \Delta V^{\mathrm{NLO}}$ holds in the dark red region. We note that for points where two local minima are of similar depth, the NLO corrections lift the broken minima, while for points where the broken minimum is significantly deeper than the unbroken, NLO corrections deepen it, resulting in stronger EWPTs.

For completeness, in Fig. 4.7, we present the effect of the running of the effective parameters on the nucleation temperature T_n and the strength of the EWPT α, see Section III.5

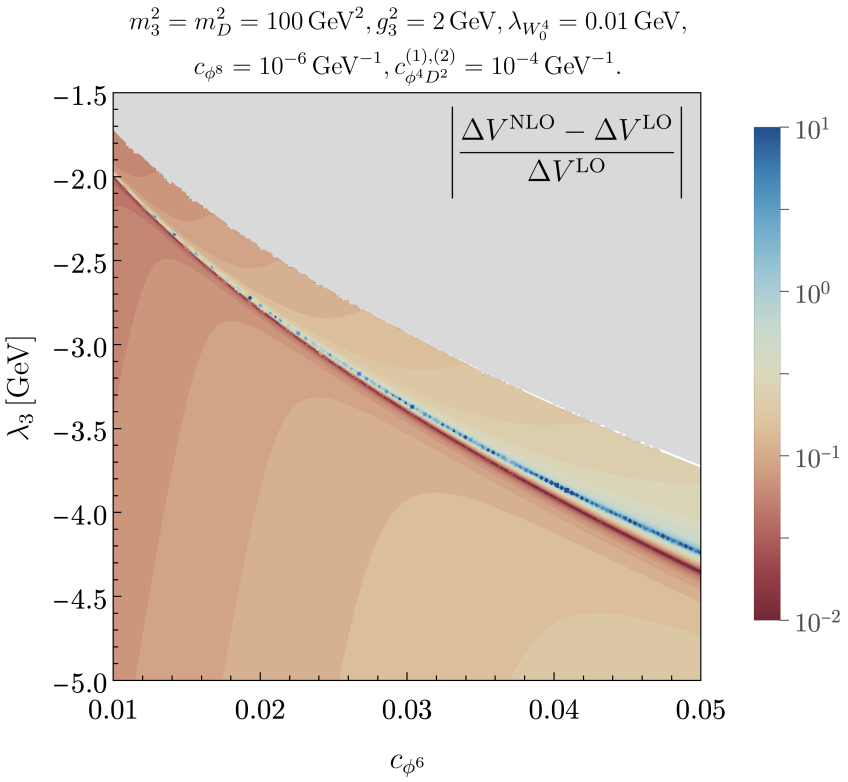

Figure 4.6: Relative shift of the potential difference ΔV between unbroken and broken minima between cases of inclusion of LO and NLO running of the effective parameters. Parameters run from $2\pi T$ down to gT, with $g = 0.1$ and $T = 100$ GeV. The gray region represents the parameter space where the broken minimum is absent in case the NLO running is included.

for definitions. For this purpose, we perform LO DR of the SMEFT [36], schematically depicted in Eq. (4.2), taking $g' = 0$ and assuming the presence of the $\bar{c}_{\phi^6}, \bar{c}_{\phi^4 D^2}, \bar{c}_{\phi^8}$ couplings in the UV at $\Lambda = 1\,\mathrm{TeV}$ with sizes according to Eq. (4.2). We obtain T_n by employing `FindBounce` [173] for the calculation of the bounce action Eq. (3.82).

As outlined above, the inclusion of the NLO running of the effective parameters in the 3D EFT changes the EWPT strength as much as LO running (around 5-10% for the example in scope). To illustrate dependence on the specific values of the BSM couplings, we also show the case where $\bar{c}_{\phi^4 D^2}^{(1)}$ is taken negative (dashed line in Fig. 4.7). It should be noted that the precise value of the shift of the EWPT strength with the inclusion of the NLO running is highly sensitive to the precise values of the beyond-SM couplings.

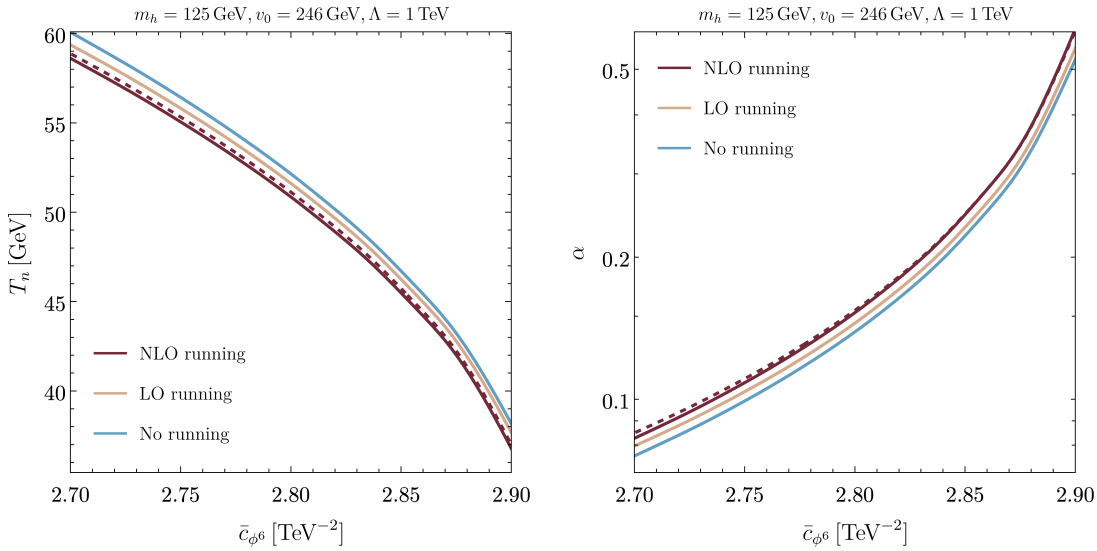

Figure 4.7: Nucleation temperature *(left)* and phase-transition strength α *(right)* determined without and with the running of the effective parameters from the hard thermal scale $2\pi T$ down to m_3 scale. The dashed line with NLO running corresponds to taking $\bar{c}^{(1)}_{\phi^4 D^2}$ to be negative.

IV.5 Discussion and relevance for lattice simulations

In this chapter, we have computed the leading corrections to the RG running of Wilson coefficients up to energy dimension four in the 3D EFT that describes the static high-temperature limit of BSM theories with heavy new physics.

The computation, which involves evaluating two-loop diagrams with up to eight external legs, is considerably simplified by the energy scaling of parameters in 3D, the absence of sub-divergences, and the small number of divergent integrals in dimensional regularization.

We remark that just including the renormalizable sextic scalar interaction — which has not been addressed before — triggers running of the quartic and sextic operators at the leading, two-loop order.

To briefly explore phenomenological implications, we focus on two cases of Higgs-field nucleation: one occurring at the soft scale, where the temporal vector modes are dynamical, and one below the soft scale, where the temporal vector modes are integrated out. In the first case, a reference example of which is the tree-level nucleation, where the enhanced sextic Higgs coupling triggers the EWPT, we have found that the NLO beta function for m_3^2 typically modifies the LO result at the percent level, though the

correction can become arbitrarily large near $\lambda_3 \approx -0.375 g_3^2$, where the LO running vanishes. The impact on the scalar potential is even more pronounced (essentially, because the running of four-, six- and eight-Higgs scalar operators is parametrically of the same order as the LO running of m_3^2). For instance, while the relative shift of the broken minimum due to super-renormalizable running is at the percent level, including the NLO running increases this by more than an order of magnitude. The shift on the energy difference between the broken and unbroken minima can also be modified by up to tens of percent, compared to the LO running, resulting in a change in the strength of the EWPT.

In the second case — nucleation below the soft scale, for example, via a radiatively generated barrier — we find that the beyond-super-renormalizable running is subleading, reflected in smaller modifications of the potential.

The counterterms for the effective operators presented in this chapter (presented in full in Appendix A) are also of direct use for future lattice simulations of the 3D EFT. In lattice simulation, counterterms are essential for relating lattice and continuum parameters [227]. Beyond our $\overline{\text{MS}}$ running, divergences in the lattice regularization scheme need to be studied when extending the 3D EFT. In the super-renormalizable case present in the literature [227, 228], only the mass counterterm is linearly divergent (in the lattice regularization). However, we find that considering the renormalizable interaction c_{ϕ^6} results in a one-loop linearly divergent counterterm for the Higgs quartic (absent in dimensional regularization), $\delta\lambda_3^L = -12\Sigma c_{\phi^6}$, where $\Sigma = 0.252731/a$ with a the lattice spacing. When accounting for higher-dimensional operators, the situation becomes more complex and as such, the full analysis of these divergences on the lattice is left for future work. We highlight that even the inclusion of the c_{ϕ^6} operator on the lattice will enable non-perturbative studies of the phase transitions with a tree-level barrier, which are currently inaccessible with the super-renormalizable 3D EFT (for SMEFT-like theories).

Altogether, the results presented in this chapter enable more accurate determinations of cosmological phase-transition parameters — and consequently of the resulting GW spectra — both within perturbation theory and in lattice simulations. In certain regions of parameter space, these corrections become quantitatively indispensable.

A natural direction for future work is the identification and analysis of UV completions that match onto the SMEFT featuring a SFOEWPT, with the goal of characterizing the underlying microscopic theories that can generate the effective couplings required to

realize the phase-transition patterns studied in this chapter.

The analysis of the running of the effective couplings in the dimensionally reduced EFT can be further extended by incorporating BSM particles within the EFT framework. For example, the inclusion of an additional singlet scalar (discussed in Chapter V) would allow for a richer thermal phase transition phenomenology; within the parameter space where the beyond-super-renormalizable operators are phenomenologically relevant, the running of the effective couplings can be expected to have a more significant impact on the EWPT phenomenology.

V – PERTURBATIVE DESCRIPTION OF THE EWPT IN THE CXSM

Everything is vague to a degree you do not realize till you have tried to make it precise.

— Bertrand Russell

While non-perturbative methods and lattice field theory provide reliable and precise descriptions of phase transitions, their computational cost prohibits comprehensive scans over large parameter spaces of BSM theories. This necessitates the development of reliable perturbative methods for detailed studies of phase transition dynamics and their phenomenological consequences. The perturbative approaches developed in the literature can be divided into two main categories — see Chapter III for the discussion of the theoretical framework and methods employed in this chapter — the traditional 4D approach and the dimensionally reduced 3D approach.

The 4D approach incorporates temperature and quantum corrections to the effective potential in the UV theory, typically employing thermal resummation techniques such as daisy resummation to improve the IR behavior [140]. Common resummation prescriptions include the Arnold–Espinosa approach [45], where only Matsubara zero modes are resummed, and the Parwani approach [191], where all bosonic modes receive thermal corrections (see Section III.4.2). The "tadpole resummation" prescription systematically accounts for daisy and superdaisy diagrams by computing thermal masses from the gap equation [39, 40, 194, 229]. Additional recent developments include a method for constructing a resummed effective potential without the high-temperature expansion [230] and Optimized Perturbation Theory to reduce renormalization scale dependence [231].

The 4D approach offers a relatively simple implementation of the one-loop effective potential that captures leading thermal corrections and provides qualitatively correct de-

scriptions of phase transitions in many SM extensions. However, the 4D approach suffers from poor perturbative behavior at high temperature, leading to substantial renormalization scale and residual gauge dependencies in the predictions for physical observables. It also exhibits IR divergences and an unsystematic treatment of thermal fluctuations in transition rate calculations [41, 44], resulting in large theoretical uncertainties in predictions for GW signals from SFOEWPTs [32, 42, 43, 232].

The dimensionally reduced 3D approach [47, 189] systematically integrates out heavy modes to obtain a low-energy EFT in three spatial dimensions that captures the relevant IR dynamics of the phase transition — the construction of the 3D EFT is discussed in detail in Section III.4. Well-defined in the high-temperature limit, this method provides more accurate predictions than the 4D approach if the transition temperature is comparable to or larger than the masses of the scalar fields undergoing phase transition.

Both the 4D and 3D approaches exhibit residual gauge dependence in predictions for physical phase transition observables. The $\hbar$-expansion [148], which systematically expands physical quantities in powers of a loop-counting parameter, ensures gauge-independent results order by order in perturbation theory. At one-loop level in the 4D approach, the $\hbar$-expansion eliminates gauge dependence but yields results that often deviate substantially from more accurate predictions in many models [148]. Beyond one-loop accuracy, consistent implementation with thermal resummation procedures is required to obtain gauge-independent formulations at finite temperature [44, 233, 234].

In this chapter, we investigate the EWPT in the cxSM, which is particularly relevant given the absence of clear new physics signals at the LHC, as the cxSM can accommodate a SFOEWPT without producing detectable signatures at current or future LHC runs [235]. This makes GW probes of the SFOEWPT especially important, requiring precise predictions for transition parameters under rigorous theoretical control. While previous studies have examined the cxSM using the 4D approach [236–241] and the 3D approach [114], a comprehensive comparison of perturbative methods across the SFOEWPT parameter space and GW detection prospects remains to be performed. We determine the parameter space regions potentially observable by LISA, with emphasis on theoretical uncertainties: residual gauge dependence, and renormalization- and matching-scale dependencies. We compare the 4D and 3D approaches to assess their respective limitations in capturing transition dynamics, and test the validity of the 3D approach by including higher-dimensional operators in the EFT Lagrangian.

V.1 Possible realizations of the first-order EWPT within the cxSM

The model used for studying the phase transition dynamics in this chapter is the SM with an additional complex scalar gauge singlet (cxSM). The cxSM is one of the simplest SM extensions that can realize a SFOEWPT. This leads to a variety of phenomenologically interesting signatures, such as GW signals produced in the early Universe which would potentially be accessible at near-future space-based GW observatories. Moreover, the cxSM can include a stable neutral particle that could serve as a viable dark matter candidate. However, we will not discuss this feature in our analysis below.

The Lagrangian density of the model in Minkowski space can be written as

$$\mathcal{L}_{\text{cxSM}} = \mathcal{L}_{\text{SM}} + \mathcal{L}_S, \tag{5.1}$$

where $\mathcal{L}_{\text{SM}}$ is the SM Lagrangian — introduced in Section II.1 — and $\mathcal{L}_{\text{S}}$ is the Lagrangian for the singlet field S. Since only the doublet Φ is charged under the $SU(2)_L \times U(1)_Y$ gauge groups, the gauge and fermionic sectors of the cxSM are identical to the SM.

The scalar sector of the cxSM consists of the doublet Φ with hypercharge $Y = 1/2$ and a complex gauge singlet S,

$$\Phi = \begin{pmatrix} G^+ \\ \frac{1}{\sqrt{2}}\left(\phi_h + h + iG^0\right) \end{pmatrix}, \quad S = \frac{1}{\sqrt{2}}(\phi_s + s + iA)\,, \tag{5.2}$$

where we expanded the real part of the neutral component of Φ and the real part of the singlet field S around the background-field configurations ϕ_h and ϕ_s, respectively.

In this chapter, we focus on a specific subclass of the cxSM in which a global $U(1)$ symmetry is imposed on the gauge singlet S [242]. Then, the scalar part of the Lagrangian is given by

$$\begin{aligned} \mathcal{L}_\Phi + \mathcal{L}_S = {} & D_\mu \Phi^\dagger D^\mu \Phi - \mu_h^2 \Phi^\dagger \Phi - \lambda_h (\Phi^\dagger \Phi)^2 \\ & + |\partial^\mu S|^2 - \frac{1}{2}\mu_s^2 |S|^2 - \frac{1}{4}\lambda_s |S|^4 - \frac{1}{2}\lambda_{hs} |S|^2 \Phi^\dagger \Phi\,, \end{aligned} \tag{5.3}$$

see Section II.1 for the definition of the covariant derivative and gauge sector of the SM. If S does not obtain a vev, the global $U(1)$ symmetry is conserved.

The tree-level scalar potential as a function of the background fields ϕ_h and ϕ_s reads

$$V_0(\phi_h, \phi_s) = \frac{\mu_h^2}{2}\phi_h^2 + \frac{\mu_s^2}{4}\phi_s^2 + \frac{\lambda_h}{4}\phi_h^4 + \frac{\lambda_{hs}}{8}\phi_h^2\phi_s^2 + \frac{\lambda_s}{16}\phi_s^4. \tag{5.4}$$

This also serves as the lowest-order version of the effective potential at zero temperature. As explained in Section III.4.1, the scalar potential is modified by zero-temperature and thermal loop corrections, leading to a temperature dependence of the vacuum structure. The thermal evolution of the cxSM scalar-field configuration can follow two qualitatively distinct patterns depending on the model parameters [236, 242]. At sufficiently high temperatures the electroweak symmetry is restored and the effective potential has a unique minimum at the symmetric point $(\phi_h, \phi_s) = (0, 0)$. As the Universe cools, either a *one-step* transition occurs directly from the symmetric phase to an electroweak-breaking minimum, or a *two-step* transition proceeds via an intermediate phase in which a singlet condensate $\phi_{s,\text{min}} \neq 0$ develops first, followed by the EWPT at a lower temperature. In both cases, the final electroweak-breaking vacuum could in principle be a mixed state $(\phi_{h,\text{min}}, \phi_{s,\text{min}})$ with both fields acquiring vevs. In the $U(1)$-symmetric model, however, a non-zero singlet vev at zero temperature spontaneously breaks the global $U(1)$, producing a massless Goldstone boson, which is phenomenologically disfavored [242]. We therefore exclude this possibility by requiring $\phi_{s,\text{min}}(T = 0) = 0$, and focus on the two-step realization, which is the primary mechanism for a SFOEWPT in the $U(1)$-symmetric cxSM [236].

It is known that, unlike in the SM, as a consequence of the additional singlet the phase evolution of the cxSM can exhibit a SFOEWPT in certain regions of parameter space. In our study, we ensure that the tree-level potential is bounded from below by choosing $\lambda_h > 0$, $\lambda_s > 0$ and $\lambda_{hs} > -2\sqrt{\lambda_h\lambda_s}$. In order to accommodate a SFOEWPT, we concentrate on positive values for the portal coupling, $\lambda_{hs} > 0$ [236]. Moreover, we demand that only the Higgs field h has a non-zero vev at zero temperature:

$$\phi_{h,\text{min}}(T = 0) = v_{\text{EW}} \approx 246\ \text{GeV}\,, \quad \phi_{s,\text{min}}(T = 0) = 0\,. \tag{5.5}$$

Allowing for a non-zero singlet vev $\phi_{s,\text{min}}$ at finite temperature, the cxSM exhibits an EWPT of the form $(0, \phi_{s,\text{min}}(T)) \to (\phi_{h,\text{min}}(T), 0)$, where $\phi_{h,\text{min}}$ is the vev of the Higgs field (visualized in Fig. 5.1).[1]

In total, the cxSM has six scalar degrees of freedom: a CP-even scalar h from the real

[1] We find that direct minimization of the loop-improved effective potential can result in a small unphysical non-zero Higgs vev in the high-temperature phase. This is further discussed in Section III.2.2.

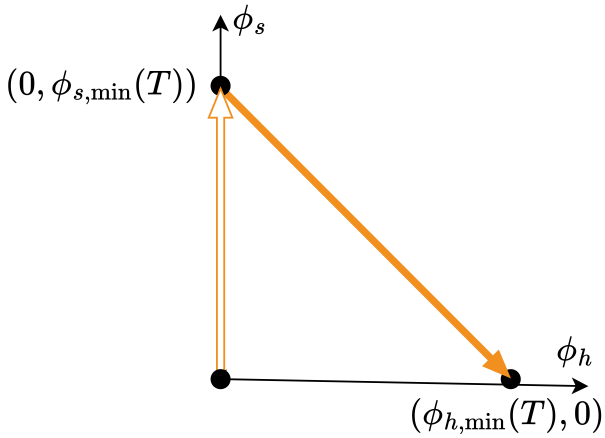

Figure 5.1: The pattern of a possible SFOEWPT in the cxSM model explored in this chapter. The arrow points in the direction of decreasing temperature.

part of the neutral component of Φ that can be identified with the detected Higgs boson at 125 GeV, three would-be Goldstone bosons $G_{0,\pm}$ from the CP-odd and the charged components of Φ, and two scalar degrees of freedom s and A from the real and imaginary parts of the singlet field S, respectively. As indicated above, we consider the case where at zero temperature only the Higgs field h has a vev, whereas the vev of the singlet field vanishes. At finite temperature we study first-order EWPTs from a $U(1)$-symmetry breaking phase in which the singlet field has a non-zero vev $\phi_{s,\min}$, into an electroweak symmetry breaking phase with a non-zero Higgs vev $\phi_{h,\min}$. We therefore consider the two background fields ϕ_h and ϕ_s: if both $\phi_h \neq 0$ and $\phi_s \neq 0$, the two CP-even fields h and s mix with each other, whereas the would-be Goldstone fields G_0 and $G^\pm$ and the other component of the singlet field A are mass eigenstates. The field-dependent mass matrix of the CP-even states h and s is given by

$$M_{hs}^2 = \begin{pmatrix} \mu_h^2 + 3\lambda_h\phi_h^2 + \frac{\lambda_{hs}\phi_s^2}{4} & \frac{\lambda_{hs}\phi_h\phi_s}{2} \\ \frac{\lambda_{hs}\phi_h\phi_s}{2} & \frac{\mu_s^2}{2} + \frac{3\lambda_s\phi_s^2}{4} + \frac{\lambda_{hs}\phi_h^2}{4} \end{pmatrix}. \tag{5.6}$$

The field-dependent mass of A is given by

$$M_A^2 = \frac{\mu_s^2}{2} + \frac{\lambda_s\phi_s^2}{4} + \frac{\lambda_{hs}\phi_h^2}{4}, \tag{5.7}$$

and for the would-be Goldstone bosons in the Landau gauge, we have

$$M_{G_{0,\pm}}^2 = \mu_h^2 + \lambda_h\phi_h^2 + \frac{\lambda_{hs}\phi_s^2}{4}. \tag{5.8}$$

Here, it should be noted that the Goldstone boson masses also receive contributions from

the gauge-fixing, which we do not display here. As addional scalar does not alter the gauge structure of the theory, the gauge-fixing contributions to the Goldstone and gauge boson masses are the same as in the SM Section III.2.2.

The cxSM has three free parameters in addition to the SM ones. We choose to treat the singlet mass m_s, the singlet quartic coupling λ_s and the portal coupling λ_{hs} as free parameters. For the SM sector, we use the Higgs boson mass m_h, the top quark mass m_t, the gauge boson masses m_W and m_Z, and the Fermi constant G_F as input parameters. Their numerical values are given in Section V.2, where we also show the tree-level relations between those input parameters and the Lagrangian parameters. We note that in notation in this chapter, a lowercase m_p refers to the physical mass of the particle p, whereas an uppercase M_p refers to the field-dependent tree-level mass parameter.

The phenomenology of the cxSM at zero temperature differs from the SM by the presence of the degenerate states s and A, which are stable due to the unbroken $U(1)$ symmetry at zero temperature. In principle, they can be dark matter candidates, but dark matter direct detection experiments and searches for the invisible decay of the 125 GeV Higgs boson (which are possible in the cxSM if the decays $h \to ss$ and $h \to AA$ are kinematically allowed) exclude this possibility except for the s-channel resonance region with dark matter masses of $m_s \approx 62.5\,\text{GeV}$ [117, 236] or for heavy masses of $m_s \gtrsim 2$ TeV [243]. It has to be noted, that the constraints from direct detection experiments can be avoided by considering a softly-broken $U(1)$-symmetry in which the state A acts as pseudo-Nambu-Goldstone dark matter candidate in the presence of a non-zero vev $\phi_{s,\text{min}}$ [244]. However, this version of the cxSM is not able to realize a SFOEWPT [245]. In our discussion, focusing on the description of a SFOEWPT in the early Universe, we do not treat the singlet states as possible dark matter candidates. Consequently, we do not limit the discussion to the parameter regions that would be consistent with experimental limits from (among others) direct detection experiments. We thus assume that the states s and A are not stable on cosmological timescales, either due to tiny $\mathbb{Z}_2$-breaking couplings facilitating the decays of s and A into SM particles, or due to the presence of an extended dark sector with particles lighter than s and A into which the latter can decay.

In such a situation, and assuming $m_s > 62.5\,\text{GeV}$ such that the presence of s and A does not give rise to exotic or invisible decays of the 125 GeV Higgs boson h, the cxSM is very challenging to experimentally distinguish from the SM. The possibility of realizing a SFOEWPT in this model has consequently been called a *nightmare scenario* [113], especially since the modifications of the Higgs sector giving rise to the phase transition

would not lead to detectable traces at the LHC [235]. However, in the upcoming decade, the LISA experiment is expected to be launched. LISA is sensitive to GWs in the frequency band that coincides with the peak frequencies of primordial GW backgrounds produced during an EWPT. Hence, LISA will offer a new and potentially unique window to test the EWPT in the $U(1)$-symmetric cxSM. It is therefore vital to provide accurate predictions for the parameters characterizing the transition with a precision that makes it possible to determine the parameter space regions that predict potentially detectable GW signals.

V.2 Relations between physical observables and Langrange parameters

In this section, we provide details about the relations between the physical parameters and those parameters entering the Lagrangian and calculations of the thermodynamic observables describing the EWPT. Explicit relations are given at the one-loop level. These relations depend on the renormalization scheme used, for which we discuss two, most commonly used, options here: the $\overline{\text{MS}}$ and $\widetilde{\text{OS}}$ prescription.

We study the dynamics of EWPT using the effective potential, which is defined in terms of the Lagrangian parameters

$$P_{\mathcal{L}} = \{\mu_h^2, \lambda_h, \mu_s^2, g, g', y_t, \lambda_s, \lambda_{hs}\}\,. \tag{5.9}$$

In order to define a scheme yielding sensible input values for those parameters we use their relation to the following set of input parameters

$$P_{\mathcal{I}} = \{G_F, m_h, m_s, m_Z, m_W, m_t, \lambda_s, \lambda_{hs}\}\,, \tag{5.10}$$

where G_F and the physical masses m_h, m_s, m_Z, m_W, m_t are in principle (i.e. if an appropriate singlet state is detected) directly accessible in measurements. Since for the cxSM there are too few physical masses to determine all parameters of the theory from them, we use the portal coupling λ_{hs} and the quartic coupling λ_s of the singlet as free input parameters (at the certain scale).

The tree-level relations for the two parameter sets are

$$\begin{aligned} g^2 &= 4\frac{m_W^2}{v_{\text{EW}}^2}, \\ g'^2 &= 4\frac{m_Z^2 - m_W^2}{v_{\text{EW}}^2}, \\ y_t^2 &= 2\frac{m_t^2}{v_{\text{EW}}^2}, \\ \mu_h^2 &= -\frac{m_h^2}{2}, \\ \lambda_h &= \frac{m_h^2}{2v_{\text{EW}}^2}, \\ \mu_s^2 &= 2m_s^2 - \frac{v_{\text{EW}}^2\,\lambda_{hs}}{2}, \end{aligned} \tag{5.11}$$

where

$$v_{\text{EW}}^2 = \frac{1}{\sqrt{2}G_F}. \tag{5.12}$$

The numerical input values we use in our analysis are

$$\begin{aligned} \{m_W, m_Z, m_h, m_t\} &= \{80.379,\ 91.1876,\ 125.1,\ 172.5\}\,\text{GeV}, \\ G_F &= 1.1663787 \times 10^{-5}\,\text{GeV}^{-2}. \end{aligned} \tag{5.13}$$

The above relations undergo modifications when working beyond the tree-level approximation and will depend on the renormalization scheme used. We identify the physical input masses as the pole masses of the theory — the propagator poles of the two-point functions of the corresponding particles. According to the renormalization prescription (RP) used to define the counterterms of the theory, the poles will appear at different values of masses $m_i^{(\text{RP})}$, i.e. from

$$\Delta_i(p^2) = \frac{i}{p^2 - \left(m_i^{(\text{RP})}\right)^2 + \Sigma_i^{(\text{RP})}(p^2)} \tag{5.14}$$

we get

$$\left(m_i^{(\text{RP})}\right)^2 = m_{i,\text{pole}}^2 + \Sigma_i^{(\text{RP})}\left(p^2 = m_{i,\text{pole}}^2\right) \tag{5.15}$$

and identify $m_{i,\text{pole}}$ with the physical input masses m_i. The self-energies consist of two parts

$$\Sigma_i^{(\text{RP})}(p^2) = \Sigma_{i,\text{proper}}^{(\text{RP})}(p^2) + \Sigma_{i,\text{tad}}^{(\text{RP})}(p^2), \tag{5.16}$$

where $\Sigma_{i,\text{proper}}^{(\text{RP})}$ are the (real parts of the) "proper" 1PI-irreducible self-energy contribu-

tions, and $\Sigma_{i,\text{tad}}^{(\text{RP})}$ are the tadpole contributions. The (non-)appearance of the latter is dictated by the choice of the tadpole scheme. Now, in order to define the correct values of Lagrangian parameters at a given loop order according to some renormalization prescription RP, we simply replace the masses in (5.11) by the values which follow from (5.15) and adjust the vev according to the scheme of choice.

We study two different RP options, namely the $\overline{\text{MS}}$ scheme and the "on-shell like" $\widetilde{\text{OS}}$ scheme as originally mentioned in [219] and as used, e.g. in the phase transition tool `BSMPT` [246] and further explained in [247]. Other appearances of this scheme are, e.g. in [42] (called, somewhat confusingly, $\overline{\text{MS}}$ scheme there), or in a varied form in [248].

V.2.1 $\overline{\text{MS}}$ scheme

In the $\overline{\text{MS}}$ scheme, we have

$$\left(m_i^{(\overline{\text{MS}})}\right)^2(\mu) = m_i^2 + \Sigma_{i,\text{proper}}^{(\overline{\text{MS}})}(m_i^2,\mu) + \Sigma_{i,\text{tad}}^{(\overline{\text{MS}})}(m_i^2,\mu), \tag{5.17}$$

where μ is the renormalization scale. Note that the tadpole contributions are also renormalized in the $\overline{\text{MS}}$ scheme here, so their finite remainders enter in our calculation. Explicitly, the $\overline{\text{MS}}$ one-loop relations for (5.11) read

$$\begin{aligned}
g^2 &= \frac{4}{v_{\text{EW}}^2}\left[m_W^2\left(1-\frac{\delta^2}{v_{\text{EW}}^2}\right) + \Sigma_W^{(\overline{\text{MS}})}(m_W^2)\right],\\
y_t^2 &= \frac{2m_t}{v_{\text{EW}}^2}\left[m_t\left(1-\frac{\delta v_{\text{EW}}^2}{v_{\text{EW}}^2}\right) + 2\Sigma_t^{(\overline{\text{MS}})}(m_t)\right],\\
\mu_h^2 &= -\frac{1}{2}\left[m_h^2 + \Sigma_\phi^{(\overline{\text{MS}})}(m_h^2)\right],\\
\lambda_h &= \frac{1}{2v_{\text{EW}}^2}\left[m_h^2\left(1-\frac{\delta v_{\text{EW}}^2}{v_{\text{EW}}^2}\right) + \Sigma_\phi^{(\overline{\text{MS}})}(m_h^2)\right],\\
\mu_s^2 &= 2\left(m_s^2 + \Sigma_s^{(\overline{\text{MS}})}(m_s^2)\right) - \frac{v_{\text{EW}}^2\lambda_{hs}}{2}\left(1+\frac{\delta v_{\text{EW}}^2}{v_{\text{EW}}^2}\right),
\end{aligned} \tag{5.18}$$

in which Σ_W and Σ_Z are the transverse parts of the vector boson self-energies. For the top self-energy, we use

$$\Sigma_t(m_t) = \Sigma_s(m_t) + \Sigma_v(m_t), \tag{5.19}$$

following the decomposition

$$\Sigma_f(p) = m_f\Sigma_s(p^2) + \not{p}\Sigma_v(p^2) + \not{p}\gamma_5\Sigma_a(p^2). \tag{5.20}$$

Concerning the vev, we choose to work in the so-called (G_F, m_W, m_Z)-scheme. We write the radiative vev shift as [2]

$$\frac{\delta v_{\text{EW}}^2}{v_{\text{EW}}^2} = \frac{\Sigma_W^{(\overline{\text{MS}})}(m_W^2)}{m_W^2} - \frac{\delta g^2}{g^2}, \tag{5.21}$$

which follows from the relation $v_{\text{EW}} = 2m_W/g$. The gauge coupling can, in turn, be expressed as

$$g^2 = \frac{8 m_W^2 G_F}{\sqrt{2}} \tag{5.22}$$

and be experimentally accessed by measuring the Fermi coupling G_F in muon decay. One-loop corrections to muon decay in the $\overline{\text{MS}}$ scheme yield

$$\frac{\delta g^2}{g^2} = \frac{\Sigma_W^{(\overline{\text{MS}})}(m_W^2) - \Sigma_W^{(\overline{\text{MS}})}(0)}{m_W^2} - \frac{g^2}{16\pi^2}\left[4\ln\frac{\mu^2}{m_W^2} + \left(\frac{7}{2}\frac{m_Z^2}{m_Z^2 - m_W^2} - 2\right)\ln\frac{m_W^2}{m_Z^2} + 6\right]. \tag{5.23}$$

Note that the expressions in Eq. (5.18) are renormalization scale dependent. This dependence is fully governed by the beta functions of the respective couplings, except for Eq. (5.18). The reason is that we do not make use of a relation of λ_{hs} to a physical observable, as we do for the other parameters. Thence, λ_{hs} is directly used as an input parameter and does not have a one-loop relation to the other parameters of the theory, so its running is not included in Eq. (5.18). Apart from that, we explicitly checked that the scale dependence in Eq. (5.18) exactly reproduces the running as expected from the known beta functions of the theory. We list those in Appendix B.

V.2.2 $\widetilde{\text{OS}}$ scheme

In the OS-like scheme (denoted $\widetilde{\text{OS}}$ in what follows) — after the $\overline{\text{MS}}$ renormalization of $V_1^{T=0}$ — one uses renormalization conditions on the effective potential in order to fix a *finite* counterterm contribution to the potential, V_{CT}, such that the minima and scalar masses of the potential do not get shifted away from their tree-level values, *viz.*

$$\begin{aligned} \frac{\partial}{\partial\phi_i}\left(V_1^{T=0} + V_{\text{CT}}\right)\Big|_{\phi_i=\langle\phi_i\rangle} &= 0, \\ \frac{\partial^2}{\partial\phi_i\partial\phi_j}\left(V_1^{T=0} + V_{\text{CT}}\right)\Big|_{\phi_i=\langle\phi_i\rangle} &= 0. \end{aligned} \tag{5.24}$$

[2] Inserting this into (5.18) yields the results presented in [249].

This can be useful for simplifying the scanning procedure over large ranges of input values for masses [246]. Note, though, that not all field combinations in (5.24) yield independent or non-trivial equations, so only a subset of fields will contribute here. The relevant ones are the tadpole equation for the field ϕ (because the vev for this component is non-zero) and the mass equations for ϕ and s. All mixed derivatives of ϕ and s vanish, and the equations involving derivatives with respect to the Goldstone fields are not independent from the rest, which can be seen by virtue of the corresponding Ward identities, e.g. in [250]. Lastly, the tadpole equation for the scalar field s is fulfilled trivially in the parameter setup we study, where $\phi_{s,\text{min}} = 0$ and does not receive radiative corrections.

The counterterm potential for the cxSM reads

$$V_{\text{CT}} = \delta\mu_h^2 \Phi^\dagger\Phi + \delta\lambda_h (\Phi^\dagger\Phi)^2 + \frac{1}{2}\delta\mu_s^2 |S|^2. \tag{5.25}$$

We only need to adjust the three counterterms in (5.25) in order to keep m_h, m_S and $\phi_{h,\text{min}}$ at their tree-level values. This is why no other counterterms are taken into account explicitly. From (5.24) we then get

$$\begin{aligned}
\delta\mu_s^2 &= -2\frac{\partial^2 V_1^{T=0}}{\partial\phi_s^2}\bigg|_{\phi_h=v_{\text{EW}},\phi_s=0}, \\
\delta\mu_h^2 &= \left(\frac{\partial^2 V_1^{T=0}}{\partial\phi_h^2} - \frac{3}{v_{\text{EW}}}\frac{\partial V_1^{T=0}}{\partial\phi_h}\right)\bigg|_{\phi_h=v_{\text{EW}},\phi_s=0}, \\
\delta\lambda_h &= -\frac{2}{v_{\text{EW}}^3}\left(v_{\text{EW}}\frac{\partial^2 V_1^{T=0}}{\partial\phi_h^2} - \frac{\partial V_1^{T=0}}{\partial\phi_h}\right)\bigg|_{\phi_h=v_{\text{EW}},\phi_s=0}.
\end{aligned} \tag{5.26a}$$

Knowing that field derivatives of the effective potential correspond to 1PI n-point functions at zero momentum, we can identify

$$\begin{aligned}
\frac{\partial^2 V_1^{T=0}}{\partial\phi_s^2}\bigg|_{\phi_h=v_{\text{EW}},\phi_s=0} &= \Sigma^{(\overline{\text{MS}})}_{\phi_s,\text{proper}}(0), \\
\frac{\partial^2 V_1^{T=0}}{\partial\phi_h^2}\bigg|_{\phi_h=v_{\text{EW}},\phi_s=0} &= \Sigma^{(\overline{\text{MS}})}_{\phi_h,\text{proper}}(0), \\
\frac{\partial V_1^{T=0}}{\partial\phi_h}\bigg|_{\phi_h=v_{\text{EW}},\phi_s=0} &= T^{(\overline{\text{MS}})}_{\phi_h},
\end{aligned} \tag{5.27a}$$

where T_{ϕ_h} are the tadpole diagrams of ϕ_h. Moreover, the trilinear Higgs coupling in this

model times the zero-momentum Higgs propagator is

$$g_{\phi_h^3}\Delta_{\phi_h}(p^2=0) = -\frac{3}{v_{\text{EW}}}, \tag{5.28}$$

and we can write

$$-\frac{3}{v_{\text{EW}}}\frac{\partial V_1^{T=0}}{\partial \phi_h} = \Sigma^{(\overline{\text{MS}})}_{\phi_h,\text{tad}}(0). \tag{5.29}$$

Using this, (5.26) can be written as

$$\begin{aligned}
\delta\mu_s^2 &= -2\Sigma_S^{(\overline{\text{MS}})}(0)\,, \\
\delta\mu_h^2 &= \Sigma^{(\overline{\text{MS}})}_{\phi,\text{proper}}(0) + \Sigma^{(\overline{\text{MS}})}_{\phi,\text{tad}}(0)\,, \\
\delta\lambda_h &= -\frac{2}{v_{\text{EW}}^2}\left(\Sigma^{(\overline{\text{MS}})}_{\phi,\text{proper}}(0) + \frac{1}{3}\Sigma^{(\overline{\text{MS}})}_{\phi,\text{tad}}(0)\right)\,.
\end{aligned} \tag{5.30}$$

This might seem counterintuitive because, despite canceling the one-loop tadpoles in (5.24) via V_{CT}, tadpole contributions still appear explicitly in (5.30).

At this point, we are able to compare the two different renormalization prescriptions, i.e. we compare (5.18) with (5.30). For μ_h^2 we find

$$(\mu_h^2)^{(\overline{\text{MS}})} - (\mu_h^2)^{(\widetilde{\text{OS}})} = \Sigma_\phi^{(\overline{\text{MS}})}(m_h^2) - \Sigma_\phi^{(\overline{\text{MS}})}(0), \tag{5.31}$$

so the two prescriptions merely differ in the momentum of the self-energies. Notice, though, that the differences for λ_h can not be expressed in such a simple manner. Notably, the corrections in the $\widetilde{\text{OS}}$ scheme are gauge-dependent despite the inclusion of tadpole contributions, because the self-energies can only be gauge-independent at the poles. The gauge dependence of Lagrangian parameters in the $\widetilde{\text{OS}}$ scheme propagates to the gauge dependence of the predictions for physical observables, even for the case where the $\hbar$-expansion (presented in Section III.2.2) of the effective potential is applied. Another major difference is that in the $\overline{\text{MS}}$ scheme also the gauge and Yukawa couplings receive radiative shifts from their relations to the physical input quantities, while in the $\widetilde{\text{OS}}$ scheme only μ_s^2, μ_h^2 and λ_h do. Lastly, both schemes introduce a renormalization scale dependence. However, in the analysis where the $\widetilde{\text{OS}}$ scheme is implemented, the renormalization scale is fixed to v_{EW} and is not run to the thermal scale.

V.3 Thermodynamic parameters

In this section, we will discuss the scale and gauge dependence of critical temperature T_c and latent heat L_c, defined in Section III.5, for the EWPT predicted in the cxSM using the following set of approaches:

- the **4D approach** with the effective potential at one-loop order, including the AE-type daisy resummation of Eq. (3.100) (unless stated otherwise) and two different sets of relations between physical input and Lagrangian parameters at the one-loop level: $\overline{\text{MS}}$ and OS-like scheme (denoted $\widetilde{\text{OS}}$), see Section V.2 for details. We evaluate the effective potential as

$$\begin{aligned} V^{4D}(\phi_h, \phi_s, T; \mu, \xi) = V_0(\phi_h, \phi_s) + V_1^{T=0}(\phi_h, \phi_s; \mu, \xi) \\ + V_1^{T\neq 0}(\phi_h, \phi_s, T; \xi) + V_{\text{daisy}}(\phi_h, \phi_s, T; \xi), \end{aligned} \tag{5.32}$$

  where we construct the one-loop temperature-dependent potential using Eq. (3.37), and add the contribution from daisy resummed diagrams employing Eq. (3.100). For the latter, we only use the LO thermal screening masses. In the $\overline{\text{MS}}$ scheme, we use one-loop improved Lagrangian parameters (Eq. (5.18)) in each part of the effective potential Eq. (5.32). In the $\widetilde{\text{OS}}$ scheme, a UV-finite counterterm piece V_{CT} is added to the potential, which shifts the parameters such that the first and second derivatives of the potential V^{4D} in the tree-level minimum $(\phi_h, \phi_s) = (v_{\text{EW}}, 0)$ are the same as the ones of the tree-level potential V_0. This ensures that the scalar vevs and masses derived from V^{4D} remain at their tree-level values within the $\widetilde{\text{OS}}$ prescription based on the effective potential, which, however, does not account for momentum-dependent radiative corrections (see Eq. (5.24) for details).

- the **3D approach** based on the high-temperature EFT using the DR (see Section III.4 for details) and $\overline{\text{MS}}$ relations.[3] In this case, we evaluate the effective

[3] To apply the $\widetilde{\text{OS}}$ scheme in the 4D approach, one makes use of the fact that the effective potential can be separated into a $T = 0$ part (first line on the right-hand side of Eq. (5.32)) and a part that explicitly depends on the temperature (second line of Eq. (5.32)). The counterterm potential is then defined using only the $T = 0$ part of the potential. In the 3D EFT approach, the explicit temperature dependence enters into all terms of the potential from the matching conditions of the effective potential parameters, such that one cannot split the potential into a $T = 0$ part and a part that explicitly depends on T. We therefore do not apply an $\widetilde{\text{OS}}$ scheme in the 3D approach.

potential up to two-loop order within the effective theory

$$V^{3D}(\phi_h, \phi_s\ \mu_{3D}, \xi) = V_0^{3D}(\phi_h, \phi_s) + V_1^{3D}(\phi_h, \phi_s; \xi) + V_2^{3D}(\phi_h, \phi_s; \mu_{3D}, \xi). \tag{5.33}$$

For simplicity, we do not indicate that the fields are three dimensional explicitly in this chapter, but it is understood whenever the fields appear in the 3D EFT expressions. The temperature dependence of the potential arises implicitly through the effective couplings (see Section III.4). The DR for the SM with an additional singlet was studied extensively in the past [196, 249, 251], and the matching relations that are relevant in this chapter can be found in [114, 251]. For illustration, here we explicitly give the leading one-loop matching conditions for the mass parameters,

$$\begin{aligned} \mu_{h,3D}^2 &= \mu_h^2 + \frac{1}{48}T^2\left(3g'^2 + 9g^2 + 12y_t^2 + 24\lambda_h + 2\lambda_{hs}\right), \\ \mu_{s,3D}^2 &= \mu_s^2 + \frac{1}{6}T^2\left(\lambda_s + \lambda_{hs}\right), \end{aligned} \tag{5.34}$$

where the $\mathcal{O}(T^2)$ terms coincide with the leading finite-temperature corrections to the classical scalar potential in the high-temperature expansion. We explore the impact of the matching accuracy on thermodynamic observables and the description of the EWPT in the cxSM in detail below.

The dependence on the *hard* matching scale μ (see Fig. 5.2 for a schematic depiction of the matching procedure) also arises implicitly through the effective couplings of the theory, whereas the dependence on the *ultrasoft* scale μ_{3D} is explicit in V_2^{3D}. Unless specified otherwise, in the 3D approach we apply full $\mathcal{O}(g^4)$ matching, asumming $\mu_h^2, \mu_s^2 \sim g^2T^2$, $\lambda_h, \lambda_s, \lambda_{hs} \sim g^2$ scaling; we work in the regime where the phase transition occurs below the soft scale, with the hard and soft modes integrated out.

In this section, we use a reference parameter point with the singlet mass fixed to $m_s = 100\,\text{GeV}$ and the singlet self-coupling fixed to $\lambda_s = 1$, while varying the remaining free parameter of the cxSM in the range $\lambda_{hs} \in [1, 1.3]$. In this parameter range, we find a thermodynamic behavior compatible with the strong EWPT. For larger values of the portal coupling λ_{hs} (with the other parameters kept fixed), we find that the low-temperature global minimum is not the electroweak-breaking one, preventing the onset of an EWPT during the evolution of the Universe. On the contrary, for smaller values of λ_{hs}, there is no strong EWPT. We further analyze parameter planes in which λ_s is kept fixed and both m_s and λ_{hs} are varied in Section V.4.3, including

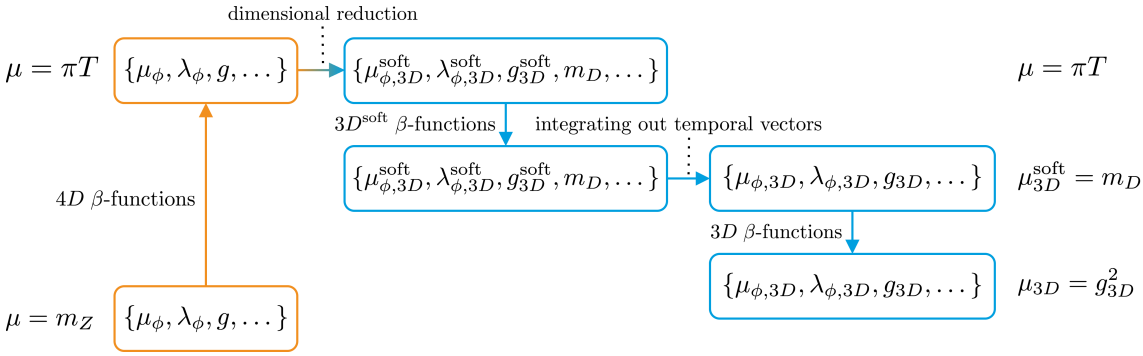

Figure 5.2: Illustration of the procedure for systematically integrating out relevant thermal scales within the DR approach used in this chapter in 3D approach. Starting from the initial scale ($\mu \sim m_Z$), Lagrangian parameters — determined from physical input parameters (see Section V.2) — are evolved to the *hard* scale ($\mu \sim \pi T$), where the full theory is matched to the dimensionally reduced EFT. The effective couplings are then evolved to the *soft* scale ($\mu^{\text{soft}}_{3D} \sim m_D$), where temporal vector modes are subsequently integrated out, yielding the final EFT used to compute thermodynamic observables at the *ultrasoft* scale, characterized by the gauge coupling ($\mu_{3D} \sim g^2_{3D}$). Beta functions relevant for the running of the couplings in the full theory and the EFT are given in Appendix B.

a phenomenological discussion of the resulting GW signals and the experimental prospects for their detection at future experiments. In the remainder of this section, unless specified otherwise (i.e. when using the $\hbar$-expansion), we directly minimize the real part of the effective potential to determine the relevant thermodynamic quantities.[4]

V.3.1 Renormalization scale dependence

We first investigate the scale dependence in the predictions for the critical temperature T_c and latent heat L_c using the different approaches discussed above. In the left plot of Fig. 5.3 we show with the solid lines the predictions for T_c as a function of λ_{hs} using the 4D approach in the $\overline{\text{MS}}$ scheme and the $\widetilde{\text{OS}}$ scheme with the orange and red lines, respectively, and using the 3D approach with the blue line. The colored shaded bands around these lines result from a variation of the renormalization and matching scale μ by a factor of 2 around the central values $\mu_0^{\overline{\text{MS}}} = \pi T_c$ and $\mu_0^{\widetilde{\text{OS}}} = v_{\text{EW}}$ in the $\overline{\text{MS}}$ and the $\widetilde{\text{OS}}$ scheme, respectively. These results were obtained from the effective potential in the Landau gauge, and the determination of the degenerate minima was carried out by numerically minimizing the loop-improved potential (without applying the $\hbar$-expansion).

[4]The imaginary part of the effective potential is related to the decay rate of the homogeneous state [252].

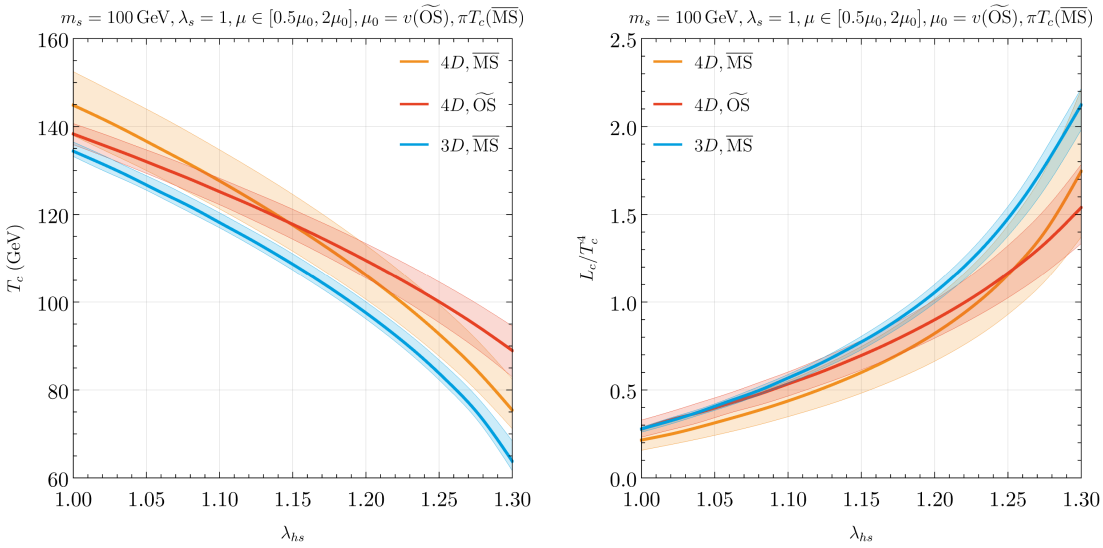

Figure 5.3: Critical temperature (*left*) and latent heat (*right*) for $m_s = 100\,\text{GeV}$, $\lambda_s = 1$, $\lambda_{hs} \in [1, 1.3]$ determined by direct potential minimization in the Landau gauge. For the 4D approaches, the shaded bands around the solid lines are obtained from a variation of the renormalization scale by a factor of 2, with the central value being fixed at $\mu = \pi T$ and $\mu = v_{\text{EW}}$ for $\overline{\text{MS}}$ and $\widetilde{\text{OS}}$ renormalization schemes, respectively (see text for details). For the 3D approach, the shaded band results from a variation of the *hard* matching scale by a factor of two around the central value $\mu = \pi T$.

The direct numerical minimization of the two-loop effective potential can run into spurious logarithmic divergence originating from the triple Higgs sunset diagram [253]. This feature is not problematic for the present investigation, since, for the case of a strong first-order phase transition, the divergence does not occur near the local minima in field space.

The widths of the bands illustrate the theoretical uncertainties related to the renormalization scale dependence. Across the entire λ_{hs} range, we find that the renormalization scale dependence is significantly reduced in the 3D approach compared to the 4D approaches.

While the orange and the red bands representing the 4D approaches overlap over the whole range of λ_{hs} shown, their slopes slightly differ. The $\overline{\text{MS}}$ scheme predicts smaller values of T_c at the upper end of the λ_{hs}-range, and the $\widetilde{\text{OS}}$ scheme predicts smaller values of T_c at the lower end of the λ_{hs}-range. This difference results from the different origins of the scale dependence. In the $\overline{\text{MS}}$ scheme, it is determined by the one-loop RGE running of the couplings, while for the $\widetilde{\text{OS}}$ scheme, it results from the scale dependence of the one-loop $\widetilde{\text{OS}}$ counterterms (which does not necessarily coincide with the RGE running).[5]

[5]For the 4D-$\overline{\text{MS}}$ approach, our findings agree with the ones reported in Ref. [236].

Additionally, differences between the two schemes arise due to the different choices for the central scales μ_0. The $\overline{\text{MS}}$ approach uses a variable central scale $\mu_0 = \pi T_c$, while the $\widetilde{\text{OS}}$ one has its central scale fixed at $\mu_0 = v_{\text{EW}}$. Therefore, a stronger parametric dependence for the former approach becomes visible, especially in the parameter regions where T_c changes quickly. Compared to the blue band representing the 3D approach, we observe that it lies below the other two bands, only showing an overlap with the other bands at the smallest values of λ_{hs} shown. This discrepancy between the 3D and the 4D approaches suggests that a scale variation with a factor of two might not be sufficient for a robust estimation of the theory uncertainty related to missing higher-order contributions in the perturbative expansion, and instead a wider scale variation or other ways to estimate the theoretical uncertainties should be considered. In addition, it should be taken into account that the 3D approach suffers from an additional theoretical uncertainty from the truncation of the high-T EFT at dimension four, which is discussed in detail in Section V.5.

In the right plot of Fig. 5.3, we show the predictions for the latent heat L_c defined in Eq. (3.112) using the three approaches, where the definitions of the solid lines and the colored bands are as in the left plot of Fig. 5.3. For the latent heat, we find a better agreement between the 4D and the 3D approaches compared to the predictions for the critical temperature T_c. As for T_c, the smallest theoretical uncertainty from the scale variation is found using the dimensionally reduced EFT. For the strongest transitions at the upper end of the depicted λ_{hs}-range, the blue band for the 3D approach lies entirely above the red band corresponding to the 4D-$\widetilde{\text{OS}}$ approach, but it still overlaps with the orange band corresponding to the 4D-$\overline{\text{MS}}$ approach. This suggests that in particular for the 4D-$\widetilde{\text{OS}}$ approach the renormalization scale variation by a factor of 2 does not fully capture the theory uncertainty from missing higher orders.

As discussed in Section III.2.1, the renormalization scale dependence in the 4D approach has different origins. The effective potential exhibits both an explicit scale dependence and an implicit scale dependence from the RGE running of the couplings and fields. In order to investigate the main sources of the uncertainty stemming from the scale variation, we show in the left plot Fig. 5.4 the predictions for T_c in the 4D-$\overline{\text{MS}}$ approach with the RGE running effects included in different parts of the effective potential. As before, the solid lines show the predictions for the central choice $\mu = \pi T_c$, while the shaded bands indicate the uncertainty in T_c from a variation of μ by a factor of 2. When including no RGE running at all (yellow), we find a sizable impact of the scale variation which can be attributed solely to the explicit scale dependencies in $V_1^{T=0}$. As expected from Eq. (3.38),

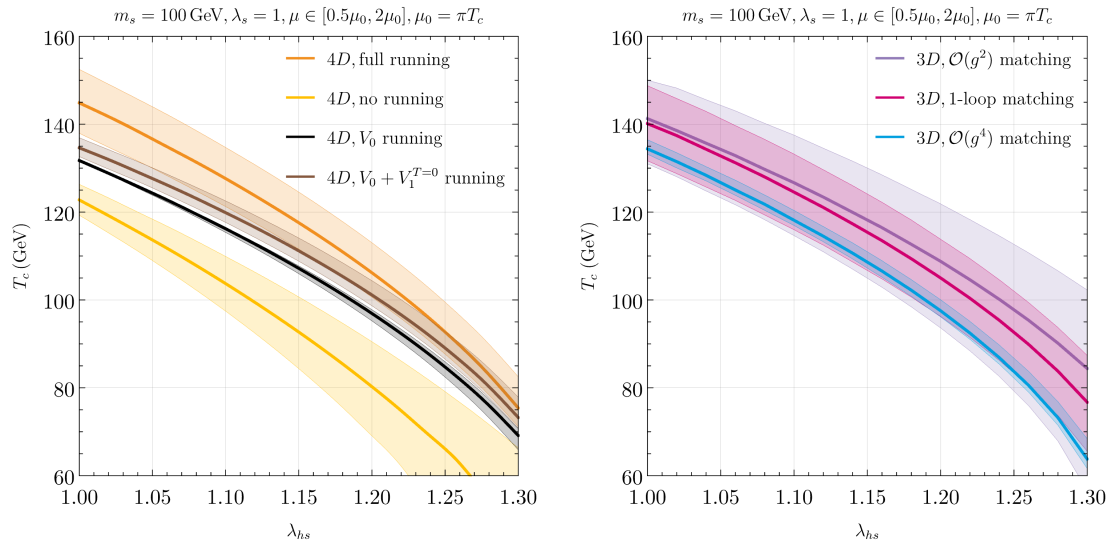

Figure 5.4: Scale-dependence of the critical temperature when using the $\overline{\text{MS}}$ input scheme in different settings: including the RGE running of Lagrangian parameters in different parts of the effective potential in the 4D approach (*left*) and using different matching orders in the 3D approach (*right*).

including the running only in the tree-level part almost completely cancels out the scale dependencies, which gives rise to the very small black uncertainty band. However, this should not be interpreted as an indication of small theory uncertainty, since the potential size of missing higher-order corrections is largely encoded in the RG-improved one-loop contributions. As such, the apparent insensitivity to the renormalization scale in this setup does not provide a reliable estimate of the theory uncertainty from the two-loop corrections or of the behavior of the perturbative expansion.

Including the running also in the zero-temperature one-loop piece of the effective potential $V_1^{T=0}$ leads to a slightly larger uncertainty band (brown). Since the one-loop RGE running included in $V_1^{T=0}$ is formally of two-loop order, this dependence on μ can be used as an estimate for missing higher-order corrections in the $T = 0$ part of the potential. The main scale dependence, however, comes from the inclusion of the parameter running in the thermal part of the effective potential, which dominates for higher temperatures (orange, showing the full result, which is the same as in the left plot of Fig. 5.3). This is apparent by the scale variation becoming more pronounced in this case, despite the scale dependence of $V_1^{T=0}$ being canceled. Moreover, as a consequence of the growing temperature corrections with increasing temperature, the orange band width grows in size for higher temperatures, while the opposite is true for the case where no running effects are included (yellow).

As discussed in Section III.4, in the 3D approach the theory uncertainty from missing higher orders can be estimated from the dependence on the hard matching scale μ (the dependence on the renormalization scale μ_{3D} is discussed below). In the right plot of Fig. 5.4 we show the scale dependence of the predictions for the critical temperature at different matching orders in the dimensionally reduced EFT. As before, the solid lines indicate the predictions for T_c with the scale set to the central choice $\mu = \pi T_c$, and the shaded bands indicate the uncertainty originating from a variation of the matching scale by a factor of 2. For the sake of separating uncertainties originating from various sources, we keep the effective potential at two-loop order for all matching orders. We observe that a matching at the leading $\mathcal{O}(g^2)$ accuracy (violet) gives rise to a significant scale dependence and a large theory uncertainty which surpasses the uncertainty from the renormalization scale dependence in the 4D approach shown in the left plot of Fig. 5.4. The scale dependence in the 3D approach is reduced at the lower end of the T_c values depicted in the plot if a matching at the full one-loop level is carried out (magenta), which contains the corrections of $\mathcal{O}(g^2)$ and partially accounts for corrections of $\mathcal{O}(g^4)$ (see Eq. (3.104)).[6] However, for the largest values of T_c shown in the plot, the dependence on the hard matching scale is barely reduced at one-loop matching accuracy. The blue band indicates the results when including two-loop contributions and a matching at full NLO $\mathcal{O}(g^4)$ is carried out. This is the same result as in the left plot of Fig. 5.3. We see that the NLO matching reduces the scale dependence over the whole range of λ_{hs} by a factor of about five. Notably, only at $\mathcal{O}(g^4)$ matching accuracy the scale dependence in the 3D approach is smaller than the renormalization scale dependence in the 4D approach shown in the left plot of Fig. 5.4. This demonstrates the necessity of working at $\mathcal{O}(g^4)$ matching accuracy in order to reduce theory uncertainties within the DR approach.

In addition to the dependence on the hard matching scale μ, the effective potential in the 3D EFT shows a dependence on the renormalization scale μ_{3D}. As shown in Eq. (5.33), in 3D the explicit dependence on the renormalization scale enters only at the two-loop level, whereas the dependence in the tree-level and one-loop pieces of the effective potential is only implicit via the RGE running of the parameters. Specifically for the cxSM, we can write

$$V^{3D} = V_0^{3D}\left(\mu^2_{h/s,3D}(\mu_{3D})\right) + V_1^{3D}\left(\mu^2_{h/s,3D}(\mu_{3D})\right) + V_2^{3D}\left(\mu_{3D};\mu^2_{h/s,3D}(\mu_{3D})\right), \tag{5.35}$$

where the explicit μ_{3D}-dependence appears in V_2^{3D}, and the RGE running of the mass

[6] Our one-loop results within the 3D EFT framework are in agreement with those presented in Ref. [114].

parameters $\mu_{h,3D}^2$ and $\mu_{s,3D}^2$ gives rise to the μ_{3D}-dependence in V_0^{3D} and V_1^{3D}.

The dependence of the critical temperature T_c on the renormalization scale μ_{3D} (for fixed μ) within the EFT is shown in Fig. 5.5 for the tree-level, one-loop and the two-loop effective potential, where we vary the scale around a central value $\mu_{3D} = g_{3D}^2$, where g_{3D} is the $SU(2)$ charge of the effective theory. The dependence on the EFT scale μ_{3D} is of far smaller magnitude than the one on the *hard* matching scale μ (see the discussion above), even if only the tree-level potential is used. In order for the μ_{3D}-variation to be visible at all in Fig. 5.5, we therefore show a variation around the central value by a factor of ten, in contrast to the factor of two for the μ-variation, and we narrow down the shown range for the portal coupling λ_{hs}. The explicit renormalization scale dependence in V_2^{3D} cancels the implicit scale dependence of the couplings $\mu_{h,3D}^2$ and $\mu_{s,3D}^2$ in the tree-level V_0^{3D}, while the residual uncanceled scale-dependence comes from including the running of couplings in V_1^{3D} and V_2^{3D}. In agreement with this expectation, we find that the renormalization scale dependence cancels to a large degree at the two-loop level (blue), while the results merely receive an overall shift but no reduction of the scale dependence when comparing the predictions at tree-level (green) and one-loop level (purple). Moreover, the overlap of the three different bands suggests a good loop convergence within the EFT.

Finally, the effective potential in the 3D EFT depends on a third soft scale μ_{3D}^{soft}, which appears at the intermediate step of integrating out temporal components of the gauge fields. We find that the residual dependence on μ_{3D}^{soft}, which appears as the scale of integrating out temporal vectors (see Fig. 5.2), is quantitatively insignificant across the parameter space investigated in this chapter.

Next, we compare the different approaches for computing the parameters characterizing the thermodynamics of bubble nucleation and the onset of the SFOEWPTs. In particular, we are interested in the renormalization scale dependence and the gauge dependence in the predictions for the parameters T_p, β/H and α (see Section III.5 for definitions), in comparing the 4D approaches and the dimensionally reduced 3D EFT. In the 4D approach, we substitute $V_0 \to V^{4D}$ of Eq. (5.32) in the bounce equation, Eq. (3.82), to compute B_T in the temperature range in which the false and the true vacua coexist. In the 3D approach, we calculate the nucleation rates (and observables which depend on those) by solving the bounce equation at LO. In addition, by substituting the loop-improved potential of Eq. (5.33) in the bounce determination, $V_0 \to V^{3D}$, we estimate the impact of higher-order corrections.

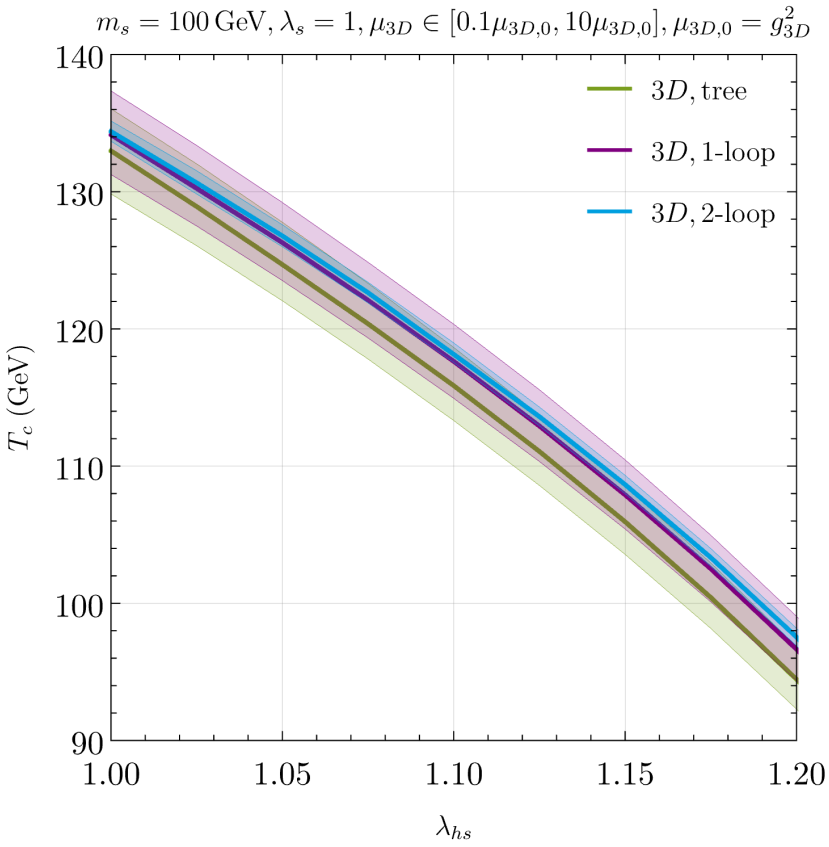

Figure 5.5: Variation of T_c with the 3D renormalization scale $\mu_{3D} \in [\mu_0/10, 10\mu_0]$ for different loop orders within the 3D approach.

In Fig. 5.6, we illustrate the renormalization scale dependence of the percolation temperature T_p (left plot), the inverse of the duration of the phase transition β/H (middle plot) and the strength of the phase transition α (right plot) calculated within the different approaches. As for the critical temperature, the scale dependence is considerably reduced in the 3D approach (blue) as compared to the 4D ones (4D-$\overline{\text{MS}}$ in orange and 4D-$\widetilde{\text{OS}}$ in red) for all three parameters. We also observe that the 4D-$\overline{\text{MS}}$ prediction aligns more closely with the 3D-$\overline{\text{MS}}$ prediction, while the 4D-$\widetilde{\text{OS}}$ approach predicts larger values of T_p (and consequently smaller values of α) for the largest values of λ_{hs}. Here, one should take into account the different choices for the central values μ_0 in the $\overline{\text{MS}}$ and the $\widetilde{\text{OS}}$ schemes, as discussed above. For the 3D approach, we show both results using the tree-level (green) and the loop-improved (blue) potential in the computation of the bounce action. The predictions using the loop-improved potential agree very well with the ones using the tree-level potential. This confirms that the loop corrections do not lead to a significant shift in the predictions for the parameters characterizing the phase transition, even though we note that using the loop-corrected potential in Eq. (3.82) is not a fully consistent loop improvement of the bounce action, as discussed in Section III.4.2.

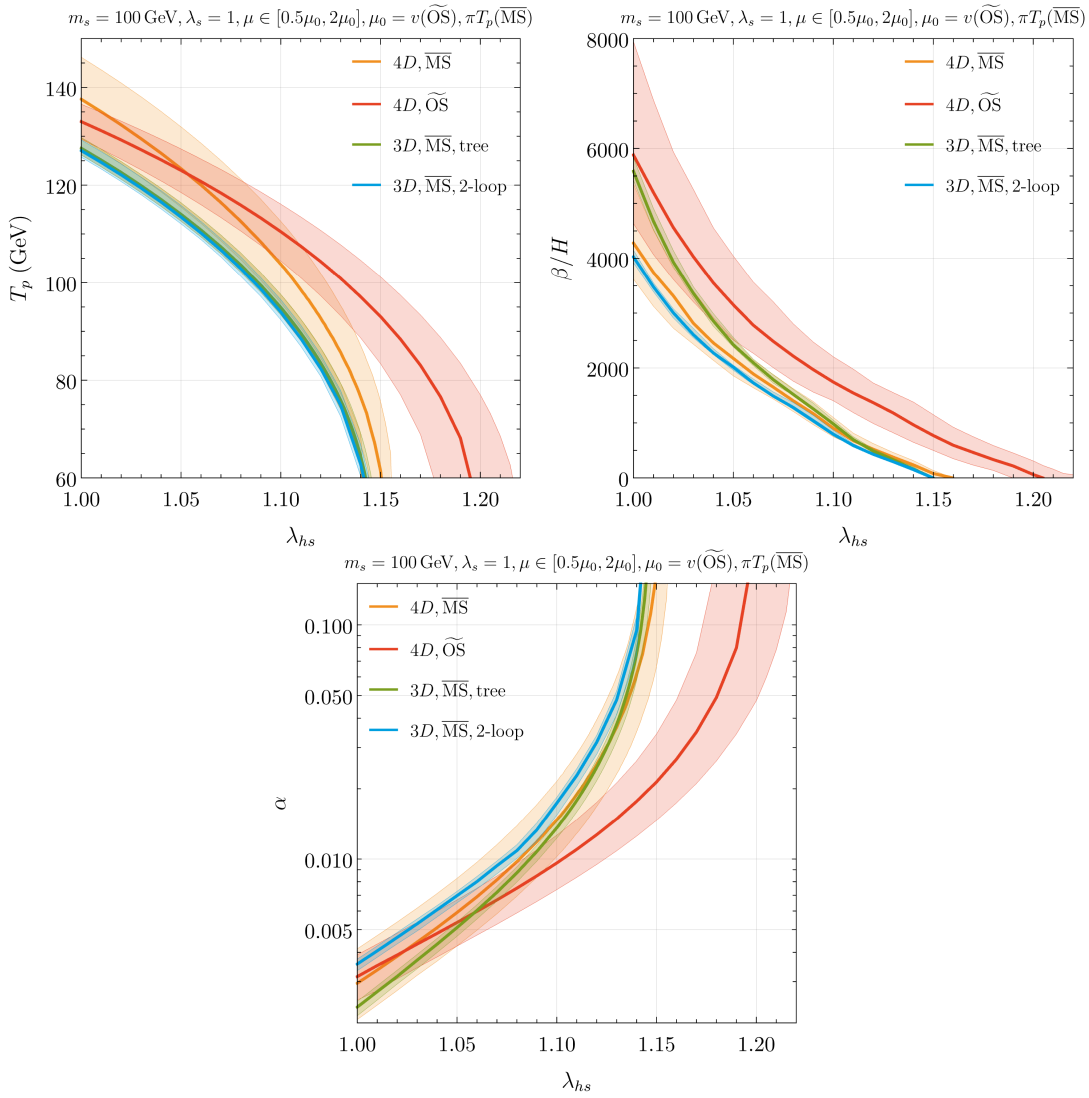

Figure 5.6: Scale-dependence of the percolation temperature T_p (*top left*), phase transition duration β/H (*top right*) and strength α (*bottom*) determined for $m_s = 100\,\text{GeV}$, $\lambda_s = 1$, $\lambda_{hs} \in [1, 1.2]$ by direct potential minimization in the Landau gauge. The bands represent the renormalization scale variation around the central values at $\mu = \pi T$ for the $\overline{\text{MS}}$ and $\mu = v$ for the $\widetilde{\text{OS}}$ renormalization schemes, respectively. For the 3D approach, the variance of the matching scale is shown.

V.3.2 Gauge dependence

Next, we compare the different methods in terms of the residual gauge-dependence of the results. For this, we adopt the same gauge-fixing condition as in Eq. (3.60), which carries over directly since the gauge structure of the cxSM is identical to that of the SM. The gauge-dependent mass eigenstates of the cxSM in different gauges follow Eq. (3.62), with the only change being taking $M_G^2 = \mu_h^2 + \lambda_h \phi_h^2 + \frac{\lambda_{hs} s^2}{4}$.

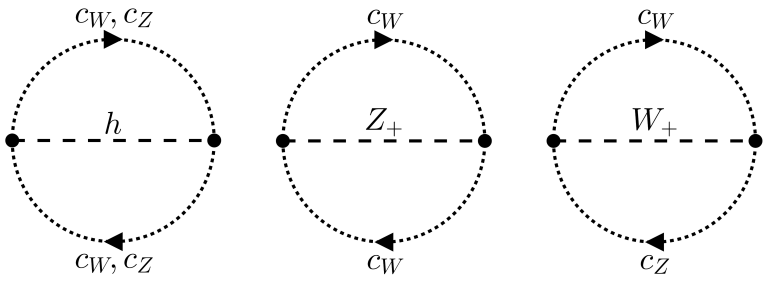

Figure 5.7: Two-loop ghost–ghost–scalar prototype diagrams that appear in the effective potential in R_ξ-gauge, but are absent in the Landau gauge. See Section III.2 for the details of the calculation of the loop-improved potential and Section III.2.2 for the gauge-dependent mass eigenvalues used in their evaluation.

In our chapter, we will employ the *background* R_ξ-gauge and take all $\xi^{W,Z,\gamma} = \xi$, except where explicitly mentioned otherwise, which allows us to analyze the numerical impact of residual gauge dependence by continuously varying the gauge-fixing parameter ξ.

Within the 3D EFT approach, we calculate the effective potential of the dimensionally reduced theory in R_ξ-gauge up to two-loop order. Compared to the algorithmically generated effective potential in `DRalgo` [197], which is computed in the Landau gauge, the two-loop potential in R_ξ-gauge contains additional diagrams, namely ghost–ghost–scalar vacuum prototype graphs (see Fig. 5.7), and the mass eigenvalues of vectors, Goldstone scalars and ghosts are altered (see Eq. (3.62) for details). After incorporating the contributions from these additional diagrams and the R_ξ-dependent masses, we explicitly checked that the expression for the potential evaluated in R_ξ-gauge becomes gauge independent in the $\hbar$-expansion (see Section III.2.2) at the tree-level minima and that it reproduces the potential in the Landau gauge in the $\xi \to 0$ limit. This serves as a highly non-trivial check of the newly introduced contributions to the potential and the intricate gauge cancellations at the two-loop level.

To estimate the theoretical uncertainty in the EWPT observables arising from residual gauge-parameter dependence, we need to define a reasonable variation range for ξ. An upper bound follows from requiring perturbativity, which schematically yields $|\xi| \lesssim 1/g \sim 10$ beyond which the loop expansion breaks down; it was also shown in [158] that taking larger values of the gauge-fixing parameter can lead to spurious Landau poles. We have therefore chosen the range $\xi \in [-10, 10]$ for the Fermi and *background* R_ξ gauges and $\xi \in [0, 10]$ for the *standard* R_ξ gauge (see the discussion below).

We begin by showing the gauge variation of T_c for different loop orders of the effective

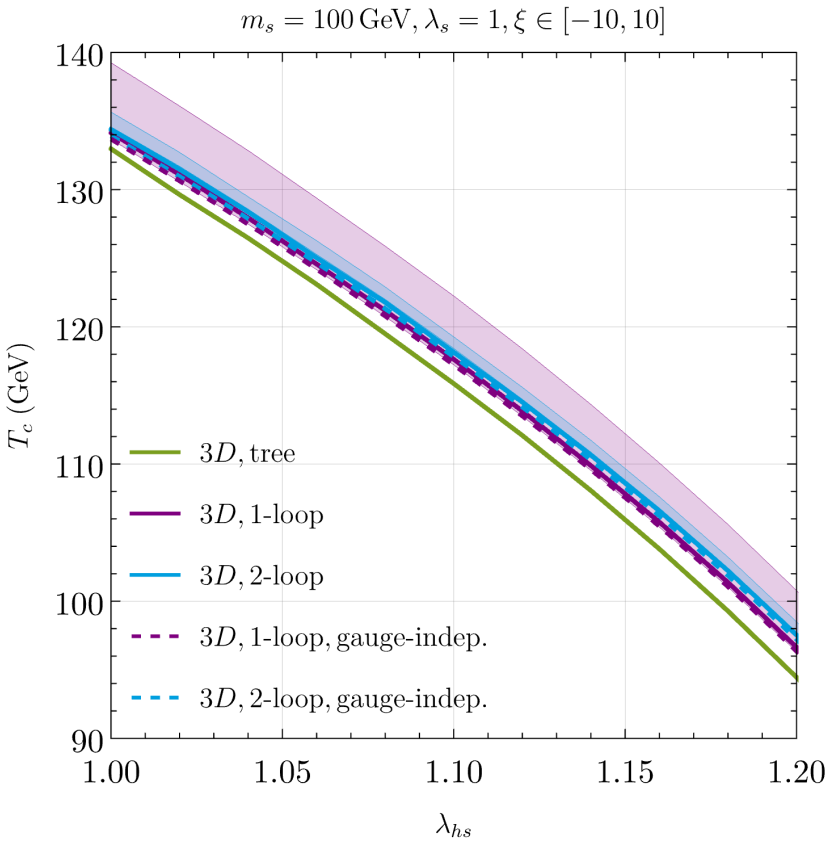

Figure 5.8: Critical temperature T_c determined for $m_s = 100\,\text{GeV}$, $\lambda_s = 1$, $\lambda_{hs} \in [1, 1.2]$ for different loop orders within the 3D approach. The bands represent variations of the gauge-fixing parameter $\xi \in [-10, 10]$ in R_ξ-gauge. Dashed lines represent the gauge-independent determination of T_c in the $\hbar$-expansion.

potential in the 3D approach with $\mathcal{O}(g^4)$ matching accuracy (see Section III.4 for details) in Fig. 5.8. The solid lines indicate the predictions for $\xi = 0$, which corresponds to the Landau gauge, and the shaded uncertainty bands show the variation of T_c when varying ξ between -10 and 10. The result for the tree-level potential (green) is only visible as a solid line because it does not depend on ξ. We find that the gauge dependence is reduced by more than a factor of three at two-loop order (blue) compared to the one-loop potential (purple). The reduction of the theory uncertainty from the residual gauge dependence strongly resembles the reduction of the scale-dependence when including higher loop orders of the effective potential as shown in Fig. 5.5. This behavior can be understood via the Nielsen identity Eq. (3.43). For the gauge-dependent results shown in Fig. 5.8, we determine the n-loop minimum $\phi_{\text{min}}^{(n)}$ of the potential via direct minimization of the n-loop potential, i.e.,

$$\frac{\partial}{\partial\phi}\left(V_0 + V_1 + \cdots + V_n\right)\big|_{\phi_{\text{min}}^{(n)}} = 0\,. \tag{5.36}$$

Inserting this into the Nielsen identity for the all-order potential yields,

$$\xi\frac{\partial}{\partial\xi}(V_0+V_1+\dots)\Big|_{\phi_{\min}^{(n)}} = C(\phi,\xi)\,\frac{\partial}{\partial\phi}\,(V_{n+1}+V_{n+2}+\dots)\Big|_{\phi_{\min}^{(n)}}. \tag{5.37}$$

Rearranging terms, we find for the order of the gauge dependence of the n-loop potential:

$$\begin{aligned}\xi\frac{\partial}{\partial\xi}(V_0+V_1+\dots+V_n)\Big|_{\phi_{\min}^{(n)}} &= \left(C(\phi,\xi)\frac{\partial}{\partial\phi}-\frac{\partial}{\partial\xi}\right)(V_{n+1}+V_{n+2}+\dots)\Big|_{\phi_{\min}^{(n)}}\\ &= \mathcal{O}(\hbar^{n+1})\,.\end{aligned} \tag{5.38}$$

Thus, the residual gauge dependence of the effective potential is of the order of $\hbar^{n+1}$, i.e. the order of the missing higher-order terms in the potential. As a consequence, the residual gauge dependence of thermodynamic quantities such as T_c decreases with increasing loop order, as demonstrated by our results in Fig. 5.8.

As discussed in Section III.2.2, a gauge-independent prediction for the critical temperature can be achieved by applying the $\hbar$-expansion. We indicate the predictions for T_c using the $\hbar$-expansion considering the different loop orders with the dashed lines in Fig. 5.8. Both at one- and two-loop order, we find that the gauge-independent $\hbar$-expansion results lie within the shaded uncertainty bands and are thus captured by the gauge variation in the direct minimization procedure. We also find that the gauge-independent predictions lie close to the Landau-gauge results shown as solid lines.

Next, we compare the different approaches defined at the beginning of this section (4D-$\overline{\text{MS}}$; 4D-$\widetilde{\text{OS}}$; 3D-$\overline{\text{MS}}$ at two-loop level with $\mathcal{O}(g^4)$ matching) in terms of the numerical impact of the residual gauge-dependence on the predictions for the critical temperature T_c and the latent heat L_c. This is depicted in Fig. 5.9 for T_c (*left* plot) and L_c (*right* plot), with the solid lines showing the result for $\xi = 0$, and the shaded bands indicate the theoretical uncertainty from the ξ-variation as discussed above. Moreover, the dashed lines show the predictions for the manifestly gauge-independent calculation, as determined using the $\hbar$-expansion about the tree-level minima of the effective potential. For the cxSM, we have to minimize along two field directions ϕ_h and ϕ_s; the

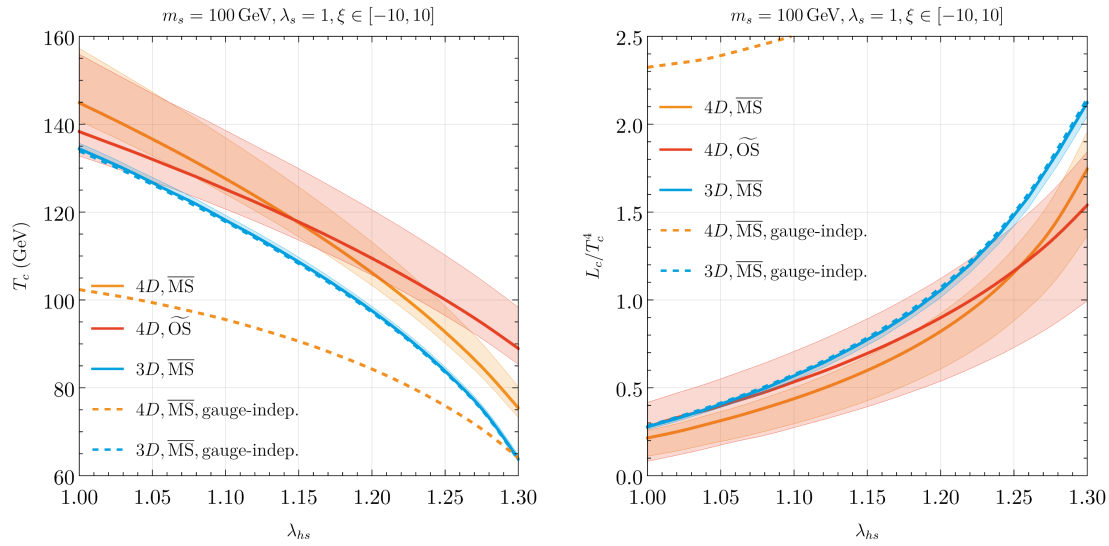

Figure 5.9: Critical temperature (*left*) and latent heat (*right*) determined for $m_s = 100\,\text{GeV}$, $\lambda_s = 1$, $\lambda_{hs} \in [1, 1.3]$. The bands represent variations of the gauge-fixing parameter $\xi \in [-10, 10]$ in R_ξ-gauge. Dashed lines represent the gauge-independent approach based on the expansion around the tree-level minimum.

corresponding $\hbar$-expansion of the potential values at the extremum then reads

$$\begin{aligned} V(\phi_{h,\text{min}}, \phi_{s,\text{min}}) &= V_0(\phi_{h,0}, \phi_{s,0}) + \hbar\, V_1(\phi_{h,0}, \phi_{s,0}) \\ &+ \hbar^2 \Bigg(V_2 - \frac{1}{2} \frac{1}{(\partial^2_{\phi_h} V_0)(\partial^2_{\phi_s} V_0) - (\partial_{\phi_h}\partial_{\phi_s} V_0)^2} \Big[(\partial^2_{\phi_s} V_0)\,(\partial_{\phi_h} V_1)^2 \\ &+ (\partial^2_{\phi_h} V_0)\,(\partial_{\phi_s} V_1)^2 - 2(\partial_{\phi_h}\partial_{\phi_s} V_0)\,(\partial_{\phi_h} V_1)\,(\partial_{\phi_s} V_1) \Big] \Bigg) \Bigg|_{\phi_{h,0}, \phi_{s,0}} + \mathcal{O}(\hbar^3)\,, \end{aligned} \tag{5.39}$$

generalizing Eq. (3.54) and where all quantities are evaluated at the tree-level minimum $\phi_h = \phi_{h,0}$ and $\phi_s = \phi_{s,0}$.

We note that in the 4D-$\widetilde{\text{OS}}$ approach the finite counterterms are gauge-dependent (see Section V.2); hence, it is not possible to perform an $\hbar$-expansion leading to a gauge-independent prediction. As already visible in Fig. 5.8, we find good agreement between the gauge-independent results and the gauge-dependent results based on the direct potential minimization in the 3D case (blue). On the contrary, there is a significant deviation between the gauge-independent results based on the $\hbar$-expansion and the ones from direct numerical minimization of the loop-corrected potential in the 4D approach, irrespective of whether the $\overline{\text{MS}}$ or the $\widetilde{\text{OS}}$ prescription is used. The gauge-independent predictions for T_c deviate by more than 50% from the results where no $\hbar$-expansion is applied, and the gauge-independent predictions for $L_c/T_c^4 \sim 2.5$–4 deviate by a fac-

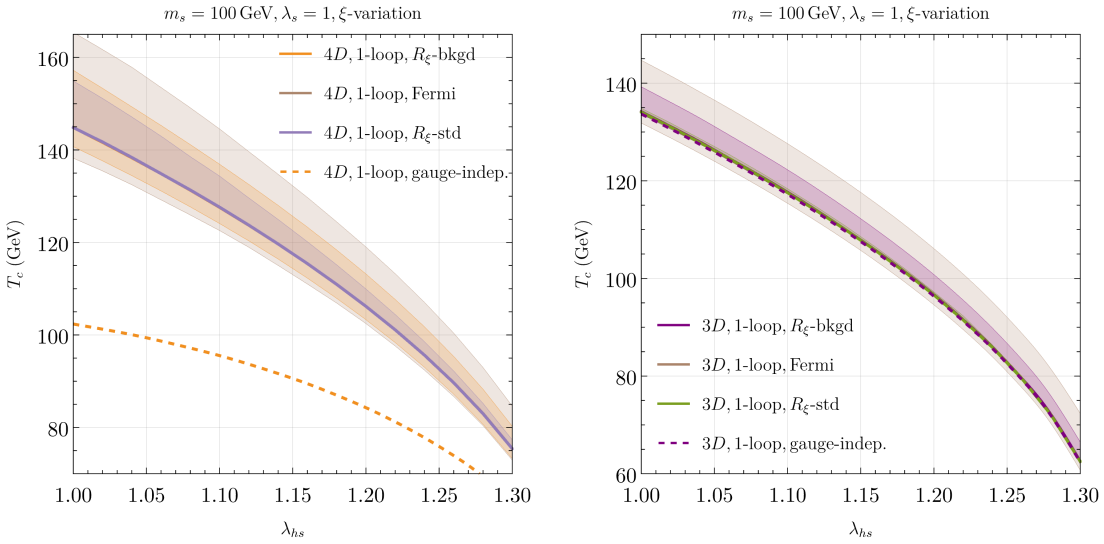

Figure 5.10: Gauge-parameter induced variation of the critical temperature for Fermi, *standard* and *background* R_ξ-gauges (see Section III.2.2 for definitions). The *left* panel shows T_c determined by minimizing the 4D effective potential with daisy resummations and input parameters determined in the $\overline{\text{MS}}$ scheme. The *right* panel shows T_c in different gauges within the 3D-$\overline{\text{MS}}$ approach at one-loop order. For the *background* R_ξ and Fermi gauges, the $\xi \in [-10, 10]$ variation is shown. In the *standard* R_ξ-gauge, $\tilde{\phi}$ is set to the tree-level minimum $\phi_{h,0}$, and the gauge-fixing parameter is varied within $\xi \in [0, 10]$. The solid and dashed lines correspond to results obtained in the Landau gauge and using a gauge-independent approach via the $\hbar$-expansion, respectively.

tor of a few across the parameter space shown on the plot. The primary source of these large discrepancies in the 4D approaches is that the tree-level minimum is significantly shifted by leading thermal loop corrections. Furthermore, in the 4D approach, the method to extract gauge-independent daisy resummation contributions, following Ref. [148], is somewhat *ad hoc*, relying on evaluating different parts of the potential at different field values. In light of the scale-dependence analysis in Section V.3.1, our results suggest that the inherent theoretical uncertainties of the 4D approach at one-loop level are captured by neither a scale variation of about a factor of two, nor by the rather large ξ variation applied here. On the contrary, the proximity of the gauge-independent and the Landau gauge result in the 3D approach once again indicates a good perturbative behavior of the effective potential.

We proceed by exploring differences in the choice of the gauge-fixing condition. A comparison between the critical temperature determined by direct minimization of the effective potential in the Fermi, *background* R_ξ and *standard* R_ξ gauges, defined in Section III.2.2, is presented in Fig. 5.10 for the 4D-$\overline{\text{MS}}$ (left plot) and 3D-$\overline{\text{MS}}$ (right plot) approaches. For a better comparison between the 3D and the 4D approaches, we use

here the one-loop effective potential in the 3D approach which is at the same loop order as the effective potential in the 4D approach. For the *background* R_ξ and Fermi gauges, we show uncertainty bands using a ξ-variation in the range $\xi \in [-10, 10]$. In the *standard* R_ξ-gauge, $\tilde{\phi}$ is set to the tree-level minimum $\phi_{h,0}$, and the gauge-fixing parameter is varied using only positive values of ξ within the range $\xi \in [0, 10]$, see the discussion below. The variation of the gauge-fixing parameter $\xi \in [-10, 10]$ in Fermi gauge results in a larger uncertainty in the T_c-determination in both the 4D and 3D approaches as compared to the *background* R_ξ-gauge, but the qualitative results are similar. However, we find that positive ξ values give rise to lower critical temperatures in Fermi gauge, while the opposite is true in the R_ξ-gauges.

For the *standard* R_ξ-gauge, we use $\tilde{\phi} = \phi_{h,0}$ in the gauge-fixing condition, thus assigning the local electroweak symmetry-breaking minimum with positive value of $\phi_{h,0}$ as the physical minimum. This gauge fixing explicitly breaks the $\phi_h \to -\phi_h$ symmetry of the effective potential, which is preserved in the other gauges. As a consequence, in the standard R_ξ-gauge the two electroweak symmetry breaking minima at $+\phi_h$ and at $-\phi_h$ are not degenerate anymore, whereas their degeneracy is preserved in the other gauges. For negative ξ-values, we find that the minimum at $\phi_s = 0$ and $\phi_h < 0$ becomes the global minimum at low temperatures. By tracing the different phases of the potential at finite temperature and computing the probabilities for an EWPT from the vacuum with $(\phi_{\text{min},s} \neq 0, \phi_{\text{min},h} = 0)$ into the vacua with $(\phi_{\text{min},s} = 0, \phi_{\text{min},h} \neq 0)$, one finds that the transition rates are larger for a transition into the vacuum corresponding to the global minimum with $\phi_{\text{min},h} < 0$. However, this contradicts the choice of setting $\tilde{\phi} = \phi_{h,0} > 0$ in the gauge-fixing conditions, as discussed above. Due to this inconsistency in the standard R_ξ-gauge, we discard these points with negative ξ-values as unphysical, and limit the variation of the gauge-fixing parameter in this gauge to positive values $\xi \in [0, 10]$ where the minimum with $\phi_{\text{min},h} > 0$ is the global minimum of the potential at $T = 0$.[7] We have verified that upon performing an $\hbar$-expansion in the *standard* R_ξ-gauge, we obtain gauge-independent results that agree with the results from other gauges after an $\hbar$-expansion.

The results for the gauge-independent determination of T_c via an $\hbar$-expansion (see Eq. (5.39)) are shown by dashed lines in Fig. 5.10. As a consequence of the $\hbar$-expansion, the results are independent of both the gauge-fixing parameter and the gauge-fixing

[7] Since $\xi = 0$ is the lower limit of the ξ-variation in the standard R_ξ-gauge, the solid lines indicating the predictions in the Landau gauge coincide with the lower edge of the uncertainty bands of the standard R_ξ-gauge.

condition. As already discussed above, the application of the $\hbar$-expansion in the 3D EFT gives rise to a result that lies within the uncertainty bands from the ξ-variation using the gauge-dependent numerical minimization of the loop potential. Hence, the 3D approach complemented with the $\hbar$-expansion provides a numerically precise and gauge-independent prediction for the critical temperature. On the contrary, in the 4D approach the application of the $\hbar$-expansion at one-loop level gives rise to a result that is gauge-independent but shows large deviations from the results using the direct minimization of the loop potential, and only the gauge-dependent results (without $\hbar$-expansion) are in agreement with the predictions of the 3D EFT.

Interestingly, we find that the loop corrections in some gauge-fixing setups can qualitatively change the vacuum structure depicted in Fig. 5.1. For large ξ-values, the high temperature phase can develop a small non-zero value $\phi_{h,\text{min}}$ of the Higgs condensate at the minimum in addition to a non-vanishing singlet vev $\phi_{s,\text{min}}$. This is analogous to the electroweak symmetry non-restoration at high temperature, a phenomenon that recently gained interest [39, 254–259]. For instance, in the *background* R_ξ gauge, for $\lambda_{hs} = \lambda_s = 1, m_s = 100\,\text{GeV}$ at $T = T_c$, this happens for $\xi \gtrsim 7$ in the 4D-$\overline{\text{MS}}$ approach. We find non-vanishing Higgs vevs in the high-T phase, both in R_ξ and Fermi gauges, while the vacuum structure with $\phi_{h,\text{min}} = 0$ in the high-T phase is preserved in the Landau gauge. In addition, the high-temperature phase does not develop a vev for the Higgs field if the $\hbar$-expansion is performed. Hence, we regard the occurrence of non-vanishing Higgs vevs in the high-T phase as an unphysical artifact of the direct minimization of the effective potential that can arise in certain gauges if the vacuum structure of the potential is not analyzed in a strictly gauge-independent way.

Next, we analyze the gauge dependence of T_p, β/H and α, which is shown in Fig. 5.11. The results are similar to the ones we observed for the scale dependence, with the 3D EFT result exhibiting a substantially smaller gauge dependence in all three parameters. One can therefore expect that the predictions for the GW signals will be significantly less affected by theoretical uncertainties in the dimensionally reduced EFT compared to the 4D approaches. In particular, the 4D-$\widetilde{\text{OS}}$ approach exhibits a notably larger dependence on the gauge-fixing parameter compared to the 4D-$\overline{\text{MS}}$ and the 3D approaches. The larger uncertainty from the gauge dependence using the $\widetilde{\text{OS}}$ prescription can be attributed to additional uncanceled gauge dependencies in the finite counterterms added to the potential, which are derived from taking derivatives of the one-loop piece of the potential with respect to the fields (see the discussion above). As for the renormalization scale variation, we show (within the 3D EFT approach) results from the tree-level bounce (which

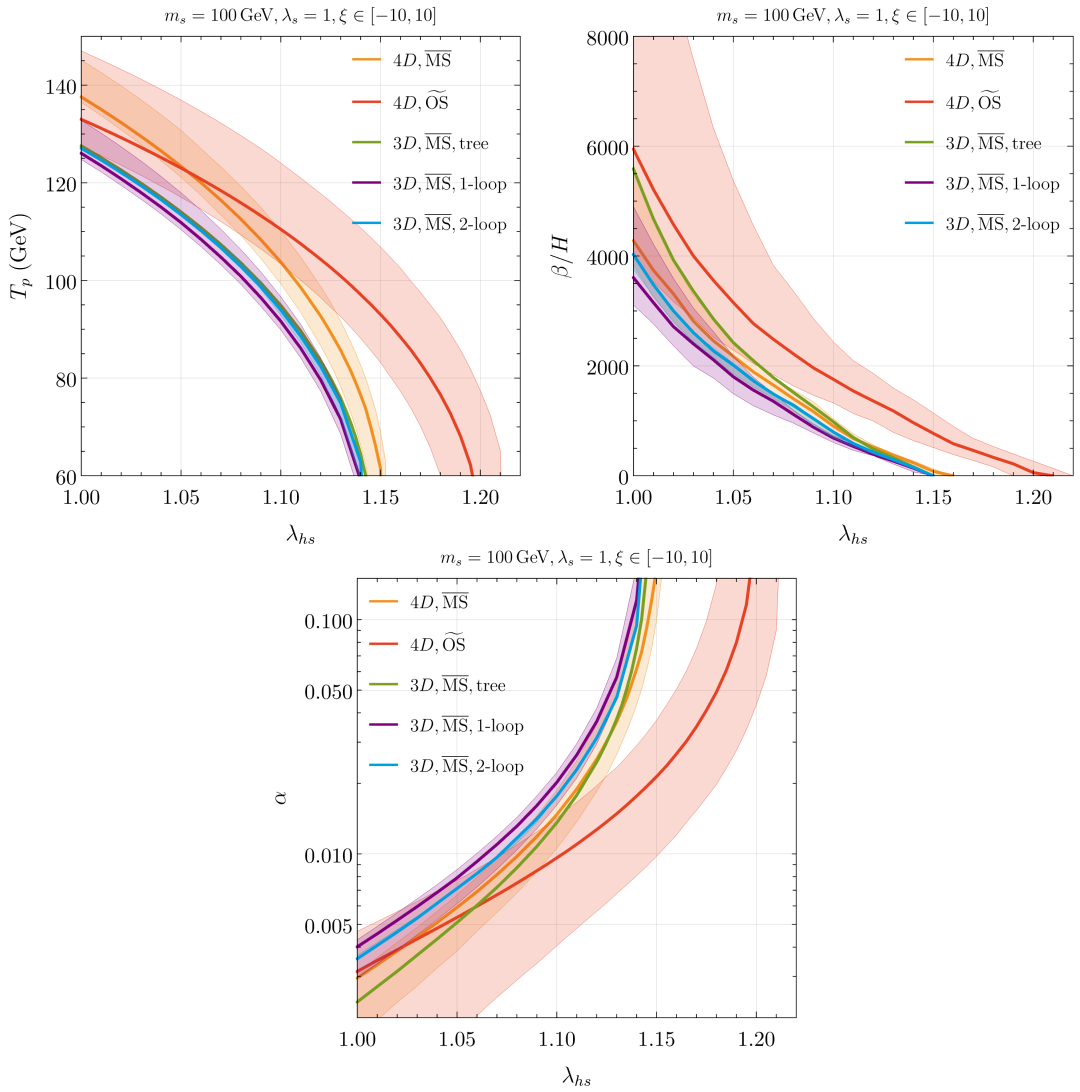

Figure 5.11: Gauge-parameter dependence of the percolation temperature T_p (*top left*), phase transition duration β/H (*top right*) and strength α (*bottom*) for $m_s = 100\,\text{GeV}, \lambda_s = 1, \lambda_{hs} \in [1, 1.2]$ in R_ξ-gauge. The bands indicate the gauge parameter variation of $\xi \in [-10, 10]$.

are inherently gauge-independent) as well as from the bounce calculation, where the tree-level potential is replaced by the effective potential. This substitution introduces a gauge dependence of the nucleation observables, but we observe that the resulting shifts are of only moderate magnitude. Similar to what we observed for T_c and L_c, we observe a gauge dependence reduction when transitioning from the one-loop to the two-loop effective potential.

V.4 Gravitational wave predictions

GWs produced during a cosmological first-order phase transition might provide a crucial probe of early Universe dynamics in the future [30, 100]. Among the primary mechanisms generating these signals, sound waves in the plasma play a dominant role in our model, which does not exhibit strongly supercooled phase transitions, rendering GW production from runaway bubble collisions irrelevant. An additional source of GW production is magnetohydrodynamic turbulence in the plasma. Its contribution to the GW signal in an EWPT with weak or intermediate strength of $\alpha \lesssim 0.1$ (see Fig. 5.15 below) is subdominant compared to the sound wave contribution [204]. Moreover, the resulting spectral shape of the GW signal caused by the turbulence depends on the fraction of energy converted into turbulent motion in the plasma, which has not yet been determined robustly in numerical simulations and would have to be treated as an additional free parameter [31]. Therefore, we do not include this contribution in our analysis in order to keep the analysis focused on the theory uncertainty resulting from the perturbative description of the SFOEWPT.

V.4.1 Spectral density

In the same manner as in the previous sections, the impact of the uncertainties from the perturbative description of the SFOEWPT on the predicted GW signals can be estimated by analyzing the gauge and scale dependence of the predicted GW spectra. The details of the calculation of the GW spectrum are described in Section III.6, and, for this chapter, we use the sound wave contribution to the GW spectrum as given in Eq. (3.123).

Scale dependence

In the left plot of Fig. 5.12 we show the predicted GW signals using the different approaches introduced in Section V.3, where the shaded bands indicate the theoretical uncertainty resulting from a variation of the renormalization scale in the 4D approaches and the hard matching scale in the 3D approach. The solid line indicates the prediction for the central scale choices as shown on top of the plots. All results shown are obtained using the Landau gauge, and we show two predictions for the 3D-$\overline{\text{MS}}$ approach using the tree-level effective potential (green) or the two-loop level potential (blue) for the determination of the bounce solution. The differences between these two predictions are

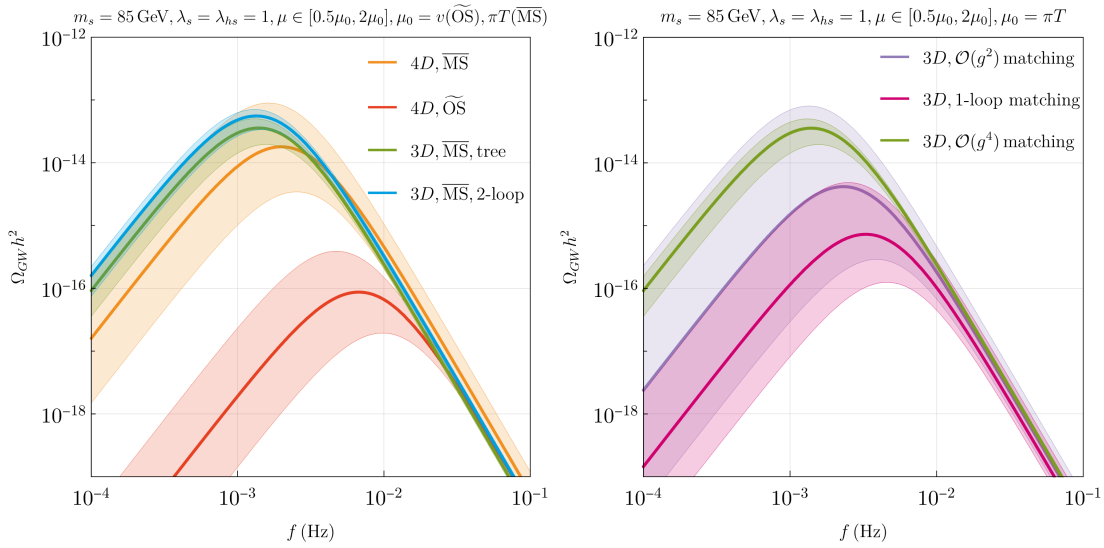

Figure 5.12: GW spectrum for $m_s = 85\,\text{GeV}$, $\lambda_s = \lambda_{hs} = 1$ evaluated in the Landau gauge. The bands indicate the renormalization scale variation around the central value $\mu = \pi T$ and $\mu = v$ for the $\overline{\text{MS}}$ and $\widetilde{\text{OS}}$ renormalization schemes, respectively. For the 3D approach, the variance of the hard matching scale is shown. In the *left* panel, we compare the 4D and 3D approaches, and the *right* panel shows the predictions for different matching orders in the 3D approach.

found to be within the uncertainty resulting from the scale variation. In line with the observations from Section V.3.1, we find that the scale dependence of the predicted GW signals is significantly smaller using the dimensionally reduced EFT compared to the 4D approaches. While the 4D-$\overline{\text{MS}}$ approach predicts a GW signal that within its uncertainties is in agreement with the predictions from the 3D EFT, the 4D-$\widetilde{\text{OS}}$ approach predicts a GW signal with a peak amplitude that is roughly three orders of magnitude smaller, and the peak frequencies differ by roughly an order of magnitude.

The discrepancy between the $\widetilde{\text{OS}}$ and the $\overline{\text{MS}}$ results mainly arises from the small parameter shifts between the physical input and Lagrangian parameters using $\widetilde{\text{OS}}$ vs. $\overline{\text{MS}}$ relations together with the strong parametric dependence of the GW spectra (see e.g. Refs. [13, 129]). While this discrepancy between the different renormalization prescriptions appears alarming at the level of individual benchmark points, it is important to note that GW predictions from SFOEWPTs are in many cases extremely sensitive to the underlying model parameters. As a result, when comparing broader regions of parameter space with the goal of identifying regions of parameter space that allow for potentially detectable GW signals, the differences between the approaches are less severe, since the parametric dependence of the GW signal tends to dominate over the scheme-related discrepancies (see Section V.4.3 for further discussion).

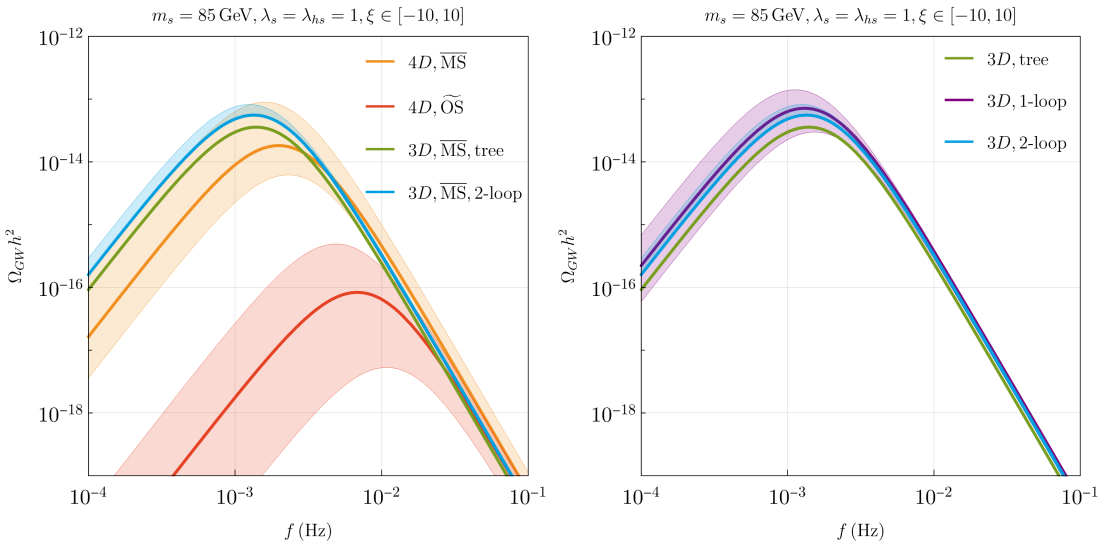

Figure 5.13: Gauge-parameter variation of $\xi \in [-10, 10]$ in the GW spectrum for $m_s = 85\,\text{GeV}$, $\lambda_s = \lambda_{hs} = 1$ in R_ξ-gauge. In the *left* panel, we compare the 4D and 3D approaches. The *right* panel shows a comparison of including different loop orders of the effective potential in the 3D approach for the bounce calculation.

In the right plot of Fig. 5.12 we show the relevance of the matching order within the 3D approach. As in the left plot, the shaded uncertainty bands result from a variation of the matching scale, while the solid lines indicate the predictions for the central scale choice, and all results were obtained in the Landau gauge. The violet, magenta and green bands belong to $\mathcal{O}(g^2)$, one-loop and $\mathcal{O}(g^4)$ matching accuracy, respectively. In line with the predictions for T_c at different matching orders as shown in Fig. 5.4, we observe a significant reduction of the scale dependence at $\mathcal{O}(g^4)$ matching accuracy also for the GW signal, whereas a matching at lower accuracy does not improve the theoretical uncertainty from the scale dependence compared to the 4D approach. This once again indicates the importance of the full $\mathcal{O}(g^4)$ matching in the DR approach.

Gauge dependence

We now turn to the residual gauge dependence in the predictions for the GW signal. Within the 3D approach, the bounce can be determined without the spurious insertion of the loop-improved effective potential by simply using the 3D tree-level potential, which yields inherently gauge-independent results. Nevertheless, we can assess the residual gauge dependence by studying the impact of substituting the loop-improved potential within the dimensionally reduced theory to determine the bounce action and varying the gauge-fixing parameter ξ. In the left plot of Fig. 5.13 we show the predictions for

the GW signal using the different approaches (the colors are defined as in the left plot of Fig. 5.12). We here used the background R_ξ-gauge in all cases, and the shown uncertainty bands arise from a variation of the gauge fixing parameter in the interval $\xi \in [-10, 10]$, while the solid lines indicate the predictions in the Landau gauge with $\xi = 0$. In a similar fashion to the scale dependence discussed above, also the residual gauge dependence is significantly reduced using the 3D approach compared to the 4D approach. The gauge-dependent 3D result using the two-loop level potential for the computation of the bounce solution is very close to the inherently gauge-independent result using the tree-level potential. The largest theory uncertainty from the residual gauge dependence is again observed for the 4D-$\widetilde{\text{OS}}$ approach.

We further scrutinize the residual gauge dependence in the dimensionally reduced EFT by showing in the right plot of Fig. 5.13 the predicted GW signals using the tree-level (green), one-loop level (purple) and two-loop level (blue) effective potentials for the computation of the bounce solutions. It is interesting to note that only the GW signal predicted using the two-loop level potential shows a very mild gauge dependence, whereas the gauge dependence of the GW signal predicted using the one-loop level potential is substantially more pronounced. Moreover, as already visible in the left plot of Fig. 5.13, the results using the two-loop level potential are in good agreement with those obtained using the tree-level potential. This comparison demonstrates that the numerical impact of using the two-loop-corrected potential is small and the induced gauge dependence remains very mild. Therefore, in the following phenomenological discussion in Section V.4.3, we use the gauge-independent tree-level potential in the 3D approach, where loop corrections are accounted for in the EFT by integrating out the dominant thermal fluctuations, providing a fully consistent computation of the bounce action.

V.4.2 Dependence on the bubble wall velocity

Although this chapter primarily focuses on the determination of thermodynamic parameters and the resulting GW signal, it is important to emphasize the role of a precise determination of the bubble wall velocity v_w in reliable GW predictions.

In Fig. 5.14, we illustrate the impact of varying the bubble wall velocity on the predicted GW spectrum, using the 3D-$\overline{\text{MS}}$ framework with a tree-level potential for the bounce calculation. As evident from the figure, the predicted GW signal is highly sensitive to the value of v_w, with variations in v_w leading to significant changes in both the peak

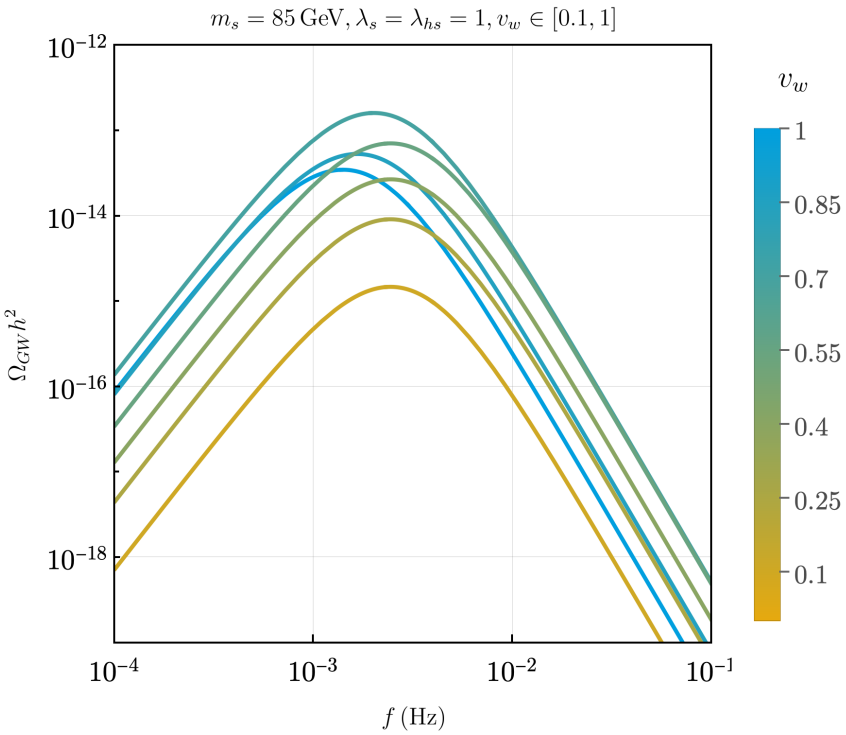

Figure 5.14: The impact of variation of the bubble wall velocity on the predicted GW signal for using the 3D-$\overline{\text{MS}}$ approach with the tree-level potential for the bounce calculation for $m_s = 85\,\text{GeV}$, $\lambda_s = \lambda_{hs} = 1$.

amplitude and moderate shifts in the peak frequency of the GW spectrum. For the specific benchmark point under scope, the highest predicted GW signal originating from the sound waves corresponds to the bubble wall velocity $v_w \simeq 0.7$.

The precise determination of the bubble wall velocity is a complex task that goes beyond the scope of this chapter (see Section III.3.2 for detailed discussion and Chapter VI for the impact of the loop corrections to the determination of the bubble wall velocity), while here we simply show the impact of varying v_w on the predicted GW signal.

V.4.3 Peak signal strengths in the (m_s, λ_{hs})-plane

In this section, we will identify and analyze more broadly the parameter space regions of the cxSM that can realize a SFOEWPT, and we quantify the theoretical uncertainty of the peak amplitude of the predicted GW signals. As was discussed in Section V.1, the cxSM has three independent BSM parameters: the singlet mass m_s, the singlet self-coupling λ_s, and the portal coupling λ_{hs}. While before we fixed m_s and λ_s and showed the predictions for the parameters describing the SFOEWPT as a function of λ_{hs}, we now scan parameter planes with varying m_s and λ_{hs}, while $\lambda_s = 1$ is kept fixed.

In the left column of Fig. 5.15, we show the (m_s, λ_{hs}) parameter plane for $\lambda_s = 1$, and the three different plots correspond to the three different methods employed in the previous sections: 4D-$\widetilde{\text{OS}}$ (top), 4D-$\overline{\text{MS}}$ (middle) and 3D-$\overline{\text{MS}}$ (bottom). The color coding in these plots is as follows: The light-gray region indicates either weak EWPTs with $\phi_{\text{min},h}(T_c)/T_c < 0.5$ or no first-order EWPT at all. The dark-gray region indicates where the minimum giving rise to the singlet vev is the global minimum through the whole thermal evolution of the Universe (down to $T = 0$), such that no EWPT can occur. The black region indicates a vacuum trapping [259], where the electroweak vacuum corresponds to the global minimum at zero temperature, but the conditions for the onset of an EWPT are never satisfied during the thermal history, and the Universe remains trapped in the false minimum in which only the singlet field has a vev.[8] Finally, the colored region indicates SFOEWPTs with $\phi_{\text{min},h}(T_c)/T_c \geq 0.5$, where the color coding shows the value of the peak amplitude of the GW signal produced during the transition. Comparing the three plots, we find that the overall shape and structure of the regions in parameter space where a first-order EWPT is predicted to be very similar for the different approaches. Also, the possible range of the peak amplitudes $\Omega_{\text{GW,peak}}h^2$ that we find are similar. The fact that the regions of parameter space predicting the strongest first-order EWPTs and the corresponding range of peak amplitudes for the GW signal remain very similar across the different approaches, despite the large discrepancies observed at the level of individual parameter points as shown in Fig. 5.12 and Fig. 5.13, is as mentioned above a consequence of the strong parametric sensitivity of the GW predictions, which dominates over the scheme-dependent differences if it is projected to parameter space regions of the cxSM.

A common feature across all approaches is that parameter points exhibiting the strongest GW signals lie near the vacuum trapping region (upper left edges of the colored regions). In this region along the diagonal, the peak amplitudes are the largest for lighter singlet masses m_s, whereas the percolation temperature grows with increasing singlet mass, rendering a weaker signal prediction for larger values of m_s. This fact can be used to define an upper bound on the singlet mass in the sense that the perturbative description of SFOEWPTs would break down for larger values of m_s. By requiring that the scalar couplings remain perturbative at the hard scale, we require the four-point vertex contributions to stay below 4π. This condition leads to the perturbativity bounds $\lambda_{hs}(\mu = \pi T) < 8\pi$ and $\lambda_s(\mu = \pi T) < 8\pi/3$, which in turn determine the upper

[8] Such a region can become viable and feature a SFOEWPT once seeded phase transitions from topological defects, such as from domain walls or cosmic strings (e.g. generated when the singlet field obtains a vev [260]) are considered. We do not include this possibility in our discussion.

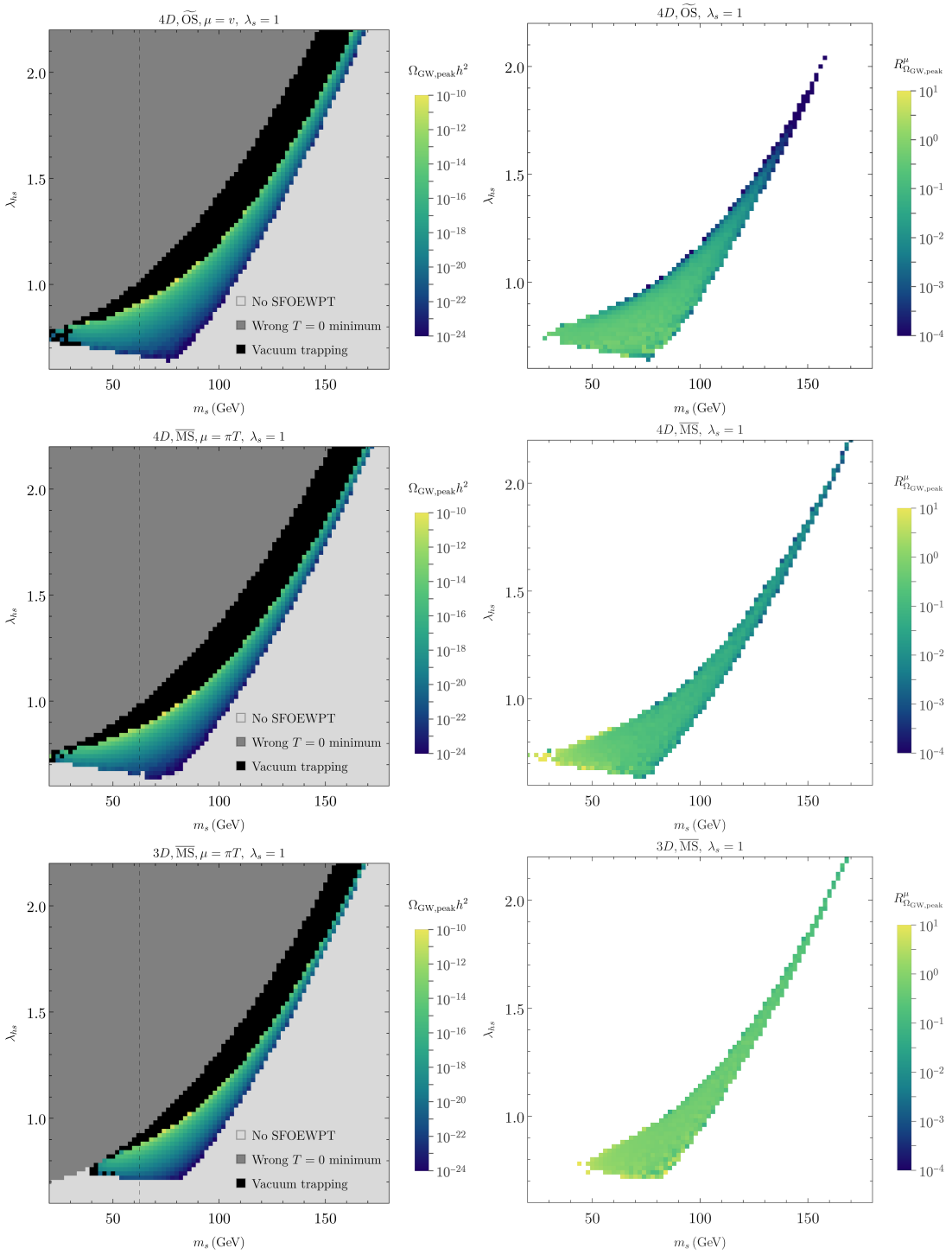

Figure 5.15: GW signal peak strength (*left*) and the corresponding scale variation ratio of Eq. (5.40) (*right*) for the 4D-$\overline{\text{MS}}$, 4D-$\widetilde{\text{OS}}$ and 3D-$\overline{\text{MS}}$ approaches in the Landau gauge. The dark gray region represents points for which no EWPT occurs, the light gray region represents points without a *strong* first-order EWPT (with $\phi_{\text{min},h}(T_c)/T_c < 1/2$) and the black region represents points with vacuum trapping. The vertical dashed line at $m_s = 62.5$ GeV indicates the region where the invisible Higgs decay channel opens.

limits on the singlet couplings at the input scale m_Z. Thence, the upper limit on the singlet mass beyond which a SFOEWPT no longer occurs for values of λ_{hs} and λ_s that are sufficiently small is approximately at 500–550 GeV (in agreement with the findings of Ref. [113]).

While for brevity, we show here only parameter planes with λ_s kept fixed, we also investigated the modifications to the parameter regions predicting a SFOEWPT for different values of λ_s. When varying the quartic singlet coupling λ_s, we find qualitatively similar features across all approaches considered. As λ_s increases, with the singlet mass held fixed, the parameter region giving rise to a strong GW signal is shifted toward higher values of λ_{hs}. Conversely, for fixed λ_{hs}, the mass range yielding a strong signal becomes narrower as λ_s decreases. Moreover, we find that the parameter region with a SFOEWPT extends to even larger mass and coupling values beyond the ranges shown in the plots.[9]

We leave a comprehensive phenomenological study of the parameter space regions suitable for GW signals that may be detectable with LISA considering the full three-dimensional parameter space of the cxSM for future work.

After having compared the different approaches for predicting the GW signals against each other, we now want to estimate the theoretical uncertainty of the GW predictions using either of the methods. In order to quantify the scale uncertainties in the predictions for the peak amplitudes of the GW signals, we introduce the ratio

$$R^{\mu}_{\Omega_{\text{GW,peak}}} = \frac{\Omega_{\text{GW,peak}}(\mu = 2\mu_0)}{\Omega_{\text{GW,peak}}(\mu = \mu_0/2)}\,, \tag{5.40}$$

where the central value μ_0 is chosen to be equal to v for the $\widetilde{\text{OS}}$ and to πT for the $\overline{\text{MS}}$ scheme. In the right plots of Fig. 5.15 we show the values of this ratio for the parameter space regions predicting a SFOEWPT (as defined in the left plots) across the different approaches. The regions with colored points do not coincide exactly between the left and the right plot in each row, because the ratio $R^{\mu}_{\Omega_{\text{GW,peak}}}$ can only be determined if both scale choices $\mu = 2\mu_0$ and $\mu = \mu_0/2$ predict a SFOEWPT. We also note that in the 3D-$\overline{\text{MS}}$ case, we determine the bounce action using the tree-level potential within the EFT. We have checked that the renormalization scale uncertainty (in this case, due to variation of the matching scale) would remain almost unchanged if the loop improved potential were taken instead. The right plots of Fig. 5.15 show that, going from top

[9] A parameter region with large portal couplings and larger singlet masses was explored in Ref. [253] in a different version of the singlet extension of the SM, where the singlet has a vev at zero temperature and thus mixes with the SM-like Higgs boson.

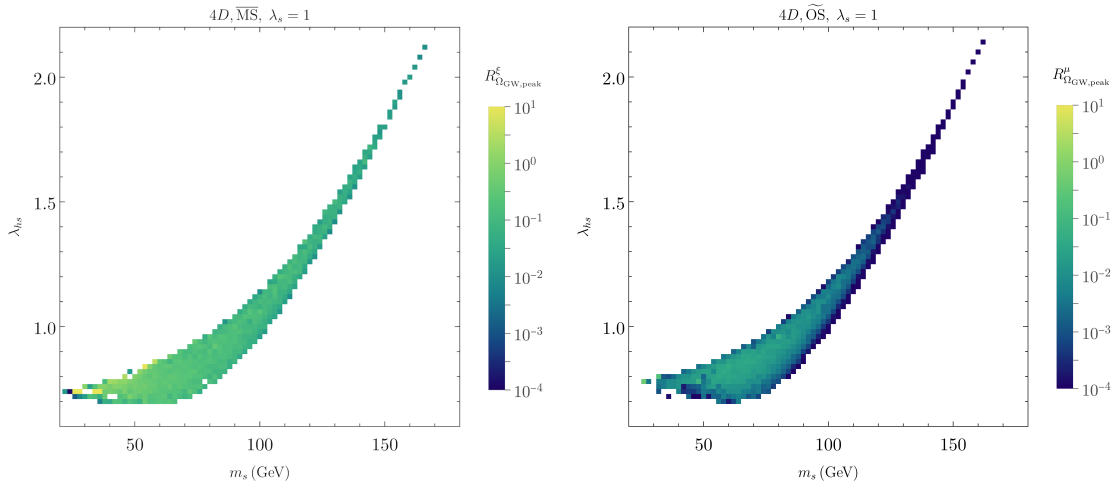

Figure 5.16: Uncertainty in the GW peak strength due to gauge-fixing parameter variation, quantified by Eq. (5.41), in the 4D-$\overline{\text{MS}}$ (*left*) and 4D-$\widetilde{\text{OS}}$ (*right*) schemes.

to bottom, i.e. from 4D-$\widetilde{\text{OS}}$ over 4D-$\overline{\text{MS}}$ to 3D-$\overline{\text{MS}}$, the scale dependence of the peak amplitudes of the GW signals are significantly reduced, as already apparent from the previous sections. The scale uncertainties of the $\Omega_{\text{GW,peak}}$ are most pronounced in the 4D-$\widetilde{\text{OS}}$ peak regions, especially at the upper left edge of the region shown where it can be as large as four orders of magnitude. This significant scale dependence in the 4D-$\widetilde{\text{OS}}$ approach is problematic since it is most severe in parameter space regions where the GW signals could be strong enough for detection by LISA. On the other hand, exploiting the hierarchies between thermal scales and using the DR approach leads to a greatly reduced uncertainty in the GW peak amplitude due to the scale variation, which is at most of one order of magnitude as is visible in the bottom right plot of Fig. 5.15.

Similarly, we assess the shift in the GW peak signal due to the variation of the gauge-fixing parameter. We do not show the gauge dependence of the 3D approach, because as discussed before, calculating the bounce action using the tree-level potential is the power-counting accurate approach here, and this is inherently gauge-independent. From our checks of individual parameter space points (see e.g. Fig. 5.13), it is clear, though, that the gauge dependence is small in the 3D approach even when including the loop-improved potential. To quantify the impact of residual gauge dependence in the 4D approach, we define for the ratio

$$R^{\xi}_{\Omega_{\text{GW,peak}}} = \frac{\Omega_{\text{GW,peak}}(\xi = 10)}{\Omega_{\text{GW,peak}}(\xi = -10)}. \tag{5.41}$$

In the left plot of Fig. 5.16 we show with the color coding the values of $R^{\xi}_{\Omega_{\text{GW,peak}}}$ using the

4D-$\overline{\text{MS}}$ potential, in the same parameter plane that was already shown in Fig. 5.15. One can observe that the variation of the gauge-fixing parameter leads to a change in the peak amplitude by approximately one order of magnitude across the entire parameter space giving rise to a SFOEWPT. This can be compared to the results using the 4D-$\widetilde{\text{OS}}$ approach that is shown in the right plot of Fig. 5.16. We observe a substantially stronger variation in the $R^{\xi}_{\Omega_{\text{GW,peak}}}$ values using the $\widetilde{\text{OS}}$ scheme, where the variation typically reaches at least two orders of magnitude and can rise to four orders of magnitude in the region predicting the strongest GW signals. As a result, the question of whether a parameter point of the cxSM predicts a GW signal that might be detectable with LISA can be answered less reliably using the 4D-$\widetilde{\text{OS}}$ approach. In the following, we present a more detailed analysis of the detectability of the GW signals with LISA in terms of the signal-to-noise ratio.

V.4.4 LISA SNR

If the SFOEWPT occurs at temperatures around 100 GeV, the resulting GW signal is expected to fall within the sensitivity range of the LISA interferometer. The detectability of such a signal can be quantified by computing the Signal-to-Noise Ratio (SNR). It can be computed as [30]:

$$\text{SNR} = \sqrt{\mathcal{T} \int_{-\infty}^{\infty} \left(\frac{\Omega_{\text{GW}}(f)h^2}{\Omega_{\text{sens}}(f)h^2} \right)^2 \mathrm{d}f}, \tag{5.42}$$

where $\Omega_{\text{sens}}(f)h^2$ is the nominal sensitivity of LISA to GW signals [261], and we assume the duration of the observations to be $\mathcal{T} = 4\,\text{years}$. Roughly speaking, if SNR $\gtrsim 1$, the GW signal is classified as detectable.[10]

Figure 5.17 presents the predicted SNRs at LISA determined using the various approaches discussed in Section V.3 for the parameter points with $m_s = 100$ GeV and varying coupling λ_{hs}. The colors represent the different approaches as in Fig. 5.6, and their theory uncertainties from the residual scale dependence (left plot) and gauge dependence (right plot) are indicated with the colored bands (see the discussion in Section V.3.1).

[10] As already mentioned before, we do not consider astrophysical foregrounds in our analysis. While we adopt a SNR threshold of 1 to assess detectability, it is worth noting that a threshold of $\mathcal{O}(10)$ is often used in a Bayesian statistical interpretation of potential signals (see also the discussion in Ref. [261]). The precise choice of the SNR threshold is of minor concern here, as the focus of this work is not on the absolute detectability of a signal, but rather on comparing the SNR predictions obtained from different computational approaches and assessing the associated theoretical uncertainties. As we will show, these uncertainties stemming from the perturbative description of the phase transition reach two orders of magnitude or more, depending on the method used, such that using the condition SNR $\gtrsim 10$ instead of 1 would not alter our conclusions.

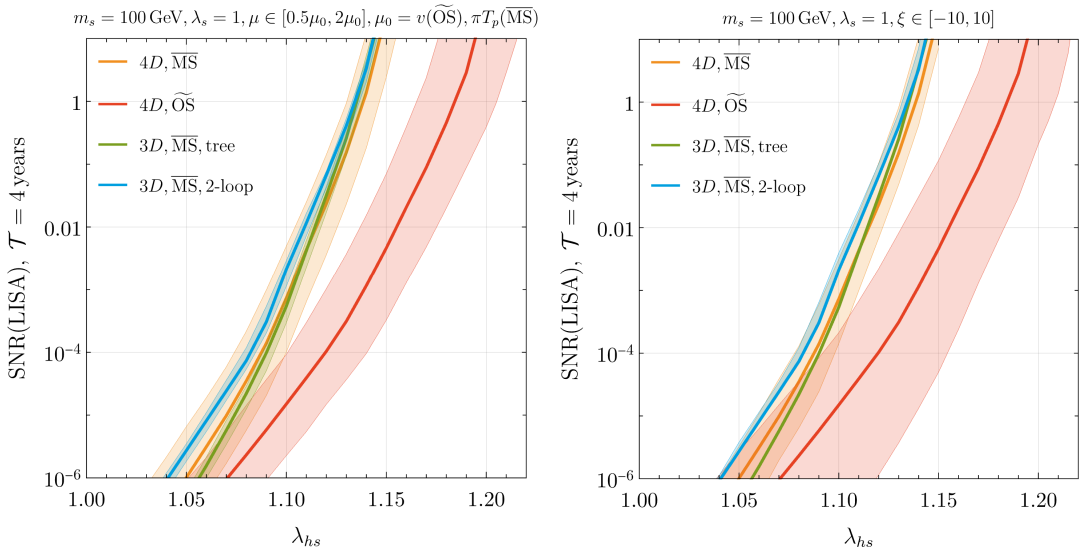

Figure 5.17: Predicted Signal-to-Noise Ratio (SNR) at LISA for $m_s = 100\,\text{GeV}$, $\lambda_s = 1$, $\lambda_{hs} \in [1, 1.2]$ and its renormalization scale (*left*) and gauge (*right*) dependencies.

We observe that the theory uncertainties are greatly reduced using the 3D-$\overline{\text{MS}}$ approach compared to the 4D approaches. Focusing on the 4D-approaches, we observe that the 4D-$\widetilde{\text{OS}}$ approach shows a more pronounced uncertainty from both the scale- and the gauge-dependence compared to the 4D-$\overline{\text{MS}}$ approach. Moreover, we observe an overall shift between the predicted SNRs from the approaches using the $\overline{\text{MS}}$ scheme and the 4D-$\widetilde{\text{OS}}$ approach. The shift between the two results can be attributed to the different choices of central renormalization/matching scales ($\mu = \pi T$ in the $\overline{\text{MS}}$ scheme and $\mu = v$ in the $\widetilde{\text{OS}}$ scheme), differences in the RGE running of the parameters, and missing momentum-dependent contributions in the $\widetilde{\text{OS}}$ scheme in the relations to the physical parameters (see Section V.2), as was discussed in more detail in relation to the differences in the prediction for the critical temperature T_c in Section V.3.1. This shift is so large that the uncertainty band of the 4D-$\widetilde{\text{OS}}$ approach does not overlap with the results from the 4D-$\overline{\text{MS}}$ approach in most parts of the displayed range of the coupling λ_{hs}, potentially indicating a poor behavior of the perturbative expansion at the considered one-loop level.

In Fig. 5.18 we show the SNR values at LISA for $\lambda_s = 1$ computed using the 3D-$\overline{\text{MS}}$ approach in the (m_s, λ_{hs}) plane. Compared to Fig. 5.15 and Fig. 5.16, the ranges for the singlet mass and the portal coupling in Fig. 5.17 are reduced to zoom into the region where high SNR values are predicted, and we only show the points predicting a GW signal with SNR $> 10^{-4}$. Despite the sizable theoretical uncertainties in the predicted SNRs across the different approaches, see the discussion above, the regions of the pa-

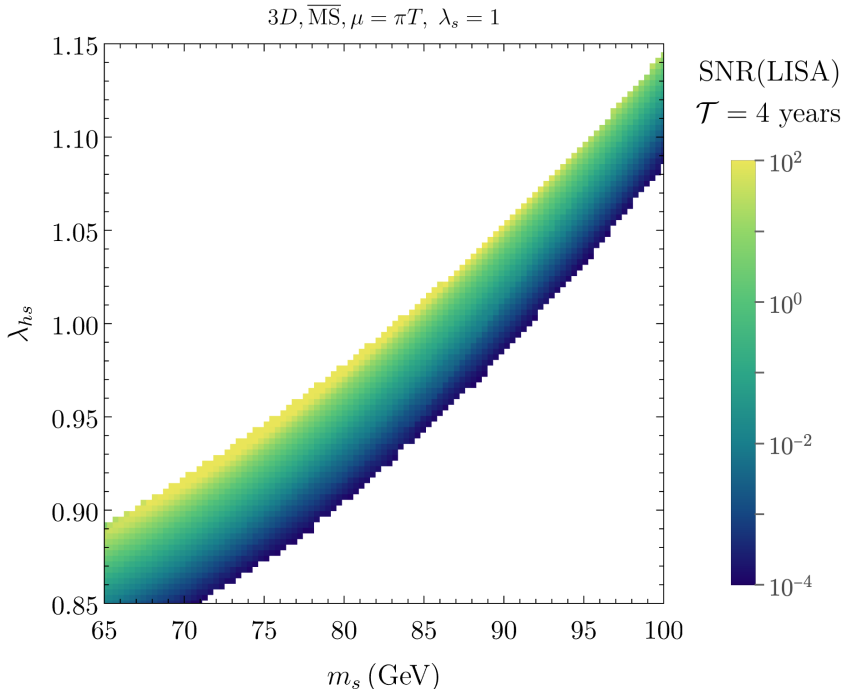

Figure 5.18: The absolute values of the SNR at LISA for $\lambda_s = 1$ obtained in the 3D-$\overline{\text{MS}}$ approach. We limit the heatmap scale at SNR $= 10^2$ to emphasize variations in lower-SNR regions, and only show points with SNR $> 10^{-4}$.

rameter space yielding SNR > 1 remain similar as a result of the extreme sensitivity of the strength of the GW signals on the model parameters m_s, λ_s and λ_{hs}. Consequently, we display in this plot only the results obtained using the 3D approach. As one can expect already from Fig. 5.15, the parameter region where SNR > 1 occupies only a rather restricted area in parameter space. Nevertheless, a detection of a GW signal at LISA consistent with a SFOEWPT would not, by itself, allow for a precise reconstruction of the underlying model parameters due to the visible approximate flat direction in the predicted SNRs, where a decrease in the SNR caused by larger singlet masses m_s can be compensated to a large extent by an increase in the portal coupling λ_{hs}. In particular, this degeneracy implies that the singlet mass cannot be tightly constrained from an experimental observation of a GW signal alone.

V.5 Validity of the EFT approach

The validity of the high-temperature EFT, which formally breaks down if $m_{h,s}/(\pi T) \gtrsim 1$, can be investigated through the impact of including higher-dimensional operators in the EFT on the obtained results. To assess the validity of truncating the EFT expansion at dimension-four operators, we perform the matching of dimension-six scalar operators

in the cxSM in the Landau gauge with the help of `DRalgo` [197]. Parametrically appearing at $\mathcal{O}(g^6)$ in the matching, they appear in the EFT tree-level potential as:

$$V_0^{3D} \supset c_{h^6}(\Phi^\dagger\Phi)^3 + c_{h^4s^2}(\Phi^\dagger\Phi)^2|S|^2 + c_{h^2s^4}\Phi^\dagger\Phi|S|^4 + c_{s^6}|S|^6, \tag{5.43}$$

and the Wilson coefficients read:

$$\begin{aligned}
c_{h^6} &= \frac{\zeta(3)}{6144\pi^4}\left(3g'^6 + 9g'^4g^2 + 9g'^2g^4 + 9g^6 + 2\left(-336y_t^6 + \lambda_{hs}^3 + 960\lambda_h^3\right)\right), \\
c_{h^4s^2} &= \frac{\zeta(3)}{512\pi^4}\lambda_{hs}\left(\lambda_{hs}(\lambda_s + \lambda_{hs}) + 12\lambda_{hs}\lambda_h + 48\lambda_h^2\right), \\
c_{h^2s^4} &= \frac{\zeta(3)}{1024\pi^4}\lambda_{hs}\left(5\lambda_s^2 + 6\lambda_s\lambda_{hs} + 2\lambda_{hs}(\lambda_{hs} + 6\lambda_h)\right), \\
c_{s^6} &= \frac{\zeta(3)}{1536\pi^4}\left(7\lambda_s^3 + \lambda_{hs}^3\right).
\end{aligned} \tag{5.44}$$

We use this subset of dimension-six operators to assess the validity of the EFT expansion. For this purpose, we do not take into account the gauge-dependence of these matching relations [36, 38], further operators at this order which include derivatives [35, 210] or corrections to the RGE running from the higher-dimensional operators, studied in Chapter IV.

It should be noted that in the dimensionally reduced theory, scalar fields have mass dimension $1/2$, hence the Wilson coefficients in Eq. (5.44) are dimensionless (see Section III.4). However, in this chapter, we refer to them as dimension-six operators, as they correspond to operators with mass dimension six in 4D.

Significant effects from these operators on thermodynamic observables and ultimately the GW signal indicate the failure of the truncation of the effective theory, i.e. the failure of the high-temperature expansion.

In the left plot of Fig. 5.19, we show how the inclusion of dimension-six operators in the EFT Lagrangian (turquoise) changes the predictions for the critical temperature T_c compared to the ones when truncating the EFT Lagrangian at dimension four (blue). For comparison, we also show the prediction using the 4D-$\overline{\text{MS}}$ approach (orange), and in all cases the bands around the solid lines show the theory uncertainty from the scale dependence. The comparison between the turquoise and the blue bands reveals that for higher temperatures adding higher-dimensional operators barely changes the thermodynamic observables, justifying the truncation of the high-temperature EFT Lagrangian in these regions. However, the difference between the turquoise and the blue bands becomes prominent for higher portal couplings, which correspond to lower critical tem-

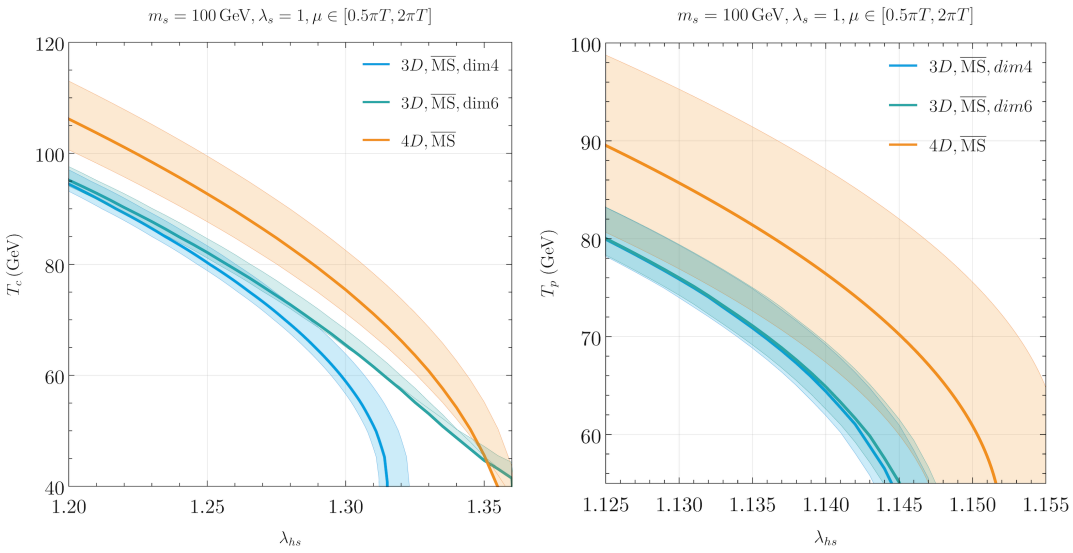

Figure 5.19: Critical (*left*) and percolation (*right*) temperatures determined within the 4D approach in the $\overline{\text{MS}}$ scheme as well as in the 3D approach in the $\overline{\text{MS}}$ scheme with and without the dimension-six operators of Eq. (5.43) in the Landau gauge for $m_s = 100\,\text{GeV}$, $\lambda_s = 1$. The bands represent the renormalization scale uncertainty, as before. Note that the parameter ranges differ between the two plots.

peratures. This indicates a breakdown of the high-temperature expansion in this regime. Notably, this issue arises precisely where the accuracy of the GW predictions is most critical, since the strength of the signal increases with decreasing transition temperature. We expect the 4D approach at low temperatures to more accurately describe the phase structure, because (apart from the, in this parameter region, small contribution from the AE-type resummation of daisy diagrams) it does not rely on high-temperature expansion. In agreement with this expectation, we observe that adding dimension-six terms to the EFT Lagrangian puts the predicted critical temperature closer to the one obtained within the 4D method for low temperatures.

In the right plot of Fig. 5.19 we show the predictions for the percolation temperature T_p, with the definition of the different bands as in the left plot discussed above. In contrast to the critical temperature, the impact of dimension-six operators on the percolation (and nucleation) temperature is significantly less significant, even for the parameter points predicting the lowest values of percolation temperature. A similar behavior was previously observed for phase transitions in the SMEFT [32, 36].

The thermodynamic observable that changes most significantly under the inclusion of the dimension-six operators in the high-T EFT is the phase transition strength α defined in Eq. (3.117). Figure 5.20 illustrates the modifications of the phase transition strength (*left* plot) and the peak amplitude of the GW signal (*right* plot), which we respectively

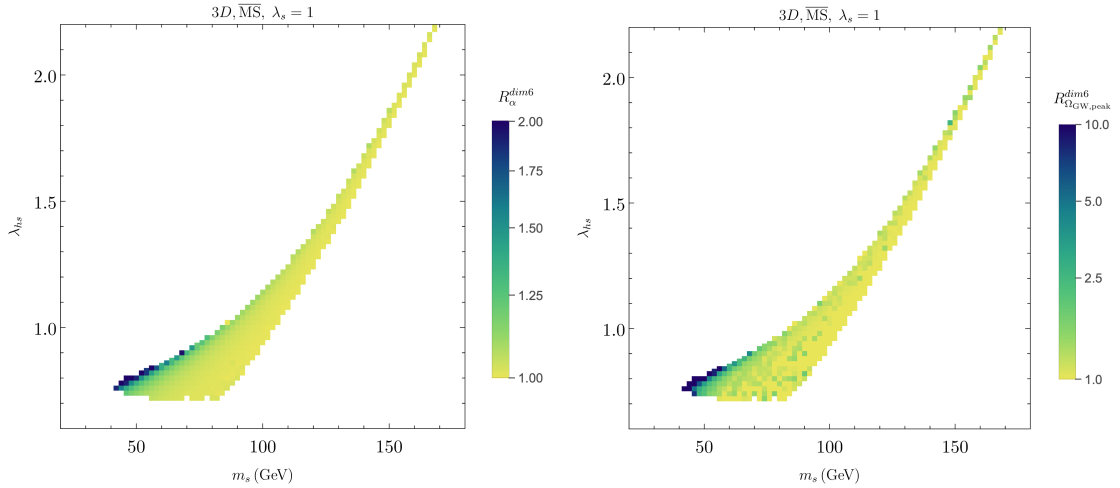

Figure 5.20: Variation ratio of Eq. (5.45) for the phase transition strength $\alpha(T_p)$ (*left*) and the GW peak strength $\Omega_{\text{GW,peak}}$ (*right*) obtained from the inclusion of dimension-six operators within the 3D approach. Note that the same colors correspond to different ranges in the two plots.

quantify in terms of the ratios

$$R_\alpha^{\text{dim6}} = \frac{\alpha[3D, \text{dim6}]}{\alpha[3D, \text{dim4}]} \quad \text{and} \quad R_{\Omega_{\text{GW,peak}}}^{\text{dim6}} = \frac{\Omega_{\text{GW,peak}}[3D, \text{dim6}]}{\Omega_{\text{GW,peak}}[3D, \text{dim4}]} \,. \tag{5.45}$$

The parameter space region predicting the strongest GW signals corresponds to the region of the lowest percolation temperatures, which in the (m_s, λ_{hs}) plane is located at the lower left corner of the banana-shaped band of points predicting a SFOEWPT (see Fig. 5.15).

The plots of Fig. 5.20 demonstrate that this is precisely the region where the truncation of the EFT Lagrangian becomes uncertain, as in this region the ratio R_α^{dim6} reaches values of about two (yellow points in the left plot). Accordingly, the peak amplitude of the GW signal given in Eq. (3.125), which for $\alpha \ll 1$ depends approximately quadratically on α, is also significantly altered. For these points, the inclusion of dimension-six operators give rise to an increase in the peak amplitudes by up to an order of magnitude, as is visible in the right plot of Fig. 5.20.

We checked that for both the strength α and the peak amplitude $\Omega_{\text{GW,peak}}$ the inclusion of dimension-six operators brings the predictions for these observables closer to the ones calculated within the 4D-$\overline{\text{MS}}$ approach. This observation could be interpreted as a hint that an accurate description of the phase transition just requires the inclusion of higher-dimensional operators beyond the renormalizable ones, instead of an indication of a complete breakdown of the high-T EFT framework. In this view, dimension-six

operators act as leading corrections that effectively capture relevant physics missing from the EFT truncated at dimension four. However, without systematically including and assessing the impact of operators of even higher dimension (such as dimension-eight terms), whose effects are expected to be smaller but not necessarily negligible, it is not possible to definitively conclude whether the observed improvement in agreement with the 4D-$\overline{\text{MS}}$ approach genuinely reflects increased predictive power, or instead indicates the onset of the breakdown of the EFT expansion.

V.6 Discussion

In this chapter, we presented a comprehensive study of the dynamics of the EWPT and the associated theory uncertainties of the predictions for physical observables characterizing the transitions in the cxSM, the SM extended by a complex gauge singlet scalar field. We focused on a scenario in which SFOEWPTs are realized in such a way that the singlet field has a non-vanishing vev before the transition and a vanishing vev after the transition. This is the simplest realization of a SFOEWPT that, if the singlet mass is larger than twice the Higgs boson mass, is expected to leave no detectable traces at the LHC. In order to investigate the robustness and precision of the perturbative description of the SFOEWPT, we compared a set of commonly used approaches. This set consists of two different input schemes in the 4D approach, the $\overline{\text{MS}}$ and the $\widetilde{\text{OS}}$ scheme, and of the 3D or high-temperature EFT approach, in which heavy modes are systematically integrated out, leading to an EFT in three spatial dimensions that captures the IR dynamics of the transition.

We presented an analysis of uncertainty bands arising from both residual scale and gauge dependence, affecting the predictions for thermodynamic observables, such as the critical temperature and latent heat, as well as the predicted GW signals and the corresponding SNRs at LISA. We showed that the uncertainties from the residual scale and gauge dependence are significantly reduced in the 3D approach. Moreover, focusing on the 4D approaches, we found that the gauge-parameter dependence in the $\widetilde{\text{OS}}$ scheme is enhanced compared to the one in the $\overline{\text{MS}}$ scheme. We showed how with increasing loop order of the effective potential in the 3D approach (up to the full two-loop effective potential in R_ξ gauge) the gauge dependence and the associated theory uncertainty is reduced order by order, and we discussed in detail how this follows from the the gauge-parameter dependence of the effective potential governed by the Nielsen identity.

In both the 4D and the dimensionally reduced 3D frameworks, we obtained gauge-independent results for the quantities characterizing the phase transition and the resulting GW signals by applying the $\hbar$-expansion. In the 4D approach, we observed that the gauge-independent results at the considered one-loop level exhibit significant numerical deviations from the gauge-dependent result where one directly minimizes the loop-corrected effective potential, indicating the need for higher-loop corrections to achieve a gauge-independent result with sufficient numerical precision. On the other hand, in the 3D EFT, the gauge-independent results obtained by making use of the $\hbar$-expansion are in excellent numerical agreement with those derived from a direct minimization of the loop-corrected potential in a gauge-dependent way. As a result, using the $\hbar$-expansion, one-loop $\overline{\text{MS}}$ relations between the model parameters, the DR with NLO matching, integrating out hard and soft scales, and the effective potential at the two-loop level, we achieved a gauge-independent and numerically precise description of SFOEWPTs in the cxSM. As the main remaining theoretical uncertainty in the parameter space regions predicting detectable GW signals at LISA, we identified the impact of higher-dimensional operators in the dimensionally reduced EFT, see the discussion below.

Despite the sizable uncertainties associated to the different approaches used to describe the phase transition dynamics, the parameter regions where SFOEWPTs occur remain similar. This is a result of the large parametric dependence of the transition strengths on the model parameters of the cxSM. While a SFOEWPT can be accommodated over wide parameter regions of the singlet mass and couplings, generating a GW signal that is potentially detectable with LISA, requires a significant amount of fine-tuning among the cxSM parameters m_s, λ_{hs} and λ_s. Regarding the occurrence of a SFOEWPT, using the perturbativity limit on scalar couplings, we obtained an upper bound on the singlet mass of $m_s \lesssim 500$–550 GeV. For larger masses of the singlet state, the coupling values that would be required to realize a SFOEWPT fall outside of the perturbative regime, such that non-perturbative (lattice) computations would be required to study whether the cxSM allows for a SFOEWPT and an associated GW signal in reach of LISA.

Although the parameter space regions predicting potentially detectable GW signals are largely consistent across the different approaches, within these parameter regions the magnitude of the predicted GW signals can vary by several orders of magnitude, depending on the specific perturbative framework employed. In particular, the 4D approach using the $\widetilde{\text{OS}}$ scheme predicts significantly smaller SNRs, typically by about two orders of magnitude, compared to the $\overline{\text{MS}}$ scheme. Moreover, the 4D-$\widetilde{\text{OS}}$ approach is subject to considerably larger theoretical uncertainties. A variation of the renormalization scale

by a factor of two can induce changes in the predicted SNRs of up to four orders of magnitude. On the other hand, the 4D approach using the $\overline{\text{MS}}$ scheme yields SNRs that are in fairly good agreement with those obtained in the dimensionally reduced 3D approach. The differences between these two approaches are smaller than the intrinsic theoretical uncertainties from the residual scale and gauge dependence associated with the 4D-$\overline{\text{MS}}$ approach, which are at the level of about one order of magnitude. Ultimately, the 3D EFT approach offers the most stable predictions in this regard. When employing NLO matching at $\mathcal{O}(g^4)$, the residual scale dependence in the SNRs is reduced by about one order of magnitude. In combination with the fact that the 3D approach can be combined with the $\hbar$-expansion to remove residual gauge dependence without discarding numerically important contributions, the application of the high-T EFT is therefore in most parts of the parameter space the most reliable and precise framework to study SFOEWPTs in the cxSM.

However, the 3D EFT approach is subject to an additional intrinsic theory uncertainty from truncating the EFT at finite operator dimension. To assess this uncertainty, we compared results including only renormalizable/dimension-four operators with those also incorporating dimension-six operators. At high temperature, both types of results agree well, indicating a reliable behavior of the EFT. However, for lower temperatures, particularly below $T_c \lesssim 80$ GeV, the dimension-six operators noticeably affect the critical temperature and enhance the predicted strength of the phase transition and GW signals. We found that the impact on the critical temperature is more pronounced than on the percolation temperature. Nevertheless, the effects on the GW signals (which are computed at percolation) remain sizable. Specifically, we observed changes in the transition strength α of up to 100% and shifts in the GW peak amplitude by up to an order of magnitude. Since stronger GW signals correlate with lower transition temperatures, these effects become relevant precisely where the prospects for a GW detection with LISA are best. Interestingly, the inclusion of dimension-six operators brings the predictions of the 3D approach closer to the results obtained using the 4D-$\overline{\text{MS}}$ approach, which may be more reliable in this regime since it relies to a much lesser extent on the high-T expansion. Still, since we included only a subset of all possible dimension-six operators, and since higher-dimensional terms are not considered with which the behavior of the EFT could be further checked, it remains unclear whether this signals a genuine improvement or merely a breakdown of the EFT. We leave a dedicated study in this direction for future work.

In addition to this study of the thermodynamic observables of the cxSM, we also dis-

cussed many of the technical details. This includes a demonstration of the cancellation of the scale dependence by including the RGE evolution of the couplings in the 4D-$\overline{\text{MS}}$ approach; the reduction of the scale dependence with increasing matching order in the 3D EFT; a comparison of the results from a direct minimization of the effective potential compared to the gauge-independent results using the $\hbar$-expansion, showing good agreement between the two types of results only in the 3D approach; a comparison of different gauge-fixing choices (R_ξ and Fermi gauges); and the reduction of explicit scale and gauge dependence when including higher loop orders of the effective potential.

VI – BUBBLE WALL DYNAMICS WITH LOOP CORRECTIONS

The career of a young theoretical physicist
consists of treating the harmonic oscillator in
ever-increasing levels of abstraction.

— Sidney Coleman

In this chapter, we focus on calculating the terminal velocity of the bubbles: the wall speed. This is a difficult quantity to calculate, and the calculations usually require both dealing with kinetic theory and hydrodynamics (see Section III.3.2). It is common in these calculations to approximate the scalar potential — that enters the calculations — as the effective potential (similar to an ad-hoc substitution of the effective potential in the bounce calculation, as discussed in Section III.4.2). This procedure, while reasonable as a first approximation, is heuristic. And one invariably has to deal with taking roots of negative squared masses that appear. These strange terms come from classical fluctuations, and so can in principle be handled numerically. For example, in the case of nucleation rates such fluctuations give rise to functional determinants.

We systematically add one-loop classical fluctuations to the wall speed calculations; thus extending partial derivative-expansion results [262], which, as we show, inadequately describe the loop corrections in the bubble background. The result is analogous to incorporating fluctuations around the bounce for nucleation-rate determination [163]. We both provide a general framework for these calculations, give specific examples and discuss the setup for more complicated cases, realized in realistic models, when the multifield, hydrodynamic and non-constant friction effects are included. We also compare our results with the effective potential approximation, showing that the latter can lead to significant deviations from the more complete result.

VI.1 Classical fluctuations and Langevin dynamics

Our goal is to describe the motion of bubble walls during first-order phase transitions. We will assume throughout this chapter that a high-temperature expansion is applicable. That is, the typical mass of the Higgs field is smaller than the temperature: $m_h \sim g^2 T \ll T$. Here g represents a generic coupling, which is assumed to be small: $g \ll 1$. Given these assumptions, the width of the bubble wall is of order $L_w \sim m_h^{-1} \gg T^{-1}$. As such, we can integrate out the quantum fluctuations that occur on length scales $L \sim T^{-1}$. This is then reflected in the fact that our effective mass parameters and couplings implicitly depend on the temperature through matching relations [49, 263], following discussion in Section III.4. Schematically, these matching relations are of the form

$$m^2 \to m^2 + \#g^2 T^2, \quad g^2 \to g^2 + \#g^4 \log T, \ \ldots \tag{6.1}$$

Another effect is that quantum fluctuations — or equivalently plasma particles — will resist the motion of any external scalar field or fluid flow. In general such dissipative effects are rather complicated. So in this chapter, we assume that the collision rates are large enough for a Chapman-Enskog expansion — which formalizes the hydrodynamic limit — to be applicable,[1] and that we can incorporate the dissipation effectively in a friction-parameter η (following Section III.3.2):

$$\ddot{\phi} = \vec{\nabla}^2 \phi - H'(\phi, \theta) - \eta u \cdot \partial \phi, \tag{6.2}$$

where u^μ is the fluid velocity. $H(\phi, \theta)$ is a Hamiltonian, which includes both the scalar tree-level potential $V(\phi)$ and interactions with other fields $H_{\text{int}}(\phi, \theta)$; interacting fields are collectively denoted here as θ.

We can conveniently split the scalar field into the background field configuration (bubble profile) $\overline{\phi}$ and fluctuation $\hat{\phi}$: $\phi = \overline{\phi} + \hat{\phi}$, where, on average, the fluctuations vanish $\langle \hat{\phi} \rangle = 0$ and the thermally averaged background configuration satisfies $\langle \overline{\phi} \rangle = \overline{\phi}$.

The remaining physics is purely classical — in the statistical mechanics sense — and fluctuations occur on length scales $L \sim (g^2 T)^{-1}$. An elegant way to incorporate such

[1] We should mention that this assumption is by no means necessary for this chapter, but the resulting formulas are simpler.

fluctuations is to introduce noise via the fluctuations-dissipation theorem [264, 265]:

$$\ddot{\phi} = \vec{\nabla}^2\phi - H'(\phi,\theta) - \eta u\cdot\partial\phi + \zeta(\vec{x},t), \tag{6.3}$$

where we require the noise, $\zeta(\vec{x},t)$, to satisfy

$$\langle\zeta(x)\zeta(x')\rangle = 2\eta T\delta^{(4)}(x-x'), \quad \langle\zeta(x)\rangle = 0. \tag{6.4}$$

A sanity-check of this setup is to consider the free ($V' = m^2\phi, H_{\text{int}} = 0$) scalar-field propagator in the plasma frame ($u^0 = 1$). In the momentum space, we have

$$\begin{aligned}\ddot{\phi} &= -E^2\phi - \eta\dot{\phi} + \zeta(\vec{k},t),\\ E^2 &= \vec{k}^2 + m^2.\end{aligned} \tag{6.5}$$

The solution can be split into an homogenous solution and an inhomogenous solution. The homogenous solution simply correspons to the decay, so we focus on the part proportional to the noise. By using variations of parameters one finds the particular solution to be:

$$\begin{aligned}\phi_p(\vec{k},t) &= \frac{1}{\omega}\int_0^t ds e^{\eta/2(s-t)}\sin\left(\frac{\omega}{2}(s-t)\right)\zeta(\vec{k},s),\\ \omega^2 &= 4(\vec{k}^2+m^2) - \eta^2,\end{aligned} \tag{6.6}$$

where we have assumed that $4(\vec{k}^2+m^2)-\eta^2 > 0$.

After averaging over the noise we then find for late times $t \gg \eta^{-1}$:

$$\left\langle\phi(\vec{k},t)\phi(\vec{k'},t)\right\rangle = \delta^{(3)}(\vec{k}+\vec{k'})\frac{T}{(\vec{k}^2+m^2)}. \tag{6.7}$$

Note that the Langevin setup is by no means necessary. For example, explicit averaging over initial states [266] is also possible. Both setups are straightforward to evaluate numerically, and can as such be compared against the result of the next sections.

Given equation (6.3) we can find the wall speed by working in the wall frame where $\dot{\phi} = 0$. To be specific, we choose the wall to be in the z direction. We first consider the wall speed to be constant for simplicity and so omit any hydrodynamic effects. The result can be generalized to include hydrodynamic effects as discussed in Section VI.5. Then we can, to the LO, omit the noise and solve for the scalar field by enforcing that it

reaches the true, and respectively the false, vacuum at $z = \pm\infty$:

$$\begin{aligned} \mathbf{eom}_{\mathrm{LO}} &= -\partial_z^2\overline{\phi}_0(z) + V'(\overline{\phi}_0(z)) + \omega_0\partial_z\overline{\phi}_0(z) = 0, \\ \lim_{z\to\infty}\overline{\phi}_0(z) &= \phi_{\mathrm{TV}}, \quad \lim_{z\to-\infty}\overline{\phi}_0(z) = \phi_{\mathrm{FV}}, \end{aligned} \tag{6.8}$$

where the friction term comes with the Lorentz-factor $\omega_0 \equiv \eta\gamma_w v_w$ after the boost to the frame of the moving bubble.

This equation can be solved numerically by shooting (or, in some cases, analytically, see example in Section VI.4). This then provides a value for ω_0, v_w and a bubble profile $\overline{\phi}_0(z)$ for the given η and $V'(\phi)$.

Given a LO value for the wall speed and a bubble profile, we can then find corrections in a perturbative manner. Later in this chapter, we will add one-loop corrections explicitly, but for illustrative purposes imagine that our equations of motion are augmented by some small term $g\Omega(z)$. Then, we can expand our original equation of motion around the LO field

$$\overline{\phi}_0(z) \to \overline{\phi}_0(z) + g\overline{\phi}_1(z), \quad \omega_0 \to \omega_0 + g\omega_1. \tag{6.9}$$

Consequently, the leading $\mathcal{O}(g)$ corrections obey the equation

$$\mathbf{eom}_{\mathrm{NLO}} = \left(-\partial_z^2 + \omega_0\partial_z + V''(\overline{\phi}_0(z))\right)\overline{\phi}_1(z) + \Omega(\overline{\phi}_0(z), z) + \omega_1\partial_z\overline{\phi}_0(z). \tag{6.10}$$

This is just an inhomogeneous ordinary differential equation that can be solved via the Green function formalism, in this case of the operator $\left(-\partial_z^2 + \omega_0\partial_z + V''(\overline{\phi}_0(z))\right)$. This means that we can directly find $\overline{\phi}_1(z)$ as:

$$\overline{\phi}_1(z) = -\int dz' G_0(z, z') \left[\Omega(\overline{\phi}_0(z'), z') + \omega_1\partial_{z'}\overline{\phi}_0(z')\right]. \tag{6.11}$$

However, note that a solution does not generally exist due to the presence of the zero mode $\overline{\phi}_0'(z)$. As such, we need to use the Fredholm alternative, which specifies that a solution only exists if

$$\omega_1 = -\frac{\int dz'\partial_{z'}\overline{\phi}_0(z')e^{-\omega_0 z'}\Omega(\overline{\phi}_0(z'), z')}{\int dz'(\partial_{z'}\overline{\phi}_0(z'))^2 e^{-\omega_0 z'}}, \tag{6.12}$$

where we have made the operator self-adjoint by the shift $\overline{\phi}_1(z) \to \overline{\phi}_1(z)e^{z\omega_0/2}$.

As such, the NLO wall speed can be found via Eq. (6.12) without having to explicitly

solve the equation of motion Eq. (6.10).[2]

VI.2 Propagators in inhomogeneous backgrounds

In this section, we evaluate the Higgs field propagator in the inhomogeneous background bubble-wall profile;[3] the propagator is simply the correlator of the field's fluctuations $\hat{\phi}$. For other particles — Goldstones, other scalars, and vectors — the result follows in exactly the same manner.

In Appendix C, we present pedagogical details on how to find the propagator in homogeneous backgrounds, which provides useful intuition for the techniques used in this section.

We assume that each field is thermalized in a Langevin setup. However, we stress that this assumption is not required; and the result without damping [266], for example, follows after setting the damping to zero in the end.

In this section, we treat the wall speed — and friction — as a constant, thus neglecting hydrodynamic effects. This is just to save ink, and we discuss the full result with non-constant friction coefficients, hydrodynamics backreactions and the determination of multifield propagators in Section VI.5.

Given the assumptions listed above, the Higgs propagator is the Green's function of the operator

$$\widehat{L}_H\hat{\phi} = \left(-\partial_z^2 - \vec{\nabla}_\perp^2 + \omega_0\partial_z + V''(\overline{\phi}_0(z)\right)\hat{\phi}, \tag{6.13}$$

where $\omega_0 = \eta\gamma_w v_w\,|_{\rm LO}$, evaluated through Eq. (6.8). As it stands, this operator is not self-adjoint, so it is useful to perform the change of basis $\hat{\phi} \to e^{-\omega_0/2z}\hat{\phi}$:

$$\widehat{L}_H \to \left(-\partial_z^2 - \vec{\nabla}_\perp^2 + W(z)\right), \quad W(z)\,[4] \equiv V''(\overline{\phi}_0(z)) + \frac{\omega_0^2}{4}. \tag{6.14}$$

The Higgs propagator $G(\vec{x},\vec{y}) = \left\langle\hat{\phi}(\vec{x},t)\hat{\phi}(\vec{y},t)\right\rangle$ satisfies the equation

$$\widehat{L}_H G(\vec{x},\vec{y}) = \delta^3(\vec{x}-\vec{y}). \tag{6.15}$$

[2] For the example given in the Section VI.4, we numerically solved Eq. (6.10) to verify that Eqs. (6.11) and (6.12) hold.

[3] See [267] for an alternative way to find the Green's function.

[4] For other particles, the only modification of the equation will be in the function $W(z)$.

We can further use the cylindrical symmetry of $\widehat{L}_H$ to write

$$G(\vec{x},\vec{y}) = \int dk \sum_m e^{im(\phi-\phi')} J_m(k\rho) J_m(k\rho') G_k(z,z'), \tag{6.16}$$

where $G_k(z,z')$ obeys the equation

$$(\partial_z^2 - k^2 - W(z)) G_k(z,z') = -2\delta(z-z'). \tag{6.17}$$

We now have but to find a one-dimensional Green's function for each value of k by solving Eq. (6.17).

To find the solution of (6.17), we solve the homogeneous equation for $z < z'$ and $z > z'$ separately, and then match the two solutions at $z = z'$ by imposing the appropriate jump conditions. To solve the homogeneous equations, we first consider the asymptotic behavior of the solutions to find two independent homogeneous solutions $G_k^<$ and $G_k^>$ of the equation.

The asymptotic behavior of the solutions is

$$\begin{aligned} z \to -\infty &: \; G_k^< \sim \exp\left[z\sqrt{k^2+W(-\infty)}\right], \; G_k^> \sim \exp\left[-z\sqrt{k^2+W(-\infty)}\right], \\ z \to \infty &: \; G_k^< \sim \exp\left[-z\sqrt{k^2+W(\infty)}\right], \; G_k^> \sim \exp\left[z\sqrt{k^2+W(\infty)}\right]. \end{aligned} \tag{6.18}$$

These give us the hint that in order to facilitate a well-behaved numerical solution it is auspicious to define

$$\begin{aligned} &G_k^< = A^<(z') T_k(z) \Psi^<(z), \; G_k^> = A^>(z') H_k(z) \Psi^>(z), \\ &\Psi^{</>}(z) = \exp\left[\pm \int_0^z \sqrt{k^2+W(s)+F(s)} ds\right]. \end{aligned} \tag{6.19}$$

for $z < z'$ and $z > z'$ respectively. The full solutions can now be found by solving the following equations numerically:

$$\begin{aligned} &T_k'' + 2\sqrt{k^2+W(z)+F(z)}\, T_k' + \frac{W'(z)+F'(z)}{2\sqrt{k^2+W(z)+F(z)}} T_k + F(z)\, T_k = 0 \\ &\text{with } T_k'(-\infty) = 0 \text{ and } T_k(-\infty) = 1, \end{aligned} \tag{6.20}$$

$$\begin{aligned} &H_k'' - 2\sqrt{k^2+W(z)+F(z)}\, H_k' + \frac{W'(z)+F'(z)}{2\sqrt{k^2+W(z)+F(z)}} H_k + F(z)\, H_k = 0 \\ &\text{with } H_k'(\infty) = 0 \text{ and } H_k(\infty) = 1. \end{aligned} \tag{6.21}$$

Here we have introduced an auxiliary function $F(z)$ such that $F(z)+W(z)\geq 0$ for all z and $F(z)\to 0$ as $z\to\pm\infty$; this is just to simplify the numerical evaluations, and the final result is, of course, independent of $F(z)$.

Finally, given $T_k(z)$ and $H_k(z)$, following the standard jumping conditions at $z=z'$, the full propagator takes the form:

$$\begin{aligned} G_k(z,z') = \left[\sqrt{k^2+W(\infty)}T_k(\infty)\right]^{-1} &[\theta(z-z')T_k(z')\Psi^<(z')H_k(z)\Psi^>(z) \\ &+\theta(z'-z)T_k(z)\Psi^<(z)H_k(z')\Psi^>(z')] \end{aligned} \tag{6.22}$$

The single point propagator, the quantity necessary to calculate one-loop corrections to the bubble (see Section VI.3), is then simply given by

$$G(\vec{x},\vec{x}) = \frac{1}{4\pi}\int_0^\infty dk k G_k(z,z). \tag{6.23}$$

In practice, one can only solve equation Eq. (6.17) for so many k, and, moreover, handling UV-divergences numerically is troublesome, hence, we split the integral of Eq. (6.23) as follows:

$$\begin{aligned} 4\pi G(\vec{x},\vec{x}) = &\underbrace{\int_0^\infty dk k G_k^{\text{free}}(z,z)}_{\text{finite in dimReg}} \\ &+\underbrace{\int_0^1 dk k\left[G_k(z,z)-G_k^{\text{free}}(z,z)\right]}_{\text{finite}} + \underbrace{\int_1^{k_{\max}} dk k\left[G_k(z,z)-G_k^{\text{WKB}}(z,z)\right]}_{\text{finite}} \\ &+\underbrace{\int_{k_{\max}}^\infty dk k\left[G_k(z,z)-G_k^{\text{WKB}}(z,z)\right]}_{\text{finite}} + \underbrace{\int_1^\infty dk k\left[G_k^{\text{WKB}}(z,z)-G_k^{\text{free}}(z,z)\right]}_{\text{finite}} \end{aligned} \tag{6.24}$$

where G_k^{free} is a free propagator of a scalar particle with the mass $m^2=W(\infty)$ and for the first integral in Eq. (6.24) the dimensional regularization was employed for UV regularization, leading to effective-potential-like result $-\frac{W(\infty)^{1/2}}{4\pi}$.

The WKB approximation (see Section VI.2.2), which is applicable for large k values, is introduced to accelerate the numerical convergence. The total integral, as it should be, does not depend on the arbitrary cut-off $k_{\max}$. The split around (the exact value is arbitrary) $k=1$ is necessary since the WKB terms diverge as $k\to 0$

VI.2.1 Handling zero-modes

Contrary to other particles, for Higgs and Goldstone propagators hit an additional obstacle due to the presence of zero-modes. Take, for example, the Higgs case, where $W(z) = V''(\overline{\phi}_0(z)) + \frac{\omega_0^2}{4}$. The zero mode is then $\partial_z\overline{\phi}_0(z)e^{-z\omega_0/2}$; the presence of zero modes is an artifact of the broken symmetry of the equation of motion by the background solution. A normal eigenfunction expansion then implies that

$$\begin{aligned} G_k(z,z') &= \frac{2}{k^2}\frac{\partial_z\overline{\phi}_0(z)e^{-z\omega_0/2}\partial_{z'}\overline{\phi}_0(z')e^{-z'\omega_0/2}}{N_\phi} + \dots, \\ N_\phi &= \int ds\partial_s\overline{\phi}_0(s)^2e^{-s\omega_0} \end{aligned} \tag{6.25}$$

The zero-mode term vanishes in the integral over k if we use dimensional regularization, but small k values are still troublesome numerically. To deal with this snag we subtract 0 from (6.24):

$$0 = -\frac{2}{N_\phi}\partial_z\overline{\phi}_0(z)^2e^{-z\omega_0}\int dkk^{-1} = -\frac{2}{N_\phi}\partial_z\overline{\phi}_0(z)^2e^{-z\omega_0}\left[\int_0^{k_{\max}} + \int_{k_{\max}}^{\infty}\right]dkk^{-1}. \tag{6.26}$$

We then explicitly add the first term to equation (6.24) for each k, while the second term effectively gives $\frac{2}{N_\phi}\partial_z\overline{\phi}_0(z)^2e^{-z\omega_0}\log k_{\max}$.

The procedure is the same for Goldstone modes; for example, for a complex scalar where $W(z) = \overline{\phi}_0(z)^{-1}V'(\overline{\phi}_0(z)) + \frac{\omega_0^2}{4}$ the zero mode is $e^{-z\omega_0/2}\overline{\phi}_0(z)$, and the procedure is identical to the Higgs case.

VI.2.2 The WKB approximation

As motivated above, it is useful to know the behavior of the propagator for very large k values. The way out is to use a WKB approximation in that regime. In particular, consider the equation (for our application, we will apply this to the homogeneous Eq. (6.17) for the solutions $G_k^{</>}$):

$$\begin{aligned} \partial_z^2\Phi_k &= A^2(z)\Phi_k, \\ A^2(z) &= k^2 + W(z). \end{aligned} \tag{6.27}$$

If $k \gg W(z)$ the z-dependence of $W(z)$ is just a minor inconvenience. This justifies the ansatz

$$\Phi_k = \exp(\epsilon^{-1} S_0 + S_1 + \epsilon S_2 \ldots), \tag{6.28}$$

where we have re-scaled $\partial_z \to \epsilon \partial_z$ to keep track of derivatives acting on $W(z)$. Following this, the solution is

$$\begin{aligned} S_0(z) &= \pm \int_0^z ds A(s), \\ S_1(z) &= -\frac{1}{2} \log |A(z)| + \text{const} \\ S_2(z) &= \int ds \frac{2AA'' - 3(A')^2}{8A^3} \end{aligned} \tag{6.29}$$

These considerations imply that for $G_k^{</>}$, expanding for large k, we find

$$\log G_k^{</>} \approx \pm \left[kz \pm \frac{1}{2k} \int ds W(s) \right] + \log \left| 1 - \frac{1}{4k^2} W(z) \right|. \tag{6.30}$$

Similar expansion can be made with the functions that appeared in our ansatz Eq. (6.19):

$$\Psi^{</>}(z) = \exp \left[\pm \int_0^z \sqrt{k^2 + W(s)} ds \right] \approx \exp \left[\pm kz \pm \frac{1}{2k} \int_0^z ds W(s) \right]. \tag{6.31}$$

Lastly, after imposing the boundary conditions, we find the asymptotic expansion for T_k and H_k:

$$\begin{aligned} T_k &\approx 1 - \frac{W(z) - W(-\infty)}{4k^2}, \\ H_k &\approx 1 - \frac{W(z) - W(\infty)}{4k^2}. \end{aligned} \tag{6.32}$$

VI.2.3 Derivative expansion

An analytic approximation to the propagator (derivative expansion) can be obtained under the assumption that the field-dependent mass is large: $\partial_z^2 \ll M^2(z)$. To derive a derivative expansion recall the equation of motion for the propagator:

$$\left[-\partial_z^2 - \vec{\nabla}_\perp^2 + W(z) \right] G(\vec{x}, \vec{x}') = \delta^3(\vec{x} - \vec{x}'). \tag{6.33}$$

Then, following [268], one can set $\vec{x}' = \vec{x} + \vec{y}$ and solve for G in powers of ∂_z. Subsequently, one finds

$$\begin{aligned} G(\vec{x},\vec{x}) = &-\frac{1}{4\pi}\sqrt{W(z)} + \frac{1}{512\pi W(z)^{5/2}}\left(\partial_z W(z)\right)^2 - \frac{1}{328\pi W(z)^{3/2}}\partial_z^2 W(z) \\ &+\frac{105}{32768\pi^2 W(z)^{11/2}}\left(\partial_z W(z)\right)^4 - \frac{77}{12288\pi^2 W(z)^{9/2}}\left(\partial_z W(z)\right)^2\partial_z^2 W(z) \\ &+\frac{3}{2048\pi^2 W(z)^{7/2}}\left(\partial_z^2 W(z)\right)^2 + \frac{1}{512\pi^2 W(z)^{7/2}}\partial_z W(z)\partial_z^3 W(z) \\ &+\frac{9}{2560\pi^2 W(z)^{5/2}}\partial_z^4 W(z)\dots\,. \end{aligned} \tag{6.34}$$

The effect of adding further-order terms within the derivative expansion is presented in Section VI.4 for a real-scalar model. As we will see, the derivative expansion does not capture the full one-loop correction to the wall speed, and in some cases, it can even give the wrong sign for the correction. This is due to the fact that the derivative expansion is an expansion in $\partial_z^2/W(z)$, which is not necessarily small in the bubble-wall background.

VI.3 One-loop corrections to the wall equation of motion

Once all relevant propagators are known we can use Eq. (6.3) to find corrections to the background-field's equation of motion:

$$\ddot{\overline{\phi}} = \vec{\nabla}^2\overline{\phi} - \eta\dot{\overline{\phi}} - V'(\overline{\phi}) - \frac{1}{2}G_H V'''(\overline{\phi}) - \frac{1}{2}G_{\theta_i\theta_j}\left.\frac{\partial^2 H'_{\rm int}(\overline{\phi},\theta)}{\partial\theta_i\partial\theta_j}\right|_{\theta=0} + \dots, \tag{6.35}$$

where θ stands for a set of fluctuating fields interacting with the scalar field ϕ; $G_{\theta_i\theta_j} = \langle\theta_i\theta_j\rangle$–Green's function, correlator of these fluctuating fields. Note here that there could be nonvanishing off-diagonal terms, for example, Goldstones-vectors mixing.

To connect with the previous section's notation,

$$\Omega(\overline{\phi}(z),z) = \frac{1}{2}G_H(z,z)V'''(\overline{\phi}(z)) + \frac{1}{2}G_{\theta_i\theta_j}(z,z)\left.\frac{\partial^2 H'_{\rm int}(\overline{\phi}(z),\theta)}{\partial\theta_i\partial\theta_j}\right|_{\theta=0}. \tag{6.36}$$

Once the single-point Green's function in the inhomogeneous background (outlined in Section VI.2) has been determined for all fluctuating fields coupled to the scalar field ϕ, we apply Eq. (6.12) and Eq. (6.36) to compute the one-loop correction to the wall speed.

VI.4 Applications

In this section, we apply the formalism described in previous sections to the specific examples and show how the results compare to the naive calculations with the derivative expansion.

VI.4.1 A real-scalar model

We proceed by considering a real singlet scalar field in 3 dimensions with the given tree-level potential

$$V(\phi) = \frac{1}{2}y\phi^2 - \frac{1}{6}\phi^3 + \frac{1}{4}x\phi^4, \tag{6.37}$$

where we have already introduced dimensionless parameters x, y and made a specific normalization of the field. This potential could, for example, arise after the DR. The potential possesses a non-trivial, symmetry-breaking vacuum state $\phi_b = \frac{\sqrt{1-16xy}+1}{4x}$ in addition to the symmetric $\phi_s = 0$.

For this specific potential, namely, which includes quadratic, cubic and quartic terms, we find that the solution to the LO equation of motion Eq. (6.8) can be found analytically in terms of the tanh anzatz:

$$\overline{\phi}_0(z) = \frac{\phi_b}{2}\left(1 + \tanh\left(\frac{z}{L_w}\right)\right), \tag{6.38}$$

with

$$L_w = \frac{\sqrt{-\frac{8xy+\sqrt{1-16xy}-1}{x}}}{y}, \tag{6.39}$$

and the wall speed is given by

$$\omega_0 = \frac{\left(-24xy + \sqrt{1-16xy}+1\right)\sqrt{-\frac{8xy+\sqrt{1-16xy}-1}{x}}}{32xy}. \tag{6.40}$$

We have also verified that the numerical solution found by shooting matches the analytical solution. Note that wall-speed scales as η^{-1} for large friction parameters.

Figure 6.1 presents the Green's function for the real singlet, computed as outlined in Section VI.2 together with the effective potential approximation. The effective potential approximation corresponds to using the LO derivative expansion, resulting in $G(z) = -\frac{\sqrt{W(z)}}{4\pi}$; as $W(z)$ may become negative, there are two options to get

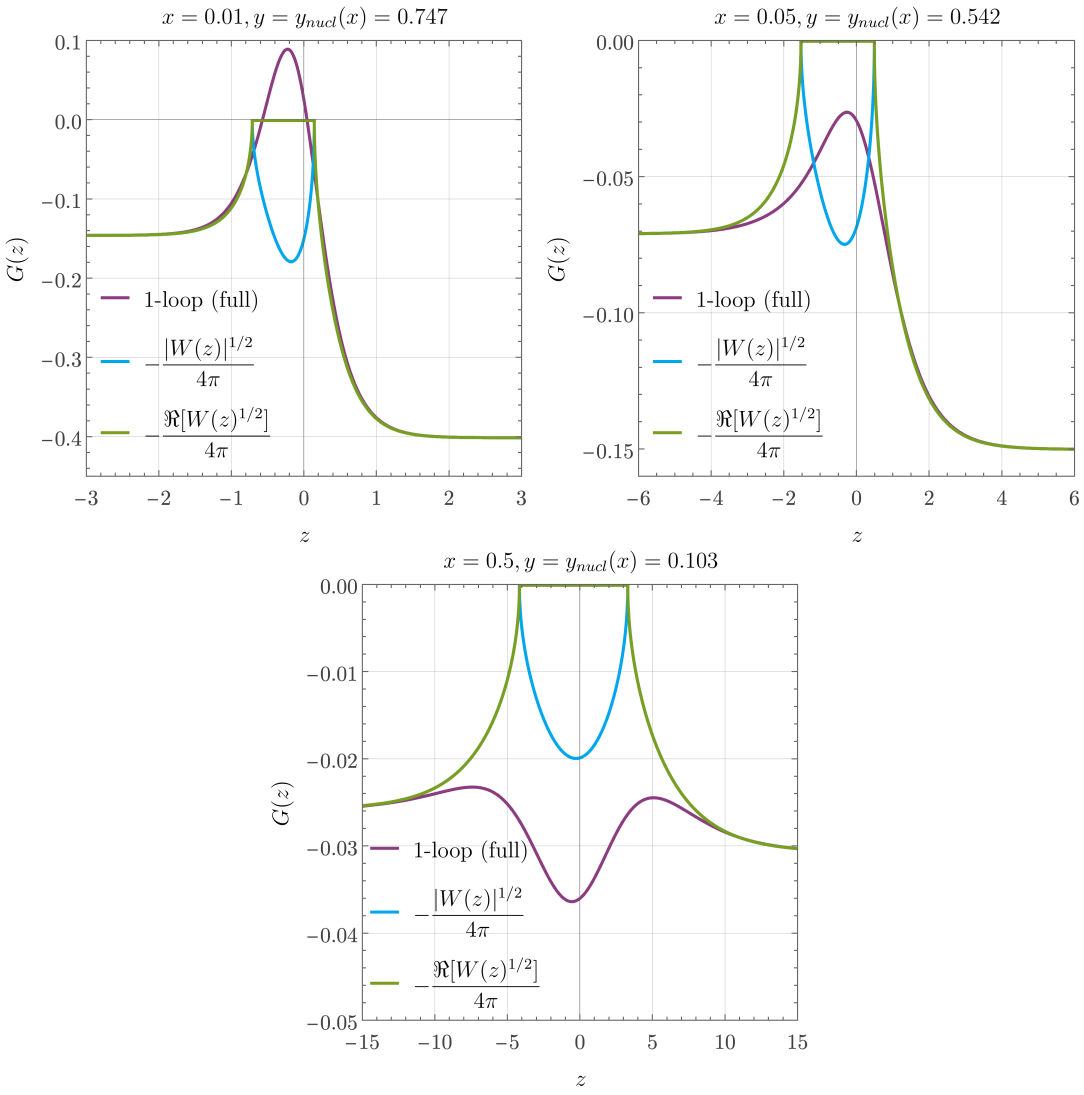

Figure 6.1: One point Higgs Green's function, for $x = 0.01$ (*top left*), $x = 0.05$ (*top right*) and $x = 0.5$ (*bottom*) evaluated at the nucleation mass value.

real-valued Green's function: taking a real part of the square root $\mathrm{Re}\,[\sqrt{W(z)}]$ or an absolute value of $W(z)$.

All plots presented are evaluated at the nucleation mass parameter $y = y_{nucl}$ for the given coupling x. In other words, $S_b(x, y = y_{nucl}) \approx 130$, where the bounce is calculated at the LO, using results from [269].

Figure Fig. 6.2 shows $\omega = \eta v_w \gamma_w$ for the potential given by Eq. (6.37); in terms of Eq. (6.12) one then finds $\Omega(\phi(z), z) = \frac{1}{2} G_H(z) V'''(\phi(z))$. As expected, the corrections get bigger for stronger coupling, in the end reaching the region of failure of the perturbative expansion, at most at $x \approx 0.24$, at which point the perturbative expansion for the effective action breaks down [270]. The full one-loop correction to the wall speed is

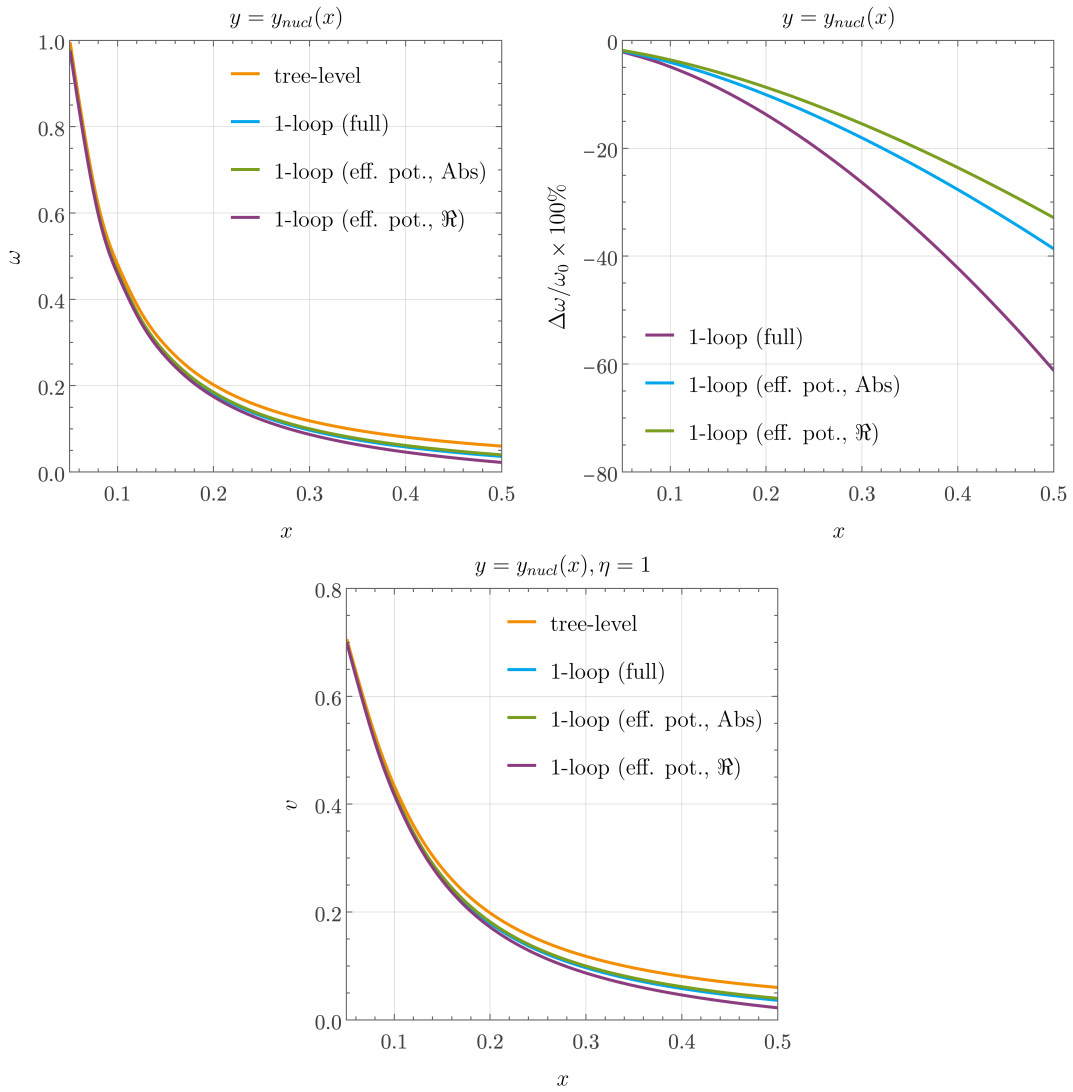

Figure 6.2: Velocity factor $\omega = \eta v_w \gamma_w$ (*top left*), relative correction to the velocity factor evaluated at tree-level (*top right*) and bubble-wall speed for $\eta = 1$ (*bottom*). Negative corrections indicate the fact that loop corrections decrease the wall speed. For the effective potential approximation, both choices for the square root are shown.

about two times larger than the correction resulting from using the effective potential approximation for the whole parameter range in the model explored; both slow down the bubble.

For completeness, in Fig. 6.3 we present the numerically evaluated Higgs propagator alongside the LO, as well as the NLO and NNLO derivative expansions for the real-scalar model discussd in this section.

The derivative expansion is valid only at large distances from the bubble wall; thus, incorporating higher-order terms does not lead to the convergence to the complete prop-

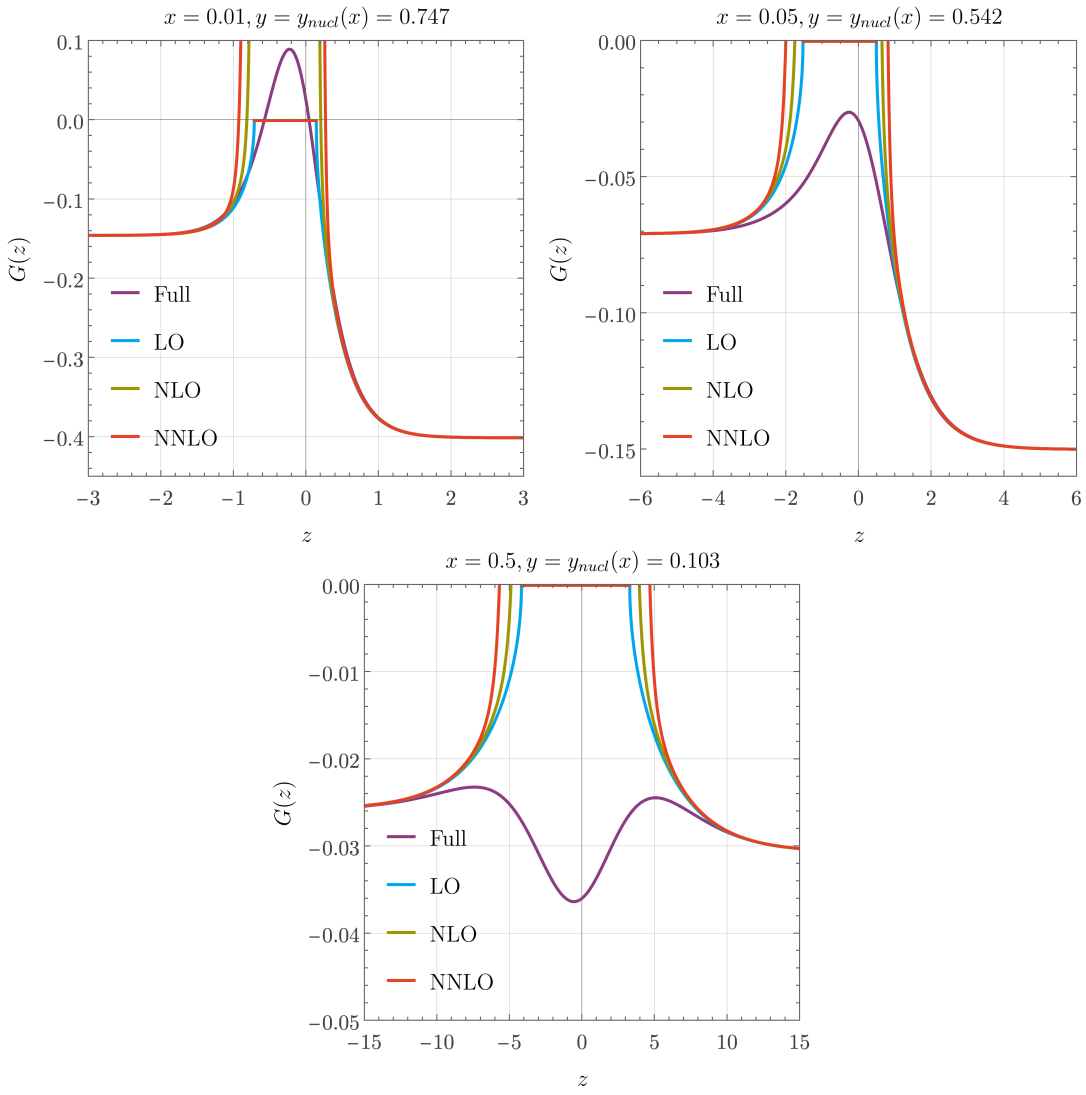

Figure 6.3: Higher derivative expansion of Higgs Green's function terms together with the full numerically evaluated propagator. A real part of Green's function is taken for the derivative expansion, omitting the spurious imaginary part.

agator in the bubble background, which is essential for accurately determining bubble profile and speed corrections.

This highlights, that the derivative expansion, while being a useful tool for analytical calculations, is not sufficient to capture the full dynamics of the bubble wall, especially in the region close to the wall where the field gradients are significant. Therefore, consistent treatment of the loop corrections, presented in this chapter, is essential for accurately determining the bubble profile and speed corrections.

VI.4.2 Radiative barriers

A radiative barrier arises when (classical) one-loop corrections overpower the tree-level potential to generate a barrier; the case of radiatively generated barriers is also discussed in Section IV.3 in the context of RG running within the 3D EFT. As an example consider an additional scalar [5] ψ:

$$H(\phi,\psi) = V(\phi) + \frac{1}{2}g_\psi^2\phi^2\psi^2, \quad V(\phi) = \frac{1}{2}m^2\phi^2 + \frac{1}{4}\lambda\phi^4 \tag{6.41}$$

A barrier can then be generated if the field-dependent mass of ψ dominates the Higgs mass:

$$g_\psi^2\phi^2 \gg V''(\phi) \sim m^2. \tag{6.42}$$

In this case, the "heavy" scalar ψ can be integrated out, and a barrier can be generated:

$$V(\phi) \to V(\phi) - \frac{1}{12\pi}(g_\psi^2\phi^2)^{3/2}. \tag{6.43}$$

Crucially, this construction is not valid when $\phi \approx 0$ — in the unbroken phase. Consequently, if we wish to find the wall speed consistently we have to modify our procedure.

In essence, we want to accommodate a barrier when $\phi \gg 0$, while simultaneously capturing the right dynamics of ψ around $\phi \approx 0$. The easiest way to accomplish this is to add and subtract the effective-potential contribution from ψ — that is $-g_\psi^2\overline{\phi}(z)\frac{1}{4\pi}\left(W_\psi(\overline{\phi})\right)^{1/2}$ — to the equation of motion of the background field while adding the full contribution from the ψ propagator.

The one-loop correction then becomes

$$\Omega(\overline{\phi}(z),z) = \frac{1}{2}G_H(z,z)V_{\rm LO}'''(\overline{\phi}(z)) + g_\psi^2\overline{\phi}(z)\left(G_{\psi\psi}(z,z) - \left[-\frac{1}{4\pi}\left(W_\psi(\overline{\phi}(z))\right)^{1/2}\right]\right), \tag{6.44}$$

and the LO potential, which enters the LO equation of motion Eq. (6.8), becomes

$$V_{\rm LO}(\phi) = V(\phi) - \frac{1}{12\pi}\left(W_\psi(\phi)\right)^{3/2}, \quad W_\psi = g_\psi^2\phi^2 + \frac{\eta_\psi^2\gamma_w^2 v_w^2}{4}. \tag{6.45}$$

We want to stress two things here. First, we have included the η_ψ term in W_ψ because the ψ field is in general damped. Second, there is no reason to suspect that $G_{\psi\psi}(z,z)$ approaches the normal effective-potential result when $z \to -\infty$. See for example Fig. 6.4.

[5] The argument for vector bosons is identical.

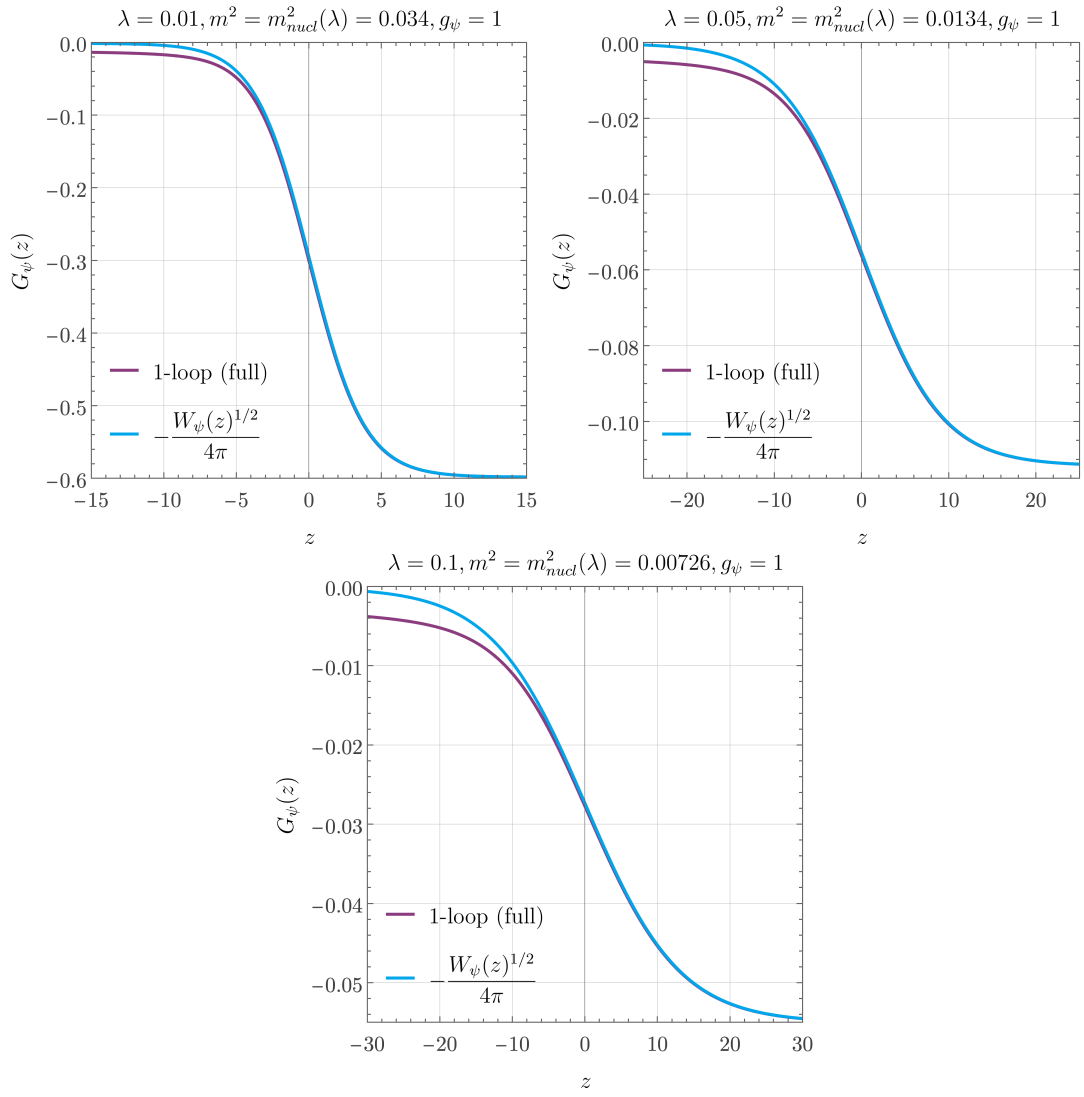

Figure 6.4: "Heavy" scalar Green's function $G_{\psi\psi}(z)$ for $\lambda = 0.01$, $g_\psi = 1$ (*top left*), $\lambda = 0.05$, $g_\psi = 1$ (*top right*) and $\lambda = 0.1$, $g_\psi = 1$ (*bottom*) evaluated at the nucleation mass value. The ψ-field damping is set to zero $\eta_\psi = 0$.

Both of these effects can significantly reduce the wall speed by lowering the effective latent heat. For example, the transition becomes second-order when $(\eta_\psi \gamma_w v_w)^2 \sim m^2/\lambda$. This implies that radiative barriers can not give rise to runaway bubbles ($v_w \to 1$). Though it should be stressed that our assumptions break down for large enough wall speeds, so this statement should be taken with a grain of salt.

The fact that the scalar equation of motion can differ from the effective-potential prediction at $\lim_{z\to\pm\infty}$ is not a surprise, and it is a direct consequence of the fact that the effective potential approximation is only valid for homogeneous field configurations. In the case of radiative barriers, the field-dependent mass of the "heavy" scalar ψ becomes small around $\phi \approx 0$ (in the unbroken phase), which leads to significant deviations from

the effective-potential prediction in this region. This is also important for hydrodynamic considerations [53–56, 179, 180, 271, 272]; for example, by giving a different prediction for the latent heat.

VI.5 Hydrodynamic considerations

Consider again the operator

$$\widehat{L}_H\hat{\phi} = \left(-\partial_z^2 - \vec{\nabla}_\perp^2 + \omega_0(z)\partial_z + V''(\overline{\phi}_0(z))\right)\hat{\phi}, \tag{6.46}$$

now with a z-dependent ω_0, as occurs if we solve the full hydrodynamic equations.

A first approximation is to incorporate $\omega_0(z)$ without adding the $\hat{\phi}$ dependence of the wall speed and temperature. In this case, we can make this operator self-adjoint with the shift $\hat{\phi} \to e^{-\frac{1}{2}\int_0^z \omega_0(s)ds}\hat{\phi}$:

$$\widehat{L}_H \to \left(-\partial_z^2 - \vec{\nabla}_\perp^2 + V''(\overline{\phi}_0(z)) + \frac{\omega_0^2}{4} - \frac{1}{2}\partial_z\omega_0(z)\right). \tag{6.47}$$

The results in Section VI.2 are the same after defining $W(z) = V''(\overline{\phi}_0(z)) + \frac{\omega_0^2}{4} - \frac{1}{2}\partial_z\omega_0(z)$. Note also that the new Higgs zero-mode is $e^{-\frac{1}{2}\int_0^z \omega_0(s)ds}\partial_z\overline{\phi}_0(z)$.

Finally, to find corrections to the LO wall speed we simply use $e^{-\int_0^z \omega_0(s)ds}\partial_z\overline{\phi}_0(z)$ in place of $e^{-z\omega_0(z)}\partial_z\overline{\phi}_0(z)$ in equation (6.12).

General equations of motion

Next, we can consider the most general equation of motion

$$\partial_z^2\phi(z) + V'(\phi,\theta) + F(\phi,\partial_z\phi,\theta) = 0, \tag{6.48}$$

where, for example, θ might represent the fluid velocity or the temperature. After we expand around a LO solution, $\phi = \overline{\phi} + \hat{\phi}$, we then get

$$\partial_z^2\hat{\phi}(z) + \delta_\phi\left[V'(\phi,\theta) + F(\phi,\partial_z\phi,\theta)\right]_{\phi=\overline{\phi}}\hat{\phi}(z) = 0. \tag{6.49}$$

Here F might be a local friction term as in Section VI.3, but F could also come from the solution of a Boltzmann equation [178], and would then, in general, be a non-local

function of ϕ. In taking the ϕ derivative we have to take into account the ϕ dependence of θ; for example, a field-dependent damping coefficient or the temperature. All in all, this ensures that $\partial_z\phi$ is a zero-mode of the above operator. The propagator can then be found as usual if we can evaluate $\partial\theta/\partial\phi$.

One-loop hydrodynamic backreactions

We can further consider the one-loop hydrodynamic backreactions. To analyze one-loop hydrodynamic correction, first, we need the hydrodynamic equations in the wall frame:[6]

$$\begin{aligned} &wv_w\gamma_w^2 = \text{const}, \\ &\frac{1}{2}(\partial_z\phi)^2 - V + wv_w^2\gamma_w^2 = \text{const}, \end{aligned} \tag{6.50}$$

where the enthalpy is of the form $w = \frac{4}{3}aT^4 - T\partial_T V$. If we omit the second-term we can then solve for v_w and T to the first order in $\hat{\phi}$:

$$\delta v = \underbrace{\frac{1}{aT^4\gamma_w^2 v_w}}_{=a_w}\left[V'(\overline{\phi}_0)\hat{\phi} - \partial_z\overline{\phi}_0\partial_z\hat{\phi}\right], \quad \delta T = -\underbrace{\frac{v_w^2+1}{4aT^3v_w^2}}_{=b_w}\left[V'(\overline{\phi}_0)\hat{\phi} - \partial_z\overline{\phi}_0\partial_z\hat{\phi}\right] \tag{6.51}$$

Adding these corrections to the Higgs equation of motion we find

$$\begin{aligned} \widehat{L}_H\hat{\phi} = &\left(-\partial_z^2 - \vec{\nabla}_\perp^2 + \omega_0\partial_z + V''(\overline{\phi}_0)\right)\hat{\phi} + \left[a_w\partial_{v_w}\omega_0\partial_z\overline{\phi}_0 + b_w\partial_T V'(\overline{\phi}_0)\right]\hat{\phi} \\ &- \left[a_w\partial_{v_w}\omega_0\partial_z\overline{\phi}_0 + b_w\partial_T V'(\overline{\phi}_0)\right]\partial_z\hat{\phi}. \end{aligned} \tag{6.52}$$

This operator can now be made self-adjoint as in the previous sub-section, and propagators for $T(z)$, $v_w(z)$, and $\hat{\phi}(z)$ can be found using the results in Section VI.2. Note that ϕ propagators will also enter the conservation of the energy-momentum tensor in various places.

Multifield propagators

Finally, we investigate the case of multiple background fields. The procedure to find multifield propagators numerically readily follows from the single-field case that we have delineated in Section VI.2 of this chapter. Consider, for example, an equation of the

[6] We here neglect the bulk and shear viscosity. If these are present we would also expect velocity and temperature fluctuations.

form

$$\left[-\vec{\nabla}^2\delta_{\theta_i\theta_j} + \omega_{\theta_i\theta_j}(z)\partial_z + M^2_{\theta_i\theta_j}(z)\right] G_{\theta_i\theta_j}(\vec{x}-\vec{y}) = \delta_{\theta_i\theta_j}\delta^3(\vec{x}-\vec{y}), \tag{6.53}$$

where θ_i, θ_j runs over all relevant fields; $\omega_{\theta_i\theta_j}(z)$ and $M^2(z)_{\theta_i\theta_j}$ are friction- and mass-matrices respectively.

The linear z-derivative terms can be removed by the shift

$$G_{\theta_i\theta_j} \to \left\{ e^{\frac{1}{2}\int_0^z \omega} G e^{-\frac{1}{2}\int_0^{z'}\omega} \right\}_{\theta_i\theta_j}. \tag{6.54}$$

This brings the equation of motion to the form:

$$\left[-\vec{\nabla}^2\delta_{\theta_i\theta_j} + W_{\theta_i\theta_j}(z)\right] G_{\theta_i\theta_j}(\vec{x}-\vec{y}) = \delta_{\theta_i\theta_j}\delta^3(\vec{x}-\vec{y}), \tag{6.55}$$

where

$$W_{\theta_i\theta_j}(z) = e^{-\frac{1}{2}\int_0^z \omega}\left[M^2_{\theta_i\theta_j}(z) + \frac{1}{4}\omega^2_{\theta_i\theta_j} - \frac{1}{2}\partial_z\omega_{\theta_i\theta_j}\right] e^{\frac{1}{2}\int_0^z \omega}. \tag{6.56}$$

To find the propagators one can follow the same steps as before. Numerically, it is the simplest to first rotate to an eigenbasis of $W_{\theta_i\theta_j}(-\infty)$, evolve the equations to $z = 0$, rotate to an eigenbasis of $W_{\theta_i\theta_j}(\infty)$, and then evolve the system to $z = \infty$. We note that an additional complication arises if mixing with vector fields is present, in which case non-trivial momentum dependence of mass matrix perplexes the calculation.

VI.6 Summary

In this chapter, we examined how loop corrections influence the equation of motion for the nucleating scalar field during a first-order phase transition, with particular attention to their effect on the bubble wall velocity. First, we calculated the correlator of nucleating scalar field fluctuations in an inhomogeneous background; then, we determined how these fluctuations affect the bubble profile and the velocity of the bubble wall.

To illustrate these calculations, we examined a case involving a nucleating real scalar field. Our results indicate that one-loop corrections reduce the wall speed, with corrections reaching up to several tens of percent compared to the tree-level velocity, and the largest effects appearing near the limits of perturbativity. The effective potential approximation — the LO term in the derivative expansion — underestimates this decrease by about a factor of two, while including higher-order terms does not resolve the dis-

crepancy. This demonstrates the breakdown of the expansion's validity for describing the bubble.

Furthermore, in the case of radiatively generated barriers, the full propagator calculation deviates from the effective-potential approximation in the unbroken phase, where the field-dependent mass of the heavy scalar becomes small. Beyond its effect on the wall profile, this deviation modifies the latent heat, which enters the hydrodynamic equations governing bubble expansion. Accounting for these corrections is therefore important for reliable predictions of the wall speed and GW signals in scenarios with radiatively generated barriers.

We have also introduced a framework capable of addressing more complex situations, including non-constant fluid velocities, multifield propagators, and hydrodynamical backreactions. Therefore, the findings of this chapter can be applied to future research in more realistic settings, incorporating extended particle content and hydrodynamical effects.

VII – CONCLUSIONS

One never notices what has been done;
one can only see what remains to be done.

— Maria Skłodowska Curie

The EWPT sits at the intersection of particle physics and cosmology. If it proceeded as a strong first-order transition in the early Universe, it could produce a stochastic GW background accessible to upcoming GW detectors. Turning this into a genuine test of BSM physics requires translating model parameters into reliable GW spectra with controlled theoretical uncertainties. The chain from a BSM model to a GW signal passes through finite-temperature field theory, phase transition thermodynamics, bubble dynamics and GW production — and at every link, theoretical uncertainties accumulate. This thesis is a program to identify, quantify, and reduce those uncertainties.

The first step in this program is the diagnosis of gauge-fixing artifacts in perturbative calculations. In Section III.2.2, we presented a general result for the $\hbar$-expansion of the effective potential and used it to organize the calculation consistently order by order, highlighting that finite-order truncations can induce sizable spurious gauge dependence in intermediate quantities. This makes gauge-parameter variation, together with residual scale dependence, useful quantitative diagnostic tools of perturbative reliability.

With the problem diagnosed, the next task is to build the infrastructure for precise calculations. In Chapter IV, we derived the full set of two-loop RGEs for all Wilson coefficients up to energy dimension four in the 3D EFT describing the high-temperature limit of BSM theories with heavy new physics encoded in the SMEFT Lagrangian. Before this work, the running of higher-dimensional operators in the 3D EFT was unknown, and keeping only the leading super-renormalizable running left a significant gap in the precision toolkit. We showed that the running induced by beyond-super-renormalizable operators can be parametrically of the same order as the nominal leading-order running,

resulting in prominent shifts in predictions of thermodynamic parameters and GW spectra. Notably, even the renormalizable sextic scalar couplings already triggers running of the quartic coupling, an effect absent in purely super-renormalizable theories and not accounted for in earlier analyses. Beyond perturbation theory, the counterterms computed in Chapter IV provide essential input for future lattice simulations of the 3D EFT with higher-dimensional operators, enabling non-perturbative studies that are currently inaccessible within the purely super-renormalizable theory.

Having established the theoretical machinery, Chapter V subjected it to a systematic stress test in the phenomenologically well-motivated cxSM. This model may realize a SFOEWPT with no direct LHC signatures, making GWs potentially the only accessible probe. We compared various perturbative approaches — 4D calculations within $\overline{\text{MS}}$ and $\widetilde{\text{OS}}$ schemes and the 3D EFT approach with different matching orders — across the full GW-relevant parameter space, using residual scale and gauge dependence as quantitative indicators of theoretical reliability. The results are instructive.

The 4D approach performs poorly, with residual scale uncertainties of orders of magnitude in the predicted GW peak strength and significant gauge-fixing artifacts, particularly in the $\widetilde{\text{OS}}$ scheme commonly employed in phenomenological studies.

The 3D EFT approach with NLO matching provides the most stable and consistent description: the scale dependence in the LISA SNR is reduced by about one order of magnitude relative to LO matching, and the $\hbar$-expansion yields results in excellent numerical agreement with direct minimization of the two-loop potential, validating the approach. The inclusion of the leading beyond-super-renormalizable operators in the 3D EFT shifts the transition strength α by up to 100% and the GW peak amplitude by up to an order of magnitude in the part of parameter space where LISA prospects are best — precisely the regime where the EFT truncation uncertainty, rather than gauge or scale dependence, is the dominant remaining theoretical error. This finding points directly back to the importance of the RGEs derived in Chapter IV, and underscores that a complete precision program for the EWPT requires the systematic inclusion of higher-dimensional operators.

Even with a perfectly controlled perturbative calculation of the thermodynamic transition parameters, there remains one crucial input to the GW spectrum that is undetermined: the bubble wall velocity. The wall speed plays a key role in GW predictions through the efficiency parameter and the overall energy budget, yet it is often computed using the effective-potential approximation, which treats the bubble as evolving in a

homogeneous background. As Chapter VI demonstrates, this heuristic approximation can lead to substantial shortcomings. Within the high-temperature expansion, we have developed a systematic one-loop approach to fluctuations in the inhomogeneous bubble background. This yields corrections to the wall equation of motion that are absent in the effective potential approach. These effects are particularly pronounced in scenarios where the barrier is generated radiatively; here, loop corrections may lead to phase transitions that do not produce runaway bubbles. The formalism is broadly applicable and can readily be extended to more complex scenarios, including multiple scalar fields, general friction forces and one-loop hydrodynamic backreactions.

Together, these contributions amount to a qualitative advance in the precision toolkit for EWPT predictions, establishing gauge-fixing and scale dependence as quantitative diagnostics and deriving the means to address them. The two-loop RGEs derived in Chapter IV provide, for the first time, a complete running framework for the 3D EFT of the SM and the SMEFT, including the effects of higher-dimensional operators. Applied to the cxSM, this precision machinery provides the first quantified comparison of perturbative approaches across the full GW-relevant parameter space, showing that the 3D EFT framework is the natural framework to systematically control residual gauge and scale dependence, and that the inclusion of higher-dimensional operators is essential for the strong EWPT. By incorporating one-loop corrections to the bubble wall velocity in an inhomogeneous background, the thesis extends the precision program beyond equilibrium thermodynamics into the non-equilibrium dynamics of bubble propagation.

This thesis paves the way for a range of follow-up precision studies of the EWPT. The loop-correction framework for the bubble wall velocity, developed here in full generality, is ready to be deployed in concrete GW-relevant BSM models, delivering more accurate wall speeds and, consequently, more reliable GW spectra. Furthermore, the two-loop RGEs derived in Chapter IV enable a systematic inclusion of higher-dimensional operators across phenomenologically interesting BSM scenarios, with the running of effective parameters in the 3D EFT now under full theoretical control. Subsequently, the counterterms computed here unlock non-perturbative lattice studies in regimes previously beyond reach, allowing perturbative predictions to be put to a direct test.

As LISA moves from design to data, the question may no longer be whether a GW signal from the EWPT is detectable, but whether our theoretical predictions are precise enough to extract BSM physics from such a signal. The work presented in this thesis is a step toward making that extraction possible.

A – COUNTERTERMS AND BETA FUNCTIONS FOR 3D EFT OF THE SM(EFT)

In this appendix, we display explicitly the counterterms and beta functions for the 3D EFT of the SM and the SMEFT, determined as explained in Chapter IV, both for the theory valid at and below the soft scale.

A.1 Results at the soft scale

At the soft scale, the dimensionally reduced theory contains both the Higgs-field scalar Φ, spatial W_i and temporal vector W_0 components, with the full operator content of Eq. (4.1). The parameter and field-strength counterterms are:

$$
\begin{aligned}
I_2^{-1}\delta Z_\phi &= 4c^{(2)}_{\phi^2W_0^2D^2}g_3^2 + 2c_{\phi^2W^2}g_3^2 + c^{(1)}_{\phi^4D^2}\left(5g_3^2 - 8\lambda_3\right) \\
&\quad + c^{(2)}_{\phi^4D^2}\left(-\frac{3}{2}g_3^2 + 2\lambda_3\right) - 2c^{(1)}_{\phi^2W_0^2D^2}\lambda_{\phi^2W_0^2}\,, \\
I_2^{-1}\delta Z_{W_0} &= c^{(1)}_{\phi^2W_0^2D^2}\left(-6g_3^2 + \frac{16}{3}\lambda_{\phi^2W_0^2}\right) + \frac{16}{3}c^{(2)}_{\phi^2W_0^2D^2}g_3^2\,, \\
I_2^{-1}\delta Z_W &= \frac{28}{3}c_{\phi^2W^2}g_3^2\,, \\
I_2^{-1}\delta m_3^2 &= -\frac{39}{16}g_3^4 - 9g_3^2\lambda_3 + 12\lambda_3^2 - 12g_3^2\lambda_{\phi^2W_0^2} + 6\lambda^2_{\phi^2W_0^2} \\
&\quad + m_3^2\Big[-18c_{\phi^2W^2}g_3^2 + c^{(1)}_{\phi^4D^2}\left(-9g_3^2 + 24\lambda_3\right) \\
&\quad\quad + c^{(2)}_{\phi^4D^2}\left(\frac{3}{2}g_3^2 - 6\lambda_3\right) + 6c^{(1)}_{\phi^2W_0^2D^2}\lambda_{\phi^2W_0^2}\Big] \\
&\quad + m_D^2\left[-24c_{\phi^2W^2}g_3^2 + c^{(1)}_{\phi^2W_0^2D^2}\left(12g_3^2 - 12\lambda_{\phi^2W_0^2}\right) - 12c^{(2)}_{\phi^2W_0^2D^2}g_3^2\right], \\
I_2^{-1}\delta m_D^2 &= g_3^4 - 6g_3^2\lambda_{\phi^2W_0^2} + 8\lambda^2_{\phi^2W_0^2} - 80g_3^2\lambda_{W_0^4} + 160\lambda^2_{W_0^4} - 16c^{(2)}_{\phi^2W_0^2D^2}g_3^2m_3^2\,, \\
I_2^{-1}\delta\lambda_3 &= c_{\phi^2W^2}\left(-\frac{27}{2}g_3^4 - 72g_3^2\lambda_3 - 48g_3^2\lambda_{\phi^2W_0^2}\right) + c_{\phi^6}\left(-18g_3^2 + 96\lambda_3\right)
\end{aligned}
\tag{A.1}
$$

$$
\begin{aligned}
&+ c^{(1)}_{\phi^4 D^2}\left(3g_3^4 - 42g_3^2\lambda_3 + 240\lambda_3^2 + 24\lambda^2_{\phi^2 W_0^2}\right)\\
&- c^{(2)}_{\phi^4 D^2}\left(\frac{13}{16}g_3^4 - 6g_3^2\lambda_3 + 56\lambda_3^2 + 6\lambda^2_{\phi^2 W_0^2}\right)\\
&+ c^{(1)}_{\phi^2 W_0^2 D^2}\left(24g_3^2\lambda_{\phi^2 W_0^2} + 36\lambda_3\lambda_{\phi^2 W_0^2} - 48\lambda^2_{\phi^2 W_0^2}\right)\\
&+ c^{(2)}_{\phi^2 W_0^2 D^2}\left(\frac{3}{2}g_3^4 - 24g_3^2\lambda_{\phi^2 W_0^2}\right)\\
&+ c^{(1)}_{\phi^4 W_0^2}\left(-12g_3^2 + 24\lambda_{\phi^2 W_0^2}\right) + c^{(2)}_{\phi^4 W_0^2}\left(-4g_3^2 + 8\lambda_{\phi^2 W_0^2}\right)\\
&+ m_3^2\left[c^{(1)}_{\phi^2 W_0^2 D^2}\left(12c^{(1)}_{\phi^4 W_0^2} + 4c^{(2)}_{\phi^4 W_0^2}\right) + c_{\phi^6}\left(96c^{(1)}_{\phi^4 D^2} - 24c^{(2)}_{\phi^4 D^2}\right)\right]\\
&+ m_D^2\left[-c^{(1)}_{\phi^2 W_0^2 D^2}\left(24c^{(1)}_{\phi^4 W_0^2} + 8c^{(2)}_{\phi^4 W_0^2}\right)\right],\\
I_2^{-1}\delta\lambda_{W_0^4} &= c^{(2)}_{\phi^2 W_0^2 D^2}\left(2g_3^4 - 8g_3^2\lambda_{\phi^2 W_0^2}\right) + c_{\phi^2 W_0^4}\left(-3g_3^2 + 16\lambda_{\phi^2 W_0^2}\right)\\
&+ c_{W_0^6}\left(-84g_3^2 + 672\lambda_{W_0^4}\right),\\
I_2^{-1}\delta\lambda_{\phi^2 W_0^2} &= c_{\phi^2 W^2}\left(12g_3^4 - 50g_3^2\lambda_{\phi^2 W_0^2} - 160g_3^2\lambda_{W_0^4}\right)\\
&+ c_{\phi^2 W_0^4}\left(-40g_3^2 + 40\lambda_{\phi^2 W_0^2} + 160\lambda_{W_0^4}\right)\\
&+ c^{(1)}_{\phi^4 W_0^2}\left(-9g_3^2 + 24\lambda_3 + 24\lambda_{\phi^2 W_0^2}\right) + c^{(2)}_{\phi^4 W_0^2}\left(-3g_3^2 + 8\lambda_3 + 8\lambda_{\phi^2 W_0^2}\right)\\
&+ c^{(1)}_{\phi^2 W_0^2 D^2}\left(4g_3^4 - 16g_3^2\lambda_{\phi^2 W_0^2} - 10\lambda^2_{\phi^2 W_0^2} + 80g_3^2\lambda_{W_0^4} - 480\lambda^2_{W_0^4}\right)\\
&+ c^{(2)}_{\phi^2 W_0^2 D^2}\left(16g_3^4 - 24g_3^2\lambda_3 - 8g_3^2\lambda_{\phi^2 W_0^2} - 80g_3^2\lambda_{W_0^4}\right)\\
&+ c^{(1)}_{\phi^4 D^2}\left(g_3^4 - 9g_3^2\lambda_{\phi^2 W_0^2} + 24\lambda_3\lambda_{\phi^2 W_0^2} + 40\lambda^2_{\phi^2 W_0^2}\right)\\
&+ c^{(2)}_{\phi^4 D^2}\left(\frac{3}{2}g_3^2\lambda_{\phi^2 W_0^2} - 6\lambda_3\lambda_{\phi^2 W_0^2} - 8\lambda^2_{\phi^2 W_0^2}\right)\\
&+ m_3^2\left[20c^{(1)}_{\phi^2 W_0^2 D^2}c_{\phi^2 W_0^4} + c^{(1)}_{\phi^4 W_0^2}\left(24c^{(1)}_{\phi^4 D^2} - 6c^{(2)}_{\phi^4 D^2}\right)\right.\\
&\quad\left. + c^{(2)}_{\phi^4 W_0^2}\left(8c^{(1)}_{\phi^4 D^2} - 2c^{(2)}_{\phi^4 D^2}\right)\right] - 40m_D^2 c^{(1)}_{\phi^2 W_0^2 D^2}c_{\phi^2 W_0^4},\\
I_2^{-1}\delta c_{\phi^6} &= 24\left(c^{(1)}_{\phi^4 W_0^2}\right)^2 + 16c^{(1)}_{\phi^4 W_0^2}c^{(2)}_{\phi^4 W_0^2} + 16\left(c^{(2)}_{\phi^4 W_0^2}\right)^2 + 204c^2_{\phi^6}\\
&+ c^{(1)}_{\phi^2 W_0^2 D^2}\left[c^{(1)}_{\phi^4 W_0^2}\left(24g_3^2 + 72\lambda_3 - 168\lambda_{\phi^2 W_0^2}\right)\right.\\
&\quad\left. + c^{(2)}_{\phi^4 W_0^2}\left(8g_3^2 + 24\lambda_3 - 56\lambda_{\phi^2 W_0^2}\right) + 90c_{\phi^6}\lambda_{\phi^2 W_0^2}\right]\\
&- 8c^{(2)}_{\phi^2 W_0^2 D^2}g_3^2\left(3c^{(1)}_{\phi^4 W_0^2} + c^{(2)}_{\phi^4 W_0^2}\right)\\
&- c_{\phi^2 W^2}g_3^2\left(48c^{(1)}_{\phi^4 W_0^2} + 16c^{(2)}_{\phi^4 W_0^2} + 162c_{\phi^6}\right)
\end{aligned}
\tag{A.1}
$$

$$
\begin{aligned}
&+ c_{\phi^6}\left[c^{(1)}_{\phi^4D^2}\left(-99g_3^2+1800\lambda_3\right)+c^{(2)}_{\phi^4D^2}\left(\frac{27}{2}g_3^2-426\lambda_3\right)\right]\\
&+ c_{\phi^8}\left(-30g_3^2+240\lambda_3\right)\\
&+ \lambda_{\phi^2W_0^2}\left[c^{(1)}_{\phi^4W_0^2}\left(96c^{(1)}_{\phi^4D^2}-24c^{(2)}_{\phi^4D^2}\right)+c^{(2)}_{\phi^4W_0^2}\left(32c^{(1)}_{\phi^4D^2}-8c^{(2)}_{\phi^4D^2}\right)\right]\\
&+ c^{(1)}_{\phi^6W_0^2}\left(-12g_3^2+36\lambda_{\phi^2W_0^2}\right)+c^{(2)}_{\phi^6W_0^2}\left(-4g_3^2+12\lambda_{\phi^2W_0^2}\right)\,,\\
I_2^{-1}\delta c_{W_0^6} &= 16\left(c_{\phi^2W_0^4}\right)^2+1488c^2_{W_0^6}-8c^{(2)}_{\phi^2W_0^2D^2}c_{\phi^2W_0^4}g_3^2\,,\\
I_2^{-1}\delta c^{(1)}_{\phi^4W_0^2} &= 80\left(c_{\phi^2W_0^4}\right)^2+80c_{\phi^2W_0^4}c^{(1)}_{\phi^4W_0^2}+16c_{\phi^2W_0^4}c^{(2)}_{\phi^4W_0^2}+48\left(c^{(1)}_{\phi^4W_0^2}\right)^2\\
&+ 16c^{(1)}_{\phi^4W_0^2}c^{(2)}_{\phi^4W_0^2}+44\left(c^{(2)}_{\phi^4W_0^2}\right)^2+96c^{(1)}_{\phi^4W_0^2}c_{\phi^6}+24c^{(2)}_{\phi^4W_0^2}c_{\phi^6}\\
&+ c^{(1)}_{\phi^2W_0^2D^2}\left[c_{\phi^2W_0^4}\left(80g_3^2+120\lambda_3-240\lambda_{\phi^2W_0^2}-960\lambda_{W_0^4}\right)\right.\\
&\quad\left.+c^{(1)}_{\phi^4W_0^2}\left(-32g_3^2-64\lambda_{\phi^2W_0^2}\right)+c^{(2)}_{\phi^4W_0^2}\left(4g_3^2-12\lambda_{\phi^2W_0^2}-32\lambda_{W_0^4}\right)\right]\\
&+ c^{(2)}_{\phi^2W_0^2D^2}\left[-g_3^2\left(80c_{\phi^2W_0^4}+16c^{(1)}_{\phi^4W_0^2}+12c^{(2)}_{\phi^4W_0^2}+48c_{\phi^6}\right)\right.\\
&\quad\left.+16c^{(2)}_{\phi^4W_0^2}\lambda_{\phi^2W_0^2}\right]\\
&- c_{\phi^2W^2}g_3^2\left(160c_{\phi^2W_0^4}+136c^{(1)}_{\phi^4W_0^2}+12c^{(2)}_{\phi^4W_0^2}\right)\\
&+ c^{(1)}_{\phi^4D^2}\left[c^{(1)}_{\phi^4W_0^2}\left(-42g_3^2+480\lambda_3+256\lambda_{\phi^2W_0^2}\right)\right.\\
&\quad\left.+c^{(2)}_{\phi^4W_0^2}\left(-4g_3^2+80\lambda_3+32\lambda_{\phi^2W_0^2}\right)+\lambda_{\phi^2W_0^2}\left(160c_{\phi^2W_0^4}+96c_{\phi^6}\right)\right]\\
&+ c^{(2)}_{\phi^4D^2}\left[c^{(1)}_{\phi^4W_0^2}\left(6g_3^2-112\lambda_3-56\lambda_{\phi^2W_0^2}\right)\right.\\
&\quad\left.+c^{(2)}_{\phi^4W_0^2}\left(2g_3^2-20\lambda_3-8\lambda_{\phi^2W_0^2}\right)-\lambda_{\phi^2W_0^2}\left(40c_{\phi^2W_0^4}+24c_{\phi^6}\right)\right]\\
&+ c^{(1)}_{\phi^6W_0^2}\left(-18g_3^2+96\lambda_3+48\lambda_{\phi^2W_0^2}\right)\\
&+ c^{(2)}_{\phi^6W_0^2}\left(-3g_3^2+16\lambda_3+8\lambda_{\phi^2W_0^2}\right)\,,\\
I_2^{-1}\delta c^{(2)}_{\phi^4W_0^2} &= 32c_{\phi^2W_0^4}c^{(2)}_{\phi^4W_0^2}+48c^{(1)}_{\phi^4W_0^2}c^{(2)}_{\phi^4W_0^2}+44\left(c^{(2)}_{\phi^4W_0^2}\right)^2+24c^{(2)}_{\phi^4W_0^2}c_{\phi^6}\\
&+ c^{(1)}_{\phi^2W_0^2D^2}c^{(2)}_{\phi^4W_0^2}\left(-44g_3^2-28\lambda_{\phi^2W_0^2}+96\lambda_{W_0^4}\right)\\
&+ c^{(2)}_{\phi^2W_0^2D^2}c^{(2)}_{\phi^4W_0^2}\left(20g_3^2-48\lambda_{\phi^2W_0^2}\right)-100c_{\phi^2W^2}c^{(2)}_{\phi^4W_0^2}g_3^2\\
&+ c^{(1)}_{\phi^4D^2}c^{(2)}_{\phi^4W_0^2}\left(-30g_3^2+240\lambda_3+160\lambda_{\phi^2W_0^2}\right)\\
&+ c^{(2)}_{\phi^4D^2}c^{(2)}_{\phi^4W_0^2}\left(-52\lambda_3-32\lambda_{\phi^2W_0^2}\right)
\end{aligned}
\tag{A.1}
$$

$$
\begin{aligned}
&+ c^{(2)}_{\phi^6 W_0^2}\left(-9g_3^2 + 48\lambda_3 + 24\lambda_{\phi^2 W_0^2}\right) ,\\
I_2^{-1}\delta c_{\phi^2 W_0^4} &= 88\left(c_{\phi^2 W_0^4}\right)^2 + 48 c_{\phi^2 W_0^4} c^{(1)}_{\phi^4 W_0^2} + 16 c_{\phi^2 W_0^4} c^{(2)}_{\phi^4 W_0^2} + 12\left(c^{(1)}_{\phi^4 W_0^2}\right)^2\\
&+ 8 c^{(1)}_{\phi^4 W_0^2} c^{(2)}_{\phi^4 W_0^2} + 12\left(c^{(2)}_{\phi^4 W_0^2}\right)^2 + 672 c_{\phi^2 W_0^4} c_{W_0^6}\\
&+ c^{(1)}_{\phi^2 W_0^2 D^2}\left[c_{\phi^2 W_0^4}\left(-32g_3^2 - 38\lambda_{\phi^2 W_0^2} - 192\lambda_{W_0^4}\right)\right.\\
&\quad \left. + c_{W_0^6}\left(168 g_3^2 + 168\lambda_{\phi^2 W_0^2} - 4032\lambda_{W_0^4}\right)\right]\\
&- c^{(2)}_{\phi^2 W_0^2 D^2} g_3^2\left(16 c_{\phi^2 W_0^4} + 24 c^{(1)}_{\phi^4 W_0^2} + 8 c^{(2)}_{\phi^4 W_0^2} + 168 c_{W_0^6}\right)\\
&- c_{\phi^2 W^2} g_3^2\left(82 c_{\phi^2 W_0^4} + 336 c_{W_0^6}\right)\\
&+ c^{(1)}_{\phi^4 D^2}\left[c_{\phi^2 W_0^4}\left(-9g_3^2 + 24\lambda_3 + 160\lambda_{\phi^2 W_0^2}\right)\right.\\
&\quad \left. + \lambda_{\phi^2 W_0^2}\left(24 c^{(1)}_{\phi^4 W_0^2} + 8 c^{(2)}_{\phi^4 W_0^2}\right)\right]\\
&+ c^{(2)}_{\phi^4 D^2}\left[c_{\phi^2 W_0^4}\left(\frac{3}{2}g_3^2 - 6\lambda_3 - 32\lambda_{\phi^2 W_0^2}\right) - \lambda_{\phi^2 W_0^2}\left(6 c^{(1)}_{\phi^4 W_0^2} + 2 c^{(2)}_{\phi^4 W_0^2}\right)\right] ,\\
I_2^{-1}\delta c^{(1)}_{\phi^4 D^2} &= c^{(1)}_{\phi^2 W_0^2 D^2}\left(2 c^{(1)}_{\phi^4 W_0^2} + \frac{2}{3} c^{(2)}_{\phi^4 W_0^2}\right) + c_{\phi^6}\left(16 c^{(1)}_{\phi^4 D^2} - 4 c^{(2)}_{\phi^4 D^2}\right) ,\\
I_2^{-1}\delta c^{(2)}_{\phi^4 D^2} &= 0 ,\\
I_2^{-1}\delta r^{(3)}_{\phi^4 D^2} &= c^{(1)}_{\phi^2 W_0^2 D^2}\left(-4 c^{(1)}_{\phi^4 W_0^2} - \frac{4}{3} c^{(2)}_{\phi^4 W_0^2}\right) + c_{\phi^6}\left(-32 c^{(1)}_{\phi^4 D^2} + 8 c^{(2)}_{\phi^4 D^2}\right) ,\\
I_2^{-1}\delta c_{\phi^8} &= \left(c^{(1)}_{\phi^4 W_0^2}\right)^2\left(-144 c^{(1)}_{\phi^2 W_0^2 D^2} + 96 c^{(1)}_{\phi^4 D^2} - 24 c^{(2)}_{\phi^4 D^2}\right)\\
&+ c^{(1)}_{\phi^4 W_0^2} c^{(2)}_{\phi^4 W_0^2}\left(-96 c^{(1)}_{\phi^2 W_0^2 D^2} + 64 c^{(1)}_{\phi^4 D^2} - 16 c^{(2)}_{\phi^4 D^2}\right)\\
&+ \left(c^{(2)}_{\phi^4 W_0^2}\right)^2\left[-80 c^{(1)}_{\phi^2 W_0^2 D^2} + 16 c^{(2)}_{\phi^2 W_0^2 D^2} + 32 c^{(1)}_{\phi^4 D^2} - 8 c^{(2)}_{\phi^4 D^2}\right]\\
&+ c^{(1)}_{\phi^2 W_0^2 D^2} c_{\phi^6}\left(180 c^{(1)}_{\phi^4 W_0^2} + 60 c^{(2)}_{\phi^4 W_0^2}\right) + 1056 c_{\phi^6} c_{\phi^8}\\
&+ c^{(1)}_{\phi^6 W_0^2}\left(72 c^{(1)}_{\phi^4 W_0^2} + 24 c^{(2)}_{\phi^4 W_0^2}\right) + c^{(2)}_{\phi^6 W_0^2}\left(24 c^{(1)}_{\phi^4 W_0^2} + 40 c^{(2)}_{\phi^4 W_0^2}\right)\\
&+ c^2_{\phi^6}\left(3456 c^{(1)}_{\phi^4 D^2} - 828 c^{(2)}_{\phi^4 D^2}\right) ,\\
I_2^{-1}\delta c^{(1)}_{\phi^6 W_0^2} &= \left(c^{(1)}_{\phi^4 W_0^2}\right)^2\left[-120 c^{(1)}_{\phi^2 W_0^2 D^2} + 480 c^{(1)}_{\phi^4 D^2} - 112 c^{(2)}_{\phi^4 D^2}\right]\\
&+ c^{(1)}_{\phi^4 W_0^2} c^{(2)}_{\phi^4 W_0^2}\left[-8 c^{(1)}_{\phi^2 W_0^2 D^2} + 32 c^{(2)}_{\phi^2 W_0^2 D^2} + 64 c^{(1)}_{\phi^4 D^2} - 16 c^{(2)}_{\phi^4 D^2}\right]\\
&+ \left(c^{(2)}_{\phi^4 W_0^2}\right)^2\left[-112 c^{(1)}_{\phi^2 W_0^2 D^2} + 176 c^{(2)}_{\phi^2 W_0^2 D^2} + 72 c^{(1)}_{\phi^4 D^2} - 16 c^{(2)}_{\phi^4 D^2}\right]\\
&- 480 c^{(1)}_{\phi^2 W_0^2 D^2}\left(c_{\phi^2 W_0^4}\right)^2
\end{aligned}
\tag{A.1}
$$

$$
\begin{aligned}
&+ c_{\phi^2 W_0^4} c^{(1)}_{\phi^4 W_0^2}\left[-400 c^{(1)}_{\phi^2 W_0^2 D^2} + 320 c^{(1)}_{\phi^4 D^2} - 80 c^{(2)}_{\phi^4 D^2}\right] \\
&+ c_{\phi^2 W_0^4} c^{(2)}_{\phi^4 W_0^2}\left[-112 c^{(1)}_{\phi^2 W_0^2 D^2} + 64 c^{(1)}_{\phi^4 D^2} - 16 c^{(2)}_{\phi^4 D^2}\right] \\
&+ 300 c^{(1)}_{\phi^2 W_0^2 D^2} c_{\phi^2 W_0^4} c_{\phi^6} + c^{(1)}_{\phi^4 W_0^2} c_{\phi^6}\left(1800 c^{(1)}_{\phi^4 D^2} - 426 c^{(2)}_{\phi^4 D^2}\right) \\
&+ c^{(2)}_{\phi^4 W_0^2} c_{\phi^6}\left(216 c^{(1)}_{\phi^4 D^2} - 54 c^{(2)}_{\phi^4 D^2}\right) \\
&+ c^{(1)}_{\phi^6 W_0^2}\left[120 c_{\phi^2 W_0^4} + 216 c^{(1)}_{\phi^4 W_0^2} + 24 c^{(2)}_{\phi^4 W_0^2} + 408 c_{\phi^6}\right] \\
&+ c^{(2)}_{\phi^6 W_0^2}\left[24 c_{\phi^2 W_0^4} + 16 c^{(1)}_{\phi^4 W_0^2} + 112 c^{(2)}_{\phi^4 W_0^2} + 48 c_{\phi^6}\right] \\
&+ c^2_{\phi^6}\left(3456 c^{(1)}_{\phi^4 D^2} - 828 c^{(2)}_{\phi^4 D^2}\right) + c_{\phi^8}\left(240 c^{(1)}_{\phi^4 W_0^2} + 48 c^{(2)}_{\phi^4 W_0^2}\right) ,
\end{aligned}
$$

$$
\begin{aligned}
I_2^{-1}\delta c^{(2)}_{\phi^6 W_0^2} &= c_{\phi^2 W_0^4} c^{(2)}_{\phi^4 W_0^2}\left[-64 c^{(1)}_{\phi^2 W_0^2 D^2} + 128 c^{(1)}_{\phi^4 D^2} - 32 c^{(2)}_{\phi^4 D^2}\right] \\
&+ c^{(1)}_{\phi^4 W_0^2} c^{(2)}_{\phi^4 W_0^2}\left[-216 c^{(1)}_{\phi^2 W_0^2 D^2} - 96 c^{(2)}_{\phi^2 W_0^2 D^2} + 768 c^{(1)}_{\phi^4 D^2} - 176 c^{(2)}_{\phi^4 D^2}\right] \\
&+ \left(c^{(2)}_{\phi^4 W_0^2}\right)^2\left[-184 c^{(1)}_{\phi^2 W_0^2 D^2} + 32 c^{(2)}_{\phi^2 W_0^2 D^2} + 424 c^{(1)}_{\phi^4 D^2} - 96 c^{(2)}_{\phi^4 D^2}\right] \\
&+ c^{(2)}_{\phi^4 W_0^2} c_{\phi^6}\left(1152 c^{(1)}_{\phi^4 D^2} - 264 c^{(2)}_{\phi^4 D^2}\right) + 144 c^{(2)}_{\phi^4 W_0^2} c^{(1)}_{\phi^6 W_0^2} + 96 c^{(2)}_{\phi^4 W_0^2} c_{\phi^8} \\
&+ c^{(2)}_{\phi^6 W_0^2}\left[48 c_{\phi^2 W_0^4} + 168 c^{(1)}_{\phi^4 W_0^2} + 216 c^{(2)}_{\phi^4 W_0^2} + 264 c_{\phi^6}\right] ,
\end{aligned}
$$

$$
\begin{aligned}
I_2^{-1}\delta c^{(1)}_{\phi^2 W_0^2 D^2} &= 0 , \\
I_2^{-1}\delta c^{(2)}_{\phi^2 W_0^2 D^2} &= 0 , \\
I_2^{-1}\delta r^{(3)}_{\phi^2 W_0^2 D^2} &= 0 , \\
I_2^{-1}\delta r^{(4)}_{\phi^2 W_0^2 D^2} &= \frac{10}{3} c^{(1)}_{\phi^2 W_0^2 D^2} c_{\phi^2 W_0^4} + c^{(1)}_{\phi^4 W_0^2}\left(4 c^{(1)}_{\phi^4 D^2} - c^{(2)}_{\phi^4 D^2}\right) \\
&\quad + c^{(2)}_{\phi^4 W_0^2}\left(\frac{4}{3} c^{(1)}_{\phi^4 D^2} - \frac{1}{3} c^{(2)}_{\phi^4 D^2}\right) , \\
I_2^{-1}\delta r^{(5)}_{\phi^2 W_0^2 D^2} &= c^{(1)}_{\phi^2 W_0^2 D^2}\left(-8 c^{(1)}_{\phi^4 W_0^2} - \frac{8}{3} c^{(2)}_{\phi^4 W_0^2}\right) , \\
I_2^{-1}\delta r^{(6)}_{\phi^2 W_0^2 D^2} &= 0 , \\
I_2^{-1}\delta c_{\phi^2 W^2} &= 0 ,
\end{aligned}
\tag{A.1}
$$

with $I_2^{-1} = 64\pi^2\epsilon$ being the two-loop $\overline{\text{MS}}$ ϵ-pole of Eq. (4.11).

Then, after performing the field redefinitions that remove redundant operators and canonically normalize the fields (see Eq. (4.13)), we obtain the following beta functions for the parameters of the theory:

$$
\begin{aligned}
\beta_{m_3^2} &= \overbrace{-\frac{39}{16}g_3^4 - 9g_3^2\lambda_3 + 12\lambda_3^2 - 12g_3^2\lambda_{\phi^2W_0^2} + 6\lambda_{\phi^2W_0^2}^2}^{\beta^{\text{LO}}_{m_3^2}} \\
&\quad + m_3^2\Big[c^{(1)}_{\phi^4D^2}\left(-14g_3^2 + 32\lambda_3\right) + c^{(2)}_{\phi^4D^2}\left(3g_3^2 - 8\lambda_3\right) \\
&\qquad - 20c_{\phi^2W^2}g_3^2 - 4c^{(2)}_{\phi^2W_0^2D^2}g_3^2 + 8c^{(1)}_{\phi^2W_0^2D^2}\lambda_{\phi^2W_0^2}\Big] \\
&\quad + m_D^2\left[c^{(1)}_{\phi^2W_0^2D^2}\left(12g_3^2 - 12\lambda_{\phi^2W_0^2}\right) - 12c^{(2)}_{\phi^2W_0^2D^2}g_3^2 - 24c_{\phi^2W^2}g_3^2\right], \\
\beta_{m_D^2} &= \overbrace{g_3^4 - 6g_3^2\lambda_{\phi^2W_0^2} + 8\lambda_{\phi^2W_0^2}^2 - 80g_3^2\lambda_{W_0^4} + 160\lambda_{W_0^4}^2}^{\beta^{\text{LO}}_{m_D^2}} \\
&\quad + m_3^2\Big[-16c^{(2)}_{\phi^2W_0^2D^2}g_3^2\Big] \\
&\quad + m_D^2\left[c^{(1)}_{\phi^2W_0^2D^2}\left(6g_3^2 - \frac{16}{3}\lambda_{\phi^2W_0^2}\right) - \frac{16}{3}c^{(2)}_{\phi^2W_0^2D^2}g_3^2\right], \\
\beta_{\lambda_3} &= -c_{\phi^2W^2}\left(\frac{27}{2}g_3^4 + 76g_3^2\lambda_3 + 48g_3^2\lambda_{\phi^2W_0^2}\right) + c_{\phi^6}\left(-18g_3^2 + 96\lambda_3\right) \\
&\quad + c^{(1)}_{\phi^4D^2}\left(3g_3^4 - 52g_3^2\lambda_3 + 256\lambda_3^2 + 24\lambda_{\phi^2W_0^2}^2\right) \\
&\quad + c^{(2)}_{\phi^4D^2}\left(-\frac{13}{16}g_3^4 + 9g_3^2\lambda_3 - 60\lambda_3^2 - 6\lambda_{\phi^2W_0^2}^2\right) \\
&\quad + c^{(1)}_{\phi^2W_0^2D^2}\left(24g_3^2\lambda_{\phi^2W_0^2} + 40\lambda_3\lambda_{\phi^2W_0^2} - 48\lambda_{\phi^2W_0^2}^2\right) \\
&\quad + c^{(2)}_{\phi^2W_0^2D^2}\left(\frac{3}{2}g_3^4 - 8g_3^2\lambda_3 - 24g_3^2\lambda_{\phi^2W_0^2}\right) \\
&\quad + c^{(1)}_{\phi^4W_0^2}\left(-12g_3^2 + 24\lambda_{\phi^2W_0^2}\right) + c^{(2)}_{\phi^4W_0^2}\left(-4g_3^2 + 8\lambda_{\phi^2W_0^2}\right) \\
&\quad + m_3^2\left[c^{(1)}_{\phi^2W_0^2D^2}\left(16c^{(1)}_{\phi^4W_0^2} + \frac{16}{3}c^{(2)}_{\phi^4W_0^2}\right) + c_{\phi^6}\left(128c^{(1)}_{\phi^4D^2} - 32c^{(2)}_{\phi^4D^2}\right)\right] \\
&\quad + m_D^2\left[-c^{(1)}_{\phi^2W_0^2D^2}\left(24c^{(1)}_{\phi^4W_0^2} + 8c^{(2)}_{\phi^4W_0^2}\right)\right], \\
\beta_{\lambda_{W_0^4}} &= c_{\phi^2W_0^4}\left(-3g_3^2 + 16\lambda_{\phi^2W_0^2}\right) + c_{W_0^6}\left(-84g_3^2 + 672\lambda_{W_0^4}\right) \\
&\quad + c^{(1)}_{\phi^2W_0^2D^2}\left(12g_3^2\lambda_{W_0^4} - \frac{32}{3}\lambda_{\phi^2W_0^2}\lambda_{W_0^4}\right) \\
&\quad + c^{(2)}_{\phi^2W_0^2D^2}\left(2g_3^4 - 8g_3^2\lambda_{\phi^2W_0^2} - \frac{32}{3}g_3^2\lambda_{W_0^4}\right),
\end{aligned}
\tag{A.2}
$$

$$
\begin{aligned}
\beta_{\lambda_{\phi^2 W_0^2}} &= c_{\phi^2 W^2}\left(12g_3^4 - 52g_3^2\lambda_{\phi^2 W_0^2} - 160g_3^2\lambda_{W_0^4}\right) \\
&+ c_{\phi^2 W_0^4}\left(-40g_3^2 + 40\lambda_{\phi^2 W_0^2} + 160\lambda_{W_0^4}\right) \\
&+ c^{(1)}_{\phi^4 W_0^2}\left(-9g_3^2 + 24\lambda_3 + 24\lambda_{\phi^2 W_0^2}\right) + c^{(2)}_{\phi^4 W_0^2}\left(-3g_3^2 + 8\lambda_3 + 8\lambda_{\phi^2 W_0^2}\right) \\
&+ c^{(1)}_{\phi^2 W_0^2 D^2}\left(4g_3^4 - 10g_3^2\lambda_{\phi^2 W_0^2} + 80g_3^2\lambda_{W_0^4} - \frac{40}{3}\lambda^2_{\phi^2 W_0^2} - 480\lambda^2_{W_0^4}\right) \\
&+ c^{(2)}_{\phi^2 W_0^2 D^2}\left(16g_3^4 - 24g_3^2\lambda_3 - \frac{52}{3}g_3^2\lambda_{\phi^2 W_0^2} - 80g_3^2\lambda_{W_0^4}\right) \\
&+ c^{(1)}_{\phi^4 D^2}\left(g_3^4 - 14g_3^2\lambda_{\phi^2 W_0^2} + 32\lambda_3\lambda_{\phi^2 W_0^2} + 40\lambda^2_{\phi^2 W_0^2}\right) \\
&+ c^{(2)}_{\phi^4 D^2}\left(3g_3^2\lambda_{\phi^2 W_0^2} - 8\lambda_3\lambda_{\phi^2 W_0^2} - 8\lambda^2_{\phi^2 W_0^2}\right) \\
&+ m_3^2\left[\frac{70}{3}c^{(1)}_{\phi^2 W_0^2 D^2}c_{\phi^2 W_0^4} + c^{(1)}_{\phi^4 W_0^2}\left(28c^{(1)}_{\phi^4 D^2} - 7c^{(2)}_{\phi^4 D^2}\right)\right. \\
&\quad \left. + c^{(2)}_{\phi^4 W_0^2}\left(\frac{28}{3}c^{(1)}_{\phi^4 D^2} - \frac{7}{3}c^{(2)}_{\phi^4 D^2}\right)\right] \\
&+ m_D^2\left[-c^{(1)}_{\phi^2 W_0^2 D^2}\left(40c_{\phi^2 W_0^4} + 8c^{(1)}_{\phi^4 W_0^2} + \frac{8}{3}c^{(2)}_{\phi^4 W_0^2}\right)\right], \\
\beta_{c_{\phi^6}} &= 24\left(c^{(1)}_{\phi^4 W_0^2}\right)^2 + 16c^{(1)}_{\phi^4 W_0^2}c^{(2)}_{\phi^4 W_0^2} + 16\left(c^{(2)}_{\phi^4 W_0^2}\right)^2 + 204c^2_{\phi^6} \\
&+ c^{(1)}_{\phi^4 W_0^2}\left[g_3^2\left(24c^{(1)}_{\phi^2 W_0^2 D^2} - 24c^{(2)}_{\phi^2 W_0^2 D^2} - 48c_{\phi^2 W^2}\right) + 80c^{(1)}_{\phi^2 W_0^2 D^2}\lambda_3\right. \\
&\quad \left. + \lambda_{\phi^2 W_0^2}\left(-168c^{(1)}_{\phi^2 W_0^2 D^2} + 96c^{(1)}_{\phi^4 D^2} - 24c^{(2)}_{\phi^4 D^2}\right)\right] \\
&+ c^{(2)}_{\phi^4 W_0^2}\left[g_3^2\left(8c^{(1)}_{\phi^2 W_0^2 D^2} - 8c^{(2)}_{\phi^2 W_0^2 D^2} - 16c_{\phi^2 W^2}\right) + \frac{80}{3}c^{(1)}_{\phi^2 W_0^2 D^2}\lambda_3\right. \\
&\quad \left. + \lambda_{\phi^2 W_0^2}\left(-56c^{(1)}_{\phi^2 W_0^2 D^2} + 32c^{(1)}_{\phi^4 D^2} - 8c^{(2)}_{\phi^4 D^2}\right)\right] \\
&+ c_{\phi^6}\left[g_3^2\left(-12c^{(2)}_{\phi^2 W_0^2 D^2} - 168c_{\phi^2 W^2} - 114c^{(1)}_{\phi^4 D^2} + 18c^{(2)}_{\phi^4 D^2}\right)\right. \\
&\quad \left. + \lambda_3\left(1888c^{(1)}_{\phi^4 D^2} - 448c^{(2)}_{\phi^4 D^2}\right) + 96c^{(1)}_{\phi^2 W_0^2 D^2}\lambda_{\phi^2 W_0^2}\right] \\
&+ \left(-12c^{(1)}_{\phi^6 W_0^2} - 4c^{(2)}_{\phi^6 W_0^2} - 30c_{\phi^8}\right)g_3^2 + 240c_{\phi^8}\lambda_3 \\
&+ \left(36c^{(1)}_{\phi^6 W_0^2} + 12c^{(2)}_{\phi^6 W_0^2}\right)\lambda_{\phi^2 W_0^2}, \\
\beta_{c_{W_0^6}} &= 16\left(c_{\phi^2 W_0^4}\right)^2 + 1488c^2_{W_0^6} - 8c^{(2)}_{\phi^2 W_0^2 D^2}c_{\phi^2 W_0^4}g_3^2 \\
&+ c_{W_0^6}\left[\left(18c^{(1)}_{\phi^2 W_0^2 D^2} - 16c^{(2)}_{\phi^2 W_0^2 D^2}\right)g_3^2 - 16c^{(1)}_{\phi^2 W_0^2 D^2}\lambda_{\phi^2 W_0^2}\right], \\
\beta_{c^{(1)}_{\phi^4 W_0^2}} &= 80\left(c_{\phi^2 W_0^4}\right)^2 + 80c_{\phi^2 W_0^4}c^{(1)}_{\phi^4 W_0^2} + 48\left(c^{(1)}_{\phi^4 W_0^2}\right)^2 + 16c_{\phi^2 W_0^4}c^{(2)}_{\phi^4 W_0^2}
\end{aligned}
\tag{A.2}
$$

$$
\begin{aligned}
&+16c^{(1)}_{\phi^4W_0^2}c^{(2)}_{\phi^4W_0^2}+44\left(c^{(2)}_{\phi^4W_0^2}\right)^2+96c^{(1)}_{\phi^4W_0^2}c_{\phi^6}+24c^{(2)}_{\phi^4W_0^2}c_{\phi^6}\\
&+c_{\phi^2W_0^4}\Bigg[g_3^2\left(80c^{(1)}_{\phi^2W_0^2D^2}-80c^{(2)}_{\phi^2W_0^2D^2}-160c_{\phi^2W^2}\right)+\frac{400}{3}c^{(1)}_{\phi^2W_0^2D^2}\lambda_3\\
&\quad+\lambda_{\phi^2W_0^2}\left(-240c^{(1)}_{\phi^2W_0^2D^2}+160c^{(1)}_{\phi^4D^2}-40c^{(2)}_{\phi^4D^2}\right)-960c^{(1)}_{\phi^2W_0^2D^2}\lambda_{W_0^4}\Bigg]\\
&+c^{(1)}_{\phi^4W_0^2}\Bigg[g_3^2\left(-26c^{(1)}_{\phi^2W_0^2D^2}-\frac{88}{3}c^{(2)}_{\phi^2W_0^2D^2}-140c_{\phi^2W^2}-52c^{(1)}_{\phi^4D^2}+9c^{(2)}_{\phi^4D^2}\right)\\
&\quad+\lambda_{\phi^2W_0^2}\left(-\frac{244}{3}c^{(1)}_{\phi^2W_0^2D^2}+256c^{(1)}_{\phi^4D^2}-56c^{(2)}_{\phi^4D^2}\right)\\
&\quad+\lambda_3\left(512c^{(1)}_{\phi^4D^2}-120c^{(2)}_{\phi^4D^2}\right)\Bigg]\\
&+c^{(2)}_{\phi^4W_0^2}\Bigg[g_3^2\left(4c^{(1)}_{\phi^2W_0^2D^2}-12c^{(2)}_{\phi^2W_0^2D^2}-12c_{\phi^2W^2}-4c^{(1)}_{\phi^4D^2}+2c^{(2)}_{\phi^4D^2}\right)\\
&\quad+\lambda_3\left(\frac{256}{3}c^{(1)}_{\phi^4D^2}-\frac{64}{3}c^{(2)}_{\phi^4D^2}\right)-32c^{(1)}_{\phi^2W_0^2D^2}\lambda_{W_0^4}\\
&\quad+\lambda_{\phi^2W_0^2}\left(-\frac{52}{3}c^{(1)}_{\phi^2W_0^2D^2}+16c^{(2)}_{\phi^2W_0^2D^2}+32c^{(1)}_{\phi^4D^2}-8c^{(2)}_{\phi^4D^2}\right)\Bigg]\\
&+c_{\phi^6}\left(-48c^{(2)}_{\phi^2W_0^2D^2}g_3^2+\left(96c^{(1)}_{\phi^4D^2}-24c^{(2)}_{\phi^4D^2}\right)\lambda_{\phi^2W_0^2}\right)\\
&+\left(-18c^{(1)}_{\phi^6W_0^2}-3c^{(2)}_{\phi^6W_0^2}\right)g_3^2+\left(96c^{(1)}_{\phi^6W_0^2}+16c^{(2)}_{\phi^6W_0^2}\right)\lambda_3\\
&+\left(48c^{(1)}_{\phi^6W_0^2}+8c^{(2)}_{\phi^6W_0^2}\right)\lambda_{\phi^2W_0^2}\,,
\end{aligned}
$$

$$
\begin{aligned}
\beta_{c^{(2)}_{\phi^4W_0^2}}&=32c_{\phi^2W_0^4}c^{(2)}_{\phi^4W_0^2}+48c^{(1)}_{\phi^4W_0^2}c^{(2)}_{\phi^4W_0^2}+44\left(c^{(2)}_{\phi^4W_0^2}\right)^2+24c^{(2)}_{\phi^4W_0^2}c_{\phi^6}\\
&+c^{(2)}_{\phi^4W_0^2}\Bigg[g_3^2\left(-38c^{(1)}_{\phi^2W_0^2D^2}+\frac{20}{3}c^{(2)}_{\phi^2W_0^2D^2}-104c_{\phi^2W^2}-40c^{(1)}_{\phi^4D^2}+3c^{(2)}_{\phi^4D^2}\right)\\
&\quad+\lambda_3\left(256c^{(1)}_{\phi^4D^2}-56c^{(2)}_{\phi^4D^2}\right)+96c^{(1)}_{\phi^2W_0^2D^2}\lambda_{W_0^4}\\
&\quad+\lambda_{\phi^2W_0^2}\left(-\frac{88}{3}c^{(1)}_{\phi^2W_0^2D^2}-48c^{(2)}_{\phi^2W_0^2D^2}+160c^{(1)}_{\phi^4D^2}-32c^{(2)}_{\phi^4D^2}\right)\Bigg]\\
&+c^{(2)}_{\phi^6W_0^2}\left(-9g_3^2+48\lambda_3+24\lambda_{\phi^2W_0^2}\right)\,,
\end{aligned}
\tag{A.2}
$$

$$
\begin{aligned}
\beta_{c_{\phi^2W_0^4}}&=88\left(c_{\phi^2W_0^4}\right)^2+48c_{\phi^2W_0^4}c^{(1)}_{\phi^4W_0^2}+12\left(c^{(1)}_{\phi^4W_0^2}\right)^2+16c_{\phi^2W_0^4}c^{(2)}_{\phi^4W_0^2}\\
&+8c^{(1)}_{\phi^4W_0^2}c^{(2)}_{\phi^4W_0^2}+12\left(c^{(2)}_{\phi^4W_0^2}\right)^2+672c_{\phi^2W_0^4}c_{W_0^6}\\
&+c_{\phi^2W_0^4}\Bigg[g_3^2\left(-20c^{(1)}_{\phi^2W_0^2D^2}-\frac{92}{3}c^{(2)}_{\phi^2W_0^2D^2}-84c_{\phi^2W^2}-14c^{(1)}_{\phi^4D^2}+3c^{(2)}_{\phi^4D^2}\right)\\
&\quad+\lambda_3\left(32c^{(1)}_{\phi^4D^2}-8c^{(2)}_{\phi^4D^2}\right)+\lambda_{\phi^2W_0^2}\left(-40c^{(1)}_{\phi^2W_0^2D^2}+160c^{(1)}_{\phi^4D^2}-32c^{(2)}_{\phi^4D^2}\right)\\
&\quad-192c^{(1)}_{\phi^2W_0^2D^2}\lambda_{W_0^4}\Bigg]
\end{aligned}
$$

$$
\begin{aligned}
&+ c^{(1)}_{\phi^4 W_0^2}\left(-24c^{(2)}_{\phi^2 W_0^2 D^2} g_3^2 + \left(32c^{(1)}_{\phi^4 D^2} - 8c^{(2)}_{\phi^4 D^2}\right)\lambda_{\phi^2 W_0^2} - 32c^{(1)}_{\phi^2 W_0^2 D^2}\lambda_{W_0^4}\right)\\
&+ c^{(2)}_{\phi^4 W_0^2}\left(-8c^{(2)}_{\phi^2 W_0^2 D^2} g_3^2 + \left(\frac{32}{3}c^{(1)}_{\phi^4 D^2} - \frac{8}{3}c^{(2)}_{\phi^4 D^2}\right)\lambda_{\phi^2 W_0^2} - \frac{32}{3}c^{(1)}_{\phi^2 W_0^2 D^2}\lambda_{W_0^4}\right)\\
&+ c_{W_0^6}\Big[g_3^2\left(168c^{(1)}_{\phi^2 W_0^2 D^2} - 168c^{(2)}_{\phi^2 W_0^2 D^2} - 336c_{\phi^2 W^2}\right) + 168c^{(1)}_{\phi^2 W_0^2 D^2}\lambda_{\phi^2 W_0^2}\\
&\quad - 4032c^{(1)}_{\phi^2 W_0^2 D^2}\lambda_{W_0^4}\Big]\,,\\
\beta_{c^{(1)}_{\phi^4 D^2}} &= 0\,,\\
\beta_{c^{(2)}_{\phi^4 D^2}} &= 0\,,\\
\beta_{c_{\phi^8}} &= \left(c^{(1)}_{\phi^4 W_0^2}\right)^2\left[-144c^{(1)}_{\phi^2 W_0^2 D^2} + 96c^{(1)}_{\phi^4 D^2} - 24c^{(2)}_{\phi^4 D^2}\right]\\
&\quad + c^{(1)}_{\phi^4 W_0^2}c^{(2)}_{\phi^4 W_0^2}\left[-96c^{(1)}_{\phi^2 W_0^2 D^2} + 64c^{(1)}_{\phi^4 D^2} - 16c^{(2)}_{\phi^4 D^2}\right]\\
&\quad + \left(c^{(2)}_{\phi^4 W_0^2}\right)^2\left[-80c^{(1)}_{\phi^2 W_0^2 D^2} + 16c^{(2)}_{\phi^2 W_0^2 D^2} + 32c^{(1)}_{\phi^4 D^2} - 8c^{(2)}_{\phi^4 D^2}\right]\\
&\quad + c_{\phi^6}\Big[192c^{(1)}_{\phi^2 W_0^2 D^2}c^{(1)}_{\phi^4 W_0^2} + 64c^{(1)}_{\phi^2 W_0^2 D^2}c^{(2)}_{\phi^4 W_0^2}\\
&\quad\quad + c_{\phi^6}\left(3552c^{(1)}_{\phi^4 D^2} - 852c^{(2)}_{\phi^4 D^2}\right) + 1056c_{\phi^8}\Big]\\
&\quad + c^{(1)}_{\phi^6 W_0^2}\left(72c^{(1)}_{\phi^4 W_0^2} + 24c^{(2)}_{\phi^4 W_0^2}\right) + c^{(2)}_{\phi^6 W_0^2}\left(24c^{(1)}_{\phi^4 W_0^2} + 40c^{(2)}_{\phi^4 W_0^2}\right)\,,\\
\beta_{c^{(1)}_{\phi^6 W_0^2}} &= -480c^{(1)}_{\phi^2 W_0^2 D^2}\left(c_{\phi^2 W_0^4}\right)^2\\
&\quad + c_{\phi^2 W_0^4}c^{(1)}_{\phi^4 W_0^2}\left[-400c^{(1)}_{\phi^2 W_0^2 D^2} + 320c^{(1)}_{\phi^4 D^2} - 80c^{(2)}_{\phi^4 D^2}\right]\\
&\quad + c_{\phi^2 W_0^4}c^{(2)}_{\phi^4 W_0^2}\left[-112c^{(1)}_{\phi^2 W_0^2 D^2} + 64c^{(1)}_{\phi^4 D^2} - 16c^{(2)}_{\phi^4 D^2}\right]\\
&\quad + 320c^{(1)}_{\phi^2 W_0^2 D^2}c_{\phi^2 W_0^4}c_{\phi^6}\\
&\quad + \left(c^{(1)}_{\phi^4 W_0^2}\right)^2\left[-136c^{(1)}_{\phi^2 W_0^2 D^2} + 480c^{(1)}_{\phi^4 D^2} - 112c^{(2)}_{\phi^4 D^2}\right]\\
&\quad + c^{(1)}_{\phi^4 W_0^2}c^{(2)}_{\phi^4 W_0^2}\left[-\frac{40}{3}c^{(1)}_{\phi^2 W_0^2 D^2} + 32c^{(2)}_{\phi^2 W_0^2 D^2} + 64c^{(1)}_{\phi^4 D^2} - 16c^{(2)}_{\phi^4 D^2}\right]\\
&\quad + \left(c^{(2)}_{\phi^4 W_0^2}\right)^2\left[-112c^{(1)}_{\phi^2 W_0^2 D^2} + 176c^{(2)}_{\phi^2 W_0^2 D^2} + 72c^{(1)}_{\phi^4 D^2} - 16c^{(2)}_{\phi^4 D^2}\right]\\
&\quad + c_{\phi^6}c^{(1)}_{\phi^4 W_0^2}\left(1824c^{(1)}_{\phi^4 D^2} - 432c^{(2)}_{\phi^4 D^2}\right) + c_{\phi^6}c^{(2)}_{\phi^4 W_0^2}\left(224c^{(1)}_{\phi^4 D^2} - 56c^{(2)}_{\phi^4 D^2}\right)\\
&\quad + c^{(1)}_{\phi^6 W_0^2}\left[120c_{\phi^2 W_0^4} + 216c^{(1)}_{\phi^4 W_0^2} + 24c^{(2)}_{\phi^4 W_0^2} + 408c_{\phi^6}\right]\\
&\quad + c^{(2)}_{\phi^6 W_0^2}\left[24c_{\phi^2 W_0^4} + 16c^{(1)}_{\phi^4 W_0^2} + 112c^{(2)}_{\phi^4 W_0^2} + 48c_{\phi^6}\right]
\end{aligned}
\tag{A.2}
$$

$$
\begin{aligned}
&+ c_{\phi^8}\left(240 c^{(1)}_{\phi^4 W_0^2} + 48 c^{(2)}_{\phi^4 W_0^2}\right) , \\
\beta_{c^{(2)}_{\phi^6 W_0^2}} &= c_{\phi^2 W_0^4} c^{(2)}_{\phi^4 W_0^2}\left[-64 c^{(1)}_{\phi^2 W_0^2 D^2} + 128 c^{(1)}_{\phi^4 D^2} - 32 c^{(2)}_{\phi^4 D^2}\right] \\
&+ c^{(1)}_{\phi^4 W_0^2} c^{(2)}_{\phi^4 W_0^2}\left[-232 c^{(1)}_{\phi^2 W_0^2 D^2} - 96 c^{(2)}_{\phi^2 W_0^2 D^2} + 768 c^{(1)}_{\phi^4 D^2} - 176 c^{(2)}_{\phi^4 D^2}\right] \\
&+ \left(c^{(2)}_{\phi^4 W_0^2}\right)^2\left[-\frac{568}{3} c^{(1)}_{\phi^2 W_0^2 D^2} + 32 c^{(2)}_{\phi^2 W_0^2 D^2} + 424 c^{(1)}_{\phi^4 D^2} - 96 c^{(2)}_{\phi^4 D^2}\right] \\
&+ c_{\phi^6} c^{(2)}_{\phi^4 W_0^2}\left(1152 c^{(1)}_{\phi^4 D^2} - 264 c^{(2)}_{\phi^4 D^2}\right) + 144 c^{(2)}_{\phi^4 W_0^2} c^{(1)}_{\phi^6 W_0^2} \\
&+ c^{(2)}_{\phi^6 W_0^2}\left[48 c_{\phi^2 W_0^4} + 168 c^{(1)}_{\phi^4 W_0^2} + 216 c^{(2)}_{\phi^4 W_0^2} + 264 c_{\phi^6}\right] \\
&+ 96 c^{(2)}_{\phi^4 W_0^2} c_{\phi^8} , \qquad \text{(A.2)} \\
\beta_{c^{(1)}_{\phi^2 W_0^2 D^2}} &= 0 , \\
\beta_{c^{(2)}_{\phi^2 W_0^2 D^2}} &= 0 , \\
\beta_{c_{\phi^2 W^2}} &= 0 , \\
\beta_{g_3^2} &= -\frac{28}{3} c_{\phi^2 W^2} g_3^4 .
\end{aligned}
$$

A.2 Results below the soft scale

Below the soft scale, the dimensionally reduced theory is given by Eq. (4.1) with only the operators including Φ and W_i being relevant. We find the parameter and field-strength counterterms of the theory to be

$$
\begin{aligned}
I_2^{-1}\delta Z_\phi &= 2c_{\phi^2W^2}g_3^2 + c^{(1)}_{\phi^4D^2}\left(5g_3^2 - 8\lambda_3\right) - c^{(2)}_{\phi^4D^2}\left(\frac{3}{2}g_3^2 - 2\lambda_3\right)\,,\\
I_2^{-1}\delta Z_W &= \frac{28}{3}c_{\phi^2W^2}g_3^2\,,\\
I_2^{-1}\delta m_3^2 &= -\frac{51}{16}g_3^4 - 9g_3^2\lambda_3 + 12\lambda_3^2\\
&\quad - m_3^2\left[18c_{\phi^2W^2}g_3^2 + c^{(1)}_{\phi^4D^2}\left(9g_3^2 - 24\lambda_3\right) - c^{(2)}_{\phi^4D^2}\left(\frac{3}{2}g_3^2 - 6\lambda_3\right)\right]\,,\\
I_2^{-1}\delta\lambda_3 &= -c_{\phi^2W^2}\left(\frac{39}{2}g_3^4 + 72g_3^2\lambda_3\right) - c_{\phi^6}\left(18g_3^2 - 96\lambda_3\right)\\
&\quad + c^{(1)}_{\phi^4D^2}\left(96c_{\phi^6}m_3^2 + 3g_3^4 - 42g_3^2\lambda_3 + 240\lambda_3^2\right)\\
&\quad - c^{(2)}_{\phi^4D^2}\left(24c_{\phi^6}m_3^2 + \frac{17}{16}g_3^4 - 6g_3^2\lambda_3 + 56\lambda_3^2\right)\,,\\
I_2^{-1}\delta c_{\phi^6} &= \frac{3}{2}c_{\phi^6}\Big[-108c_{\phi^2W^2}g_3^2 - c^{(1)}_{\phi^4D^2}\left(66g_3^2 - 1200\lambda_3\right)\\
&\quad + c^{(2)}_{\phi^4D^2}\left(9g_3^2 - 284\lambda_3\right) + 136c_{\phi^6}\Big] - 30c_{\phi^8}\left(g_3^2 - 8\lambda_3\right)\\
I_2^{-1}\delta c_{\phi^8} &= 12c_{\phi^6}\left(288c^{(1)}_{\phi^4D^2}c_{\phi^6} - 69c^{(2)}_{\phi^4D^2}c_{\phi^6} + 88c_{\phi^8}\right)\,,\\
I_2^{-1}\delta c^{(1)}_{\phi^4D^2} &= 4c_{\phi^6}\left(4c^{(1)}_{\phi^4D^2} - c^{(2)}_{\phi^4D^2}\right)\,,\\
I_2^{-1}\delta c^{(2)}_{\phi^4D^2} &= 0\,,\\
I_2^{-1}\delta r^{(3)}_{\phi^4D^2} &= -8c_{\phi^6}\left(4c^{(1)}_{\phi^4D^2} - c^{(2)}_{\phi^4D^2}\right)\,,\\
I_2^{-1}\delta c_{\phi^2W^2} &= 0\,,
\end{aligned}
\tag{A.3}
$$

where we have factored out $I_2^{-1} = 64\pi^2\epsilon$ — the two-loop $\overline{\text{MS}}$ ϵ-pole of Eq. (4.11).

Then, following the shifts to remove the redundant operator and to canonically normalize the fields (see Eq. (4.18)), we find the following beta functions for the parameters of the theory:

$$
\begin{aligned}
\beta_{m_3^2} &= \overbrace{-\frac{51}{16}g_3^4 - 9g_3^2\lambda_3 + 12\lambda_3^2}^{\beta^{\rm LO}_{m_3^2}} \\
&\quad + m_3^2\left[c^{(1)}_{\phi^4D^2}\left(-14g_3^2 + 32\lambda_3\right) + c^{(2)}_{\phi^4D^2}\left(3g_3^2 - 8\lambda_3\right) - 20c_{\phi^2W^2}g_3^2\right], \\
\beta_{\lambda_3} &= -c_{\phi^2W^2}\left(\frac{39}{2}g_3^4 + 76g_3^2\lambda_3\right) + c_{\phi^6}\left(-18g_3^2 + 96\lambda_3\right) \\
&\quad + c^{(1)}_{\phi^4D^2}\left(128c_{\phi^6}m_3^2 + 3g_3^4 - 52g_3^2\lambda_3 + 256\lambda_3^2\right) \\
&\quad + c^{(2)}_{\phi^4D^2}\left(-32c_{\phi^6}m_3^2 - \frac{17}{16}g_3^4 + 9g_3^2\lambda_3 - 60\lambda_3^2\right), \\
\beta_{c_{\phi^6}} &= c_{\phi^6}\Big[-168c_{\phi^2W^2}g_3^2 + c^{(1)}_{\phi^4D^2}\left(-84g_3^2 + 1888\lambda_3\right) \\
&\quad + c^{(2)}_{\phi^4D^2}\left(18g_3^2 - 448\lambda_3\right) + 204c_{\phi^6}\Big] \\
&\quad - 30c_{\phi^8}\left(g_3^2 - 8\lambda_3\right), \\
\beta_{c_{\phi^8}} &= 12c_{\phi^6}\left(296c^{(1)}_{\phi^4D^2}c_{\phi^6} - 71c^{(2)}_{\phi^4D^2}c_{\phi^6} + 88c_{\phi^8}\right), \\
\beta_{c^{(1)}_{\phi^4D^2}} &= 0, \\
\beta_{c^{(2)}_{\phi^4D^2}} &= 0, \\
\beta_{c_{\phi^2W^2}} &= 0, \\
\beta_{g_3^2} &= -\frac{28}{3}c_{\phi^2W^2}g_3^4.
\end{aligned}
\tag{A.4}
$$

A.3 Inclusion of the $U(1)_Y$

For completeness, we also calculate the contributions to the two-loop counterterms considering the extension of Eq. (4.1) to include a $U(1)_Y$ gauge symmetry with charge g_3'. The following operators are added to the tree-dimensional theory of Eq. (4.1), below the soft scale:

$$\mathcal{L}_{3D} \supset \frac{1}{4}B_{rs}B_{rs} + c_{\phi^2B^2}|\Phi|^2 B_{rs}B_{rs} + c_{\phi^2WB}(\Phi^\dagger\sigma^I\Phi)W^I_{rs}B_{rs}\,. \tag{A.5}$$

The counterterms in Eq. (4.12) receive the following additional contributions:

$$\begin{aligned}
I_2^{-1}\delta Z_\phi &= -\frac{2}{3}c_{\phi^2B^2}g_3'^2 - 2c_{\phi^2WB}g_3'g_3 - \frac{5}{3}c^{(1)}_{\phi^4D^2}g_3'^2 - \frac{1}{6}c^{(2)}_{\phi^4D^2}g_3'^2\,,\\
I_2^{-1}\delta Z_W &= \frac{4}{3}c_{\phi^2WB}g_3'g_3 - 4c_{\phi^2W^2}g_3'^2\,,\\
I_2^{-1}\delta Z_B &= 4c_{\phi^2WB}g_3'g_3 - \frac{4}{3}c_{\phi^2B^2}g_3'^2 - 12c_{\phi^2B^2}g_3^2\,,\\
I_2^{-1}\delta m_3^2 &= \frac{5}{16}g_3'^4 + \frac{9}{8}g_3'^2g_3^2 - 3g_3'^2\lambda_3\\
&\quad + m_3^2\left[6c_{\phi^2B^2}g_3'^2 + 6c_{\phi^2WB}g_3'g_3 + 3g_3'^2c^{(1)}_{\phi^4D^2} + \frac{3}{2}g_3'^2c^{(2)}_{\phi^4D^2}\right],\\
I_2^{-1}\delta\lambda_3 &= c_{\phi^2B^2}\left(\frac{9}{2}g_3'^4 + \frac{13}{2}g_3'^2g_3^2 - 24g_3'^2\lambda_3\right) + \frac{13}{2}c_{\phi^2W^2}g_3'^2g_3^2\\
&\quad + c_{\phi^2WB}\left(6g_3'^3g_3 + 4g_3'g_3^3 - 24g_3'g_3\lambda_3\right) + 6c_{\phi^6}g_3'^2\\
&\quad + c^{(1)}_{\phi^4D^2}\left(g_3'^4 + 2g_3'^2g_3^2 - 14g_3'^2\lambda_3\right) + c^{(2)}_{\phi^4D^2}\left(\frac{15}{6}g_3'^4 + \frac{23}{8}g_3'^2g_3^2 - 4g_3'^2\lambda_3\right),\\
I_2^{-1}\delta c_{\phi^6} &= c_{\phi^6}\left[54g_3'^2c_{\phi^2B^2} + 54c_{\phi^2WB}g_3'g_3 + 33c^{(1)}_{\phi^4D^2}g_3'^2 - \frac{27}{2}c^{(2)}_{\phi^4D^2}g_3'^2\right] + 10c_{\phi^8}g_3'^2\,,
\end{aligned} \tag{A.6}$$

in which we only list those that receive nonzero contributions at the considered accuracy.

B – BETA FUNCTIONS IN THE CXSM

This appendix collects the one-loop beta functions for the cxSM used in the analysis in Chapter V within the 4D theory and dimensionally reduced 3D EFT valid at and below the soft scale.

Beta functions in the 4D theory

The beta functions in the 4D theory, defined as $\beta_i \equiv 16\pi^2 \mu dc_i/d\mu$ read

$$
\begin{aligned}
\beta_{g^2} &= -\frac{19g^4}{3}, \\
\beta_{g'^2} &= \frac{41g'^4}{3}, \\
\beta_{y_t^2} &= \frac{9y_t^4}{2} - y_t^2\left(\frac{9g^2}{4} + \frac{17g'^2}{12} + 8g_S^2\right), \\
\beta_{\mu_h^2} &= \frac{3}{2}\mu_h^2\left(8\lambda_h + 4y_t^2 - 3g^2 - g'^2\right) + \frac{1}{2}\lambda_{hs}\mu_s^2, \\
\beta_{\lambda_h} &= \frac{9g^4}{8} + \frac{3g^2g'^2}{4} + \frac{3g'^4}{4} - 6y_t^4 + \lambda_h\left(12y_t^2 - 9g^2 - 3g'^2\right) + 24\lambda_h^2 + \frac{\lambda_{hs}^2}{4}, \\
\beta_{\mu_s^2} &= 2\lambda_{hs}\mu_h^2 + 4\lambda_s\mu_s^2, \\
\beta_{\lambda_s} &= 5\lambda_s + 2\lambda_{hs}, \\
\beta_{\lambda_{hs}} &= \lambda_{hs}\left(2\lambda_s - \frac{9}{2}g^2 - \frac{3}{2}g'^2 + 6y_t^2 + 2\lambda_{hs} + 12\lambda_h\right),
\end{aligned}
\tag{B.1}
$$

where only the top-quark Yukawa coupling is retained. The results have been cross-checked against `DRalgo` [197].

The one-loop beta functions are gauge-independent; however, they become gauge-dependent at two loops. The gauge fixing parameters also run, starting from one loop. Two-loop beta functions for the SM in a generalized gauge are available in [151].

Beta functions in the 3D EFT at the soft scale

Following DR, the scalar mass parameters of the soft 3D EFT run with the renormalization scale μ_{3D}^{soft}. The one-loop beta functions, obtained as outlined in Chapter IV, read

$$\begin{aligned}
\beta^{3D,\text{soft}}_{\mu^{2,\text{soft}}_{h,3D}} &= \frac{5}{16}g'^{4,\text{soft}}_{3D} - \frac{39}{16}\,g^{4,\text{soft}}_{3D} + \frac{9}{8}g'^{2,\text{soft}}_{3D}\,g^{2,\text{soft}}_{3D} - 3\lambda^{\text{soft}}_{h,3D}\left(g'^{2,\text{soft}}_{3D} + 3g^{2,\text{soft}}_{3D}\right) + 12\lambda^{2,\text{soft}}_{h,3D} \\
&\quad + \frac{1}{4}\lambda^{2,\text{soft}}_{hs,3D} - 6g^{2,\text{soft}}_{3D}\,\lambda^{\text{soft}}_{h^2W_0^2,3D} + 4\lambda^{\text{soft}}_{h^2G_0^2,3D}\left(\lambda^{\text{soft}}_{h^2G_0^2,3D} - 6g^{2,\text{soft}}_{S,3D}\right) \\
&\quad + \frac{3}{2}\lambda^{2,\text{soft}}_{h^2W_0^2,3D} + \frac{1}{2}\lambda^{2,\text{soft}}_{h^2B_0^2,3D} + 3\lambda^{2,\text{soft}}_{h^2W_0B_0,3D}\,, \\
\beta^{3D,\text{soft}}_{\mu^{2,\text{soft}}_{s,3D}} &= \lambda^{2,\text{soft}}_{s,3D} + \lambda^{2,\text{soft}}_{hs,3D} - \lambda^{\text{soft}}_{hs,3D}\left(g'^{2,\text{soft}}_{3D} + 3g^{2,\text{soft}}_{3D}\right) \\
&\quad - 12g^{2,\text{soft}}_{3D}\,\lambda^{\text{soft}}_{s^2W_0^2,3D} + \lambda^{2,\text{soft}}_{s^2B_0^2,3D} + 3\lambda^{2,\text{soft}}_{s^2W_0^2,3D}\,.
\end{aligned} \tag{B.2}$$

Here $\lambda^{\text{soft}}_{h^2G_0^2,3D}$, $\lambda^{\text{soft}}_{h^2W_0^2,3D}$, $\lambda^{\text{soft}}_{h^2B_0^2,3D}$, $\lambda^{\text{soft}}_{h^2W_0B_0,3D}$, $\lambda^{\text{soft}}_{s^2W_0^2,3D}$, and $\lambda^{\text{soft}}_{s^2B_0^2,3D}$ are the quartic couplings with the temporal components of the gauge fields generated by DR. The running of the Debye masses m_D^2 is omitted, as it first receives corrections at $\mathcal{O}(g^6)$ [49]. The results are in agreement with those from `DRalgo`.

Note that we do not include effects of the higher-dimensional operators in the running in analyses in Chapter V, hence only the mass parameters run.

Beta functions in the 3D EFT below the soft scale

After integrating out the temporal gauge-boson components at the soft scale, the scalar mass parameters of the 3D EFT valid below the soft scale run as

$$\begin{aligned}
\beta^{3D}_{\mu^2_{h,3D}} &= \frac{5}{16}g'^4_{3D} - \frac{51}{16}\,g^4_{3D} + \frac{9}{8}g'^2_{3D}g^2_{3D} \\
&\quad - 3\lambda_{h,3D}\left(g'^2_{3D} + 3g^2_{3D}\right) + 12\lambda^2_{h,3D} + \frac{1}{4}\lambda^2_{hs,3D}\,, \\
\beta^{3D}_{\mu^2_{s,3D}} &= -\lambda_{hs,3D}\left(g'^2_{3D} + 3g^2_{3D}\right) + \lambda^2_{s,3D} + \lambda^2_{hs,3D}\,.
\end{aligned} \tag{B.3}$$

C – PROPAGATORS IN A HOMOGENEOUS BACKGROUND

While Section VI.2 focused on determining the propagator in an inhomogeneous background, it is instructive to review the corresponding derivation in a homogeneous background. This exercise also builds intuition for the techniques used in Section VI.2.

First, consider the massless case. In three dimensions, the two-point function (propagator) satisfies

$$\vec{\nabla}_x^2 G(\vec{x},\vec{y}) = -\delta^{(3)}(\vec{x}-\vec{y}). \tag{C.1}$$

The solution is already known (up to normalization): the Coulomb potential,

$$G(\vec{x},\vec{y}) = \frac{1}{4\pi\,|\vec{x}-\vec{y}|}, \tag{C.2}$$

but it is useful to rederive this result in cylindrical coordinates, since the same strategy generalizes to the inhomogeneous case where the background field depends on z.

In cylindrical coordinates, we write

$$\begin{aligned} \vec{\nabla}^2 &= \partial_z^2 + \rho^{-1}\partial_\rho(\rho\partial_\rho) + \rho^{-2}\partial_\phi^2, \\ \delta^{(3)}(\vec{x}-\vec{y}) &= \frac{4\pi}{\rho}\delta(\rho-\rho')\delta(\phi-\phi')\delta(z-z')\,, \end{aligned} \tag{C.3}$$

To emphasize the z dependence, we represent the remaining delta functions as

$$\begin{aligned} 2\pi\delta(\phi-\phi') &= \sum_{m=-\infty}^{m=\infty} e^{im(\phi-\phi')}, \\ \frac{1}{\rho}\delta(\rho-\rho') &= \int_0^\infty dk k J_0(k\rho)J_0(k\rho'). \end{aligned} \tag{C.4}$$

motivated by the fact that these are eigenfunctions of $\rho^{-1}\partial_\rho(\rho\partial_\rho) + \rho^{-2}\partial_\phi^2$ with eigenvalue k^2.

We then use the ansatz

$$G(\vec{x},\vec{y}) = \int dk k \sum_m G_k(z,z') e^{im(\phi-\phi')} J_m(k\rho) J_m(k\rho') \,, \tag{C.5}$$

which, upon substitution into the Laplacian, yields k^2 from the radial and angular derivatives.

Assuming the propagator equation holds independently for each m and k, we obtain the following equation for G_k:

$$(\partial_z^2 - k^2) G_k = -2\delta(z-z') \tag{C.6}$$

This is solved by treating the regions $z < z'$ and $z > z'$ separately, where the delta function vanishes.

$$\begin{aligned} G_k^< &= A^<(z') e^{zk} + B^<(z') e^{-zk}, \\ G_k^> &= A^>(z') e^{zk} + B^>(z') e^{-zk}. \end{aligned} \tag{C.7}$$

Requiring bounded solutions as $z \to \pm\infty$ implies $B^<(z') = A^>(z') = 0$.

The final step is to impose boundary conditions at $z = z'$. The propagator must be continuous at $z = z'$, while its derivative must be discontinuous to reproduce the delta function. This gives

$$\begin{aligned} A^<(z') e^{z'k} &= B^>(z') e^{-z'k}, \\ kA^<(z') e^{z'k} - kB^>(z') e^{-z'k} &= -2. \end{aligned} \tag{C.8}$$

Solving these conditions yields the Green's function in k space,

$$G_k = k^{-1} e^{-k|z-z'|}. \tag{C.9}$$

For an inhomogeneous background, the steps are analogous (see Section VI.2), but the equation for G_k has explicit coordinate dependence and must be solved numerically in each domain.

Combining the results above, we obtain

$$G(\vec{x},\vec{y}) = \int dk \sum_m e^{im(\phi-\phi')} J_m(k\rho) J_m(k\rho') e^{-k|z-z'|} = \frac{1}{4\pi\,|\vec{x}-\vec{y}|}\,, \tag{C.10}$$

where the last equality uses the identities

$$\sum_m e^{im(\phi-\phi')} J_m(k\rho) J_m(k\rho') = \frac{1}{4\pi} J_0(wk), \tag{C.11}$$

where $w^2 = \rho^2 + \rho'^2 - 2\rho\rho'\cos(\phi-\phi')$ is the relative transverse distance, together with

$$\int_0^\infty dk J_0(wk) e^{-k|z-z'|} = \frac{1}{|\vec{x}-\vec{y}|}. \tag{C.12}$$

So far we have treated a massless theory. The same steps apply to a massive theory:

$$\left[\vec{\nabla}_x^2 - m^2\right] G(\vec{x},\vec{y}) = -\delta^{(3)}(\vec{x}-\vec{y}). \tag{C.13}$$

Following the same procedure, we find

$$G(\vec{x},\vec{y}) = \frac{1}{4\pi}\int dk \frac{k}{\sqrt{k^2+m^2}} J_0(wk) e^{-\sqrt{k^2+m^2}|z-z'|} = \frac{e^{-rm}}{4\pi r}, \tag{C.14}$$

where $r = |\vec{x}-\vec{y}|$.

Importantly, the propagator diverges when $\vec{x} \to \vec{y}$, equivalently $r \to 0$. Physically, this is the same UV divergence that appears in loop calculations (see, e.g., Chapter IV). To treat it, it is convenient to use dimensional regularization in $d = 3 - 2\epsilon$, where the propagator takes the form

$$G(\vec{x},\vec{y}) \underset{\text{dimReg}}{=} \frac{\left(\frac{\exp(\gamma_E)\mu^2}{4\pi}\right)^\epsilon \left(\frac{m}{r}\right)^{\frac{1}{2}-\epsilon} K_{\frac{1}{2}-\epsilon}(mr)}{(2\pi)^{\frac{3}{2}-\epsilon}}. \tag{C.15}$$

Expanding for small r gives

$$G(\vec{x},\vec{x}) \underset{\text{dimReg}}{=} \frac{e^{\gamma\epsilon} m^{1-2\epsilon}\mu^{2\epsilon}\Gamma\left(\epsilon-\frac{1}{2}\right)}{8\pi^{3/2}} \underset{\epsilon\to 0}{=} -\frac{m}{4\pi} + \mathcal{O}(\epsilon)\,. \tag{C.16}$$

Finally, it is instructive to see how this divergence appears in cylindrical coordinates.

In $d = 3 - 2\epsilon$ dimensions, Eq. (C.14) becomes

$$G(\vec{x},\vec{y}) \underset{\text{dimReg}}{=} \int dk \frac{J_{-\epsilon}(kw)\left(2^{\epsilon-2}\pi^{\epsilon-1}w^{3/2}\left(\frac{w}{k}\right)^{-\frac{3}{2}+\epsilon}e^{|z-z'|\left(-\sqrt{k^2+m^2}\right)}\right)}{\sqrt{k\left(k^2+m^2\right)}}, \tag{C.17}$$

which in the limit $w \to 0$ and $z \to z'$ gives

$$G(\vec{x},\vec{x}) \underset{\text{dimReg}}{=} \int dk \frac{2^{2\epsilon-2}\pi^{\epsilon-1}k^{1-2\epsilon}}{\Gamma(1-\epsilon)\sqrt{k^2+m^2}} \underset{\epsilon\to 0}{=} \int dk \frac{k}{4\pi\sqrt{k^2+m^2}}. \tag{C.18}$$

As expected, the divergence appears in the large-k limit, corresponding to short-distance behavior. In fact, the integral above is the one-loop bubble integral in momentum space after the angular integrations are performed. Given this large-k behavior, in inhomogeneous backgrounds (discussed in Section VI.2) one can isolate the divergence by introducing a cutoff k_{max}: evaluate the integral numerically for $k \leq k_{\text{max}}$, treat $k \geq k_{\text{max}}$ analytically, and handle the divergence in dimensional regularization.

BIBLIOGRAPHY

[1] Andrii Dashko and Andreas Ekstedt. "Bubble-wall speed with loop corrections". In: *JHEP* 03 (2025), p. 024. DOI: 10.1007/JHEP03(2025)024. arXiv: 2411.05075 [hep-ph].

[2] Mikael Chala, Andrii Dashko, and Guilherme Guedes. "Running couplings in high-temperature effective field theory". In: *Phys. Rev. D* 113.5 (2026), p. 055026. DOI: 10.1103/ptqg-5g38. arXiv: 2510.26878 [hep-ph].

[3] Thomas Biekötter, Andrii Dashko, Maximilian Löschner, and Georg Weiglein. "Perturbative aspects of the electroweak phase transition with a complex singlet and implications for gravitational wave predictions". In: (Nov. 2025). arXiv: 2511.14831 [hep-ph].

[4] Andrii Dashko and Maximilian Löschner. *Work in Progress.*

[5] Andrei Dmitrievich Sakharov. "Violation of CP Invariance, C asymmetry, and baryon asymmetry of the universe". In: *Pisma Zh. Eksp. Teor. Fiz.* 5 (1967), pp. 32–35. DOI: 10.1070/PU1991v034n05ABEH002497.

[6] V. A. Kuzmin, V. A. Rubakov, and M. E. Shaposhnikov. "On the Anomalous Electroweak Baryon Number Nonconservation in the Early Universe". In: *Phys. Lett. B* 155 (1985), p. 36. DOI: 10.1016/0370-2693(85)91028-7.

[7] Andrew G. Cohen, D. B. Kaplan, and A. E. Nelson. "Progress in electroweak baryogenesis". In: *Ann. Rev. Nucl. Part. Sci.* 43 (1993), pp. 27–70. DOI: 10.1146/annurev.ns.43.120193.000331. arXiv: hep-ph/9302210.

[8] Jorinde van de Vis, Jordy de Vries, and Marieke Postma. "Bubble Trouble: a Review on Electroweak Baryogenesis". In: (Aug. 2025). arXiv: 2508.09989 [hep-ph].

[9] B. P. Abbott et al. "Observation of Gravitational Waves from a Binary Black Hole Merger". In: *Phys. Rev. Lett.* 116.6 (2016), p. 061102. DOI: 10.1103/PhysRevLett.116.061102. arXiv: 1602.03837 [gr-qc].

[10] Gabriella Agazie et al. "The NANOGrav 15 yr Data Set: Evidence for a Gravitational-wave Background". In: *Astrophys. J. Lett.* 951.1 (2023), p. L8. DOI: 10.3847/2041-8213/acdac6. arXiv: 2306.16213 [astro-ph.HE].

[11] Christophe Grojean, Geraldine Servant, and James D. Wells. "First-order electroweak phase transition in the standard model with a low cutoff". In: *Phys. Rev. D* 71 (2005), p. 036001. DOI: 10.1103/PhysRevD.71.036001. arXiv: hep-ph/0407019.

[12] Djuna Croon, Verónica Sanz, and Graham White. "Model Discrimination in Gravitational Wave spectra from Dark Phase Transitions". In: *JHEP* 08 (2018), p. 203. DOI: 10.1007/JHEP08(2018)203. arXiv: 1806.02332 [hep-ph].

[13] Thomas Biekötter et al. "The trap in the early Universe: impact on the interplay between gravitational waves and LHC physics in the 2HDM". In: *JCAP* 03 (2023), p. 031. DOI: 10.1088/1475-7516/2023/03/031. arXiv: 2208.14466 [hep-ph].

[14] S. L. Glashow. "Partial Symmetries of Weak Interactions". In: *Nucl. Phys.* 22 (1961), pp. 579–588. DOI: 10.1016/0029-5582(61)90469-2.

[15] F. Englert and R. Brout. "Broken Symmetry and the Mass of Gauge Vector Mesons". In: *Phys. Rev. Lett.* 13 (1964). Ed. by J. C. Taylor, pp. 321–323. DOI: 10.1103/PhysRevLett.13.321.

[16] Peter W. Higgs. "Broken Symmetries and the Masses of Gauge Bosons". In: *Phys. Rev. Lett.* 13 (1964). Ed. by J. C. Taylor, pp. 508–509. DOI: 10.1103/PhysRevLett.13.508.

[17] Steven Weinberg. "A Model of Leptons". In: *Phys. Rev. Lett.* 19 (1967), pp. 1264–1266. DOI: 10.1103/PhysRevLett.19.1264.

[18] H. Fritzsch, Murray Gell-Mann, and H. Leutwyler. "Advantages of the Color Octet Gluon Picture". In: *Phys. Lett. B* 47 (1973), pp. 365–368. DOI: 10.1016/0370-2693(73)90625-4.

[19] David J. Gross and Frank Wilczek. "Ultraviolet Behavior of Nonabelian Gauge Theories". In: *Phys. Rev. Lett.* 30 (1973). Ed. by J. C. Taylor, pp. 1343–1346. DOI: 10.1103/PhysRevLett.30.1343.

[20] Takeo Matsubara. "A New approach to quantum statistical mechanics". In: *Prog. Theor. Phys.* 14 (1955), pp. 351–378. DOI: 10.1143/PTP.14.351.

[21] L. Dolan and R. Jackiw. "Symmetry Behavior at Finite Temperature". In: *Phys. Rev. D* 9 (1974), pp. 3320–3341. DOI: 10.1103/PhysRevD.9.3320.

[22] Steven Weinberg. "Gauge and Global Symmetries at High Temperature". In: *Phys. Rev. D* 9 (1974), pp. 3357–3378. DOI: 10.1103/PhysRevD.9.3357.

[23] Andrei D. Linde. "Infrared Problem in Thermodynamics of the Yang-Mills Gas". In: *Phys. Lett. B* 96 (1980), pp. 289–292. DOI: 10.1016/0370-2693(80)90769-8.

[24] K. Kajantie, M. Laine, K. Rummukainen, and Mikhail E. Shaposhnikov. "Is there a hot electroweak phase transition at $m_H \gtrsim m_W$?" In: *Phys. Rev. Lett.* 77 (1996), pp. 2887–2890. DOI: 10.1103/PhysRevLett.77.2887. arXiv: hep-ph/9605288.

[25] F. Csikor, Z. Fodor, and J. Heitger. "Endpoint of the hot electroweak phase transition". In: *Phys. Rev. Lett.* 82 (1999), pp. 21–24. DOI: 10.1103/PhysRevLett.82.21. arXiv: hep-ph/9809291.

[26] Georges Aad et al. "Observation of a new particle in the search for the Standard Model Higgs boson with the ATLAS detector at the LHC". In: *Phys. Lett. B* 716 (2012), pp. 1–29. DOI: 10.1016/j.physletb.2012.08.020. arXiv: 1207.7214 [hep-ex].

[27] Serguei Chatrchyan et al. "Observation of a New Boson at a Mass of 125 GeV with the CMS Experiment at the LHC". In: *Phys. Lett. B* 716 (2012), pp. 30–61. DOI: 10.1016/j.physletb.2012.08.021. arXiv: 1207.7235 [hep-ex].

[28] Arthur Kosowsky, Michael S. Turner, and Richard Watkins. "Gravitational Radiation from Colliding Vacuum Bubbles". In: *Phys. Rev. D* 45 (1992), pp. 4514–4535. DOI: 10.1103/PhysRevD.45.4514.

[29] Marc Kamionkowski, Arthur Kosowsky, and Michael S. Turner. "Gravitational radiation from first order phase transitions". In: *Phys. Rev. D* 49 (1994), pp. 2837–2851. DOI: 10.1103/PhysRevD.49.2837. arXiv: astro-ph/9310044.

[30] Chiara Caprini et al. "Detecting gravitational waves from cosmological phase transitions with LISA: an update". In: *JCAP* 03 (2020), p. 024. DOI: 10.1088/1475-7516/2020/03/024. arXiv: 1910.13125 [astro-ph.CO].

[31] Chiara Caprini et al. "Gravitational waves from first-order phase transitions in LISA: reconstruction pipeline and physics interpretation". In: *JCAP* 10 (2024), p. 020. DOI: 10.1088/1475-7516/2024/10/020. arXiv: 2403.03723 [astro-ph.CO].

[32] Djuna Croon et al. "Theoretical uncertainties for cosmological first-order phase transitions". In: *JHEP* 04 (2021), p. 055. DOI: 10.1007/JHEP04(2021)055. arXiv: 2009.10080 [hep-ph].

[33] David J. Weir. "Gravitational waves from a first order electroweak phase transition: a brief review". In: *Phil. Trans. Roy. Soc. Lond. A* 376.2114 (2018). [Erratum: Phil.Trans.Roy.Soc.Lond.A 381, 20230212 (2023)], p. 20170126. DOI: 10.1098/rsta.2017.0126. arXiv: 1705.01783 [hep-ph].

[34] Peter Athron et al. "Cosmological phase transitions: From perturbative particle physics to gravitational waves". In: *Prog. Part. Nucl. Phys.* 135 (2024), p. 104094. DOI: 10.1016/j.ppnp.2023.104094. arXiv: 2305.02357 [hep-ph].

[35] Mikael Chala, Juan Carlos Criado, Luis Gil, and Javier López Miras. "Higher-order-operator corrections to phase-transition parameters in dimensional reduction". In: *JHEP* 10 (2024), p. 025. DOI: 10.1007/JHEP10(2024)025. arXiv: 2406.02667 [hep-ph].

[36] Mikael Chala and Guilherme Guedes. "The high-temperature limit of the SM(EFT)". In: *JHEP* 07 (2025), p. 085. DOI: 10.1007/JHEP07(2025)085. arXiv: 2503.20016 [hep-ph].

[37] Mikael Chala, Maria Cristina Fiore, and Luis Gil. "Hot news on the phase-structure of the SMEFT". In: (2025). arXiv: 2507.16905 [hep-ph].

[38] Fabio Bernardo, Philipp Klose, Philipp Schicho, and Tuomas V. I. Tenkanen. "Higher-dimensional operators at finite temperature affect gravitational-wave predictions". In: *JHEP* 08 (2025), p. 109. DOI: 10.1007/JHEP08(2025)109. arXiv: 2503.18904 [hep-ph].

[39] Pedro Bittar, Subhojit Roy, and Carlos E. M. Wagner. "Self Consistent Thermal Resummation: A Case Study of the Phase Transition in 2HDM". In: (Apr. 2025). arXiv: 2504.02024 [hep-ph].

[40] Henning Bahl, Marcela Carena, Aurora Ireland, and Carlos E. M. Wagner. "Improved thermal resummation for multi-field potentials". In: *JHEP* 09 (2024), p. 153. DOI: 10.1007/JHEP09(2024)153. arXiv: 2404.12439 [hep-ph].

[41] Andreas Ekstedt and Johan Löfgren. "A Critical Look at the Electroweak Phase Transition". In: *JHEP* 12 (2020), p. 136. DOI: 10.1007/JHEP12(2020)136. arXiv: 2006.12614 [hep-ph].

[42] Marek Lewicki et al. "Impact of theoretical uncertainties on model parameter reconstruction from GW signals sourced by cosmological phase transitions". In: *Phys. Rev. D* 110.2 (2024), p. 023538. DOI: 10.1103/PhysRevD.110.023538. arXiv: 2403.03769 [hep-ph].

[43] Oliver Gould and Paul M. Saffin. "Perturbative gravitational wave predictions for the real-scalar extended Standard Model". In: *JHEP* 03 (2025), p. 105. DOI: 10.1007/JHEP03(2025)105. arXiv: 2411.08951 [hep-ph].

[44] Peter Athron et al. "How arbitrary are perturbative calculations of the electroweak phase transition?" In: *JHEP* 01 (2023), p. 050. DOI: 10.1007/JHEP01(2023)050. arXiv: 2208.01319 [hep-ph].

[45] Peter Brockway Arnold and Olivier Espinosa. "The Effective potential and first order phase transitions: Beyond leading-order". In: *Phys. Rev. D* 47 (1993). [Erratum: Phys.Rev.D 50, 6662 (1994)], p. 3546. DOI: 10.1103/PhysRevD.47.3546. arXiv: hep-ph/9212235.

[46] Oliver Gould and Tuomas V. I. Tenkanen. "On the perturbative expansion at high temperature and implications for cosmological phase transitions". In: *JHEP* 06 (2021), p. 069. DOI: 10.1007/JHEP06(2021)069. arXiv: 2104.04399 [hep-ph].

[47] Thomas Appelquist and Robert D. Pisarski. "High-Temperature Yang-Mills Theories and Three-Dimensional Quantum Chromodynamics". In: *Phys. Rev. D* 23 (1981), p. 2305. DOI: 10.1103/PhysRevD.23.2305.

[48] Leo Karkkainen, P. Lacock, B. Petersson, and T. Reisz. "Dimensional reduction and color screening in QCD". In: *Nucl. Phys. B* 395 (1993), pp. 733–746. DOI: 10.1016/0550-3213(93)90055-T.

[49] K. Farakos, K. Kajantie, K. Rummukainen, and Mikhail E. Shaposhnikov. "3-D physics and the electroweak phase transition: Perturbation theory". In: *Nucl. Phys. B* 425 (1994), pp. 67–109. DOI: 10.1016/0550-3213(94)90173-2. arXiv: hep-ph/9404201.

[50] K. Kajantie, M. Laine, K. Rummukainen, and Mikhail E. Shaposhnikov. "Generic rules for high temperature dimensional reduction and their application to the standard model". In: *Nucl. Phys. B* 458 (1996), pp. 90–136. DOI: 10.1016/0550-3213(95)00549-8. arXiv: hep-ph/9508379.

[51] Michela D'Onofrio and Kari Rummukainen. "Standard model cross-over on the lattice". In: *Phys. Rev. D* 93.2 (2016), p. 025003. DOI: 10.1103/PhysRevD.93.025003. arXiv: 1508.07161 [hep-ph].

[52] Guy D. Moore and Tomislav Prokopec. "Bubble wall velocity in a first order electroweak phase transition". In: *Phys. Rev. Lett.* 75 (1995), pp. 777–780. DOI: 10.1103/PhysRevLett.75.777. arXiv: hep-ph/9503296.

[53] Stefania De Curtis et al. "Bubble wall dynamics at the electroweak phase transition". In: *JHEP* 03 (2022), p. 163. DOI: 10.1007/JHEP03(2022)163. arXiv: 2201.08220 [hep-ph].

[54] Wen-Yuan Ai, Benoit Laurent, and Jorinde van de Vis. "Model-independent bubble wall velocities in local thermal equilibrium". In: *JCAP* 07 (2023), p. 002. DOI: 10.1088/1475-7516/2023/07/002. arXiv: 2303.10171 [astro-ph.CO].

[55] Benoit Laurent and James M. Cline. "First principles determination of bubble wall velocity". In: *Phys. Rev. D* 106.2 (2022), p. 023501. DOI: 10.1103/PhysRevD.106.023501. arXiv: 2204.13120 [hep-ph].

[56] Dietrich Bodeker and Guy D. Moore. "Can electroweak bubble walls run away?" In: *JCAP* 05 (2009), p. 009. DOI: 10.1088/1475-7516/2009/05/009. arXiv: 0903.4099 [hep-ph].

[57] David Tong. *Lectures on the Standard Model*. http://www.damtp.cam.ac.uk/user/tong/standardmodel.html. 2022.

[58] David Tong. *Lectures on Cosmology*. http://www.damtp.cam.ac.uk/user/tong/cosmo.html. 2019.

[59] Mark Thomson. *Modern Particle Physics*. New York: Cambridge University Press, 2013. ISBN: 978-1107034266.

[60] Scott Dodelson. *Modern Cosmology*. Amsterdam: Academic Press, 2003. ISBN: 978-0122191411.

[61] Daniel Baumann. *Cosmology*. Cambridge University Press, 2022. ISBN: 978-1108838078.

[62] D. Hanneke, S. Fogwell, and G. Gabrielse. "New Measurement of the Electron Magnetic Moment and the Fine Structure Constant". In: *Phys. Rev. Lett.* 100 (2008), p. 120801. DOI: 10.1103/PhysRevLett.100.120801. arXiv: 0801.1134 [physics.atom-ph].

[63] M. Breidenbach et al. "Observed Behavior of Highly Inelastic Electron-Proton Scattering". In: *Phys. Rev. Lett.* 23 (1969), pp. 935–939. DOI: 10.1103/PhysRevLett.23.935.

[64] R. Brandelik et al. "Evidence for Planar Events in e^+e^- Annihilation at High Energies". In: *Phys. Lett. B* 86 (1979), pp. 243–249. DOI: 10.1016/0370-2693(79)90542-X.

[65] T. D. Lee and Chen-Ning Yang. "Question of Parity Conservation in Weak Interactions". In: *Phys. Rev.* 104 (1956), pp. 254–258. DOI: 10.1103/PhysRev.104.254.

[66] C. S. Wu et al. "Experimental Test of Parity Nonconservation in Beta Decay". In: *Phys. Rev.* 105 (1957), pp. 1413–1415. DOI: 10.1103/PhysRev.105.1413.

[67] S. Schael et al. "Precision electroweak measurements on the Z resonance". In: *Phys. Rept.* 427 (2006), pp. 257–454. DOI: 10.1016/j.physrep.2005.12.006. arXiv: hep-ex/0509008.

[68] Chen-Ning Yang and Robert L. Mills. "Conservation of Isotopic Spin and Isotopic Gauge Invariance". In: *Phys. Rev.* 96 (1954). Ed. by Jong-Ping Hsu and D. Fine, pp. 191–195. DOI: 10.1103/PhysRev.96.191.

[69] David J. Gross and R. Jackiw. "Effect of Anomalies on Quasi-Renormalizable Theories". In: *Phys. Rev. D* 6 (1972), pp. 477–493. DOI: 10.1103/PhysRevD.6.477.

[70] Edward Witten. "An SU(2) Anomaly". In: *Phys. Lett. B* 117 (1982), pp. 324–328. DOI: 10.1016/0370-2693(82)90728-6.

[71] M. Gell-Mann. "The interpretation of the new particles as displaced charge multiplets". In: *Nuovo Cim.* 4.S2 (1956), pp. 848–866. DOI: 10.1007/BF02748000.

[72] Kazuhiko Nishijima. "Charge Independence Theory of V Particles". In: *Prog. Theor. Phys.* 13.3 (1955), pp. 285–304. DOI: 10.1143/PTP.13.285.

[73] H. David Politzer. "Reliable Perturbative Results for Strong Interactions?" In: *Phys. Rev. Lett.* 30 (1973), pp. 1346–1349. DOI: 10.1103/PhysRevLett.30.1346.

[74] R. L. Workman et al. "Review of Particle Physics". In: *PTEP* 2022 (2022), p. 083C01. DOI: 10.1093/ptep/ptac097.

[75] C. Abel et al. "Measurement of the Permanent Electric Dipole Moment of the Neutron". In: *Phys. Rev. Lett.* 124 (2020), p. 081803. DOI: 10.1103/PhysRevLett.124.081803. arXiv: 2003.03389 [hep-ex].

[76] Jihn E. Kim and Gianpaolo Carosi. "Axions and the strong CP problem". In: *Rev. Mod. Phys.* 82 (2010), pp. 557–602. DOI: 10.1103/RevModPhys.82.557. arXiv: 0807.3125 [hep-ph].

[77] Georges Aad et al. "Combined Measurement of the Higgs Boson Mass from the H$\to\gamma\gamma$ and H$\to$ZZ$^*\to 4\ell$ Decay Channels with the ATLAS Detector Using s=7, 8, and 13 TeV pp Collision Data". In: *Phys. Rev. Lett.* 131.25 (2023), p. 251802. DOI: 10.1103/PhysRevLett.131.251802. arXiv: 2308.04775 [hep-ex].

[78] Armen Tumasyan et al. "A portrait of the Higgs boson by the CMS experiment ten years after the discovery." In: *Nature* 607.7917 (2022). [Erratum: Nature 623, (2023)], pp. 60–68. DOI: 10.1038/s41586-022-04892-x. arXiv: 2207.00043 [hep-ex].

[79] Georges Aad et al. "A detailed map of Higgs boson interactions by the ATLAS experiment ten years after the discovery". In: *Nature* 607.7917 (2022). [Erratum: Nature 612, E24 (2022)], pp. 52–59. DOI: 10.1038/s41586-022-04893-w. arXiv: 2207.00092 [hep-ex].

[80] Georges Aad et al. "Search for non-resonant Higgs boson pair production in the $b\bar{b}b\bar{b}$ final state with the ATLAS detector". In: *JHEP* 06 (2023), p. 153. DOI: 10.1007/JHEP06(2023)153. arXiv: 2301.03212 [hep-ex].

[81] F. Abe et al. "Observation of top quark production in $\bar{p}p$ collisions". In: *Phys. Rev. Lett.* 74 (1995), pp. 2626–2631. DOI: 10.1103/PhysRevLett.74.2626. arXiv: hep-ex/9503002.

[82] S. Abachi et al. "Observation of the top quark". In: *Phys. Rev. Lett.* 74 (1995), pp. 2632–2637. DOI: 10.1103/PhysRevLett.74.2632. arXiv: hep-ex/9503003.

[83] N. Aghanim et al. "Planck 2018 results. VI. Cosmological parameters". In: *Astron. Astrophys.* 641 (2020), A6. DOI: 10.1051/0004-6361/201833910. arXiv: 1807.06209 [astro-ph.CO].

[84] Adam G. Riess et al. "A Comprehensive Measurement of the Local Value of the Hubble Constant with 1 km/s/Mpc Uncertainty from the Hubble Space Telescope and the SH0ES Team". In: *Astrophys. J. Lett.* 934 (2022), p. L7. DOI: 10.3847/2041-8213/ac5c5b. arXiv: 2112.04510 [astro-ph.CO].

[85] Licia Verde, Tommaso Treu, and Adam G. Riess. "Tensions between the Early and the Late Universe". In: *Nature Astron.* 3 (2019), p. 891. DOI: 10.1038/s41550-019-0902-0. arXiv: 1907.10625 [astro-ph.CO].

[86] S. Navas et al. "Review of particle physics". In: *Phys. Rev. D* 110.3 (2024), p. 030001. DOI: 10.1103/PhysRevD.110.030001.

[87] Gianfranco Bertone, Dan Hooper, and Joseph Silk. "Particle dark matter: Evidence, candidates and constraints". In: *Phys. Rept.* 405 (2005), pp. 279–390. DOI: 10.1016/j.physrep.2004.08.031. arXiv: hep-ph/0404175.

[88] F. Zwicky. "Die Rotverschiebung von extragalaktischen Nebeln". In: *Helv. Phys. Acta* 6 (1933), pp. 110–127.

[89] S. Perlmutter et al. “Measurements of Ω and Λ from 42 high redshift supernovae”. In: *Astrophys. J.* 517 (1999), pp. 565–586. DOI: 10.1086/307221. arXiv: astro-ph/9812133.

[90] Adam G. Riess et al. “Observational evidence from supernovae for an accelerating universe and a cosmological constant”. In: *Astron. J.* 116 (1998), pp. 1009–1038. DOI: 10.1086/300499. arXiv: astro-ph/9805200.

[91] Alan H. Guth. “The Inflationary Universe: A Possible Solution to the Horizon and Flatness Problems”. In: *Phys. Rev. D* 23 (1981), pp. 347–356. DOI: 10.1103/PhysRevD.23.347.

[92] Andrei D. Linde. “A New Inflationary Universe Scenario: A Possible Solution of the Horizon, Flatness, Homogeneity, Isotropy and Primordial Monopole Problems”. In: *Phys. Lett. B* 108 (1982), pp. 389–393. DOI: 10.1016/0370-2693(82)91219-9.

[93] Daniel Baumann. “Inflation”. In: *Theoretical Advanced Study Institute in Elementary Particle Physics: Physics of the Large and the Small*. 2011, pp. 523–686. DOI: 10.1142/9789814327183_0010. arXiv: 0907.5424 [hep-th].

[94] M. Laine. “Electroweak phase transition beyond the standard model”. In: *4th International Conference on Strong and Electroweak Matter*. June 2000, pp. 58–69. DOI: 10.1142/9789812799913_0005. arXiv: hep-ph/0010275.

[95] David N. Schramm and Michael S. Turner. “Big bang nucleosynthesis enters the precision era”. In: *Rev. Mod. Phys.* 70 (1998), pp. 303–318. DOI: 10.1103/RevModPhys.70.303. arXiv: astro-ph/9706069.

[96] Richard H. Cyburt, Brian D. Fields, Keith A. Olive, and Tsung-Han Yeh. “Big Bang Nucleosynthesis: 2015”. In: *Rev. Mod. Phys.* 88 (2016), p. 015004. DOI: 10.1103/RevModPhys.88.015004. arXiv: 1505.01076 [astro-ph.CO].

[97] J. Antoniadis et al. “The second data release from the European Pulsar Timing Array: III. Search for gravitational wave signals”. In: *Astron. Astrophys.* 678 (2023), A50. DOI: 10.1051/0004-6361/202347432. arXiv: 2306.16214 [astro-ph.HE].

[98] Daniel J. Reardon et al. “Search for an Isotropic Gravitational-wave Background with the Parkes Pulsar Timing Array”. In: *Astrophys. J. Lett.* 951 (2023), p. L6. DOI: 10.3847/2041-8213/acdd02. arXiv: 2306.16215 [astro-ph.HE].

[99] T. W. B. Kibble. “Topology of Cosmic Domains and Strings”. In: *J. Phys. A* 9 (1976), pp. 1387–1398. DOI: 10.1088/0305-4470/9/8/029.

[100] Chiara Caprini et al. "Science with the space-based interferometer eLISA. II: Gravitational waves from cosmological phase transitions". In: *JCAP* 04 (2016), p. 001. DOI: 10.1088/1475-7516/2016/04/001. arXiv: 1512.06239 [astro-ph.CO].

[101] Pierre Auclair et al. "Cosmology with the Laser Interferometer Space Antenna". In: *Living Rev. Rel.* 26.1 (2023), p. 5. DOI: 10.1007/s41114-023-00045-2. arXiv: 2204.05434 [astro-ph.CO].

[102] Leszek Roszkowski, Enrico Maria Sessolo, and Sebastian Trojanowski. "WIMP dark matter candidates and searches—current status and future prospects". In: *Rept. Prog. Phys.* 81.6 (2018), p. 066201. DOI: 10.1088/1361-6633/aab913. arXiv: 1707.06277 [hep-ph].

[103] Joerg Jaeckel and Andreas Ringwald. "The Low-Energy Frontier of Particle Physics". In: *Ann. Rev. Nucl. Part. Sci.* 60 (2010), pp. 405–437. DOI: 10.1146/annurev.nucl.012809.104433. arXiv: 1002.0329 [hep-ph].

[104] A. Boyarsky et al. "Sterile neutrino Dark Matter". In: *Prog. Part. Nucl. Phys.* 104 (2019), pp. 1–45. DOI: 10.1016/j.ppnp.2018.07.004. arXiv: 1807.07938 [hep-ph].

[105] Bernard Carr, Kazunori Kohri, Yuuiti Sendouda, and Jun'ichi Yokoyama. "Constraints on primordial black holes". In: *Rept. Prog. Phys.* 84.11 (2021), p. 116902. DOI: 10.1088/1361-6633/ac1e31. arXiv: 2002.12778 [astro-ph.CO].

[106] Jonathan L. Feng. "Dark Matter Candidates from Particle Physics and Methods of Detection". In: *Ann. Rev. Astron. Astrophys.* 48 (2010), pp. 495–545. DOI: 10.1146/annurev-astro-082708-101659. arXiv: 1003.0904 [astro-ph.CO].

[107] Joan Elias-Miro et al. "Higgs mass implications on the stability of the electroweak vacuum". In: *Phys. Lett. B* 709 (2012), pp. 222–228. DOI: 10.1016/j.physletb.2012.01.010. arXiv: 1112.3022 [hep-ph].

[108] Giuseppe Degrassi et al. "Higgs mass and vacuum stability in the Standard Model at NNLO". In: *JHEP* 08 (2012), p. 098. DOI: 10.1007/JHEP08(2012)098. arXiv: 1205.6497 [hep-ph].

[109] Dario Buttazzo et al. "Investigating the near-criticality of the Higgs boson". In: *JHEP* 12 (2013), p. 089. DOI: 10.1007/JHEP12(2013)089. arXiv: 1307.3536 [hep-ph].

[110] F. R. Klinkhamer and N. S. Manton. "A Saddle Point Solution in the Weinberg-Salam Theory". In: *Phys. Rev. D* 30 (1984), p. 2212. DOI: 10.1103/PhysRevD.30.2212.

[111] Peter B. Arnold and Larry D. McLerran. "Sphalerons, Small Fluctuations and Baryon Number Violation in Electroweak Theory". In: *Phys. Rev. D* 36 (1987), p. 581. DOI: 10.1103/PhysRevD.36.581.

[112] Stefano Profumo, Michael J. Ramsey-Musolf, and Gabe Shaughnessy. "Singlet Higgs phenomenology and the electroweak phase transition". In: *JHEP* 08 (2007), p. 010. DOI: 10.1088/1126-6708/2007/08/010. arXiv: 0705.2425 [hep-ph].

[113] David Curtin, Patrick Meade, and Chiu-Tien Yu. "Testing Electroweak Baryogenesis with Future Colliders". In: *JHEP* 11 (2014), p. 127. DOI: 10.1007/JHEP11(2014)127. arXiv: 1409.0005 [hep-ph].

[114] Philipp Schicho, Tuomas V. I. Tenkanen, and Graham White. "Combining thermal resummation and gauge invariance for electroweak phase transition". In: *JHEP* 11 (2022), p. 047. DOI: 10.1007/JHEP11(2022)047. arXiv: 2203.04284 [hep-ph].

[115] G. C. Dorsch, S. J. Huber, and J. M. No. "A strong electroweak phase transition in the 2HDM after LHC8". In: *JHEP* 10 (2013), p. 029. DOI: 10.1007/JHEP10(2013)029. arXiv: 1305.6610 [hep-ph].

[116] L. Fabian, S. J. Huber, K. Kim, and T. Sekiguchi. "Electroweak phase transition and gravitational wave phenomenology with extensions of the Higgs sector". In: *Phys. Rev. D* 104 (2021), p. 035023. DOI: 10.1103/PhysRevD.104.035023. arXiv: 2012.09181 [hep-ph].

[117] Thomas Biekötter and Mathias Pierre. "Higgs-boson visible and invisible constraints on hidden sectors". In: *Eur. Phys. J. C* 82.11 (2022), p. 1026. DOI: 10.1140/epjc/s10052-022-10990-x. arXiv: 2208.05505 [hep-ph].

[118] Anke Biekötter, Benjamin D. Pecjak, Darren J. Scott, and Tommy Smith. "Electroweak input schemes and universal corrections in SMEFT". In: *JHEP* 07 (2023), p. 115. DOI: 10.1007/JHEP07(2023)115. arXiv: 2305.03763 [hep-ph].

[119] Sven Heinemeyer, Margarete Mühlleitner, Kateryna Radchenko, and Georg Weiglein. "Higgs pair production in the 2HDM: impact of loop corrections to the trilinear Higgs couplings and interference effects on experimental limits". In: *Eur. Phys. J. C* 85 (2025), p. 437. DOI: 10.1140/epjc/s10052-025-14124-x. arXiv: 2403.14776 [hep-ph].

[120] Hiren H. Patel and Michael J. Ramsey-Musolf. "Stepping Into Electroweak Symmetry Breaking: Phase Transitions and Higgs Phenomenology". In: *Phys. Rev. D* 88 (2013), p. 035013. DOI: 10.1103/PhysRevD.88.035013. arXiv: 1212.5652 [hep-ph].

[121] Lauri Niemi, Michael J. Ramsey-Musolf, Tuomas V. I. Tenkanen, and David J. Weir. "Thermodynamics of a Two-Step Electroweak Phase Transition". In: *Phys. Rev. Lett.* 126.17 (2021), p. 171802. DOI: 10.1103/PhysRevLett.126.171802. arXiv: 2005.11332 [hep-ph].

[122] Satoshi Iso, Nobuchika Okada, and Yuta Orikasa. "The minimal B-L model naturally realized at TeV scale". In: *Phys. Rev. D* 80 (2009), p. 115007. DOI: 10.1103/PhysRevD.80.115007. arXiv: 0909.0128 [hep-ph].

[123] Alexandros Karam and Kyriakos Tamvakis. "Dark matter and neutrino masses from a classically scale-invariant multi-Higgs portal". In: *Phys. Rev. D* 92 (2015), p. 075010. DOI: 10.1103/PhysRevD.92.075010. arXiv: 1511.07597 [hep-ph].

[124] Ryusuke Jinno and Masahiro Takimoto. "Probing a classically conformal B-L model with gravitational waves". In: *Phys. Rev. D* 95 (2017), p. 015020. DOI: 10.1103/PhysRevD.95.015020. arXiv: 1604.05588 [hep-ph].

[125] Thomas Appelquist and Claude W. Bernard. "Strongly Interacting Higgs Bosons". In: *Phys. Rev. D* 22 (1980), p. 200. DOI: 10.1103/PhysRevD.22.200.

[126] F. Feruglio. "The Chiral approach to the electroweak interactions". In: *Int. J. Mod. Phys. A* 8 (1993), pp. 4937–4972. DOI: 10.1142/S0217751X93001946. arXiv: hep-ph/9301281.

[127] P. H. Damgaard, A. Haarr, D. O'Connell, and A. Tranberg. "Electroweak Baryogenesis and Standard Model Violation". In: *JHEP* 02 (2016), p. 107. DOI: 10.1007/JHEP02(2016)107. arXiv: 1512.01963 [hep-ph].

[128] B. Grzadkowski, M. Iskrzynski, M. Misiak, and J. Rosiek. "Dimension-Six Terms in the Standard Model Lagrangian". In: *JHEP* 10 (2010), p. 085. DOI: 10.1007/JHEP10(2010)085. arXiv: 1008.4884 [hep-ph].

[129] Thomas Biekötter et al. "First shot of the smoking gun: probing the electroweak phase transition in the 2HDM with novel searches for A $\longrightarrow$ ZH in $\ell^+\ell^- t\bar{t}$ and $\nu\nu b\bar{b}$ final states". In: *JHEP* 01 (2024), p. 107. DOI: 10.1007/JHEP01(2024)107. arXiv: 2309.17431 [hep-ph].

[130] Michael J. Ramsey-Musolf, Tuomas V. I. Tenkanen, and Van Que Tran. "Refining Gravitational Wave and Collider Physics Dialogue via Singlet Scalar Extension". In: (Sept. 2024). arXiv: 2409.17554 [hep-ph].

[131] Thomas Biekötter and María Olalla Olea-Romacho. "Benchmarking a fading window: electroweak baryogenesis in the C2HDM, LHC constraints after Run 2 and prospects for LISA". In: *JHEP* 12 (2025), p. 040. DOI: 10.1007/JHEP12(2025)040. arXiv: 2505.09670 [hep-ph].

[132] Michel Le Bellac. *Thermal Field Theory*. Cambridge Monographs on Mathematical Physics. Cambridge University Press, Mar. 2011. ISBN: 978-0-511-88506-8, 978-0-521-65477-7. DOI: 10.1017/CBO9780511721700.

[133] Mikko Laine and Aleksi Vuorinen. *Basics of Thermal Field Theory*. Vol. 925. Springer, 2016. DOI: 10.1007/978-3-319-31933-9. arXiv: 1701.01554 [hep-ph].

[134] F. J. Dyson. "The S matrix in quantum electrodynamics". In: *Phys. Rev.* 75 (1949), pp. 1736–1755. DOI: 10.1103/PhysRev.75.1736.

[135] Sidney R. Coleman and Erick J. Weinberg. "Radiative Corrections as the Origin of Spontaneous Symmetry Breaking". In: *Phys. Rev. D* 7 (1973), pp. 1888–1910. DOI: 10.1103/PhysRevD.7.1888.

[136] R. Jackiw. "Functional evaluation of the effective potential". In: *Phys. Rev. D* 9 (1974), p. 1686. DOI: 10.1103/PhysRevD.9.1686.

[137] L. F. Abbott. "Introduction to the Background Field Method". In: *Acta Phys. Polon. B* 13 (1982), p. 33.

[138] S. Y. Lee and Alain M. Sciaccaluga. "Evaluation of Higher Order Effective Potentials with Dimensional Regularization". In: *Nucl. Phys. B* 96 (1975), pp. 435–444. DOI: 10.1016/0550-3213(75)90341-7.

[139] Marc Sher. "Electroweak Higgs Potentials and Vacuum Stability". In: *Phys. Rept.* 179 (1989), pp. 273–418. DOI: 10.1016/0370-1573(89)90061-6.

[140] Mariano Quiros. "Finite temperature field theory and phase transitions". In: *ICTP Summer School in High-Energy Physics and Cosmology*. Jan. 1999, pp. 187–259. arXiv: hep-ph/9901312.

[141] Michael Dine et al. "Towards the theory of the electroweak phase transition". In: *Phys. Rev. D* 46 (1992), pp. 550–571. DOI: 10.1103/PhysRevD.46.550. arXiv: hep-ph/9203203.

[142] Masako Bando, Taichiro Kugo, Nobuhiro Maekawa, and Hiroaki Nakano. "Improving the effective potential". In: *Phys. Lett. B* 301 (1993), pp. 83–89. DOI: 10.1016/0370-2693(93)90725-W. arXiv: hep-ph/9210228.

[143] Anders Andreassen, William Frost, and Matthew D. Schwartz. "Consistent Use of Effective Potentials". In: *Phys. Rev. D* 91.1 (2015), p. 016009. DOI: 10.1103/PhysRevD.91.016009. arXiv: 1408.0287 [hep-ph].

[144] Reijiro Fukuda and Taichiro Kugo. "Gauge Invariance in the Effective Action and Potential". In: *Phys. Rev. D* 13 (1976), p. 3469. DOI: 10.1103/PhysRevD.13.3469.

[145] N. K. Nielsen. "On the Gauge Dependence of Spontaneous Symmetry Breaking in Gauge Theories". In: *Nucl. Phys. B* 101 (1975), pp. 173–188. DOI: 10.1016/0550-3213(75)90301-6.

[146] Dimitrios Metaxas and Erick J. Weinberg. "Gauge independence of the bubble nucleation rate in theories with radiative symmetry breaking". In: *Phys. Rev. D* 53 (1996), pp. 836–843. DOI: 10.1103/PhysRevD.53.836. arXiv: hep-ph/9507381.

[147] Lisa P. Alexander and Apostolos Pilaftsis. "The One-Loop Effective Potential in Non-Linear Gauges". In: *J. Phys. G* 36 (2009), p. 045006. DOI: 10.1088/0954-3899/36/4/045006. arXiv: 0809.1580 [hep-ph].

[148] Hiren H. Patel and Michael J. Ramsey-Musolf. "Baryon Washout, Electroweak Phase Transition, and Perturbation Theory". In: *JHEP* 07 (2011), p. 029. DOI: 10.1007/JHEP07(2011)029. arXiv: 1101.4665 [hep-ph].

[149] OEIS Foundation Inc. *The On-Line Encyclopedia of Integer Sequences*. 2026. URL: https://oeis.org.

[150] Stephen P. Martin. "Taming the Goldstone contributions to the effective potential". In: *Phys. Rev. D* 90.1 (2014), p. 016013. DOI: 10.1103/PhysRevD.90.016013. arXiv: 1406.2355 [hep-ph].

[151] Stephen P. Martin and Hiren H. Patel. "Two-loop effective potential for generalized gauge fixing". In: *Phys. Rev. D* 98.7 (2018), p. 076008. DOI: 10.1103/PhysRevD.98.076008. arXiv: 1808.07615 [hep-ph].

[152] Will Loinaz and R. S. Willey. "Gauge dependence of lower bounds on the Higgs mass derived from electroweak vacuum stability constraints". In: *Phys. Rev. D* 56 (1997), pp. 7416–7426. DOI: 10.1103/PhysRevD.56.7416. arXiv: hep-ph/9702321.

[153] J. R. Espinosa, M. Garny, and T. Konstandin. "Interplay of Infrared Divergences and Gauge-Dependence of the Effective Potential". In: *Phys. Rev. D* 94.5 (2016), p. 055026. DOI: 10.1103/PhysRevD.94.055026. arXiv: 1607.08432 [hep-ph].

[154] Stephen P. Martin. "Effective potential at three loops". In: *Phys. Rev. D* 96.9 (2017), p. 096005. DOI: 10.1103/PhysRevD.96.096005. arXiv: 1709.02397 [hep-ph].

[155] Peter Brockway Arnold, Eric Braaten, and Stamatis Vokos. "Resolving the unitary gauge puzzle of thermal phase transitions". In: *Phys. Rev. D* 46 (1992), pp. 3576–3586. DOI: 10.1103/PhysRevD.46.3576.

[156] Sander Mooij and Marieke Postma. "Goldstone bosons and a dynamical Higgs field". In: *JCAP* 09 (2011), p. 006. DOI: 10.1088/1475-7516/2011/09/006. arXiv: 1104.4897 [hep-ph].

[157] Mathias Garny and Thomas Konstandin. "On the gauge dependence of vacuum transitions at finite temperature". In: *JHEP* 07 (2012), p. 189. DOI: 10.1007/JHEP07(2012)189. arXiv: 1205.3392 [hep-ph].

[158] Luca Di Luzio and Luminita Mihaila. "On the gauge dependence of the Standard Model vacuum instability scale". In: *JHEP* 06 (2014), p. 079. DOI: 10.1007/JHEP06(2014)079. arXiv: 1404.7450 [hep-ph].

[159] S. Heinemeyer, M. Mühlleitner, K. Radchenko, and G. Weiglein. "Higgs pair production in the 2HDM: impact of loop corrections to the trilinear Higgs couplings and interference effects on experimental limits". In: *Eur. Phys. J. C* 85.4 (2025), p. 437. DOI: 10.1140/epjc/s10052-025-14124-x. arXiv: 2403.14776 [hep-ph].

[160] Johannes Braathen, Sven Heinemeyer, Andrea Parra Arnay, and Alain Verduras Schaeidt. "Impact of one-loop corrections to trilinear scalar couplings on di-Higgs production in the RxSM". In: *Eur. Phys. J. C* 85.10 (2025), p. 1153. DOI: 10.1140/epjc/s10052-025-14770-1. arXiv: 2507.02569 [hep-ph].

[161] Sidney Coleman. *Aspects of Symmetry: Selected Erice Lectures*. Cambridge, U.K.: Cambridge University Press, 1985. ISBN: 978-0-521-31827-3. DOI: 10.1017/CBO9780511565045.

[162] Sidney R. Coleman. "The Fate of the False Vacuum. 1. Semiclassical Theory". In: *Phys. Rev. D* 15 (1977). [Erratum: Phys.Rev.D 16, 1248 (1977)], pp. 2929–2936. DOI: 10.1103/PhysRevD.16.1248.

[163] Curtis G. Callan Jr. and Sidney R. Coleman. "The Fate of the False Vacuum. 2. First Quantum Corrections". In: *Phys. Rev. D* 16 (1977), pp. 1762–1768. DOI: 10.1103/PhysRevD.16.1762.

[164] Andreas Ekstedt, Oliver Gould, and Joonas Hirvonen. "BubbleDet: a Python package to compute functional determinants for bubble nucleation". In: *JHEP* 12 (2023), p. 056. DOI: 10.1007/JHEP12(2023)056. arXiv: 2308.15652 [hep-ph].

[165] Sidney R. Coleman, V. Glaser, and Andre Martin. "Action Minima Among Solutions to a Class of Euclidean Scalar Field Equations". In: *Commun. Math. Phys.* 58 (1978), pp. 211–221. DOI: 10.1007/BF01609421.

[166] Andrei D. Linde. "Fate of the False Vacuum at Finite Temperature: Theory and Applications". In: *Phys. Lett. B* 100 (1981), pp. 37–40. DOI: 10.1016/0370-2693(81)90281-1.

[167] Andrei D. Linde. "Decay of the False Vacuum at Finite Temperature". In: *Nucl. Phys. B* 216 (1983). [Erratum: Nucl.Phys.B 223, 544 (1983)], p. 421. DOI: 10.1016/0550-3213(83)90072-X.

[168] Ian Affleck. "Quantum Statistical Metastability". In: *Phys. Rev. Lett.* 46 (1981), p. 388. DOI: 10.1103/PhysRevLett.46.388.

[169] J. S. Langer. "Statistical theory of the decay of metastable states". In: *Annals Phys.* 54 (1969), pp. 258–275. DOI: 10.1016/0003-4916(69)90153-5.

[170] J. S. Langer and L. A. Turski. "Hydrodynamic Model of the Condensation of a Vapor near Its Critical Point". In: *Phys. Rev. A* 8 (6 Dec. 1973), pp. 3230–3243. DOI: 10.1103/PhysRevA.8.3230. URL: https://link.aps.org/doi/10.1103/PhysRevA.8.3230.

[171] Oliver Gould and Joonas Hirvonen. "Effective field theory approach to thermal bubble nucleation". In: *Phys. Rev. D* 104.9 (2021), p. 096015. DOI: 10.1103/PhysRevD.104.096015. arXiv: 2108.04377 [hep-ph].

[172] Guy D. Moore and Kari Rummukainen. "Electroweak bubble nucleation, nonperturbatively". In: *Phys. Rev. D* 63 (2001), p. 045002. DOI: 10.1103/PhysRevD.63.045002. arXiv: hep-ph/0009132.

[173] Victor Guada, Miha Nemevšek, and Matevž Pintar. "FindBounce: Package for multi-field bounce actions". In: *Comput. Phys. Commun.* 256 (2020), p. 107480. DOI: 10.1016/j.cpc.2020.107480. arXiv: 2002.00881 [hep-ph].

[174] Carroll L. Wainwright. "CosmoTransitions: Computing Cosmological Phase Transition Temperatures and Bubble Profiles with Multiple Fields". In: *Comput. Phys. Commun.* 183 (2012), pp. 2006–2013. DOI: 10.1016/j.cpc.2012.04.004. arXiv: 1109.4189 [hep-ph].

[175] J. R. Espinosa. "A Fresh Look at the Calculation of Tunneling Actions". In: *JCAP* 07 (2018), p. 036. DOI: 10.1088/1475-7516/2018/07/036. arXiv: 1805.03680 [hep-th].

[176] J. R. Espinosa and T. Konstandin. "A Fresh Look at the Calculation of Tunneling Actions in Multi-Field Potentials". In: *JCAP* 01 (2019), p. 051. DOI: 10.1088/1475-7516/2019/01/051. arXiv: 1811.09185 [hep-th].

[177] Francesco Costa et al. "ELENA: a software for fast and precise computation of first order phase transitions and gravitational waves production in particle physics models". In: (Sept. 2025). arXiv: 2510.00289 [hep-ph].

[178] Guy D. Moore and Tomislav Prokopec. "How fast can the wall move? A Study of the electroweak phase transition dynamics". In: *Phys. Rev. D* 52 (1995), pp. 7182–7204. DOI: 10.1103/PhysRevD.52.7182. arXiv: hep-ph/9506475.

[179] Dietrich Bodeker and Guy D. Moore. "Electroweak Bubble Wall Speed Limit". In: *JCAP* 05 (2017), p. 025. DOI: 10.1088/1475-7516/2017/05/025. arXiv: 1703.08215 [hep-ph].

[180] Thomas Konstandin and Jose M. No. "Hydrodynamic obstruction to bubble expansion". In: *JCAP* 02 (2011), p. 008. DOI: 10.1088/1475-7516/2011/02/008. arXiv: 1011.3735 [hep-ph].

[181] Andreas Ekstedt et al. "How fast does the WallGo? A package for computing wall velocities in first-order phase transitions". In: *JHEP* 04 (2025), p. 101. DOI: 10.1007/JHEP04(2025)101. arXiv: 2411.04970 [hep-ph].

[182] Mark Hindmarsh, Stephan J. Huber, Kari Rummukainen, and David J. Weir. "Numerical simulations of acoustically generated gravitational waves at a first order phase transition". In: *Phys. Rev. D* 92.12 (2015), p. 123009. DOI: 10.1103/PhysRevD.92.123009. arXiv: 1504.03291 [astro-ph.CO].

[183] Daniel Cutting, Mark Hindmarsh, and David J. Weir. "Vorticity, kinetic energy, and suppressed gravitational wave production in strong first order phase transitions". In: *Phys. Rev. Lett.* 125.2 (2020), p. 021302. DOI: 10.1103/PhysRevLett.125.021302. arXiv: 1906.00480 [hep-ph].

[184] Nabeen Bhusal et al. “Slow-down of expanding bubbles in the early Universe”. In: (2026). arXiv: 2603.22397 [hep-ph].

[185] Thomas Konstandin, Germano Nardini, and Ingo Rues. “From Boltzmann equations to steady wall velocities”. In: *JCAP* 09 (2014), p. 028. DOI: 10.1088/1475-7516/2014/09/028. arXiv: 1407.3132 [hep-ph].

[186] Andreas Ekstedt, Thomas Konstandin, and Jorinde van de Vis. “Scalar damping in cosmological phase transitions”. In: (Dec. 2025). arXiv: 2512.16663 [hep-ph].

[187] Tomasz Krajewski et al. “From friction scaling to an efficient method for estimating bubble wall velocity”. In: (Mar. 2026). arXiv: 2603.24583 [astro-ph.CO].

[188] Jose R. Espinosa, Thomas Konstandin, Jose M. No, and Geraldine Servant. “Energy Budget of Cosmological First-order Phase Transitions”. In: *JCAP* 06 (2010), p. 028. DOI: 10.1088/1475-7516/2010/06/028. arXiv: 1004.4187 [hep-ph].

[189] Paul H. Ginsparg. “First Order and Second Order Phase Transitions in Gauge Theories at Finite Temperature”. In: *Nucl. Phys. B* 170 (1980), pp. 388–408. DOI: 10.1016/0550-3213(80)90418-6.

[190] Andreas Ekstedt, Philipp Schicho, and Tuomas V. I. Tenkanen. “Cosmological phase transitions at three loops: The final verdict on perturbation theory”. In: *Phys. Rev. D* 110.9 (2024), p. 096006. DOI: 10.1103/PhysRevD.110.096006. arXiv: 2405.18349 [hep-ph].

[191] Rajesh R. Parwani. “Resummation in a hot scalar field theory”. In: *Phys. Rev. D* 45 (1992). [Erratum: Phys.Rev.D 48, 5965 (1993)], p. 4695. DOI: 10.1103/PhysRevD.45.4695. arXiv: hep-ph/9204216.

[192] James M. Cline, Kimmo Kainulainen, and Michael Trott. “Electroweak Baryogenesis in Two Higgs Doublet Models and B meson anomalies”. In: *JHEP* 11 (2011), p. 089. DOI: 10.1007/JHEP11(2011)089. arXiv: 1107.3559 [hep-ph].

[193] M. Laine, M. Meyer, and G. Nardini. “Thermal phase transition with full 2-loop effective potential”. In: *Nucl. Phys. B* 920 (2017), pp. 565–600. DOI: 10.1016/j.nuclphysb.2017.04.023. arXiv: 1702.07479 [hep-ph].

[194] David Curtin, Patrick Meade, and Harikrishnan Ramani. “Thermal Resummation and Phase Transitions”. In: *Eur. Phys. J. C* 78.9 (2018), p. 787. DOI: 10.1140/epjc/s10052-018-6268-0. arXiv: 1612.00466 [hep-ph].

[195] J. S. Langer. “Metastable states”. In: *Physica* 73.1 (1974), pp. 61–72. DOI: 10.1016/0031-8914(74)90226-2.

[196] Oliver Gould. "Real scalar phase transitions: a nonperturbative analysis". In: *JHEP* 04 (2021), p. 057. DOI: 10.1007/JHEP04(2021)057. arXiv: 2101.05528 [hep-ph].

[197] Andreas Ekstedt, Philipp Schicho, and Tuomas V. I. Tenkanen. "DRalgo: A package for effective field theory approach for thermal phase transitions". In: *Comput. Phys. Commun.* 288 (2023), p. 108725. DOI: 10.1016/j.cpc.2023.108725. arXiv: 2205.08815 [hep-ph].

[198] Alan H. Guth and Erick J. Weinberg. "Cosmological Consequences of a First Order Phase Transition in the SU(5) Grand Unified Model". In: *Phys. Rev. D* 23 (1981), p. 876. DOI: 10.1103/PhysRevD.23.876.

[199] Stephan J. Huber and Thomas Konstandin. "Production of gravitational waves in the nMSSM". In: *JCAP* 05 (2008), p. 017. DOI: 10.1088/1475-7516/2008/05/017. arXiv: 0709.2091 [hep-ph].

[200] John Ellis, Marek Lewicki, and José Miguel No. "On the Maximal Strength of a First-Order Electroweak Phase Transition and its Gravitational Wave Signal". In: *JCAP* 04 (2019), p. 003. DOI: 10.1088/1475-7516/2019/04/003. arXiv: 1809.08242 [hep-ph].

[201] Peter Athron, Lachlan Morris, and Zhongxiu Xu. "How robust are gravitational wave predictions from cosmological phase transitions?" In: *JCAP* 05 (2024), p. 075. DOI: 10.1088/1475-7516/2024/05/075. arXiv: 2309.05474 [hep-ph].

[202] Mark Hindmarsh, Stephan J. Huber, Kari Rummukainen, and David J. Weir. "Shape of the acoustic gravitational wave power spectrum from a first order phase transition". In: *Phys. Rev. D* 96.10 (2017). [Erratum: Phys.Rev.D 101, 089902 (2020)], p. 103520. DOI: 10.1103/PhysRevD.96.103520. arXiv: 1704.05871 [astro-ph.CO].

[203] Chiara Caprini, Ruth Durrer, and Geraldine Servant. "The stochastic gravitational wave background from turbulence and magnetic fields generated by a first-order phase transition". In: *JCAP* 12 (2009), p. 024. DOI: 10.1088/1475-7516/2009/12/024. arXiv: 0909.0622 [astro-ph.CO].

[204] Pierre Auclair et al. "Generation of gravitational waves from freely decaying turbulence". In: *JCAP* 09 (2022), p. 029. DOI: 10.1088/1475-7516/2022/09/029. arXiv: 2205.02588 [astro-ph.CO].

[205] Huai-Ke Guo, Kuver Sinha, Daniel Vagie, and Graham White. "Phase Transitions in an Expanding Universe: Stochastic Gravitational Waves in Standard and Non-Standard Histories". In: *JCAP* 01 (2021), p. 001. DOI: 10.1088/1475-7516/2021/01/001. arXiv: 2007.08537 [hep-ph].

[206] John Ellis, Marek Lewicki, and José Miguel No. "Gravitational waves from first-order cosmological phase transitions: lifetime of the sound wave source". In: *JCAP* 07 (2020), p. 050. DOI: 10.1088/1475-7516/2020/07/050. arXiv: 2003.07360 [hep-ph].

[207] Jorinde van de Vis et al. "WallGo investigates: Theoretical uncertainties in the bubble wall velocity". In: (Oct. 2025). arXiv: 2510.27691 [hep-ph].

[208] K. Kajantie, M. Laine, K. Rummukainen, and Mikhail E. Shaposhnikov. "The Electroweak phase transition: A Nonperturbative analysis". In: *Nucl. Phys. B* 466 (1996), pp. 189–258. DOI: 10.1016/0550-3213(96)00052-1. arXiv: hep-lat/9510020.

[209] Oliver Gould et al. "Nonperturbative analysis of the gravitational waves from a first-order electroweak phase transition". In: *Phys. Rev. D* 100.11 (2019), p. 115024. DOI: 10.1103/PhysRevD.100.115024. arXiv: 1903.11604 [hep-ph].

[210] Mikael Chala, Luis Gil, and Zhe Ren. "Phase transitions in dimensional reduction up to three loops". In: *Chin. Phys.* 49.12 (2025), p. 123105. DOI: 10.1088/1674-1137/adf322. arXiv: 2505.14335 [hep-ph].

[211] J. O'Dwyer and H. Osborn. "Epsilon Expansion for Multicritical Fixed Points and Exact Renormalisation Group Equations". In: *Annals Phys.* 323 (2008), pp. 1859–1898. DOI: 10.1016/j.aop.2007.10.005. arXiv: 0708.2697 [hep-th].

[212] Samarth Kapoor and Shiroman Prakash. "Bifundamental multiscalar fixed points in d=3-ε". In: *Phys. Rev. D* 108.2 (2023), p. 026002. DOI: 10.1103/PhysRevD.108.026002. arXiv: 2112.01055 [hep-th].

[213] Johan Henriksson. "The tricritical Ising CFT and conformal bootstrap". In: *JHEP* 08 (2025), p. 031. DOI: 10.1007/JHEP08(2025)031. arXiv: 2501.18711 [hep-th].

[214] Eliel Camargo-Molina, Rikard Enberg, and Johan Löfgren. "A catalog of first-order electroweak phase transitions in the Standard Model Effective Field Theory". In: *JHEP* 08 (2025), p. 113. DOI: 10.1007/JHEP08(2025)113. arXiv: 2410.23210 [hep-ph].

[215] Gino Isidori, Felix Wilsch, and Daniel Wyler. "The standard model effective field theory at work". In: *Rev. Mod. Phys.* 96.1 (2024), p. 015006. DOI: 10.1103/RevModPhys.96.015006. arXiv: 2303.16922 [hep-ph].

[216] Martin B. Einhorn and Jose Wudka. "The Bases of Effective Field Theories". In: *Nucl. Phys. B* 876 (2013), pp. 556–574. DOI: 10.1016/j.nuclphysb.2013.08.023. arXiv: 1307.0478 [hep-ph].

[217] Johan Löfgren, Michael J. Ramsey-Musolf, Philipp Schicho, and Tuomas V. I. Tenkanen. "Nucleation at Finite Temperature: A Gauge-Invariant Perturbative Framework". In: *Phys. Rev. Lett.* 130.25 (2023), p. 251801. DOI: 10.1103/PhysRevLett.130.251801. arXiv: 2112.05472 [hep-ph].

[218] Andreas Ekstedt, Oliver Gould, and Johan Löfgren. "Radiative first-order phase transitions to next-to-next-to-leading order". In: *Phys. Rev. D* 106.3 (2022). [Erratum: Phys.Rev.D 110, 019901 (2024)], p. 036012. DOI: 10.1103/PhysRevD.106.036012. arXiv: 2205.07241 [hep-ph].

[219] Erick J. Weinberg. "Radiative corrections as the origin of spontaneous symmetry breaking". PhD thesis. Harvard U., 1973. arXiv: hep-th/0507214.

[220] Krzysztof A. Meissner and Hermann Nicolai. "Conformal Symmetry and the Standard Model". In: *Phys. Lett. B* 648 (2007), pp. 312–317. DOI: 10.1016/j.physletb.2007.03.023. arXiv: hep-th/0612165.

[221] Maciej Kierkla, Bogumila Swiezewska, Tuomas V. I. Tenkanen, and Jorinde van de Vis. "Gravitational waves from supercooled phase transitions: dimensional transmutation meets dimensional reduction". In: *JHEP* 02 (2024), p. 234. DOI: 10.1007/JHEP02(2024)234. arXiv: 2312.12413 [hep-ph].

[222] Andrei I. Davydychev and J. B. Tausk. "Two loop selfenergy diagrams with different masses and the momentum expansion". In: *Nucl. Phys. B* 397 (1993), pp. 123–142. DOI: 10.1016/0550-3213(93)90338-P.

[223] Adam Alloul et al. "FeynRules 2.0 - A complete toolbox for tree-level phenomenology". In: *Comput. Phys. Commun.* 185 (2014), pp. 2250–2300. DOI: 10.1016/j.cpc.2014.04.012. arXiv: 1310.1921 [hep-ph].

[224] Thomas Hahn. "Generating Feynman diagrams and amplitudes with FeynArts 3". In: *Comput. Phys. Commun.* 140 (2001), pp. 418–431. DOI: 10.1016/S0010-4655(01)00290-9. arXiv: hep-ph/0012260.

[225] Vladyslav Shtabovenko, Rolf Mertig, and Frederik Orellana. "FeynCalc 10: Do multiloop integrals dream of computer codes?" In: *Comput. Phys. Commun.* 306 (2025), p. 109357. DOI: 10.1016/j.cpc.2024.109357. arXiv: 2312.14089 [hep-ph].

[226] Renato M. Fonseca, Pablo Olgoso, and José Santiago. "Renormalization of general Effective Field Theories: formalism and renormalization of bosonic operators". In: *JHEP* 07 (2025), p. 135. DOI: 10.1007/JHEP07(2025)135. arXiv: 2501.13185 [hep-ph].

[227] M. Laine. "Exact relation of lattice and continuum parameters in three-dimensional SU(2) + Higgs theories". In: *Nucl. Phys. B* 451 (1995), pp. 484–504. DOI: 10.1016/0550-3213(95)00356-W. arXiv: hep-lat/9504001.

[228] K. Farakos, K. Kajantie, K. Rummukainen, and Mikhail E. Shaposhnikov. "3-d physics and the electroweak phase transition: A Framework for lattice Monte Carlo analysis". In: *Nucl. Phys. B* 442 (1995), pp. 317–363. DOI: 10.1016/0550-3213(95)80129-4. arXiv: hep-lat/9412091.

[229] C. Glenn Boyd, David E. Brahm, and Stephen D. H. Hsu. "Resummation methods at finite temperature: The Tadpole way". In: *Phys. Rev. D* 48 (1993), pp. 4963–4973. DOI: 10.1103/PhysRevD.48.4963. arXiv: hep-ph/9304254.

[230] Pablo Navarrete, Risto Paatelainen, Kaapo Seppänen, and Tuomas V. I. Tenkanen. "Cosmological phase transitions without high-temperature expansions". In: (July 2025). arXiv: 2507.07014 [hep-ph].

[231] Lucas G. Câmara, Marcus Benghi Pinto, and Rudnei O. Ramos. "Scale dependence improvement of the quartic scalar field thermal effective potential in the optimized perturbation theory". In: (Sept. 2025). arXiv: 2509.07250 [hep-ph].

[232] Yongzhao Zhu, Jie Liu, Renhui Qin, and Ligong Bian. "Theoretical uncertainties in first-order electroweak phase transitions". In: *Phys. Rev. D* 112.1 (2025), p. 015018. DOI: 10.1103/f4gr-hycg. arXiv: 2503.19566 [hep-ph].

[233] Andreas Ekstedt and Johan Löfgren. "On the relationship between gauge dependence and IR divergences in the $\hbar$-expansion of the effective potential". In: *JHEP* 01 (2019), p. 226. DOI: 10.1007/JHEP01(2019)226. arXiv: 1810.01416 [hep-ph].

[234] Renhui Qin and Ligong Bian. "First-order electroweak phase transition with a gauge-invariant approach". In: *Phys. Rev. D* 111.5 (2025), p. L051702. DOI: 10.1103/PhysRevD.111.L051702. arXiv: 2408.09677 [hep-ph].

[235] A. Ashoorioon and T. Konstandin. "Strong electroweak phase transitions without collider traces". In: *JHEP* 07 (2009), p. 086. DOI: 10.1088/1126-6708/2009/07/086. arXiv: 0904.0353 [hep-ph].

[236] Cheng-Wei Chiang, Michael J. Ramsey-Musolf, and Eibun Senaha. "Standard Model with a Complex Scalar Singlet: Cosmological Implications and Theoretical Considerations". In: *Phys. Rev. D* 97.1 (2018), p. 015005. DOI: 10.1103/PhysRevD.97.015005. arXiv: 1707.09960 [hep-ph].

[237] Felipe F. Freitas et al. "Impact of SM parameters and of the vacua of the Higgs potential in gravitational waves detection". In: *JCAP* 03.03 (2022), p. 046. DOI: 10.1088/1475-7516/2022/03/046. arXiv: 2108.12810 [hep-ph].

[238] Gi-Chol Cho, Chikako Idegawa, and Eibun Senaha. "Electroweak phase transition in a complex singlet extension of the Standard Model with degenerate scalars". In: *Phys. Lett. B* 823 (2021), p. 136787. DOI: 10.1016/j.physletb.2021.136787. arXiv: 2105.11830 [hep-ph].

[239] Wenxing Zhang, Yizhou Cai, Michael J. Ramsey-Musolf, and Lei Zhang. "Testing complex singlet scalar cosmology at the Large Hadron Collider". In: *JHEP* 01 (2024), p. 051. DOI: 10.1007/JHEP01(2024)051. arXiv: 2307.01615 [hep-ph].

[240] Dilip Kumar Ghosh, Debadrita Mukherjee, Koustav Mukherjee, and Rohan Pramanick. "Complex Scalar Singlet Model: Electroweak Phase Transition and Gravitational Waves". In: (Nov. 2025). arXiv: 2511.13426 [hep-ph].

[241] Minyuan Jiang, Ligong Bian, Weicong Huang, and Jing Shu. "Impact of a complex singlet: Electroweak baryogenesis and dark matter". In: *Phys. Rev. D* 93.6 (2016), p. 065032. DOI: 10.1103/PhysRevD.93.065032. arXiv: 1502.07574 [hep-ph].

[242] Vernon Barger et al. "Complex Singlet Extension of the Standard Model". In: *Phys. Rev. D* 79 (2009), p. 015018. DOI: 10.1103/PhysRevD.79.015018. arXiv: 0811.0393 [hep-ph].

[243] Giorgio Arcadi, Francesco Costa, Andreas Goudelis, and Oleg Lebedev. "Higgs portal dark matter freeze-in at stronger coupling: observational benchmarks". In: *JHEP* 07 (2024), p. 044. DOI: 10.1007/JHEP07(2024)044. arXiv: 2405.03760 [hep-ph].

[244] Christian Gross, Oleg Lebedev, and Takashi Toma. "Cancellation Mechanism for Dark-Matter–Nucleon Interaction". In: *Phys. Rev. Lett.* 119.19 (2017), p. 191801. DOI: 10.1103/PhysRevLett.119.191801. arXiv: 1708.02253 [hep-ph].

[245] Kristjan Kannike and Martti Raidal. "Phase Transitions and Gravitational Wave Tests of Pseudo-Goldstone Dark Matter in the Softly Broken U(1) Scalar Singlet Model". In: *Phys. Rev. D* 99.11 (2019), p. 115010. DOI: 10.1103/PhysRevD.99.115010. arXiv: 1901.03333 [hep-ph].

[246] Philipp Basler et al. "BSMPT v3 a tool for phase transitions and primordial gravitational waves in extended Higgs sectors". In: *Comput. Phys. Commun.* 316 (2025), p. 109766. DOI: 10.1016/j.cpc.2025.109766. arXiv: 2404.19037 [hep-ph].

[247] P. Basler et al. "Strong First Order Electroweak Phase Transition in the CP-Conserving 2HDM Revisited". In: *JHEP* 02 (2017), p. 121. DOI: 10.1007/JHEP02(2017)121. arXiv: 1612.04086 [hep-ph].

[248] Cédric Delaunay, Christophe Grojean, and James D Wells. "Dynamics of non-renormalizable electroweak symmetry breaking". In: *Journal of High Energy Physics* 2008.04 (2008), pp. 029–029. ISSN: 1029-8479. DOI: 10.1088/1126-6708/2008/04/029. URL: http://dx.doi.org/10.1088/1126-6708/2008/04/029.

[249] Lauri Niemi, Philipp Schicho, and Tuomas V. I. Tenkanen. "Singlet-assisted electroweak phase transition at two loops". In: *Phys. Rev. D* 103.11 (2021). [Erratum: Phys.Rev.D 109, 039902 (2024)], p. 115035. DOI: 10.1103/PhysRevD.103.115035. arXiv: 2103.07467 [hep-ph].

[250] Ansgar Denner, Georg Weiglein, and Stefan Dittmaier. "Application of the background field method to the electroweak standard model". In: *Nucl. Phys. B* 440 (1995), pp. 95–128. DOI: 10.1016/0550-3213(95)00037-S. arXiv: hep-ph/9410338.

[251] Philipp M. Schicho, Tuomas V. I. Tenkanen, and Juuso Österman. "Robust approach to thermal resummation: Standard Model meets a singlet". In: *JHEP* 06 (2021), p. 130. DOI: 10.1007/JHEP06(2021)130. arXiv: 2102.11145 [hep-ph].

[252] Erick J. Weinberg and Ai-qun Wu. "Understnading complex perturbative effective potentials". In: *Phys. Rev. D* 36 (1987), p. 2474. DOI: 10.1103/PhysRevD.36.2474.

[253] Lauri Niemi and Tuomas V. I. Tenkanen. "Investigating two-loop effects for first-order electroweak phase transitions". In: *Phys. Rev. D* 111.7 (2025), p. 075034. DOI: 10.1103/PhysRevD.111.075034. arXiv: 2408.15912 [hep-ph].

[254] Patrick Meade and Harikrishnan Ramani. "Unrestored Electroweak Symmetry". In: *Phys. Rev. Lett.* 122.4 (2019), p. 041802. DOI: 10.1103/PhysRevLett.122.041802. arXiv: 1807.07578 [hep-ph].

[255] Iason Baldes and Géraldine Servant. "High scale electroweak phase transition: baryogenesis \& symmetry non-restoration". In: *JHEP* 10 (2018), p. 053. DOI: 10.1007/JHEP10(2018)053. arXiv: 1807.08770 [hep-ph].

[256] Alfredo Glioti, Riccardo Rattazzi, and Luca Vecchi. "Electroweak Baryogenesis above the Electroweak Scale". In: *JHEP* 04 (2019), p. 027. DOI: 10.1007/JHEP04(2019)027. arXiv: 1811.11740 [hep-ph].

[257] Marcela Carena, Claudius Krause, Zhen Liu, and Yikun Wang. "New approach to electroweak symmetry nonrestoration". In: *Phys. Rev. D* 104.5 (2021), p. 055016. DOI: 10.1103/PhysRevD.104.055016. arXiv: 2104.00638 [hep-ph].

[258] Oleksii Matsedonskyi, James Unwin, and Qingyun Wang. "Electroweak symmetry non-restoration from dark matter". In: *JHEP* 12 (2021), p. 167. DOI: 10.1007/JHEP12(2021)167. arXiv: 2107.07560 [hep-ph].

[259] Thomas Biekötter et al. "Fate of electroweak symmetry in the early Universe: Non-restoration and trapped vacua in the N2HDM". In: *JCAP* 06 (2021), p. 018. DOI: 10.1088/1475-7516/2021/06/018. arXiv: 2103.12707 [hep-ph].

[260] Simone Blasi and Alberto Mariotti. "Domain Walls Seeding the Electroweak Phase Transition". In: *Phys. Rev. Lett.* 129.26 (2022), p. 261303. DOI: 10.1103/PhysRevLett.129.261303. arXiv: 2203.16450 [hep-ph].

[261] Chiara Caprini et al. "Reconstructing the spectral shape of a stochastic gravitational wave background with LISA". In: *JCAP* 11 (2019), p. 017. DOI: 10.1088/1475-7516/2019/11/017. arXiv: 1906.09244 [astro-ph.CO].

[262] Guy D. Moore. "Electroweak bubble wall friction: Analytic results". In: *JHEP* 03 (2000), p. 006. DOI: 10.1088/1126-6708/2000/03/006. arXiv: hep-ph/0001274.

[263] K. Farakos et al. "Results from 3-D electroweak phase transition simulations". In: *Nucl. Phys. B Proc. Suppl.* 47 (1996). Ed. by T. D. Kieu, B. H. J. McKellar, and A. J. Guttmann, pp. 705–708. DOI: 10.1016/0920-5632(96)00155-7. arXiv: hep-lat/9509086.

[264] Dietrich Bodeker. "From hard thermal loops to Langevin dynamics". In: *Nucl. Phys. B* 559 (1999), pp. 502–538. DOI: 10.1016/S0550-3213(99)00435-6. arXiv: hep-ph/9905239.

[265] Peter Brockway Arnold, Dam T. Son, and Laurence G. Yaffe. "Effective dynamics of hot, soft nonAbelian gauge fields. Color conductivity and log(1/alpha) effects". In: *Phys. Rev. D* 59 (1999), p. 105020. DOI: 10.1103/PhysRevD.59.105020. arXiv: hep-ph/9810216.

[266] Gert Aarts and Jan Smit. "Finiteness of hot classical scalar field theory and the plasmon damping rate". In: *Physics Letters B* 393.3–4 (Feb. 1997), pp. 395–402. ISSN: 0370-2693. DOI: 10.1016/s0370-2693(96)01624-3. URL: http://dx.doi.org/10.1016/S0370-2693(96)01624-3.

[267] Takahiro Kubota. "Green's functions in the presence of a bubble wall". In: *JHEP* 07 (2024), p. 290. DOI: 10.1007/JHEP07(2024)290. arXiv: 2406.00668 [hep-th].

[268] I. G. Moss, D. J. Toms, and W. A. Wright. "The Effective Action at Finite Temperature". In: *Phys. Rev. D* 46 (1992), pp. 1671–1679. DOI: 10.1103/PhysRevD.46.1671.

[269] Andreas Ekstedt. "Higher-order corrections to the bubble-nucleation rate at finite temperature". In: *Eur. Phys. J. C* 82.2 (2022), p. 173. DOI: 10.1140/epjc/s10052-022-10130-5. arXiv: 2104.11804 [hep-ph].

[270] Andreas Ekstedt. "Convergence of the nucleation rate for first-order phase transitions". In: *Phys. Rev. D* 106.9 (2022), p. 095026. DOI: 10.1103/PhysRevD.106.095026. arXiv: 2205.05145 [hep-ph].

[271] Wen-Yuan Ai, Bjorn Garbrecht, and Carlos Tamarit. "Bubble wall velocities in local equilibrium". In: *JCAP* 03.03 (2022), p. 015. DOI: 10.1088/1475-7516/2022/03/015. arXiv: 2109.13710 [hep-ph].

[272] Glauber C. Dorsch, Stephan J. Huber, and Thomas Konstandin. "A sonic boom in bubble wall friction". In: *JCAP* 04.04 (2022), p. 010. DOI: 10.1088/1475-7516/2022/04/010. arXiv: 2112.12548 [hep-ph].